Faculty of Engineering Science
Departtment of Chemical Engineering
SMaRT Division
Celestijnenlaan 200J
B-3001 HEVERLEE, BELGIUM
tel. + 32 16 32 23 42
https://cit.kuleuven.be/smart

Alexis André

INVESTIGATING THE LINEAR AND NONLINEAR RHEOLOGY OD MODEL POLYMER MELTS

November 2023

KU LEUVEN

ARENBERG DOCTORAL SCHOOL
FACULTY OF ENGINEERING SCIENCE

Investigating the linear and nonlinear rheology of model polymer melts

Alexis André

Supervisors:
Prof. Christian Clasen
Prof. Evelyne van Ruymbeke

Dissertation presented in partial fulfilment
of the requirements for the degree of
of Engineering Science (PhD):
Chemical Engineering

November 2023

Investigating the linear and nonlinear rheology of model polymer melts

Alexis André

Supervisors:
Prof. Christian Clasen (KULeuven)
Prof. Evelyne van Ruymbeke (UCLouvain)

Members of the Examination Committee:
Prof. Ruth Cardinaels (KULeuven)
Prof. Charles-André Fustin (UCLouvain)
Prof. Michel Cloitre (ESPCI Paris, France)
Dr. Filip Oosterlinck (DSM Materials, The Netherlands)

Dissertation presented in partial fulfilment of the requirements for the degree of Doctor of Engineering Science (PhD): Chemical Engineering

November 2023

Uitgegeven in eigen beheer, Alexis André, Louvain-la-Neuve

Acknowledgments

I would like to warmly thank my supervisors, Prof. Evelyne van Ruymbeke and Prof. Christian Clasen, for their guidance, support and insightful feedback throughout my PhD journey. I truly appreciate the freedom you have given me on this project. To Evelyne, thank you for introducing me to the world of molecular rheology. Throughout these years, I have greatly valued your kindness, accessibility, and enthusiasm for the research. To Christian, thank you for the warm welcome you provided in the SMaRT lab. I am also grateful for the scientific discussions and your help for proofreading the manuscripts.

I am also thankful to the other members of my examination committee, Prof. Charles-André Fustin, Prof. Ruth Cardinaels, Prof. Michel Cloitre and Dr. Filip Oosterlinck for their valuable suggestions that enriched the quality of this thesis. I would also like to express my gratitude to Prof. Adhemar Bultheel for chairing this committee.

I extend my thanks to Prof. Richard Hoogenboom and Dr. Jente Verjans for the stimulating collaboration on the rheology of supramolecular polymers., as well as Prof. Salvatore Costanzo for helping me familiarize myself with nonlinear shear measurements.

Next, I wish to thank the lab managers and technicians, Naima and Pascal at UCLouvain, and Anja and Carlo at KULeuven for their help in resolving the technical problems that happen too often during a PhD thesis.

My heartfelt thanks also go to Anne, Rose-Anne, Beatrice, Ann, and Michelle

for their assistance with the complex administrative procedures associated with a joint PhD.

A special mention to my lab mates from both the IMCN institute and the SMaRT group for creating an enjoyable and stimulating atmosphere. The engaging discussions and moments of laughter made the challenges of research more bearable. I especially want to mention the the "pre-COVID generation" at UCLouvain: Clément, Rowanne, Nicolas, Céline, Maxime, Nuofei, Sina, Taisir, and Yanzhao, as well as the post-COVID one: Alex, Pierrot, and Anahita. I would also like to mention my office mates at KULeuven: Yanshen, Pramod, Margot, Pramod, Luca, Jarno, and Sebastian and the other members of the SMaRT lab who contributed to the nice atmosphere in the SMaRT group: Kenneth, Iurii, Jessica, Alina, Maxwell, Stijn, Benedetta, Souhaila, Hamza, Stelios, Jens, Iurii, Tess, An-Sofie, Lingyue, Xiangmeng, Tobias, Vince, Jelle, and Charlotte.

Last but not least, I want to express my gratitude to my family for their invaluable support and continuous encouragement.

Summary

The aim of this PhD project is to bring new insight to understand the rheological properties of polymeric systems at the molten state. The flow properties of well-defined polymeric melts are studied based on a set of different rheological techniques. In most instances, these rheological experiments are combined with predictions of molecular models to effectively capture the diverse contributions that influence the material's rheological response. These contributions arise from factors such as the segmental motion of chains, the disentanglement process, and the dissociation of the supramolecular junctions. The ultimate goal is to develop general guidelines for controlling the design of polymeric materials based on a deep understanding of their rheological behavior.

This PhD dissertation is divided into eight chapters. The first two chapters introduce the fundamental concept of viscoelasticity, review molecular models used to describe the rheological responses of polymeric melts and associative polymers, and present the experimental techniques used in this work. After this introductory section, the manuscript transitions to the experimental part. This part is organized in such a manner that the studied systems become increasingly complex.

In Chapter 3, we investigate the elongation properties of linear polystyrene (PS) melts of different molar masses, diluted or not, in styrene oligomers at various concentration. This systematic study allows a discussion on the influence of concentration and molar mass on the steady-state elongational viscosity of polymer melts and to highlight scaling relations. The resulting scaling laws

are then rationalised based on the theories presented in the introduction. This investigation effectively stresses the influence of the molecular environment on the stretching of the polymeric chains in extensional flow.

Then, in Chapter 4, the linear rheology of unentangled associative polymer based on ureidopyrimidinone (UPy) moieties is modelled using a modified "sticky Rouse" model proposed in the literature. This sticky Rouse model considers the non-affine spatial fluctuation of the supramolecular junctions, the random placement of the junctions, as well as the contributions of the dangling ends. The resulting model was found to capture accurately the experimental results.

Afterwards, in Chapter 5, we investigate the linear rheology of entangled associative systems based on metal-ligand coordination. The tailorable properties of these systems are explored by varying the quantity and the nature of the metal ions. The viscoelastic responses are subsequently successfully modelled by adapting the tube-based time marching algorithm (TMA) developed by van Ruymbeke *et al.*[1] to these supramolecular systems.

In Chapter 6, the linear and nonlinear shear rheology of unentangled associative polymers based on metal-ligand complexations is studied. The viscoelastic responses observed in these systems exhibit intriguing characteristics, such as an unusually high rubbery plateau, a transient strain hardening behavior, as well as an yield strain that remains independent of the applied strain rate. These features are discussed based on the molecular theories outlined in the introduction of this manuscript.

Subsequently, in Chapter 7, an experimental route is proposed to investigate the shear properties of unentangled polymeric melts in fast flows. This investigation includes the design of a novel rheometer tool, which aims to perform orthogonal superposition measurements on high viscous samples. This design is subsequently validated using computational fluid dynamics (CFD) simulations.

In conclusion, Chapter 8 provides a comprehensive summary of the contributions presented in this PhD dissertation, along with potential future prospects.

Table of contents

List of abbreviations and symbols

Abbreviations

Symbol	Definition
AA	Acrylic acid
BDS	Broadband dielectric spectroscopy
CFD	Computational fluid dynamics
CLF	Contour length fluctuation
CCR	Convective constraint release
CPP	Cone-partitioned plate
CR	Constraint release
CR-Rouse	Constraint release Rouse
DE	Doi-Edwards
DEMG	Doi-Edwards-Marrucci-Grizzuti
DEP	Diethyl phthalate
DMA	Dynamic mechanical analysis
DSC	Differential scanning calorimetry
DTD	Dynamic tube dilation
EIP	Extended interchain pressure
FENE	Finite extensible nonlinear Elasticity
FSR	Filament stretching rheometer

GLaMM	Graham-Likthman-McLeish-Milner
HEUR	Hydrophobically modified urethane-ethoxylate
IP	Interchain pressure
KWW	Kohlrausch-Williams-Watts
LAOS	Large amplitude oscillatory shear
LVE	Linear viscoelastic
MD	Molecular dynamics
MLD	Mead-Larson-Doi
MSBP	Metallo-supramolecular bulk polymer
NEMD	Non-equilibrium molecular dynamics
NGC	Narrow gap Couette
NLVE	Nonlinear viscoelastic
NMR	Nuclear magnetic resonance
ODTT	Order-disorder transition Temperature
OS	Oligomeric styrene
OSR	Orthogonal superposition
PB	Polybutadiene
PBA	Poly(butyl acrylate)
PCN	Primitive chain network
PDMS	Polydimethylsiloxane
PI	Polyisoprene
PMA	Poly (methyl acrylate)
PMMA	Polymethyl methacrylate
PSMA-Na	Poly(styrene-co-sodium methacrylate)
PSR	Parallel superposition
PtBS	Poly(tert-butylstyrene)
PVA	Poly(vinyl alcohol)
RAFT	Reversible addition-fragmentation chain-transfer
SAOS	Small amplitude oscillatory shear
SAXS	Small-angle X-ray scattering
SEC	Size exclusion chromatography
TDD	Time-dependent diffusion
THF	Tetrahydrofuran

TMA	Time marching algorithm
tpy	Terpyridine
TSRS	Time-shear rate superposition
TTS	Time temperature superposition
UPy	Ureidopyrimidinone
WLF	Williams-Landel-Ferry

Roman symbols

Symbol	Definition	SI unit
a	Tube diameter	[m]
a_0	Initial tube diameter	[m]
a_T, a'_T, a_{T_g}	Horizontal shift factor	[-]
A	Surface area	[m^2]
A_{nm}	Rouse matrix	[-]
b	Length of a Kuhn segment	[m]
B	Squared Brownian force intensity	[N^2]
$\mathbf{C^{-1}}$	Finger strain tensor	[-]
c_1	Empirical parameter in the WLF equation	[-]
c_2	Empirical parameter in the WLF equation	[K]
D	Diffusion coefficient	[m^2/s]
D_c	Diffusion coefficient of the center of mass	[m^2/s]
De	Deborah number	[-]
E_a	Activation energy	[J/mol]
E_{bind}	Binding energy	[J/mol]
F	Force	[N]
F_B	Thermal force	[N]
F^{so}	Order parameter	[-]
F_c^{so}	Critical order parameter	[-]
Đ	Polydispersity index	[-]
g	Gravitational acceleration	[m/s^2]
g	Number of Kuhn segments per spring	[-]

G	Shear modulus	[Pa]
G'	Storage modulus	[Pa]
G''	Loss modulus	[Pa]
$G'_{\parallel}$	Parallel storage modulus	[Pa]
$G''_{\parallel}$	Parallel loss modulus	[Pa]
$G'_{\perp}$	Orthogonal storage modulus	[Pa]
$G''_{\perp}$	Orthogonal loss modulus	[Pa]
G_e	Entanglement modulus	[Pa]
G_g	Glassy modulus	[Pa]
G'_{KWW}	Storage modulus defined by KWW function	[Pa]
G''_{KWW}	Loss modulus defined by KWW function	[Pa]
G_N^0	Plateau modulus	[Pa]
G_{Rouse}	Rouse modulus	[Pa]
G_{SR}	Sticky Rouse modulus	[Pa]
Gr	Graessley number	[-]
Gr_c	Critical Graessley number	[-]
k	Spring constant	[N/m]
$\mathbf{K}$	Velocity gradient tensor	[1/s]
K_1 or K_2	Equilibrium constant	[m^3/mol]
K_{ass}	Association constant	[m^3/mol]
l	Entanglement length	[m]
L	Length of the sample	[m]
L_0	Initial length of the sample	[m]
L_{cyl}	Length of the cylinder	[m]
L_{eq}	Equilibrium length of the primitive path	[m]
L_{pp}	Length of the primitive path	[m]
m	Mass of the sample	[kg]
M	Molar mass	[kg/mo]
M_i	Torque	[N.m]
M_e	Molar mass between entanglements	[kg/mol]
$M_{e,0}$	Initial molar mass between entanglements	[kg/mol]
M_s	Molar mass between stickers	[kg/mol]
M_n	Number average molar mass	[kg/mol]

M_w	Weight average molar mass	[kg/mol]
M_K	Molar mass of a Kuhn segment	[kg/mol]
M_L	Molar mass of the long components	[kg/mol]
M_S	Molar mass of the short components	[kg/mol]
M_{UPy}	Molar mass between UPy groups	[kg/mol]
n	Power law index	[-]
N	Number of Kuhn segments per chain	[-]
N_e	Number of Kuhn segments per entanglement strand	[-]
N_s	Number of stickers per chain	[-]
N_{agg}	Number of stickers per aggregate	[-]
N_{part}	Number of available partners	[-]
N_{ret}	Number of returns	[-]
N_{rev}	Rotational speed	[1/s]
p	Fraction of sticky beads	[-]
p_{free}	Fraction of open stickers	[-]
p_{surv}	Survival fraction of the initial tube	[-]
p_R	Probability of return	[-]
p_{CLF}	Survival probability of a segment by fluctuation	[-]
p_{rep}	Survival probability of a segment by reptation	[-]
p_{free}	Rouse modulus	[Pa]
$P(X)$	Probability density function	[-]
$\mathbf{q}$	Position of a sticky bead	[m]
$\mathbf{r}$	Position of a bead	[m]
r_B	Ratio of B under flow to that at equilibrium	[-]
r_ζ	Ratio of ζ under flow to that at equilibrium	[-]
r_κ	Ratio of κ under flow to that at equilibrium	[-]
$R(t)$	Radius of the sample	[m]
R_i	Radius of the inner cylinder	[m]
R_0	Radius of the outer cylinder	[m]
R_0	Initial radius	[m]
$\mathbf{S}$	Orientation tensor	[-]
t	Time	[s]
t', t''	Shift factors	[s]

T	Temperature	[K]
T_g	Glass transition temperature	[K]
T_{ref}	Reference temperature	[K]
Tr	Trouton number	[-]
u	Spring length	[m]
U	Potential energy	[J]
$\mathbf{v}$	Velocity vector	[m/s]
V_{strand}	Volume of a network strand	[m^3]
$\mathbf{W}$	Conformation tensor	[-]
Wi_d	Reptation Weissenberg number	[-]
Wi_R	Rouse Weissenberg number	[-]
x_{trans}	Transition fluctuation depth	[-]
z_0	Axial displacement	[m]
Z, Z_e	Number of entanglements per chain	[-]

Greek symbols

Symbol	Definition	SI unit
α	Dynamic dilation exponent	[-]
γ or γ_0	Shear strain	[-]
$\dot{\gamma}$	Shear rate	[s^{-1}]
γ_{max}	Yield strain	[-]
δ	Loss angle	[-]
δ	Time step	[s]
δ	Radius ratio	[-]
ϵ	Hencky strain	[-]
$\dot{\epsilon}$	Hencky strain rate	[s^{-1}]
ζ	Friction coefficient	[kg/s]
ζ_0	Monomeric friction coefficient	[kg/s]
ζ_{eq}	Monomeric friction coefficient at equilibrium	[kg/s]
η	Viscosity	[Pa · s]
η_0	Zero-shear viscosity	[Pa · s]

η^+	Shear stress growth coefficient	[Pa · s]
η_E	Extensional viscosity	[Pa · s]
η_E^+	Tensile stress growth viscosity	[Pa · s]
η_{max}	Peak viscosity	[Pa · s]
κ	Spring constant	[N/m]
λ	Stretch ratio	[-]
λ_{max}	Maximum stretch ratio	[-]
λ_p	p^{th} non zero eigenvalue of the Rouse-Zimm matrix	[-]
Λ_0	Initial aspect ratio	[-]
μ	Unrelaxed fraction of the initial tube	[-]
ν	Volume fraction	[-]
ρ	Density	[kg/m^3]
$\boldsymbol{\sigma}$	Stress tensor	[Pa]
τ or τ_0	Shear stress	[Pa]
τ	Relaxation time	[s]
τ_0	Kuhn segment relaxation time	[s]
τ_b	Bond lifetime	[s]
τ_d	Disengagement time	[s]
τ_e	Rouse relaxation time between two entanglements	[s]
τ_e^*	Sticky Rouse relaxation time between entanglements	[s]
τ_p	Rouse time of a sub-chain of N/p Kuhn segments	[s]
τ_s	Retraction time	[s]
τ_w	Weight average relaxation time	[s]
τ_{fluc}	Fluctuation time	[s]
τ_{rep}	Reptation time	[s]
τ_{rep}^*	Sticky reptation time	[s]
$\tau_{activated}$	Activated fluctuations time	[s]
τ_{early}	Early fluctuations time	[s]
τ_{open}	Duration of the open stage	[s]
τ_R	Rouse relaxation time	[s]
τ_S	Sticker lifetime	[s]
τ_{rel}	Relaxation time	[s]
ϕ	Survival fraction of the initial tube	[-]

ϕ	Volume fraction of the polymeric chains	[-]
ϕ_{open}	Concentration of open stickers	[-]
Φ	Unrelaxed fraction of a polymer	[-]
ω	Angular frequency	[s^{-1}]

Constants

Symbol	Definition	Value
k_B	Boltzmann constant	1.3806×10^{-23} JK^{-1}
N_A	Avogadro constant	6.022×10^{23} mol^{-1}
R	Ideal gas constant	8.314 J $K^{-1}mol^{-1}$

Chapter 1

State of the art

1.1 Introduction

Nowadays, polymeric materials are ubiquitous, finding their application in a large variety of fields such as packaging, biomedical devices, advanced electronics, automative industry or textile industry. Their extensive usage is due, in part, to their ease of processing.

However, in many of the polymer processing methods, the occurrence of flow instabilities limits the maximum throughput, thereby affecting the process efficiency. For instance, during the extrusion of thermoplastics, the extrudates can experience distortions that span from minor scratches and roughness to large irregularities in cross-sectional area and shape in the case of excessive throughputs (see Figure 1.1 (a)). In melt spinning, a flow instability known as "draw resonance" can occur beyond a specific take-up speed, causing periodic variations in the fiber radius (see Figure 1.1 (b)). Research has indicated that the elastic response of polymeric fluids plays a crucial role in stabilizing draw resonance. This explains why highly branched melts, such as low-density polyethylenes (LDPE), exhibit enhanced stability against draw resonance compared to less branched polymers like high-density polyethylene (HDPE) or lin-

ear low-density polyethylene (LLDPE). The presence of branching in polymers promotes "extension thickening", which means an increase in extensional viscosity with the strain. In the industrial context, extensional thickening is often seen as a coveted property as it is stabilizing factor in numerous processing methods.[2-5]

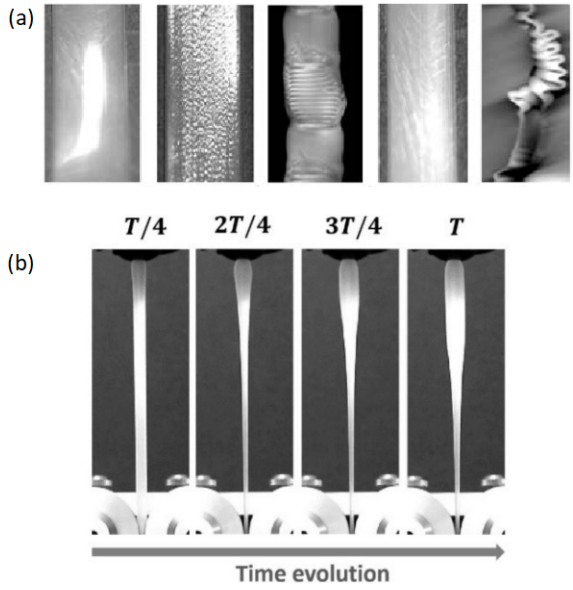

Figure 1.1: Examples of instabilities in polymer processing : (a) Extrusion instabilities observed for polyethylene. In the first photo, the extrudate appears defect-free. (b) Draw resonance instability during melt spinning, captured within one period of oscillation. Panel (a) is adapted from [6] and Panel (b) is adapted from [7].

These examples highlight the significance of understanding the flow dynamics of polymers for optimizing industrial processing techniques. Rheology, the science of flow and deformation of matter, plays an important role in this regard by developing constitutive models that relate the stress response of polymer fluids and their deformation history. These models not only contribute to enhancing processability but can also aid in designing new materials with enhanced mechanical strength.

In this work, our focus lies on molecular constitutive equations that bridge the gap between the macroscopic viscoelastic properties of polymers and the dynamics of polymeric chains at the molecular level. Additionally, our experimental investigation will center on examining the flow behavior of polymeric melts in shear and uniaxial extension flow, as many industrial processes often involve complex flows that combine these two types of flow.

In this chapter, we will begin by providing an overview of the flow kinematics and material functions associated with simple shear and uniaxial extension flows. We will then introduce the fundamental concepts of linear and nonlinear viscoelasticity. Afterward, we will review molecular rheological models designed for polymer melts and supramolecular polymers.

1.2 Description of the flows

This section contains established knowledge, which is summarized in reference textbooks.[8-10]

1.2.1 Simple shear flow

Figure 1.2 presents an illustrative example of a typical rheological experiment for the simple shear deformation. In this experiment, a fluid is placed between two parallel plates with an area dA separated by a distance dy. While one plate remains stationary, the other plate moves a distance dx, resulting in a shear strain equal to $\gamma_{xy} = \dfrac{dx}{dy}$.

The velocity field of the flow can thus be expressed as follows:

$$v_x = \dot{\gamma} y \qquad v_y = 0 \qquad v_z = 0 \tag{1.1}$$

Here $\dot{\gamma}$ represents the shear rate, which is time derivative of the strain γ_{xy}.

In order to displace the top parallel plate, a force dF is required. The shear stress, defined as the ratio of the force dF to the area dA, is directly related

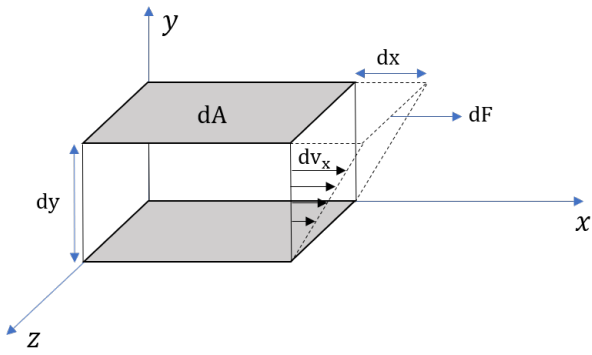

Figure 1.2: Scheme of a shear flow.

to the shear rate via a time-dependent function known as the stress growth coefficient $\eta^+(t,\dot{\gamma})$.

$$\tau_{xy} = \frac{d\mathrm{F}}{d\mathrm{A}} = \eta^+(t,\dot{\gamma})\dot{\gamma} \tag{1.2}$$

If the shear flow is continued until reaching a steady-state, $\eta^+(t,\dot{\gamma})$ becomes time-independent and equal to the viscosity of the fluid $\eta(\dot{\gamma})$.

Consider a fluid element initially located at $(x,y) = (0,y_0)$. Its position at a later time t is given by $(x,y) = (\dot{\gamma}y_0t, y_0)$. This illustrates that, in shear flow, the fluid elements are separated linearly in time. Such flows are called "weak flows" because they alter with difficulty the internal structure of a fluid.

As shown in Figure 1.3, simple shear flow is a combination of rotational and elongational flows, which play a crucial role in the deformation of polymeric chains. Specifically, when exposed to shear flow, polymeric chains tend to orient and stretch. However, the rotational component of the flow induces deviations from the direction of greatest stretch, causing the chains to tumble. This tumbling phenomenon limits the extent of chain stretching. Consequently, the chains undergo a succession of stretch/compression cycles as shown in panel (b) of Figure 1.3.

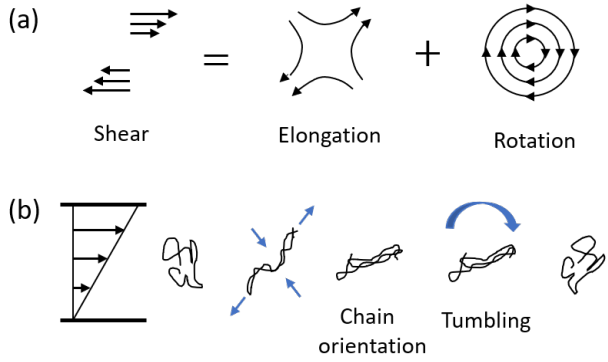

Figure 1.3: (a) Shear flow is a combination of rotational and elongational components. (b) Illustration of a polymeric coil under shear flow. Adapted from [11].

1.2.2 Uniaxial extensional flow

Figure 1.4 depicts a fluid subjected to a uniaxial extensional flow. The sample of initial length L_0 undergoes elongation along the z axis while, experiencing contraction along the two remaining axis due to volume conservation.

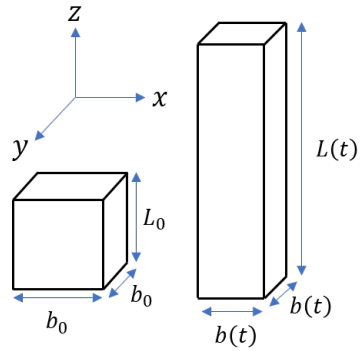

Figure 1.4: Scheme of a uniaxial extensional flow

In the case of an incompressible fluid, the velocity field in an uniaxial exten-

sional flow is described by the following equations:

$$v_x = -\dot{\epsilon}x/2 \qquad v_y = -\dot{\epsilon}y/2 \qquad v_z = \dot{\epsilon}z \tag{1.3}$$

In this context, the elongational strain rate $\dot{\epsilon}$ is assumed to be constant and defined as follows:

$$\dot{\epsilon} = \frac{1}{L}\frac{dL}{dt}, \tag{1.4}$$

Here, L denotes the length of the sample at time t.

Upon integrating equation 1.3, it can be observed that that the fluid elements separate exponentially in time.

$$x(t) = x_0 \exp(-\dot{\epsilon}t/2) \qquad y(t) = y_0 \exp(-\dot{\epsilon}t/2) \qquad z(t) = z_0 \exp(\dot{\epsilon}t) \tag{1.5}$$

Consequently, uniaxial extension is characterized by a strong stretching, making it effective at orienting and stretching polymeric chains. Unlike shear flow, extensional flow does no have vorticity and thus leads to a continuous stretching of the chains, as illustrated in Figure 1.5.

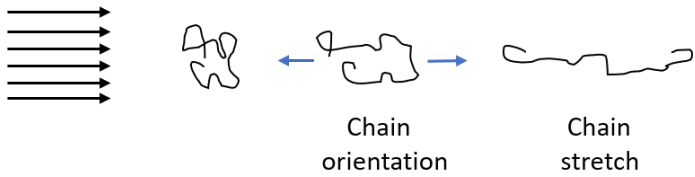

Figure 1.5: Illustration of polymeric coils under uniaxial extensional flow. Adapted from [9].

As for shear flow, the extensional stress growth coefficient $\eta_E^+(t, \dot{\epsilon})$ is defined as follows:

$$\sigma_z - \sigma_x = \eta_E^+(t, \dot{\epsilon})\dot{\epsilon} \tag{1.6}$$

When steady extensional flow is achieved, $\eta_E^+(t, \dot{\epsilon})$ becomes time independent

and equal to the extensional viscosity of the fluid $\eta_E(\dot{\epsilon})$.

1.3 The Pipkin diagram

Characterisation of polymeric fluids involves a large variety of rheological experiments. These experiments can be classified into different flow regimes by assigning them a strain amplitude γ_0 and a characteristic timescale τ_{exp}. The time τ_{exp} is often combined with the characteristic relaxation time of the measuring fluid τ_{rel} to express the dimensionless number $De = \dfrac{\tau_{rel}}{\tau_{exp}}$ called Deborah number. To visually represent the various flow regimes, a two-dimensional graph known as the Pipkin diagram (depicted in Figure 1.6) is commonly used.[12] In this diagram, the vertical axis corresponds to the strain amplitude γ_0, while the horizontal axis represents the Deborah number De.

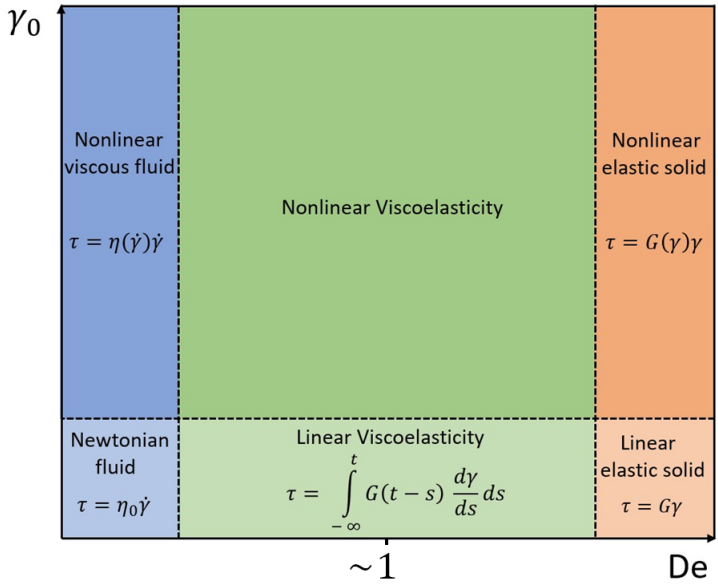

Figure 1.6: Pipkin diagram. Adapted from [12].

In this diagram, the limit of small strains, indicated by the light-colored regions, corresponds to the linear regime, where the deformation is sufficiently small to not modify the internal structure of the material. This region is often used to

characterize the material at equilibrium.

In the linear regime, at low De, the material adopts a viscous behavior with a constant viscosity η_0, in a similar way to a Newtonian fluid. Its stress response is therefore directly proportional to the strain rate and the energy of deformation is dissipated through the friction between the molecules. In contrast, when $De \gg 1$, the material behaves as an elastic solid and follows Hooke's laws. Much like a spring, the stress is proportional to the strain, and the energy of deformation is stored in the material. Between these two extremes, the material adopts an intermediate behavior known as linear viscoelasticity.

As the strain amplitude γ_0 is increased, we transition into the nonlinear regime of deformation, where the internal state of the material is significantly modified. In the case of polymeric fluids, the constituent polymer chains undergo orientation and stretching as discussed earlier. These effects have a profound impact on the flow behavior of the material. Most of the industrial polymer processes operate in this regime.

In a similar fashion to the linear regime, the left edge corresponds to the limit of pure viscous behavior, while, along the right edge, a pure elastic behavior is restored. Also, when large deformation γ_0 is applied at intermediate De, nonlinear viscoelastic behavior starts to manifest.

The rheometric flows typically cover the linear and nonlinear viscoelastic regions, which are represented by the green area in the Pipkin diagram. The upcoming sections specifically focus on important aspects of the linear and nonlinear viscoelastic regimes of polymeric melts.

1.4 Linear viscoelasticity

In a relaxation test, a constant and sudden strain of magnitude γ_0 is applied and the resulting stress response is measured over time. This experiment allows for the determination of the relaxation modulus $G(t)$ which is defined as the

ratio of the stress to the strain.

$$G(t) = \frac{\tau(t)}{\gamma_0} \tag{1.7}$$

In the linear regime of deformation, the stress at time t arising from a small shear strain $\delta\gamma$ applied at time $t' < t$ is given by

$$\tau(t) = G(t - t')\delta\gamma_i \tag{1.8}$$

If N small deformations $\delta\gamma(t_i)$ are applied in the past at various time t_i, the resulting stress at time t is obtained by summing all the individual stress contributions arising from these incremental shearing deformations.

$$\tau(t) = \sum_{i=1}^{N} G(t - t')\delta\gamma_i(t') \qquad \text{for} \quad t > t_N \tag{1.9}$$

By letting $\delta\gamma(t_i)$ approaches zero and N approaches infinity, the stress response can be evaluated by the following integral.

$$\tau(t) = \int_{-\infty}^{t} G(t - s)\frac{d\gamma}{ds}ds \tag{1.10}$$

This equation can then be generalized to different types of flows by replacing the stress τ and the strain γ by the stress tensor σ_{ij} and the infinitesimal strain tensor γ_{ij}.

$$\sigma_{ij}(t) = \int_{-\infty}^{t} G(t - s)\dot{\gamma}_{ij}(s)ds \tag{1.11}$$

This constitutive equation represents the general form of the "Boltzmann superposition principle". This principle holds true when the response of the material is linear and time-invariant. An important implication of this principle is that the relaxation modulus $G(t)$ contains all the necessary information to fully characterize the linear viscoelastic behavior of the material.

For example, in a simple shear flow with a constant shear rate, the Boltzmann superposition principle (equation 1.11) predicts the following expression for the

stress growth coefficient :

$$\eta^{+}(t) = \frac{\sigma(t)}{\dot{\gamma}} = \int_{-\infty}^{t} G(s)ds \tag{1.12}$$

On the other hand, in the case of a uniaxial extensional flow, equation 1.11 yields the following expression for the extensional stress growth coefficient.

$$\eta_E^{+}(t) = \frac{\sigma_{zz} - \sigma_{xx}}{\dot{\epsilon}} = 3\int_{-\infty}^{t} G(s)ds \tag{1.13}$$

Dividing equations 1.13 by equation 1.12 results in the following ratio commonly referred to as the Trouton ratio Tr.

$$Tr = \frac{\eta_E^{+}(t)}{\eta^{+}(t)} = 3 \tag{1.14}$$

The Trouton ratio is an important result which allows to relate the extensional properties with the shear properties in the linear regime.

A popular phenomenological model that is used to describe the linear response of polymeric fluids is the generalized Maxwell model. In this model, the relaxation modulus $G(t)$ is expressed as the following sum of exponentials.

$$G(t) = \sum_{k=1}^{N} G_k \exp\left(-\frac{t}{\tau_k}\right) \tag{1.15}$$

Each term in the sum corresponds to a specific relaxation mode, characterized by a time constant τ_k and a front factor G_k. The set of parameters $[G_i,\tau_i]$ defines the discrete relaxation spectrum of a material.

Using the Boltzmann superposition principle, the generalized Maxwell model predicts the following expression for the extensional stress growth coefficient.

$$\eta_E^{+}(t) = 3\sum_{k=1}^{N} G_k\tau_k \left(1 - \exp\left(-\frac{t}{\tau_k}\right)\right) \tag{1.16}$$

As observed in Figure 1.7, the prediction of the generalized Maxwell model fits very well the extensional response of polymeric materials at low rates or small deformation. The rapid increase of the experimental data obtained at higher deformations indicates the onset of nonlinear viscoelastic behavior.

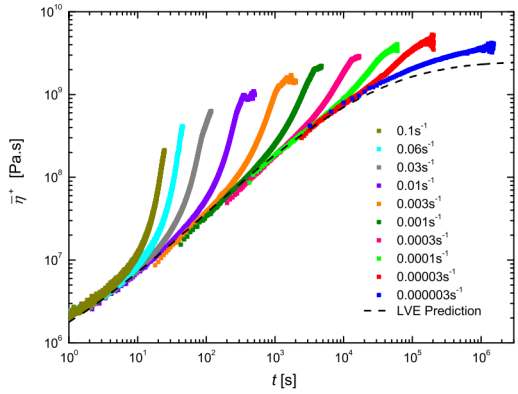

Figure 1.7: The extensional stress growth coefficient $\eta_E^+(t)$ of polystyrene at various stretching rates. The dashed lines are obtained using equation 1.16. Reproduced from [13].

1.4.1 Small amplitude oscillatory shear (SAOS)

In practice, applying a step strain to determine $G(t)$ is not the most optimal method for characterizing the linear viscoelastic regime. In this approach, accurately probing the early relaxation is challenging due to the difficulty in generating an instantaneous deformation. Additionally, at longer times, the signal becomes noisy, complicating the acquisition of accurate data for the terminal regime.

An alternative and widely used experiment method to characterize the linear response is small amplitude oscillatory shear (SAOS). This approach involves applying a sinusoidal signal, either shear strain or shear stress, to the sample. In the case of a strain-controlled experiment, a sinusoidal strain $\gamma = \gamma_0 \sin(\omega t)$ is imposed to the sample in the linear regime of deformation. The resulting

shear stress is also sine wave, but phase-shifted by an angle δ.

$$\tau(t) = \tau_0 \sin(\omega t + \delta) \tag{1.17}$$

Using classical trigonometric identities, the shear stress can be decomposed into two components : one that is in phase with the strain and one that is delayed by 90° with respect to the strain.

$$\tau(t) = \tau_0(\cos(\delta)\sin(\omega t) + \sin(\delta)\cos(\omega t)) \tag{1.18}$$

These components can be represented by two material functions : the storage modulus $G'(\omega)$ and the loss modulus $G''(\omega)$ in the following way.

$$\tau(t) = \gamma_0(G'(\omega)\sin(\omega t) + G''(\omega)\cos(\omega t)) \tag{1.19}$$

Here $G'(\omega)$ and $G''(\omega)$ are given by

$$G'(\omega) = \frac{\tau_0}{\gamma_0}\cos(\delta) \qquad G''(\omega) = \frac{\tau_0}{\gamma_0}\sin(\delta) \tag{1.20}$$

The storage modulus $G'(\omega)$ is proportional to the in-phase component and thus reflects the elastic response of the sample while the loss modulus is proportional to the out of phase component and represents the viscous response of the sample.

In the case of a Newtonian fluid, the storage modulus $G'(\omega)$ is zero while the loss modulus is given by $G''(\omega) = \eta\omega$. In contrast, a viscoelastic fluid displays non-zero values for both $G'(\omega)$ and $G''(\omega)$, with their magnitudes depending on the frequency ω.

Using equation 1.11, it is possible to derive the following connections between $G(t)$ and $G'(\omega)$ as well as $G''(\omega)$.

$$G'(\omega) = \omega\int_0^\infty G(t)\sin(\omega t)dt \qquad G''(\omega) = \omega\int_0^\infty G(t)\cos(\omega t)dt \tag{1.21}$$

Based on these expressions, the generalized Maxwell model domain can be expressed in the frequency domain as follows.

$$G'(\omega) = \sum_{i=1}^{N} \frac{G_i(\omega\tau_i)^2}{1+(\omega\tau_i)^2} \qquad G''(\omega) = \sum_{i=1}^{N} \frac{G_i(\omega\tau_i)}{1+(\omega\tau_i)^2} \tag{1.22}$$

Panel (a) of Figure 1.8 shows the storage and loss moduli of a fluid characterized by a singe Maxwell element. At low frequencies, the fluid demonstrates viscous behavior with G' scaling as ω^2 and G'' scaling as ω, indicative of a fully relaxed sample. In contrast, at high frequencies, a constant storage modulus G' and decreasing loss moduli G'' are obtained, similar to the behavior of a rubber. In reality, polymeric materials encompass a spectrum of relaxation times, resulting in a broadening of the relaxation peak of G'' and causing the decrease in the storage modulus G' to be more gradual and smoother, as shown by panel (b).

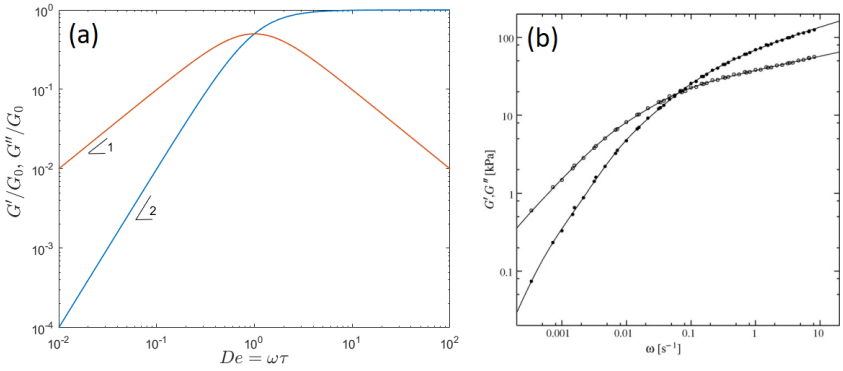

Figure 1.8: (a) Prediction of a single Maxwell fluid. (b) Linear viscoelastic data of an industrial polymer. Panel (b) is adapted from [14].

1.5 Nonlinear viscoelasticity

Pipkin famously marked the interior of the nonlinear viscoelastic regime with a question mark, stating that *"Nothing very systematic is known"* about this region.[12] This lack of knowledge is due to the absence of universal constitutive

equations capable of fully describing all nonlinear viscoelastic behaviors.

Despite this difficulty, numerous nonlinear models have been proposed over time, including both empirical continuum models and molecular models. For instance, Lodge proposed the rubber liquid model which can be retrieved by modifying the general form of the Boltzmann superposition principle.[9,15,16] In the case of large deformation, where the deformed and non-deformed states are significantly different from each other, the infinitesimal strain tensor γ_{ij} is no longer valid. In that case, the Finger tensor C_{ij}^{-1} can be used to describe such finite strain. By substituting the infinitesimal strain tensor in equation 1.11 by the Finger tensor and by integrating by parts, the resulting equation can be obtained.

$$\sigma_{ij}(t) = \int_{-\infty}^{t} \frac{dG(t-t')}{dt'} C_{ij}^{-1}(t,t')dt' \tag{1.23}$$

Using the generalized Maxwell model to describe $G(t)$, the resulting constitutive allows to predict qualitatively important properties of the nonlinear viscoelasticity of polymeric fluids such as strain hardening in uniaxial extensional flow and nonzero first normal stress difference. Nevertheless, the model has strong limitations, as it fails to predict shear thinning and predicts an infinite extensional viscosity at finite stretching rate.[10] To overcome these limitations, more advanced models based on a molecular approach are needed.

1.6 Molecular rheology of polymeric melt

In order to predict the rheological responses of polymeric systems, various types of molecular theories are used including single chain models.

This type of model specifically examines the dynamics of individual polymeric chains whose behavior is representative of the behavior exhibited by all the similar chains in the polymer. In this section, we first introduce the bead-spring model of Rouse which is the most popular model to capture the rheology of unentangled flexible polymers. Then, we introduce the tube model which describes the dynamics of entangled polymers.

Figure 1.9: A single polymeric chain in its environment. Adapted from [17].

1.7 The Rouse model

The dynamics of an unentangled polymeric chains can be described using the bead-spring model proposed by Rouse.[9,10,18] In this model, a polymeric chain is viewed as a series of N beads connected by $N-1$ massless springs (see Figure 1.10). N is often taken as the number of Kuhn segments in the polymer. The springs account for the elastic force generated by the polymeric subchains. Moreover, the motion of the beads results in a viscous drag, which represents the friction between the chain and its surroundings. The latter is made up of neighbouring chains and solvent.

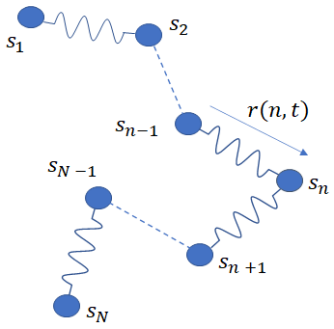

Figure 1.10: Bead-spring model.

In this model, the motion of the beads is influenced by three forces : the drag force, the elastic spring force and the random Brownian force. As a consequence, the position of the n^{th} bead at time t denoted $\mathbf{r}(n,t)$ is given by the following force balance.

$$\zeta_0 \left(\frac{\partial \mathbf{r}(n,t)}{\partial t} - \mathbf{K} \cdot \mathbf{r}(n,t) \right) = -\frac{3k_B T}{b^2} \sum_{m=0}^{N} A_{nm} \mathbf{r}(m,t) + \mathbf{F}_{\mathrm{B}}(n,t) \qquad (1.24)$$

The first term on the left-hand side of equation 1.24 represents the drag force experienced by the n^{th} bead. It is proportional to the friction coefficient ζ_0 of an individual bead and to the difference between the velocity of the n^{th} bead and the velocity of the medium, given by $\mathbf{K} \cdot \mathbf{r}(n,t)$, where $\mathbf{K}$ is the velocity gradient of the applied flow.

The second term on the right-hand side of equation 1.24 represents the elastic force originating from the stretching of the spring connecting the n^{th} bead to its neighboring beads. The constant of proportionality is given by $\kappa = \dfrac{3k_B T}{b^2}$ for pure harmonic springs.

The third term on the right-hand side of equation 1.24, $\mathbf{F}_{\mathrm{B}}(n,t)$, represents the random Brownian force exerted on the n^{th} bead at a time t due to thermal fluctuations. The Brownian force is assumed to be a stochastic process with zero mean. Additionally, the magnitude of the Brownian force is related to the friction coefficient ζ_0 via the fluctuation-dissipation theorem.

$$\langle \mathbf{F}_B(n,t) \rangle = 0 \qquad \langle \mathbf{F}_B(n,t) \mathbf{F}_B(m,t') \rangle = 2\zeta_0 k_B T \delta_{nm} \delta(t - t') \qquad (1.25)$$

In the equations above, the angle brackets denote the time-average value of the quantity, $\delta(t - t')$ the Dirac delta function and δ_{nm} the Kronecker delta.

The Rouse matrix A_{nm}, which appears in the second term on the right-hand side of equation (1.24), characterizes the connectivity of the linear chain. This symmetric matrix with dimensions $N \times N$ is given by

$$A_{nm} = \begin{bmatrix} 1 & -1 & & & \\ -1 & 2 & -1 & & \\ & \ddots & \ddots & \ddots & \\ & & -1 & 2 & -1 \\ & & & -1 & 1 \end{bmatrix}$$

One way to obtain a solution for this set of equations in the linear regime is by diagonalizing it into a set of independent equations. By doing so, Rouse obtained the following expression for the relaxation modulus.

$$G(t) = \frac{\rho RT}{M} \sum_{p=1}^{N} \exp(-t/\tau_p) \tag{1.26}$$

Here ρ is the density of the polymeric material, T the absolute temperature, R the ideal gas constant and M the mass of the polymeric chains. Moreover, the relaxation times τ_p can be expressed as the quotient $\frac{\zeta_0}{\kappa\lambda_p}$, where λ_p represents the p^{th} non zero eigenvalue of the matrix A_{nm}. An analytical solution of τ_p is given by

$$\tau_p = \frac{1}{4\sin^2(\frac{p\pi}{2N})} \frac{\zeta_0 b^2}{3k_B T} \tag{1.27}$$

Using the approximation $\sin^2(x) \approx x^2$ valid for small x, τ_p can be written as follows:

$$\tau_p \approx \left(\frac{N}{p}\right)^2 \frac{\zeta_0 b^2}{3\pi^2 k_B T} \tag{1.28}$$

The time τ_p corresponds to the relaxation time of a subchain containing (N/p) Kuhn segments. Thus, the relaxation of a Kuhn segment τ_0 is obtained when $p = N$, while the relaxation time of the whole chain is obtained when $p = 1$ and is given by

$$\tau_R \approx \frac{N^2 b^2}{3\pi^2 k_B T} \zeta_0 \propto M^2 \tag{1.29}$$

The time τ_R is called the Rouse time and scales as the square of the molar mass of the chains M. Figure 1.11 shows the spectrum of relaxation time and the

predictions of G' and G'' of the Rouse model. As observed, when sufficiently far from the terminal regime, equation 1.26 predict that G' and G'' scale as the square root of the frequency.

It is also worth-mentioning that the Rouse process predicts that the linear viscoelastic moduli of polymers of the same nature (i.e. same ζ_0 and κ) overlap at short times.

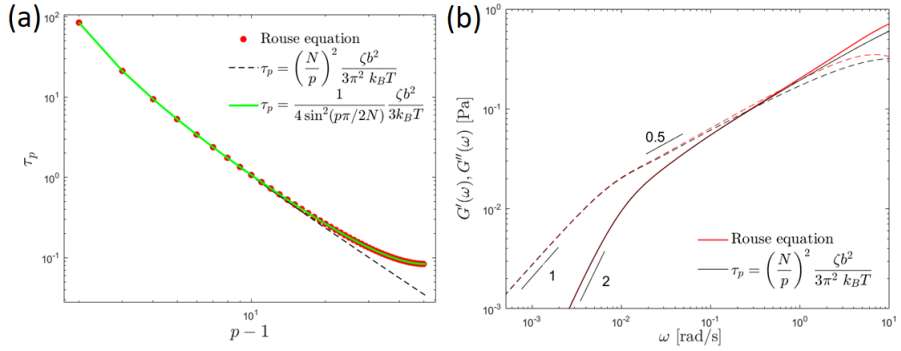

Figure 1.11: (a) Spectrum of relaxation time predicted by the Rouse equation. (b) Relaxation modulus predicted by the Rouse equation.

Nonetheless, in a wide varieties of polymers, the motion of the chains is significantly hindered. The obstruction can be caused by the presence of entanglements and/or supramolecular bonds. In that case, the Rouse process stops after reaching these obstacles.

In the upcoming sections of this manuscript, we discuss different approaches to model the relaxation modulus in these cases. First, we will introduce the tube model, which helps us to understand the behavior of entangled polymeric melts. Next, we will outline the viscoelastic responses of both unentangled and entangled supramolecular polymers.

1.8 Rheology of polymer melts: the tube model

The tube model, based on the seminal ideas of de Gennes, Doi and Edwards is one of the most successful model which allows to predict the linear viscoelastic

response of entangled polymeric fluids.[19,20] In this model, the entanglements confine the test chain in an tubelike region (see Figure 1.12), restricting its motion in the transverse direction.

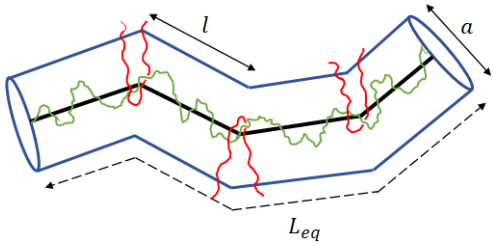

Figure 1.12: A polymeric chain (green) confined in a tube defined by the entanglement network (red) and its corresponding primitive path (black).

Each subchain between two entanglements follows Gaussian statistics, with its end-to-end distance determined by $l = \sqrt{N_e b^2}$, where N_e represents the number of Kuhn segments between two entanglements. It follows that the test chain can itself be modeled as a random flight of $Z = \left(\frac{M}{M_e} + 1\right)$ steps of length l. The latter is called the primitive path and corresponds to the curvilinear axis of the tube. Doi and Edwards also demonstrated that the diameter of the tube a at equilibrium is equivalent to the entanglement spacing l.

The relaxation process of entangled polymer chains can be divided into two stages: the Rouse relaxation within the tube and the disengagement of the chains from their initial tube. The next sections provide a concise overview of these mechanisms.

1.8.1 Rouse relaxation within the tube

In the short-time regime, the entangled chains undergo a Rouse process, akin to unentangled melts. Subchains smaller than the average spacing between two entanglements can move freely in all three dimensions and thus relax by the classical Rouse process. This relaxation involves timescales shorter than the Rouse relaxation time of an entanglement strand denoted as τ_e and given

by

$$\tau_e \approx \frac{N_e^2 b^2}{3\pi^2 k_B T}\zeta_0 \tag{1.30}$$

After τ_e, entanglements suppress all the remaining Rouse modes, except the longitudinal ones. The latter relax stress by transporting subchains from one tube segment to another, readjusting the length of the entangled strands to achieve uniform chain tension. Based on this, Likhtman and McLeish derived the following expression for the Rouse modulus of an entangled melt.[21]

$$G_{Rouse}(t) = G_e \left(\frac{1}{5Z} \sum_{p=1}^{Z-1} \exp\left(-\frac{p^2 t}{\tau_R}\right) + \frac{1}{Z} \sum_{p=N}^{Z} \exp\left(-\frac{2p^2 t}{\tau_R}\right) \right) \tag{1.31}$$

Here, the first term denotes the fast Rouse relaxation of segments shorter than the entanglement spacing while, the second term corresponds to the slow longitudinal modes.

1.8.2 Disengagement of the chain

As time progresses, the chains start to feel the influence of their neighboring chains via the entanglements and thus become confined in their tubes. To relax their configurations, the chains must escape their tube. In the linear regime, this occurs through three distinct mechanisms: reptation, Contour Length Fluctuation (CLF), and Constraint Release (CR).

1.8.2.1 Reptation

Due to thermal agitation, the chains progressively diffuse out of the tube by sliding back and forth along its curvilinear axis. Once a part of the molecule is out the tube, it can adopt a new random orientation that do not carry any stress. The chain thus relaxes completely when the whole tube is vacated. An illustration of this process called reptation is shown in Figure 1.13. In order to solve the mathematical problem of reptation, Doi and Edwards assumed that the length of the primitive path is constant and equal to its equilibrium value $L_{eq} = Zl$.[20] Under these assumptions, they have shown that the problem

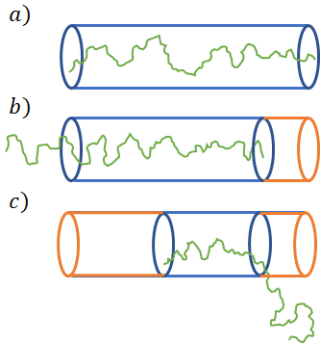

Figure 1.13: Relaxation of tube segments by reptation. The unrelaxed and the relaxed segments are depicted in blue and in orange respectively.

reduces to a one dimensional diffusion equation.

$$\frac{\partial p_{surv}(s,t)}{\partial t} = D_c \frac{\partial^2 p_{surv}(s,t)}{\partial s^2} \tag{1.32}$$

Here $p_{surv}(s,t)$ corresponds to the survival probability of the infinitesimal portion of the tube at time t and localized at the position s. D_c is the diffusion constant of the center of mass of the chain. An expression of D_c can be obtained using the Einstein's relationship.

$$D_c = \frac{k_B T}{\zeta_0 N} \tag{1.33}$$

The boundary and the initial conditions of equation 1.32 are given by

$$p_{surv}(x,0) = 1 \quad \text{for } x \in [0,1] \tag{1.34}$$

$$p_{surv}(0,t) = p_{surv}(L,t) = 0 \tag{1.35}$$

The survival fraction of the initial tube segments $p_{rept}(t)$ can be calculated by integrating this function $p_{surv}(s,t)$ along the whole chain.

$$p_{rept}(t) = \frac{1}{L}\int_0^L p(s,t)ds = \frac{8}{\pi^2}\sum_{p\ \text{odd}}\frac{1}{p^2}\exp\left(-\frac{p^2 D_c t}{L_{eq}^2}\right) \tag{1.36}$$

Assuming that only reptation contributes to the relaxation of the chains, the relaxation modulus $G(t)$ can be written as

$$G(t) = G_N^0 p_{rept}(t) = G_N^0\frac{8}{\pi^2}\sum_{p\ \text{odd}}\frac{1}{p^2}\exp\left(-\frac{p^2 D_c t}{L_{eq}^2}\right), \tag{1.37}$$

where $G_N^0 = \frac{4}{5}\frac{\rho RT}{M_e}$ is the plateau modulus. The spectrum of relaxation times predicted by equation 1.37 is narrow and largely dominated by the longest relaxation time τ_{rep} known as the reptation time.

$$\tau_{rept} = \frac{L_{eq}^2}{D_c} = \tau_e\left(\frac{N}{N_e}\right)^3 \propto M^3 \tag{1.38}$$

The reptation time is therefore proportional to the cube of the molar mass of the chains M. However, experimental studies have shown that the power-law exponent of the longest relaxation time ranges from 3 to 3.6. This deviation is caused by the presence of an additional mechanism of relaxation called Contour Length Fluctuation (CLF).

1.8.2.2 Contour Length Fluctuation (CLF)

In reality, the contour length of the primitive path incessantly fluctuates with time. Because of this continuous motion, a polymeric chain can shrink temporarily in its tube, leaving its extremities empty. This temporary retraction leads to the relaxation of the chain ends. As a result, the reptation motion of the chains occurs in a tube of length $L_{eq} - \Delta L$, with ΔL being the part of the tube entirely relaxed by CLF. Likhtman and McLeish obtained the following formula through simulations for the corrected longest relaxation time τ_d.[20]

$$\tau_d = 3Z^3\tau_e\left(1 - \frac{3.38}{\sqrt{Z}} + \frac{4.17}{Z} - \frac{1.55}{Z^{\frac{3}{2}}} + O(Z^{-2})\right) \tag{1.39}$$

The dependence of the molar mass of the term in brackets illustrates the fact that CLF tends to be more significant for shorter chains. This explains why the power-law exponent of the relaxation evolves from around 3.6 for barely entangled chains to 3 for highly entangled chains.

In the literature, different expressions are used to describe the spectrum of relaxation times due to CLF. A popular approach consists of dividing the spectrum into two parts.[1,22] This can done by evaluating the potential energy $U(x)$ due to the retraction of an arm of a chain (half of a chain), initially at equilibriuum, at the position x.[1,22-24] The expression of $U(x)$ is dominated by the arm entropic force and the tube constraint and is given by

$$U(x) = \frac{3k_BT}{2Nb^2}(L_{eq}x)^2 + \text{constant} \tag{1.40}$$

Here x corresponds to a coordinate which follows the curvilinear axis of the tube and is normalized such that it ranges from 0 at the chain ends to 1 at the center of the chain.

When $U(x) < k_BT$, the motion of the arm is not influenced by the tube. The chain ends therefore adopt a unconstrained Rouse-like behavior. In this regime of "early fluctuations", the relaxation times are given by

$$\tau_{early}(x) = \frac{9\pi^3}{16}\left(\frac{Z}{2}\right)^2 \tau_R x^4 \tag{1.41}$$

When $U(x) > k_BT$, the retraction becomes much more difficult as it involves deeper segments. The chain has to adopt a highly wrinkled and entropically unfavorable conformation to vacate the corresponding part of the tube, as illustrated in Figure 1.14. For this reason, the relaxation is considerably slowed down and an exponentially increasing time is required.

$$\tau_{activated}(x) = \tau_0 \exp\left(\frac{U(x)}{k_BT}\right) \tag{1.42}$$

Here τ_0 corresponds to an arbitrary waiting time.

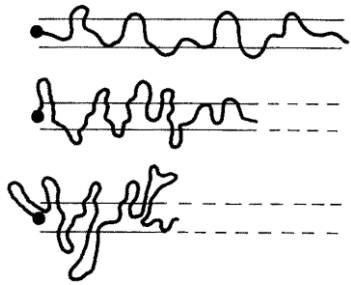

Figure 1.14: Illustration of CLF mechanism. The chains ends adopt highly wrinkled conformations to relax. Reproduced from [17].

The fluctuation depth x_{trans} such that $U(x_{trans}) = k_BT$ corresponds to the transition between the early-time chain end fluctuations and the activated fluctuations. Chain ends of length lower than x_{trans} relax by a Rouse-like motion while longer segments fluctuate in the potential $U(x)$. Based on this idea, van Ruymbeke *et al.* proposed the following expression to describe the spectrum of fluctuation times $\tau_{fluc}(x)$.[1]

$$\tau_{fluc}(x) = \begin{cases} \tau_{early}(x), & \text{if } x < x_{trans}. \\ \tau_{early}(x) \exp\left(\dfrac{\Delta U(x_{trans} \rightarrow x)}{k_BT}\right), & \text{if } x \geq x_{trans}. \end{cases} \tag{1.43}$$

The probability $p_{CLF}(x,t)$ that the segment localised at the coordinate x at time t is not relaxed by CLF can therefore be evaluated by:

$$p_{CLF}(x,t) = \exp\left(-\frac{t}{\tau_{fluc}(x)}\right) \tag{1.44}$$

1.8.2.3 Constraint Release (CR)

So far, only the motion of the test chain was considered. However, the matrix chains can also relax via reptation and CLF, enabling the release and the renewal of the entanglements constraints of the test chain.

This mechanism called Constraint Release (CR) is particularly important for

the relaxation of polydisperse polymers. In these types of systems, the test chain contains entanglements with neighbouring chains of different lengths. As the disentanglement process occurs at timescales comparable to the terminal time of the chains, some entanglements have shorter lifetimes than others, causing them to disappear more rapidly. This disentanglement enables the test chain to disorient its local configuration and thus to partially relax before its intrinsic reptation time (see Figure 1.15).

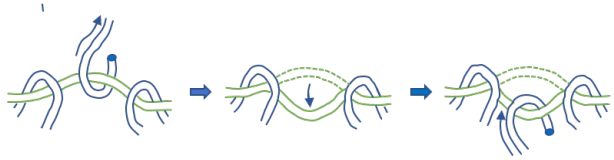

Figure 1.15: The local configuration of a polymeric chain (green) is relaxed by a constraint release event. Adapted from [25].

Different approaches to treat CR exist in the literature. In this following sections, we introduce two cases: the double reptation theory and the dynamic tube dilation.

Double reptation theory

The double reptation theory, developed by Tuminello, Tsenoglou and des Cloizeaux, offers a simple description of CR.[26-28] In des Cloizeaux's version of the theory, entanglements are viewed as stress points arising from interactions between two chains, with disentanglement occuring when one of the two chains relaxes. The relaxation modulus is then determined by summing the contributions from all surviving entanglements. Consequently, if the chains relax independently, this approach results in a relaxation modulus that is directly proportional to the square of the survival fraction of the initial tube $p_{surv}(t)$.

$$G(t) = G_N^0 p_{surv}^2(t) \tag{1.45}$$

Thus, in absence of CLF, the double reptation theory simply replaces $p_{rep}(t)$ by $p_{rep}^2(t)$, resulting in a terminal relaxation time equal to $\tau_{rep}/2$. In the case

of a polydisperse polymer, $G(t)$ is obtained by the following mixing rule.

$$G(t) = G_N^0 \left(\sum_i \nu_i \mu_i(t) \right)^2 \tag{1.46}$$

Here $_i$ and $\mu_i(t)$ refer respectively to the volume fraction of the chains and to the unrelaxed fraction of their initial tubes. Equation 1.46 provides a decent prediction for the linear rheology of polymers that exhibit typical polydispersities found in commercial samples. However, it is not valid when the polymers include chains with well-separated relaxation times.[29]

Dynamic tube dilation

The dynamic tube dilation (DTD) initially proposed by Marrucci provides a more accurate and sophisticated solution of CR.[30] When the time scale of the experiment is significantly longer than an entanglement's lifetime, these entanglements are created and eliminated with such speed that they do not impede the motion of the test chain anymore. Consequently, these entanglements can be disregarded, leading to an increase of the dimensions of the tube. This increase is modeled on the basis that the relaxed fraction of the polymer behaves similarly to a solvent for the test chain. Under this assumption, the molar mass between entanglements M_e is expressed as the following function of time.

$$M_e(t) = \frac{M_{e,0}}{\Phi(t)^\alpha} \tag{1.47}$$

Here $\Phi(t)$ correponds to the unrelaxed fraction of the polymer at time t and α is the dynamic dilation exponent. Experimental measurements of α typically yield values ranging from 1 to 1.3.[31,32]

As a result, the tube dilates and shortens as follows:

$$L_{eq}(t) = L_{eq,0}\Phi(t)^{\alpha/2} \tag{1.48}$$

$$a(t) = \frac{a_0}{\Phi(t)^{\alpha/2}} \tag{1.49}$$

Here $L_{eq,0}$ and a_0 denote the initial length and diameter of the tube, respectively.

This change of topology leads to the following rescaling of the reptation time $\tau_{rep}(t)$.

$$\tau_{rep}(t) = \tau_{rep,0}\Phi(t)^{\alpha} \tag{1.50}$$

In the DTD, when a small fraction of long chains is diluted in a matrix of short chains, the tube can dilate faster that the chain is able to explore it. This implies that a long chain that is only entangled with short chains relaxes as soon as the short chains relax. However, in reality, the long chains cannot explore their tubes faster than an unconstrained Rouse process. This limitation gives rise to the concept of supertube, wherein the long chains can only explore a narrower Rouse-limited tube concentric to the "supertube" predicted by the DTD. Gradually, this Rouse-limited tube expands until it reaches the diameter of the supertube. This mechanism, introduced by Viovy *et al.* and further investigated by Milner *et al.*, is called contraint-release Rouse (CR-Rouse) and provides a lower bound for $\Phi(t_i)$.[33–35]

$$\Phi(t_i) \geq \Phi(t_{i-1})\sqrt{\frac{t_{i-1}}{t_i}} \tag{1.51}$$

When CR-Rouse is taken into account, the relaxation modulus is given by

$$G(t) = \frac{\rho RT}{M_{e,0}}\phi(t)\Phi^{\alpha}(t) \tag{1.52}$$

Here, the function $\phi(t)$ corresponds to the survival fraction of the initial thin tube.

Equation 1.52 illustrates that the relaxation modulus is governed by the interplay of two functions: one that characterizes the relaxation due to motion of the test chain (i.e. $\phi(t)$), and the other describing the relaxation caused by motion of the neighbouring chains $\Phi^{\alpha}(t)$. The latter function is always larger than or equal to the former one due to the inequality 1.51. In the case of double reptation, both functions are identical and given by $\phi(t)$.

1.8.3 Predictive approaches for the LVE response

In the literature, several approaches which include the fundamental processes of reptation, CLF, and CR have been developed to predict the linear viscoelastic responses of polymer melts. However, many of these approaches include mathematical and physical approximations, necessitating a compromise between equation complexity and prediction accuracy. Here, in this section, we introduce two approaches. The first one is relatively simple and relies on the double reptation theory while the second one is more sophisticated and employs DTD and CR-Rouse.

1.8.3.1 Time-dependent diffusion (TDD) reptation

Des Cloizeaux proposed a model which allows to integrate reptation and CLF with the double reptation theory.[28] To achieve this, he introduced a time-dependent effective diffusion coefficient $D(t)$ in equation 1.32. At short times, the behavior of $D(t)$ is dominated by the unconstrained Rouse motion of the chains, resulting in an evolution with $t^{-1/2}$. Subsequently, at longer times, the mechanism of reptation becomes dominant, causing $D(t)$ to converges to D_c. Based on this, Des Cloizeaux derived the following form for $D(t)$.

$$D(t) = D_c \left(1 + \sum_{n=1}^{\infty} \exp\left(\frac{-n^2 t}{\tau_i}\right)\right) \tag{1.53}$$

Here $\tau_i = \sigma \dfrac{\tau_{rep}}{Z}$ denotes a Rouse time and σ a material-dependent parameter which describes the relative importance of CLF. The relationship between σ and M_e is not clear yet.[36]

Combining equation 1.32 with equation 1.53 results in the following expression for the fraction of original entanglements $\mu(t)$ surviving at time t.

$$\mu(t) = \frac{8}{\pi^2} \sum_{\text{odd q}} \frac{1}{q^2} \exp\big(-q^2 w(t)\big) \tag{1.54}$$

Here the function $w(t)$ in equation 1.54 is given by

$$w(t) = \frac{t}{\tau_{rep}} + \frac{\alpha}{Z} g\left(\frac{tZ}{\alpha\tau_{rep}}\right) \tag{1.55}$$

where $g(x)$ is defined as:

$$g(x) = \sum_{m=1}^{\infty} \frac{1 - \exp(-m^2 x)}{m^2} \tag{1.56}$$

As observed, the expression of $w(t)$ includes two terms. The first term accounts for the relaxation through reptation while the second term captures the contributions of the relaxation arising from CLF. Substituting equation 1.54, 1.55 and 1.56 into equations 1.46 allows to express the relaxation modulus into a relatively concise equation.

$$G(t) = \frac{64}{\pi^4} G_N^0 \left(\sum_i \nu_i \sum_{\text{odd q}} \frac{1}{q^2} \exp(-q^2 w_i(t))\right)^2 \tag{1.57}$$

However, Likhtman and McLeish showed that the treatment of CLF by des Cloizeaux is significantly imprecise.[21] Furthermore, as discussed above, the double reptation theory does not provide a precise approximation of CR and is valid only for smooth molar mass distribution.

1.8.3.2 Time marching algorithm (TMA)

A more advanced approach to predict quantitatively the linear response of polymers can be achieved by treating CR by DTD and CR-Rouse. Here, the relaxation modulus of polydisperse systems cannot be expressed analytically due to the complex interdependence of the spectrum of relaxation times with the survival fraction of the tube. According to the DTD picture, the relaxed fraction of the polymer behaves like a solvent for the remaining unrelaxed segments, modifying their reptation and fluctuation times. As these changes occur continuously over time, finding an analytical solution becomes impossible.

To address this issue, Van Ruymbeke *et al.* developed a time marching algorithm (TMA) to predict the LVE response of polydisperse systems.[1] This algorithm involves discretizing the time axis and computing the survival probabilities $p_{surv}(x_i, t_k)$ of a segment x_i at a time t_k using the corresponding values obtained at a previous time t_{k-1}. In this approach, $p_{surv}(x_i, t_k)$ is given by the product between the probabilities that the tube segments survive by reptation $p_{rep}(t_k)$ and by CLF $p_{CLF}(t_k)$.

$$p_{surv}(x_i, t_k) = p_{rep}(x_i, t_k) p_{CLF}(x_i, t_k) \tag{1.58}$$

Here, the probabilities $p_{rep}(x_i, t_k)$ and $p_{CLF}(x_i, t_k)$ can be evaluated via

$$p_{rep}(x_i, t_k) = p_{rep}(x_i, t_{k-1}) p_{rep}(x_i, [t_{k-1}, t_k]) \tag{1.59}$$

$$p_{CLF}(x_i, t_k) = p_{CLF}(x_i, t_{k-1}) p_{CLF}(x_i, [t_{k-1}, t_k]) \tag{1.60}$$

The square brackets $[t_{k-1}, t_k]$ in equation 1.59 and 1.60 refers to the time interval between t_{k-1} and t_k. Assuming that this time interval is sufficiently small to disregard any significant variation in the relaxation time within this interval, the variations of the survival probabilities can be evaluated using the equations below:

$$p_{rep}(x_i, [t_{k-1}, t_k]) = \exp\left(\frac{-\Delta t}{\tau_{rep}(t_k)}\right) \tag{1.61}$$

$$p_{CLF}(x_i, [t_{k-1}, t_k]) = \exp\left(\frac{-\Delta t}{\tau_{fluc}(x_i, t_k)}\right) \tag{1.62}$$

The values of $\tau_{rep}(t_k)$ and $\tau_{fluc}(x_i, t_k)$ can be computed with equations 1.38,1.50 and 1.43. Based on that, the relaxation modulus $G(t_i)$ is obtained by the following expression.

$$G(t_k) = G_N^0 \left(\sum_i \nu_i \int_{x=0}^{1} p_{surv}(x_i, t_k) dx_i \right) \Phi^\alpha(t) = G_N^0 \phi(t) \Phi^\alpha(t) \tag{1.63}$$

Here the CR-Rouse-limited fraction is given by $\Phi^{\alpha}(t_k) = \max\left(\phi(t_k), \phi(t_{k-1})\sqrt{\frac{t_{k-1}}{t_k}}\right)$.

As shown by the work of Shahid *et al.*, the resulting algorithm predicts very well the linear viscoelastic responses of entangled linear polymers (see Figure 1.16).[31]

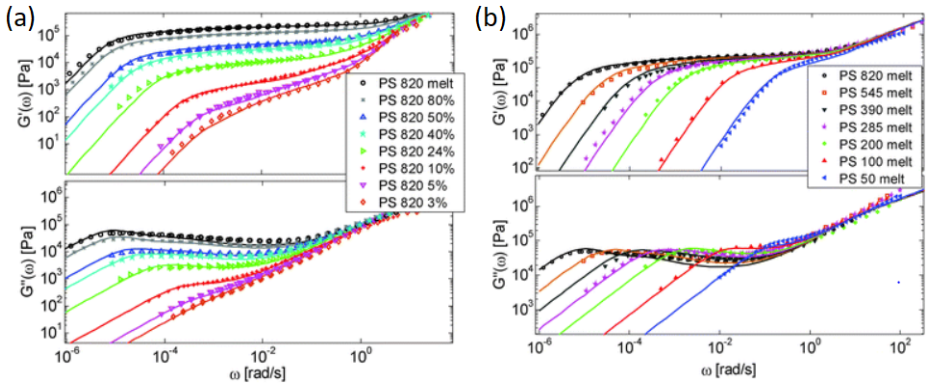

Figure 1.16: Dynamic moduli of polystyrene (PS) melts. Panel (a) exhibits the LVE response of long PS chains with a molar mass of 820 kg/mol diluted with oligomeric styrene of 8.8 kg/mol at different weight fraction. Panel (b) displays the LVE of monodisperse PS melts at various molar masses. The symbols are the experiments results while the solid lines correspond to the predictions of the TMA. Reproduced from [31].

1.8.4 Universality in the linear regime

Upon reviewing the preceding sections, it appears that the spectrum of relaxation times of a polymeric melt is entirely defined by three distinct parameters: the molar mass between two entanglements M_e, the relaxation time of an entanglement strand τ_e and the number of entanglements Z. According to the tube model, polymers with different chemistries in either the melt state or in solution exhibit identical flow dynamics when they possess the same number of entanglements Z. This universal behavior is well demonstrated by the work of Wingstrand *et al.* who measured the linear responses of poly(methyl methacrylate) (PMMA) and polystyrene (PS) for $Z = 7$ and $Z = 20$.[37] As shown in Figure 1.17, the LVE response of the samples with the same Z overlap when

the dynamic moduli are normalized with the plateau modulus $G_N^0 = \frac{4}{5}\frac{\rho RT}{M_e}$ and the frequency is scaled by τ_e.

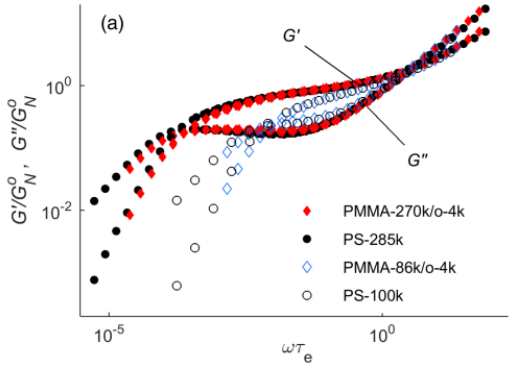

Figure 1.17: Dimensionless LVE data of PS and PMMA melts. Closed symbols refer to samples with $Z \approx 20$, while open symbols indicate samples with $Z \approx 7$. Reproduced from [37].

1.8.5 The nonlinear viscoelastic regime

When subjected to sufficiently large and rapid deformation, polymeric chains can orient, unravel and stretch, which affects significantly their relaxation behavior. To account for these effects, additional mechanisms such as large orientation of tube segments, chain stretching, and convective constraint release (CCR) need to be introduced in the tube model.

Large orientation of the tube segments

When exposed to strain rates larger than $1/\tau_d$, the polymeric chains cannot disengage from their tubes and thus cannot maintain their equilibrium conformations. Consequently, the tube segments align themselves in the direction of the deformation. During chain orientation, the entanglement strands maintain their Gaussian distribution and thus, the length of the primitive path L_{pp} remains equal to the equilibrium length of the tube L_{eq}. The Doi-Edwards (DE) model was the first to incorporate this mechanism.[20] Nevertheless, the DE model failed to predict the upturn of the extensional viscosity observed

for polymeric solutions at high strain rates and also predicts excessive shear-thinning.[10]

Chain stretching

Subsequently, Marrucci and Grizzuti introduced a crucial modification to the DE theory. They included a characteristic time scale τ_S for chain retraction, resulting in the development of the Doi-Edward-Marrucci-Grizzuti (DEMG) theory.[38] In this theory, as the applied strain rate exceeds $1/\tau_S$, the chains start to stretch, causing the elongation of the entanglement strands. As a result, the length of the primitive path L_{pp} surpasses L_{eq}. When a chain is fully extended, its primitive path is given by $L_{pp} = Nb$. The maximum stretch ratio is therefore determined by $\lambda_{max} = \dfrac{Nb}{Zl} = \sqrt{N_e}$. Following the cessation of flow, the chains retract in their tubes through Rouse motion in a time equal to τ_S. Since the retraction requires motion at the scale of the whole chain, the time τ_S is approximately equal to τ_R. The extent of chain stretching is particularly important for strong flows such as uniaxial elongation.

Convective constraint release (CCR)

Despite the introduction of chain stretching, the DEMG theory still overestimates the extent of shear thinning. In order to adress this issue, Marrucci introduced the mechanism of convective constraint release (CCR).[39]

When matrix chains are subjected to stretch, they can relax via retraction, which may result in the loss of entanglements on the test chain. This new constraint release mechanism called Convective Constraint Release (CCR) imposes a disentanglement that occurs at a rate proportional to the flow rate. When a uniaxial extensional flow with a controlled stretching rate $\dot{\epsilon}$ is imposed, the impact of CCR is insignificant, as at high strain rates, the chains are persistently strongly stretched, making entanglements unimportant to their flow behavior. In contrast, in shear flows with constant $\dot{\gamma}$, the polymeric chains undergo a succession of stretch/retraction cycles due to the vorticity of the flow. This makes CCR a mechanism of prime importance in shear flow.[9]

1.8.5.1 Weissenberg number

The onset of orientation of the tube segments and chains streching can be captured using a dimensionless number called Weissenberg number Wi.[40,41] This number compares the strain rate of the flow (either in shear or in extensional flow) with a characteristic relaxation time τ of the polymeric fluid.

$$\mathrm{Wi} = \dot{\epsilon}\tau \qquad (1.64) \qquad\qquad \mathrm{Wi} = \dot{\gamma}\tau \qquad (1.65)$$

Using the reptation time τ_{rep} and the Rouse relaxation time τ_R as τ defines the reptation Weissenberg number Wi_d and the Rouse Weissenberg number Wi_R. Figure 1.18 depicts the three levels of chain deformation using the Weissenberg number.

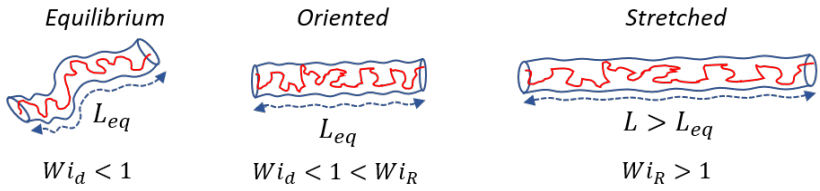

Figure 1.18: Depending on the applied strain rates, a chain can be at the equilibrium state, oriented or stretched.

1.8.6 Theoretical predictions

Several models have been proposed to incorporate the nonlinear effects of orientation of the tube segments, chain stretching and CCR into the tube model, such as the Mead-Larson-Doi (MLD) model and the Graham-Likthman-McLeish-Milner (GLaMM) model.[42,43] These models have made significant progress in capturing the nonlinear rheological behavior of polymeric fluids. However, despite their advancements, significant discrepancies between their predictions and experimental results still exist. This can be attributed to imprecise descriptions of the underlying mechanisms, as well as the presence of potential additional mechanisms which are not accounted for in these models.

1.8.7 Comparison of theory with data for linear polymers

In this section, we briefly review the performances of nonlinear tube model in shear and extensional flow.

1.8.8 Nonlinear viscoelastic regime in shear flow

The incorporation of orientation of tube segments, CCR and tube retraction in tube-based models has led to predictions that are in qualitative agreement with experimental results in shear flow. These models successfully capture the experimentally observed strain softening behavior of entangled polymeric melts, characterized by a large overshoot associated with the orientation of tube segments and chain stretching (see Figure 1.19 (a)).[44]

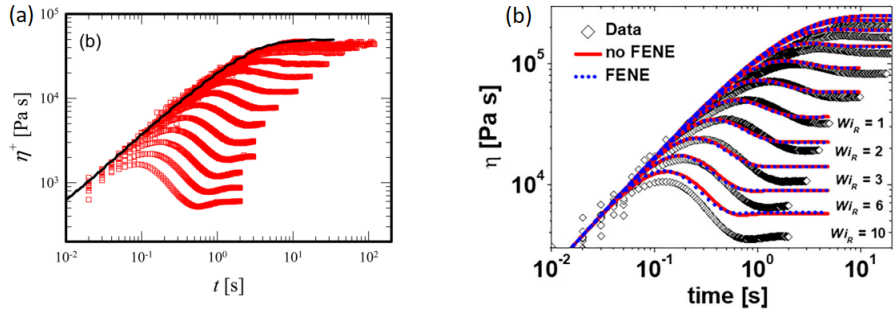

Figure 1.19: Panel (a) displays the stress growth coefficient of entangled polystyrene melts. Panel (b) compares the predictions of the GLaMM model alongside experimental data of PS melts. Panel (a) and panel (b) are reproduced from [45] and [44], respectively.

However, at high shear rates, entangled polymeric melts also exhibit a slight undershoot that is not predicted by most of the tube-based molecular models. Costanzo *et al.* attributed the origin of this undershoot to chain tumbling,[45] a mechanism noticed in previous non-equilibrium molecular dynamics (NEMD) simulations by Kim *et al.* for barely entangled polymers.[46] These simulations revealed a bimodal probability distribution of the end-to-end vector, **R**, at high shear rates, arising from individual chains undergoing phases of high extension

followed by short periods of fast rotational tumbling. Later, Masubuchi *et al.* investigated tumbling by Primitive Chain Network (PCN) simulation. The simulations satisfactorily replicated the stress growth coefficient observed in PS melts and demonstrated that both orientation and chain stretching are affected by tumbling.[47] Costanzo *et al.* introduced tumbling in the tube model using a semiphenomenological approach based on molecular dynamics (MD) simulations of Sefiddashi *et al.*[45,48] However, a precise molecular description of this mechanism is still missing.

Costanzo *et al.* assessed the universal behavior of polymeric systems in the nonlinear shear regime at moderate Wi_R.[45] They achieved this by preparing entangled polystyrene (PS) melts and solutions with the same number of entanglements Z, which resulted in an equivalent linear viscoelastic response. They found that these systems exhibit comparable normalized transient nonlinear shear response (see panel (a) of Figure 1.20), indicating that the nonlinear shear regime at moderate Wi_R is solely determined by M_e, τ_e, and Z, similar to the linear regime.

Additionally, the authors demonstrated that the steady-state viscosities of different polymeric systems, when normalized by the product of G_N^0 and their terminal relaxation time (τ_m), adopt a universal shear thinning behavior when expressed as a function of the Weissenberg number $\mathrm{Wi}_m = \dot{\epsilon}\tau_m$ based on the terminal time. They found that the exponent of the high shear rate power law is equal to -0.82 (see panel (b) in Figure 1.20).

1.8.9 Nonlinear in extensional flow

Figure 1.21 shows the schematic predictions of the extensional viscosity according to the DEMG model.[49] As observed, this nonlinear tube model predicts four distinct regimes.[49]

- First, when the extension rate $\dot{\epsilon}$ is lower than $1/\tau_d$, the chains constantly escape their confinement tube via reptation enabling the chains to preserve their equilibrium conformations, resulting in a constant viscosity equal to $\eta_E = 3\eta_0$.

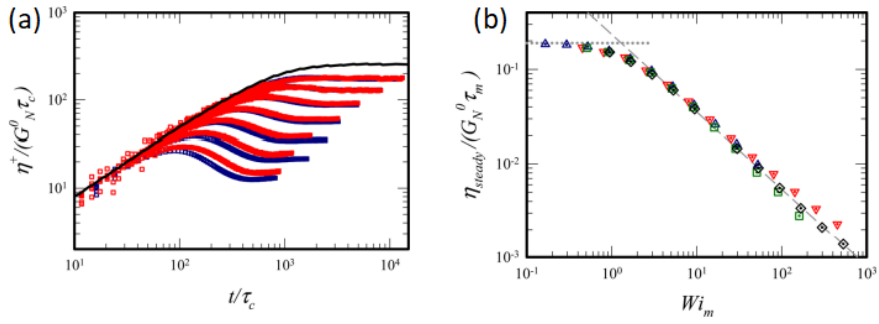

Figure 1.20: (a) Normalized shear stress coefficient of PS 133k (in blue) and PS285k/2k (47% wt) (in red) for different Wi_R. The Wi_R ranges from 0.108 to 3.42 and both systems contain $Z \approx 13.9$. τ_c is derived from a different model than the tube model, but it is equivalent to τ_e. (b) Normalized steady viscosity of PS 133k (in blue), PS285k/2k (47%wt) (red), PS185k (green), and PS285k/2k (65%wt) (black). Panel (a) and panel (b) are reproduced from [45].

- Second, when $1/\tau_{rep} < \dot{\epsilon} < 1/\tau_R$, the flow orients the tube segments along the extension axis. In this regime, the stress saturates and the viscosity decreases as $\eta_E \sim \dot{\epsilon}^{-1}$.
- Third, when $\dot{\epsilon}$ exceeds $1/\tau_R$, the chains start to stretch, which lead to an upturn of the viscosity.
- Fourth, at high strain rates, the chains become fully extended and the viscosity reaches a plateau.

However, the experimental data reveals stark divergences from these predictions.[50]

The first deviation from the theory is illustrated in Figure 1.22, which displays the normalized steady extensional responses of PS solutions and melts with the same number of entanglements Z. As observed, the behavior of the systems differs substantially. The most diluted polymeric solutions exhibit reasonable agreement with the predictions of the tube model, demonstrating the expected thinning behavior followed an the upturn of the viscosity. However, as the concentration of the solutions increases, the viscosity shows a shift from a marked upturn to a monotonic thinning behavior. The regime III and IV are

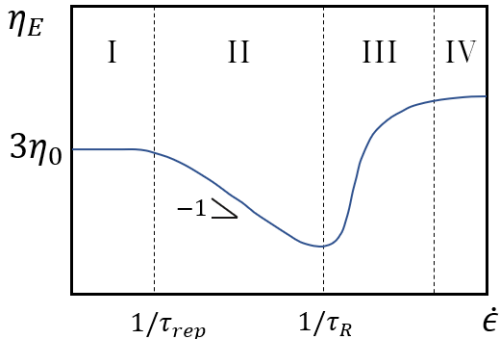

Figure 1.21: Extensional viscosity η_E as a function of the stretching rate $\dot{\epsilon}$, as predicted by the standard tube-model. Adapted from [49].

thus effectively erased in PS polymeric melts, indicating that the universality of entangled polymeric systems is no longer applicable in extensional flow.[51] It should be noted that, according to Ianniruberto,[52] this breakdown of universality was expected, as the PS melts and solutions shown in Figure 1.23 have different finite extensibilities $\lambda_{max} = \sqrt{N_e/\phi}$ and thus should lead to different asymptotic values of the viscosity in region IV. However, Ianniruberto demonstrated that this difference in extensibility alone cannot account for the order-of-magnitude difference between the melt and the solutions.[52]

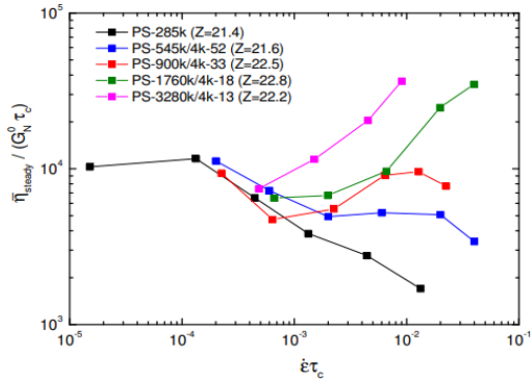

Figure 1.22: Normalized extensional viscosity as a function of the Weissenberg number for different PS polymers with same values of Z. Reproduced from [51].

Moving on, Figure 1.23 presents a second substantial inconsistency with the theory. As it is readily seen, polymeric melts of different nature but with similar values of Z exhibit fundamentally different flow behaviors. Specifically, PS melts demonstrate a monotonic increase in viscosity (see panel (a)), while poly(n-butyl acrylate) (PnBA) melts display an extension steady-thickening behavior (see panel (b)). In a similar vein, Morelly *et al.* have also reported different power-law exponents in the extension steady-thinning regime for PMMA, PS, and poly(tert-butylstyrene) (PtBS) melts.[53]

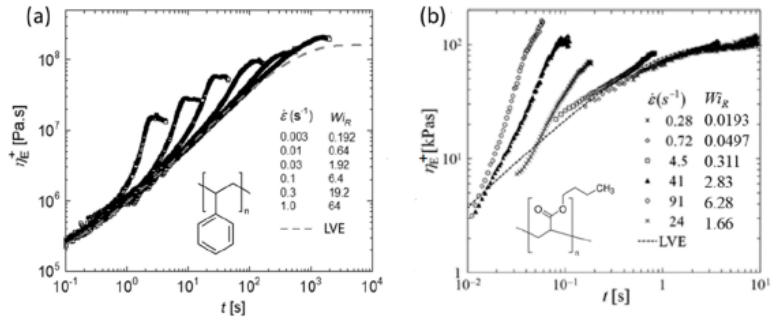

Figure 1.23: (a) Extensional stress growth coefficient of PS melt of 185 kg/mol at 130 ℃. (b) Extensional stress growth coefficient of PnBA melt of 200 kg/mol at 21.5 ℃. Panel (a) and (b) are adapted from [54] and [55], respectively.

Lastly, Huang *et al.* uncovered another significant deviation from the standard tube model.[56] In particular, they discovered that solutions of PS chains with a molecular weight of 545k, when diluted at the same concentration with short chain styrene oligomers (with molar masses ranging from 1k to 4k), exhibited distinct extensional responses, as shown in Figure 1.24. The surprising nature of this result stems from the fact that the short chains, which do not undergo stretching, were not expected to significantly impact the extensional responses of these systems.

These unexpected behaviors suggest that additional mechanisms need to be added in the molecular picture to correctly describe the extensional rheology of polymeric systems.

Marrucci and Ianniruberto first proposed the interchain pressure effect (IP) as

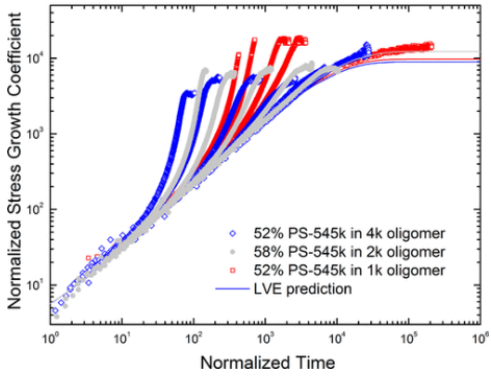

Figure 1.24: Comparison of the normalized extensional stress growth coefficient of PS melts of 545 kg/mol diluted with oligomeric styrene of different molar masses. Reproduced from [56].

an explanation for the observed behavior of PS polymer melts.[49] According to this model, a polymeric chain exerts an entropic force on the tube walls due to its spatial confinement. This force counteracts the flow-induced reduction of the tube diameter. As the tube diameter decreases with the imposed deformation, the pressure builds up against the walls, eventually reaching a steady state when the opposing forces balance each other. This mechanism leads to the introduction of one nonlinear parameter τ_a called the tube diameter relaxation time, which is expected to scale with τ_R. Built upon this concept, Wagner and Rolón-Garrido developed a constitutive equation known as the Extended Interchain Pressure (EIP) model, of which the predictions are in quantitative agreement with the entire response of monodisperse PS melts.[57] The EIP model was also successfully applied to PS solutions in oligomeric styrene (OS)[58] and in diethyl phthalate (DEP).[59] However, this approach involves two distinct values of τ_R: one for the polymeric solutions and another for the corresponding melt, which is questionable as a Rouse process should not depend on the concentration. Narissima *et al.* later addressed this issue by proposing that interchain pressure can be transmitted by oligomeric solvents as well, and the effectiveness of this transmission is influenced by the molar mass of the solvent molecules.[60] The main prediction of this rework is that polymer concentration and molar mass of the solvent (if larger than a quarter of M_e)

have no effect on the steady-state elongational viscosity η_E. Nevertheless, the EIP model still fails to describe the observed extension thickening behavior obtained for well-entangled monodisperse PnBA.

Alternatively, Ianniruberto *et al.* and Yaoita *et al.* explained the non universal behavior of polymeric melts and solutions by the idea of flow-induced reduction of monomeric friction.[61–63] When subjected to sufficiently fast flow, the local environment of the chains becomes highly anisotropic, causing a decrease in the monomeric friction coefficient ζ_0. This, in turn, leads to a reduction in the Rouse relaxation time τ_R and a lower level of chain stretching. This hypothesis was scrutinized and reinforced by several MD simulations such as those done by Ianniruberto *et al.*[64] and Masubuchi *et al.*[65] As solvent molecules tend to stay isotropic, dilution tends to impede the reduction of friction. This effect allows to explain the difference of behavior between polymer melts and solutions. Indeed, Desai and Larson succeeded to retrieve the monotonic extension thinning of the melt and the extension thickening of the solution by introducing a friction coefficient ζ, which depends on a stretch/orientation parameter, in the DEMG model.[66] This mechanism can also account for the different rheological behavior observed for polymers with varying chemical structures. For instance, Masubuchi *et al.* have attributed the extension-thickening behavior of PnBA to the presence of flexible side-groups that are difficult to orient, thus acting as solvents and screening the interactions between the backbone segments.[67] Finally, the effect of the molar mass of the solvent on the elongational viscosity can be explained by the presence of nematic interactions between the short molecules and the long and oriented polymeric chains. The solvent with a molar mass of 4 kg/mol is more readily oriented compared to the one of 1 kg/mol solvent, which leads to a greater reduction of friction, and consequently a lower viscosity. On this basis,[56] Ianniruberto developed a multi-mode model, which could successfully fit the extensional properties of the PS solutions of Huang *et al.*. Their model includes a nematic interaction parameter ϵ, which is defined as a ratio of the order parameter of the solvent molecules to the order parameter of the long polymeric chains.[52] This new non-linear parameter varies with the molar mass of the solvent molecules. It vanishes for the smallest solvent molecule investigated,[68] and, according to the data of Shahid *at al.*, remains

constant above an oligomeric molecular weight of 9k for PS.[69]

To further investigate this idea of reduction of monomeric friction , Matsumiya *et al.* measured the extensional responses of unentangled PS and poly(p-tert-butylstyrene) melts.[70] Concentrating the investigations on unentangled systems allows to eliminate the complex dynamics resulting from the entanglements. As observed in Figure 1.25, both systems exhibit an extension-thickening behavior followed by extension-thinning with increasing strain rates. They demonstrated that such behavior cannot be explained by the Rouse model alone and an additional consideration of flow-induced reduction of friction is necessary to explain this phenomenon. They successfully modeled the steady

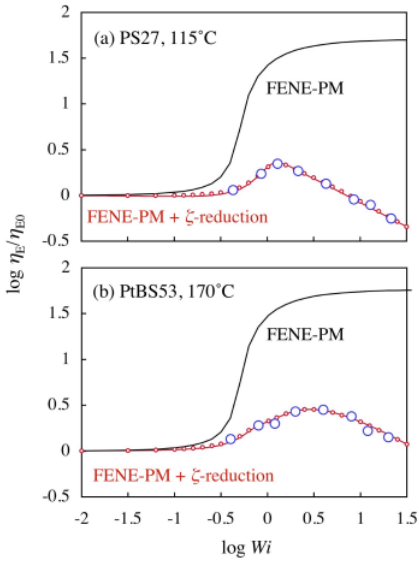

Figure 1.25: Normalized extensional viscosity expressed as a function of Wi_R of an unentangled (a) PS melt and a (b) PtBS melt. The symbols correspond to the data while the solid lines represent the predictions of the FENE-PM model with (red) or without reduction of friction. FENE-PM model refers to a Rouse model with a pre-averaged FENE-spring constant. Reproduced from [70].

state data by using a finite extensible nonlinear elasticity (FENE) bead-spring

model and by fitting experimentally the ζ reduction. However, their model failed to reproduce the transient stress growth coefficient $\eta_E^+(t)$ and the relaxation data of the polymeric melts. They hypothesized that, on start-up and cessation of fast flows, the transient ζ reduction was delayed compared to the stress evolution. As a result, the ζ reduction would be fully characterized not only by the stretch and orientation but also by their rate of change. This idea was further investigated by Ianniruberto *et al.* by means of Brownian simulations of Fraenkel chains.[71] A rather good quantitative fit of the start-up data and most of the relaxation data was obtained with their model thanks to the introduction of a time delay for the ζ reduction in the fastest flow.

In addition to the ζ reduction, Watanabe and coworkers proposed that an additional factor contributing to the deviation of the experimental data from the classical Rouse model is the violation of the fluctuation-dissipation theorem.[72-74] Based on this idea, they derive a constitutive equations for unentangled polymeric melts based on the Rouse model with a friction coefficient $\zeta(t)$, a Brownian force intensity $B(t)$ and a spring constant $\kappa(t)$ that are allowed to change under flow. The integral version of this equation is given by[75]

$$\boldsymbol{\sigma}(t) = \int_{-\infty}^{t} \frac{\kappa(t)}{\kappa(t')} M(t,t') \mathbf{C}^{-1}(t,t') dt' \tag{1.66}$$

with $M(t,t') = \dfrac{dG(t-t')}{dt'}$ being the memory function defined as

$$M(t,t') = \sum_{p=1}^{N} \frac{\nu}{2} \frac{B(t')}{\zeta(t')} \frac{1}{\tau_p(t')} \exp\left(\int_{-\infty}^{t} \frac{dt''}{\tau_p(t'')} \right) \tag{1.67}$$

Here, the times $\tau_p(t)$ are given by $\dfrac{\zeta(t)}{2\lambda_p \kappa(t)}$. It is worth noting that when the variables $B(t)$, $\kappa(t)$, and $\zeta(t)$ remain constant over time, the Lodge constitutive equation (equation 1.23) with the relaxation modulus $G(t)$ of the Rouse modulus (equation 1.26) is retrieved. According to this equation, since the Lodge equation does not predict shear thinning, any observed shear thinning in an unentangled melt is solely attributable to the fluctuations of κ, ζ, and B during

flow. Later, Watanabe *et al.* reanalysed the Rouse model with expressing ζ and B in terms of anisotropic tensorial form.[76,77]

The variation of $\kappa(t)$ is mathematically captured by the inverse Langevin function, which is derived from the non-Gaussian statistical theory of rubber elasticity. As this function has no exact analytical form, approximations of this function, such as the normalized Padé approximation or the Warner approximation, are generally used.[9]

In order to make predictions using equation 1.66, it is necessary to assume arbitrary functional forms for ζ and B. For instance, Iannirubertо *et al.* described the reduction of friction via the following ansatz:[64]

$$\frac{\zeta}{\zeta_{eq}} = \left(1 + \left(\frac{F^{so}}{F_c^{so}}\right)^{\alpha}\right)^{-n/\alpha} \tag{1.68}$$

Here F^{so} is the Kuhn segment order parameter, while F_c^{so}, α and n are fitting parameters. Experimental data and simulations results are therefore crucial to gain insight into the evolution of ζ and B with the flow and thus to develop precise analytical expressions that describe their changes with the flow.

In a recent study, Jiang and van Ruymbeke performed NEMD simulations to investigate the variations of B and ζ with the strain rates in different planar flows, including simple shear and uniaxial extension.[78] Their findings confirmed that both B and ζ exhibit changes with strain rates. However, their work also revealed that the changes in B are relatively minor compared to the variations observed in ζ in extensional flow

Later, Masubuchi *et al.* conducted a study where they compared the results of PCN simulations with experimental data of Costanzo *et al.*[45] of monodisperse entangled PS melts under to shear and extensional flow.[79] They tested two different friction reduction equations and investigated the impact of the potential deviations from the fluctuation dissipation theorem. The results showed that regardless of whether the fluctuation-dissipation theorem was upheld or violated, both friction models reasonably described the experimental data. This finding supports that the the violation does not significantly affect the predic-

tions of nonlinear rheology.

1.9 Rheology of supramolecular polymers

In this section, our focus turns to the dynamics of supramolecular polymers. We begin with a brief general introduction to contextualize the topic, and then we provide a concise review of molecular models used to describe the rheological response of such polymers.

1.9.1 Background

The inclusion of non-covalent bonds in conventional polymers offers a means of connecting polymeric chains. As illustrated in panel (a) of Figure 1.26, these bonds typically rely on weak interactions such as hydrogen bonding,[80] π-π stacking,[81,82] ionic interactions,[83] hydrophobic interactions[84,85] or metal-ligand complexation.[86,87] Each of these interactions exhibits varying strength and directionality.

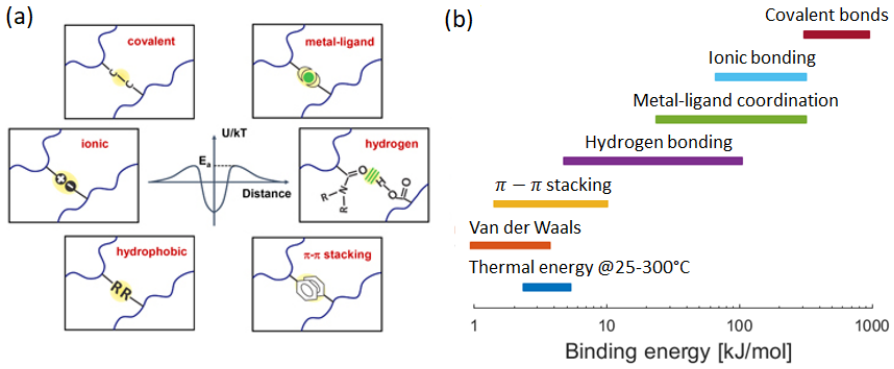

Figure 1.26: (a) Representation of different types of interactions including covalent bonding and physical interactions. (b) Binding energies associated with various types of interactions. Panel (a) and panel (b) are adapted from [88] and [89], respectively.

Panel (b) of Figure 1.26 compares the typical binding energies associated with these various types of bonds as well as the covalent bonds. As observed, the co-

valent bonds surpasses widely the thermal energy k_BT, allowing them to remain stable at room temperature and ambient pressure. In contrast, weak physical bonds tend to have energies much closer to the thermal energy, making them less stable. Consequently, the association and dissociation of the bonds can take place within our observation time frame, rendering them reversible.

The reversible nature of these bonds can confer valuable properties including the ability to respond to external triggers such as pH,[90,91] temperature[92] or irradiation.[93] A notable example of achieving high thermal responsiveness was demonstrated by Sijbesma *et al.*,[94] who employed noncovalent binding motifs based on hydrogen bonding. These motifs were attached to both ends of low molecular weight linear polysiloxane. At low temperatures, this material formed extended linear chains with high molar mass, exhibiting rheological behavior similar to well-entangled polymers. However, as the temperature increases, the dissociation rate of the noncovalent bonds increases significantly. This results in depolymerization, causing a drastic decrease in melt viscosity and improved processability of the material.

Furthermore, these bonds can also impart shape-memory[95,96] or self-healing[97–99] properties. The latter are well exemplified by the supramolecular rubber developed by Leibler and co-workers.[99] The rubber is based on a mixture of randomly branched ditopic and tritopic oligomers that contain diverse H-bonding groups. The presence of branches and the diversity of oligomers effectively prevent phase separation. As shown in the panel (a) of Figure 1.27, the system is capable of self-repair at room temperature when cut or torn into pieces, owing to the presence of physical associations. The mending occurs when the broken pieces come into contact, with no need for heat or excessive pressure. Once repaired, the sample regains its original extensibility.

In addition, weak physical bonds can also be used to improve the toughness of materials. For example, Suo and coworkers developed a double network hydrogel by combining covalently a ionically crosslinked alginate with a covalently crosslinked polyacrylamide.[100] The non-covalent network serves as a sacrificial network that dissipates energy by undergoing breakage during stretching, while the covalent network maintains the integrity of the material. As a result,

the hybrid gel exhibits a massive increase of the extensibility. Additionally, the material can partially recover part of its original properties after moderate stretching due to the reversible nature of the first network.

Finally, one can also mention that the reversible nature of the bonds in supramolecular polymers play a critical role in physiological processes, such as the folding of proteins or the winding and unwinding of DNA.[102]

Rheology provides a valuable approach to study the dynamics of physical bonds in supramolecular polymers. Indeed, the reversible junctions widely affect the viscoelastic properties of supramolecular polymers. The inclusion of supramolecular moieties, often referred to as "stickers" in the rheology community, typically translates into a much longer relaxation time and an increase of the level of the rubbery plateau. The precise evolution of these material properties depends on numerous factors such as the position of the stickers along the polymer backbone, the number of associations on each sticker, and the occurence of phase separations with their resulting morphologies.[103] The plethora of combinations allows to tune the supramolecular polymers to exhibit a wide range of rheological properties.

In this work, we specifically study the rheology of linear chains where the associative groups are located as side groups along the chain. Throughout this work, these systems are referred to as "sticky polymers". Moreover, all the chains are interconnected, resulting in the formation of a network. Therefore, in the forthcoming sections, we present viscoelastic models that are applicable to unentangled and entangled sticky polymers, as well as associative polymers containing large aggregates of stickers.

1.9.2 The Sticky Rouse model

For unentangled systems with pairwise associating units, the sticky motion of the chains is well captured by the sticky Rouse model.[104,105] In this model, the spectrum of relaxation times is divided into two groups: the "fast modes" and the "slow modes".

At length scale shorter than the average length between two associative bonds,

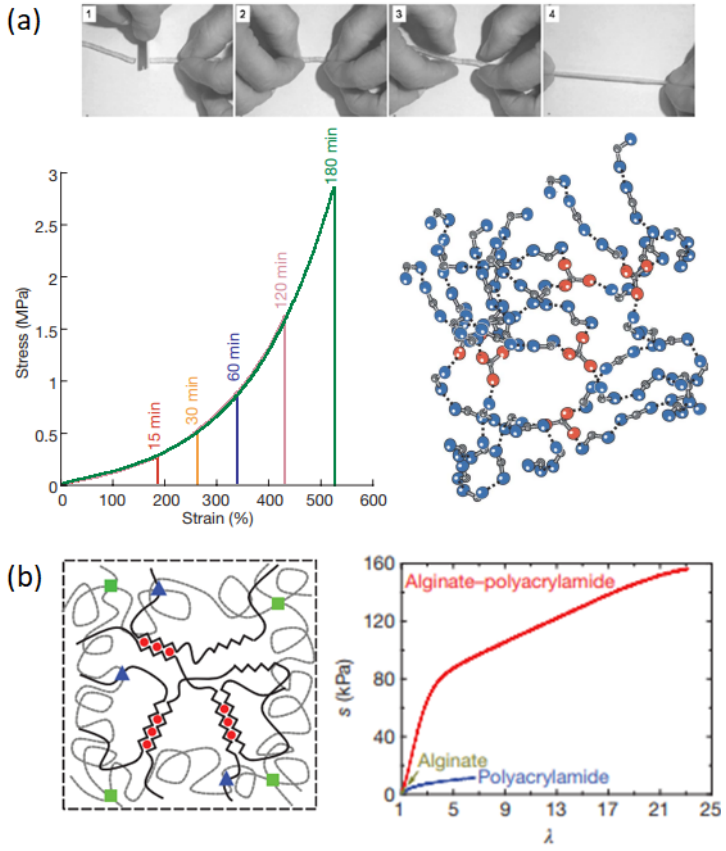

Figure 1.27: (a) Illustration of the self-healing capability of a supramolecular network based on H-bonds. The four steps depict 1) cutting the sample, 2) mending the cut parts together, 3) healing of the material, and 4) stretching the healed sample. The stress-strain behavior after various healing times at 40 ℃ is shown in the bottom left figure. The cut parts are brought into contact at 20 ℃ immediately after being cut. (b) Scheme of an alginate-polyacrylamide hybrid gel. The alginate network (represented by red circles) is intertwined with the polyacrylamide gel (represented by green squares), and both networks are interconnected by covalent crosslinks (represented by blue triangles). The stress-strain behavior is shown for the polyacrylamide gel, the alginate network, and the double network. Panel (a) is adapted from [99] and [101], while panel (b) is adapted from [100].

the relaxation is not influenced by the connectivity of the chains. As a result, the corresponding relaxation modes called "fast modes" are described by the classical Rouse process detailed in Section 1.7. In this high-frequency regime, the dynamic moduli are thus expected to vary with the square root of the frequency. This regime stops at a time scale equal to $\tau \sim \tau_0 \left(\frac{N}{N_s}\right)^2$, where τ_0 and N_s are the relaxation time of a Kuhn segment and the number of stickers along the chains, respectively.

Subsequently, the successive breaking and reformation of the supramolecular junctions allow the chains to relax further. The presence of associative bonds introduces additional drag that affects the motion of the chains. As a result, the slow modes, which are associated with the collective motion of segments larger than the segments between two stickers, are uniformly delayed and can be described by a low order Rouse process. Therefore, the dynamic moduli are again expected to evolve with the square root of the frequency. Moreover, according to the sticky Rouse model, the longest relaxation of the associative system is equal to $\tau_{rel} \sim \tau_S N_s^2$, where τ_S represents the sticker lifetime.

In the intermediate region, where time scales are shorter than τ_S and longer than $\tau \sim \tau_0 \left(\frac{N}{N_s}\right)^2$, a rubbery plateau with a modulus equal to $G = \frac{\rho RT}{M_s}$ is predicted. Here, M_s denotes to the average molar mass between two stickers.

Based on these considerations, Chen *et al.* described the relaxation modulus of unentangled supramolecular polymers using the following expression.[105]

$$G(t) = \frac{\rho RT}{M} \left[\sum_{p=1}^{N_s} \exp\left(\frac{-tp^2}{\tau_S N_s^2}\right) + \sum_{p=N_s+1}^{N} \exp\left(\frac{-tp^2}{\tau_0 N^2}\right) \right] \tag{1.69}$$

This relatively simple equation has been extensively employed in the literature to describe experimental data of unentangled supramolecular polymers.[106–108] However, it has been observed that while this equation qualitatively captures the linear viscoelastic response, there are notable discrepancies, particularly

in the plateau region of the relaxation modulus. These deviations are well illustrated in Figure 1.28, where the prediction of the sticky Rouse model is compared with the linear response of an associative polymer.

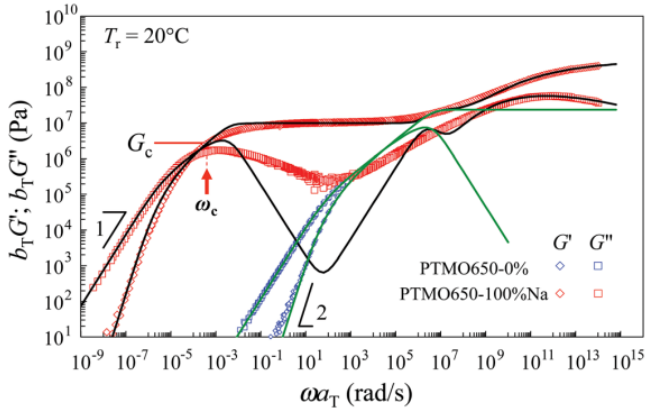

Figure 1.28: Storage and loss moduli of poly(tetramethylene oxide) (PTMO) ionomer based on sulfonated phthalates with sodium counterions (red) and it neutral counterpart (blue). The solid lines represents the predictions obtained with equations 1.69. Reproduced from [105].

Various reasons have been suggested and investigated in the literature to explain these discrepancies. One important reason is the assumption made in equation 1.69 that the supramolecular junctions are equally spaced along the backbone, which does not accurately represent the random distribution of stickers often observed in associative systems. Additionally, other factors such as the contributions from dangling ends, the non-affine spatial fluctuations of the bounded stickers, and the presence of a distribution of sticker lifetimes can also contribute significantly to these discrepancies. These effects will be further investigated and discussed in detail in Chapter 4.

1.9.3 The Sticky Reptation model

Above the critical molar mass for chain entanglement, the sticky motion of the chains is widely affected. To describe this behavior, the relaxation modulus needs to be modified using the sticky reptation model, which was developed

by Leibler *et al.*[109] In this model, the chains diffuse along the curvilinear axis of their tube by a reptative motion hindered by the successive breaking and reformation of the junctions. This model predicts the scaling laws shown in Figure 1.29.

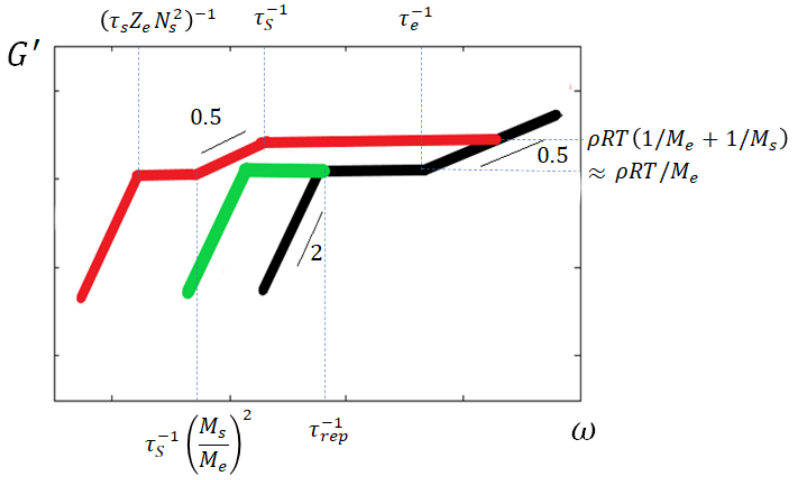

Figure 1.29: Scaling laws for entangled associative polymers when $M_e > M_s$ (red) and $M_e < M_s$ (green) and for entangled polymeric melts (black).

In the literature, we typically distinguish two cases: when the average molar mass between two entanglements M_e is greater than the average molar mass between two stickers M_s, and vice versa.[110]

In the the first case ($M_e > M_s$), after the initial Rouse process, a first plateau manifests. Its magnitude G depends on the density of the obstacles, which include both entanglements and supramolecular junctions. Consequently, G can be expressed as:

$$G = \rho RT \left(\frac{1}{M_e} + \frac{1}{M_s} \right) \tag{1.70}$$

Once the stickers dissociate, the strands between two entanglements relax through the sticky Rouse process. This relaxation process takes place in a timescale equal to $\tau_e^* \sim \tau_S \left(\frac{M_e}{M_s} \right)^2$.

After τ_e^*, the chains start to experience the topological constraints exerted by the neighboring chains through the entanglements. Consequently, a second plateau of magnitude $G_N^0 \sim \frac{\rho RT}{M_e}$ emerges solely due to the presence of entanglements. This plateau persists until the sticky reptation takes place in a time equal to $\tau_{rep}^* = \tau_e^* Z_e^3 = \tau_S N_s^2 Z_e$, where $Z_e = M/M_e$ is the mean number of entanglements along a chain.

In the second case ($M_e < M_s$), initially adressed by Chen *et al.*, some segments between entanglements can relax without requiring the dissociation of reversible crosslinks. Consequently, G is well approximated by G_N^0 and the drop occurring between the two plateaus at τ_S^{-1} vanishes, leading to the formation of a unique plateau.[110]

In the original theory proposed by Leibler *et al.*, relaxation due to CLF and CR is neglected.[109] Chen *et al.* adressed this limitation by adapting the double reptation model developed Des Cloizeaux[28] (see section 1.8.3.1) to associative entangled polymers. The modification made in their approach is to replace the reptation time τ_{rep} by the sticky reptation time τ_{rep}^* in equation 1.57. This modified version of the model showed good quantitative agreement with the data. However, it still imprecisely captures CLF and CR, indicating the need for further refinement to accurately describe the LVE response of such systems.[110]

1.9.4 Dynamics of associative polymers with clusters

In many cases, supramolecular polymers form microphase-separated clusters, rather than pure pairwise associations. The presence of such clusters in a supramolecular polymer has a profound impact on its rheological properties.

When the temperature is lower than the T_g of the clusters, or the melting temperature T_m in the case of crystalline clusters, the systems are analogous to crosslinked rubber. The bonds are effectively permanent, which prevent the system to flow. In contrast, at high temperature, the clusters become dynamic, thus enabling the polymer to relax completely. The specific details of this relaxation process remain an area of intense investigation and research.

Semenov and Rubinstein proposed that aggregated stickers can be envisioned as a dense core with polymer backbones arranged in loops resembling petals in a flower-like micelle.[111] The resulting aggregates are connected through polymeric bridges leading to the formation of a transient network. In the case of polymeric melts, the proportion of loops is expected to be small, and thus the number of bridges per aggregate is approximately equal to the number of stickers per aggregate.[112] A schematic depiction of the resulting structure is shown in Figure 1.30

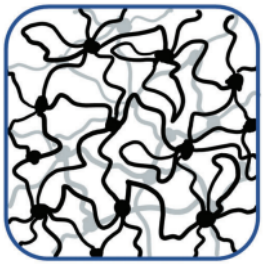

Figure 1.30: Schematic structure of a supramolecular polymers in presence of large aggregates of stickers. Adapted from [112].

Based on this picture, Semenov and Rubinstein developed a scaling theory, where the chain-level relaxation, resulting from either the sticky Rouse or the reptative motion of the chains, is decoupled from the terminal flow. The latter is governed by the positional rearrangement of the micelles. Specifically, in order to completely relieve the stress, the micelles need to reorganize via hopping events, which are characterized by a particularly high activation energy. The hopping process of a micelle necessitates to break all connections and relax all entanglements with the old neighbors, and to create new bridges with new ones. Consequently, this mechanism is expected to be drastically slower than the sticky motion of the chains and thus would dominate the terminal stress relaxation.[111,112]

However, the Semenov-Rubinstein theory is in disagreement with recent studies conducted by Mordvinkin *et al.*,[113-115] wherein the macroscopic and microscopic properties of supramolecular systems that contain unordered clus-

ters were investigated. The investigations involved the use of multiple experimental techniques, such as a specific solid-state NMR relaxometry technique (MQ-NMR), which is sensitive to single-chain relaxation, broadband dielectric spectroscopy (BDS), which provides insights into the sticker dynamics, and dynamic mechanical analysis (DMA) which assesses the bulk relaxation. The experimental results revealed that the longest relaxation time obtained from DMA were remarkably similar to those obtained from MQ-NMR. This finding led the authors to conclude that the terminal relaxation in these systems is predominantly governed by the single-chain relaxation mechanism, rather than the micellar rearrangement, as proposed by Semenov and Rubinstein. Additionally, the observed magnitude of the rubbery plateau of their systems closely matched the values predicted by the rubber elasticity theory (see equation 1.70). Based on these observations, the authors suggested that the mechanisms of sticky Rouse and sticky reptation are still applicable to supramolecular systems containing large aggregates.

Furthermore, the BDS measurements revealed a relaxation process that falls within the intermediate regime between the segmental motion of the chains and the terminal relaxation. This relaxation process displayed a similar temperature dependence as the longest relaxation times observed with MQ-NMR or DMA, indicating that it reflects the motion of the supramolecular junctions. In addition, the absolute time scale associated to this relaxation process was found to vary with the size of the alkyl side chain of the sticky groups, as illustrated in panel (a) of Figure 1.31. Interestingly, this variation showed an inverse order compared to the relaxation modes probed using MQ-NMR, DMA and conductivity. Based on these findings, the authors concluded that the relaxation process detected by BDS is not associated to the lifetime of the bonds, but rather corresponds to an intra-aggregate rearrangement caused by the motion of the junctions in the clusters.[113]

Building upon these findings, Mordvinkin *et al.* proposed a pathway for the relaxation of supramolecular polymers containing large clusters.[113] This pathway, illustrated in panel (b) of Figure 1.31, suggests that the relaxation of the system begins with the segmental relaxation of the chains, followed by the

intra-cluster relaxation. Subsequently, the sticky bonds dissociate, enabling the diffusion of the polymeric chains, which leads to the complete relaxation of the system.

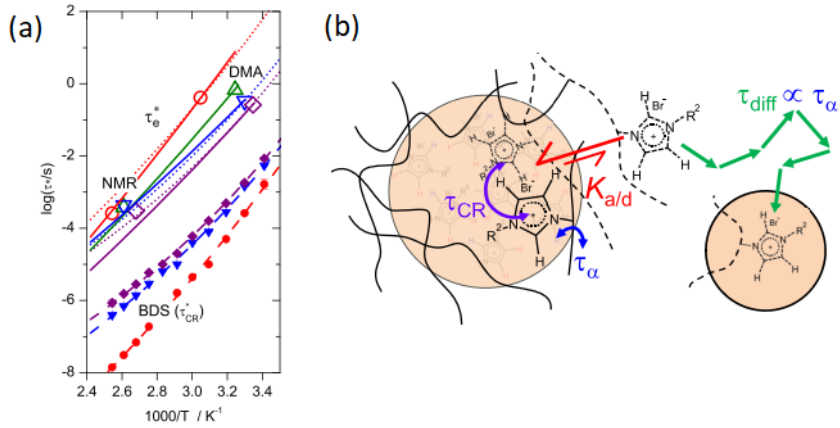

Figure 1.31: (a) Comparison of τ_e^* obtained from DMA measurements (solid lines) and NMR measurements (dotted lines) for ionomers based on butyl rubber with varying alkyl side chains. The timescales τ_{CR}^* obtained through BDS measurements are depicted in dashed lines. (b) Hierarchical sequence of relaxation mechanisms proposed by Mordvinkin *et al.* for supramolecular systems with aggregates: segmental relaxation of the chains, followed by intra-cluster relaxation, dissociation of stickers, and finally diffusive motion of the polymeric chains. Reproduced from [113].

However, the model proposed by Mordvinkin *et al.* is unable to explain the large reinforcement of the relaxation modulus as well as the extremely long relaxation times obtained in certain supramolecular polymers. This led Sokolov and coworkers to conclude that the terminal relaxation in these systems is still governed by a network rearrangement involving partner exchange between the aggregates. The specific microscopic details of this partner exchange mechanism are not very clear yet.[116]

In the original theory of Rubinstein and Semenov, stickers hop by first dissociating from one micellar core and then diffuse as free stickers until they encounter another core with which they can associate. However, hybrids molecular dynamics/Monte Carlo (MD/MC) simulations revealed the existence of alterna-

tive routes with lower energy barriers which allows the stickers to transition between clusters.[117] If two clusters are located in close proximity, they may merge into a single, entropically unfavorable large cluster. Subsequently, this unstable cluster breaks up into two new smaller clusters which may contain different stickers than the original clusters. This partner exchange process, depicted in Figure 1.32, leads to a structural rearrangement of the network without requiring the dissociations of the stickers from the network.

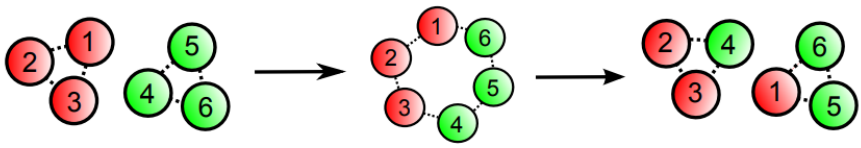

Figure 1.32: Scheme of a partner exchange event between two clusters (green and red) containing three stickers. Reproduced from [117].

However, Sokolov *et al.* argue that this partner-exchange mechanism is not applicable to polymeric systems with well separated clusters; This is because the merging of such clusters is not feasible due to the presence of multiple chains between them.[116] Thus, a critical assessment of this partner exchange mechanism is still needed as there is currently a lack of microscopic evidence to support its detailed description.

In situations where the clusters have a very long lifetime, their relaxation can be disregarded. Building upon this assumption, Hawke *et al.* developed a statistical model, shown in Figure 1.33, that accurately fits the LVE responses of entangled hydrolysed poly(n-butyl acrylate) (PnBA) copolymers with different densities of sticky groups.[118] These sticky groups, consisting of acrylic acid (AA), can form either stable aggregates or short-lived pairwise associations via H-bonds between AA units.

As illustrated in the left panel of Figure 1.33, the polymers contain three distinct groups of associative chains: (1) cluster-free chains that relax via sticky reptation, (2) star-like chains containing only one aggregate that relax via hindered CLF and (3) chains with multiple aggregates containing trapped segments unable to relax and dangling ends that relax via hindered CLF.

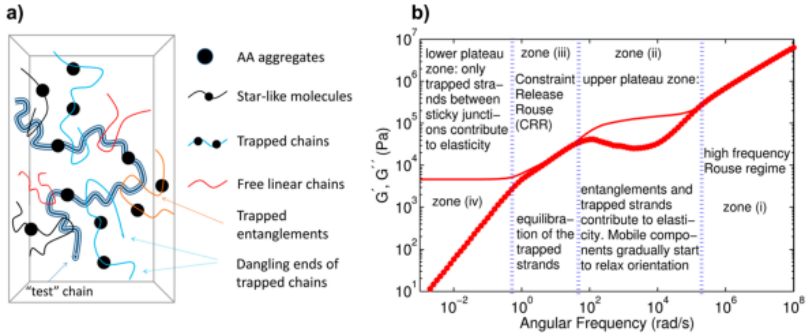

Figure 1.33: Scaling laws of the storage modulus for reversible network. Adapted from [118].

As depicted in the right panel of Figure 1.33, accounting for the relaxation of these polymer fractions leads to the prediction of the following four different regimes in the LVE response.

- At high frequency, the subchains smaller than the average spacing between two entanglements or stickers relax via a Rouse process.
- Then, an upper plateau zone where elasticity is contributed by both entanglements and trapped segments is obtained. Also, in this step, the cluster-free chains and the dangling ends relax.
- Afterwards, once all the entanglements of the mobile components are relaxed, a CRR process enables the trapped segments to equilibrate.
- Finally, the dissociation of the aggregates allow to relieve the remaining stress. As the breaking of the aggregates is a much slower process than the equilibration of the trapped segments, a second plateau appears. In the case of of the model of Hawke *et al.*, the terminal relaxation time is assumed to be infinite due to the very high stability of the clusters.

Finally, the formation of crystalline cluster is also reported to have wide consequences on the viscoelastic response of polymeric system. Crystalline structure are typically observed when unentangled and short backbones are used, specifically with telechelic precursors.[119]

For example, Ghiassinejad *et al.* investigated the dynamics and structure of unentangled hydrogenated polybutadiene (PB) end-capped by terpyridine (tpy) ligands.[120] Based on a SAXS analysis, it was found that the addition of transition metal ions in the samples lead to a microphase separation of metal complexes into a crystalline structure below the order-disorder transition temperature (ODTT). As shown in Figure 1.34, this crystalline structure provides a significant reinforcement as evidenced by the magnitude of the plateau modulus, well above the value predicted if all the complexes acted as pure crosslinking points. The quantity of metal ions influenced the morphology of the phase-separated structure, resulting in the formation of either lamellar or hexagonal morphologies, with notable effects on the ODTT and the linear viscoelastic (LVE) responses of the material.

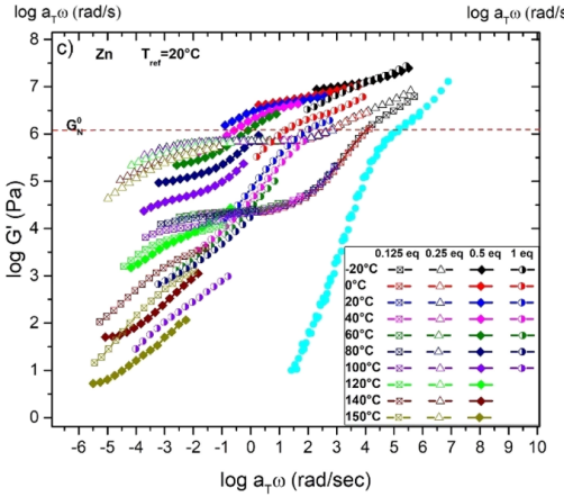

Figure 1.34: Storage and loss moduli of unentangled telechelic PB end-capped by tpy ligands, incorporating different amounts of Zn(II). The data have been shifted using the Williams-Landel-Ferry (WLF) equation. The results highlight a substantial reinforcement effect attributed to the presence of a crystalline structure. Furthermore, the response of the samples exhibits noticeable variations depending on the quantity of Zn(II) ions, indicating the formation of distinct crystalline structures. Reproduced from [120].

Another very common system that often displays ordered arrangements is the

supramolecular polymers based on quadruple hydrogen-bonding ureidopyrimidinone (UPy) groups. For instance, Botterhuis *et al.* demonstrated that UPy moieties in short polydimethylsiloxane (PDMS) chains align laterally through π-π stacking interactions, resulting in the formation of nanofibers.[121]

1.10 Lifetime of the physical bonds

As discussed above, the lifetime of a sticker τ_S plays a crucial role in the dynamics of supramolecular systems. Its temperature dependence is often described by the following Arrhenius-type equation:[88]

$$\tau_S = \tau_\nu(T) \exp\left(\frac{E_a}{RT}\right) \tag{1.71}$$

Here, τ_ν corresponds to a local attempt time, while E_a is the activation energy for sticker dissociation. The time τ_ν depends on the chain mobility at a local level, and therefore exhibits the same temperature dependence as the segmental relaxation of the precursor chains. The temperature-dependent behavior of these precursors is commonly described using the Williams-Landel-Ferry (WLF) equation when approaching temperatures close to T_g. This behavior transitions to an Arrhenius equation when operating at temperatures at least one hundred degrees higher than T_g.[9]

It is also worth-mentioning that the activation energy E_a is distinct from the binding energy E_{bind}, as it results from the combination of E_{bind} and an additional activation barrier ΔE for debonding.[122]

Recently, Ghosh and Schweizer have raised doubts about the validity of equation 1.71.[123] Through an analysis of experimental data of the literature, they discovered that using equation 1.71 led to unphysical results, such as negative activation energies or activation energies close to zero. Based on these observations, they proposed a model, wherein the temperature dependence of the pre-exponential factor is weaker than what is predicted by equation 1.71 and is chemistry dependent. A plausible explanation for this weaker dependence is that, since only small displacements are involved during the unbinding process

of the stickers, the local viscous resistance caused by the nonsticky monomers is described by a length-scale-dependent local viscosity due to non-Markovian effects. However, further refinement is still necessary to improve the predictive capabilities of their model.

In addition, according to the bond lifetime renormalization model proposed by Rubinstein and Semenov,[122] the sticker lifetime τ_S differs from the actual bond lifetime τ_b in the case of pairwise associations. This is because the stress related to the long-range dynamics only starts to relax when one of the initially paired stickers has found a new partner. After τ_b, a supramolecular junction dissociates and starts a random walk. As the latter occurs in a relatively compact space, it is likely that the junction returns multiple times to its initial partner before finding a new sticker. As a result, the lifetime τ_S is given by the following sum:

$$\tau_S = \tau_b N_{ret} + \tau_{open}, \tag{1.72}$$

Here N_{ret} is the number of times a sticker returns to its original parter and τ_{open} the time during which a sticker engages in a random walk until it forms a new bond with a partner.

In contrast, in the case of large aggregate of stickers, the bond lifetime renormalization can be disregarded when the binding energy E_{bind} falls within the range $N_{agg}^{1/2} < \frac{E_{bind}}{k_B T} < N_{agg}^{4/3}$, where N_{agg} is the mean number of stickers per aggregate. The reason for this comes from the fact that aggregates can host a variable number of stickers and the energy change after a sticker hopping event is less than the thermal energy $k_B T$.[111]

The bond lifetime renormalization model has been demonstrated by Gold *et al.* in the case of entangled transient polyisoprene (PI) networks based on binary H-bonds.[124] To validate the model, the rheological time τ_S was compared with the H-bond lifetime, which can be probed by BDS, as each dissociation and association event changes the dipole moment. As observed in Figure 5.16, the experimental results, revealed a difference of more than 2 orders of magnitude between the sticker lifetime and the actual bond lifetime, in accordance with equation 1.72.

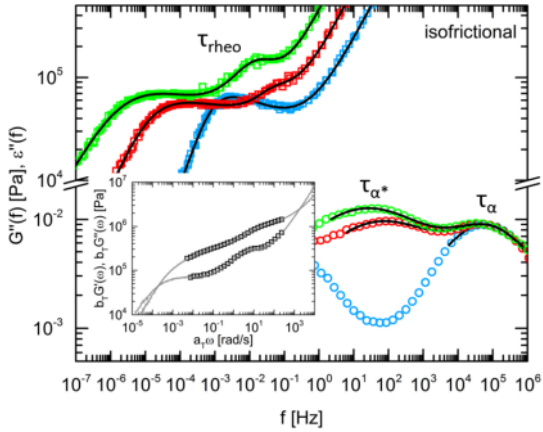

Figure 1.35: Loss modulus G'' and loss factor ϵ'' of entangled PI melt (blue) and entangled associative PI based on H-bonds (green and red). The sticker lifetime (τ_{rheo}) is determined from the end of the first rubbery plateau, as predicted by the sticky reptation model (Section 1.29). The bond lifetime (τ_{α^*}) is obtained from the second peak of the loss factor. Reproduced from [124].

1.11 Time-temperature superposition (TTS) principle

The different temperature dependences of the relaxation processes of the supramolecular systems explains the observed violation of the time-temperature superposition (TTS) principle, making these systems thermorheologically complex. However, it is still possible to apply the TTS principle in a restricted time-temperature range to capture the temperature dependence of the relaxation mechanism specific to that region.[88,125] This concept is well illustrated in Figure 1.36, where the linear responses of unentangled associative polymers with pendant groups is shown at different temperatures.

In panel (a), the dynamic moduli of the supramolecular polymers are shifted by a horizontal shift factor a'_T to achieve superimposition of the linear responses at high frequencies. As expected, these shifts lead to a failure in the superposition

in the low-frequency part due to the stronger temperature dependence of the mechanism of the sticker dissociation.

In contrast, in panel (b), the moduli are shifted by a factors a_T so that the data coincide at low frequencies. As observed, the curves cease to superimpose at high frequencies, when the segmental motions starts to contribute to the stress relaxation.

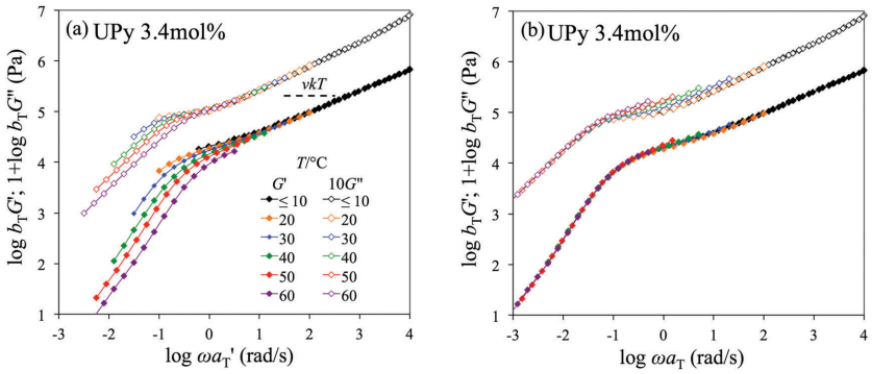

Figure 1.36: Test of the time-temperature superposition (TTS) principle for the dynamic moduli of poly(n-butyl) acrylate (PnBA) functionalized with UPy groups. In panel (a), the data are shifted by a factor a'_T to superimpose the high-frequency region. In panel (b), the data are shifted by a factor a_T to superimpose the low-frequency region. Adapted from [125].

By analyzing the resulting shift factors a_T and a'_T, it is possible to determine the activation energy E_a (using equation 1.71) as well as the parameters c_1 and c_2 of the WLF equation.

Based on this procedure, pseudo-mastercurves valid for one specific temperature are often built. These pseudo-mastercurves differ from classical mastercurves in that their breadth varies with absolute temperature, reflecting the distinct temperature dependencies of the relaxation processes. Hence, when selecting the reference temperature T_{ref} for the mastercurves, careful consideration must be given to ensure that both high and low frequency parts can be observed. Once T_{ref} is established, the moduli obtained at $T > T_{ref}$ are shifted to achieve superposition at high frequencies. Conversely, below T_{ref},

the moduli are shifted to superimpose the low-frequency region. Such pseudo-mastercurves have been built for numerous systems containing pairwise assso-ciations or aggregates[110,126-128] An exemple of a pseudo-mastercurve is shown in Figure 1.37.

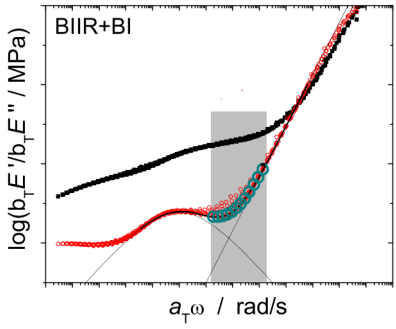

Figure 1.37: Pseudo-mastercurve of a supramolecular ionic networks (Bromobutyl rubber physically functionalized with butylylimidazole moieites). The grey area shows the experimental time window. Adapted from [113].

1.11.1 The nonlinear viscoelastic regime in associative polymers

The nonlinear regime of associative polymeric melts has been studied much less compared to the the linear regime. Despite this, several molecular models have been developed to describe the nonlinear rheology of reversible networks.

Among them, one of the most widely used is the transient network theory, which was initially proposed by Green and Tobolsky[129] and later refined by Lodge[16] and Yamamoto.[130] This theory was originally developed to explain the viscoelastic response of entangled polymeric fluids. It is based on the idea that the polymeric chains connect with each other through bridges to form a transient and reversible network. These junctions disassociate and reassociate due to the random thermal motion and/or excessive tension along the chains caused by the affine deformation of the network. A key assumption of this theory is that the network strands (subchains between by two successive junctions) always reform in the equilibrium state. Nevertheless, as explained by

Tanaka and Edwards, their theories remain semiphenomenological due to the lack of knowledge about the mechanism of dissociation and reassociation of the supramolecular junctions.[131]

Later, Tanaka and Edwards improved and adapted their work to derive a detailed molecular theory for transient supramolecular networks formed by unentangled telechelic polymers. Their model predicts the single-Maxwellian relaxation in the linear viscoelastic regime observed experimentally, notably by Annable *et al.*[84] in the case of hydrophobically modified ethoxylated polyurethane (HEUR) solutions. This peculiar relaxation is due to the fact that telechelic chains can relax entirely by simply detaching one of their associative bonds. In the nonlinear regime, a monotonic shear thinning behavior is obtained after the Newtonian plateau due to the detachment and immediate retraction of dangling chains.

This behavior is in contrast with the observed shear thickening obtained at intermediate shear rates in numerous associative polymers such as telechelic and non telechelic ionomers both at the molten state and in solutions.[132–135] This observed shear thickening has been attributed to a non-Gaussian behavior of the elastically active chains[136–138] or a flow-induced increase of the number of supramolecular bridges.[134,139] Later, in the context of a transient network composed of strings of HEUR flower micelles, Suzuki *et al.* noticed that the increase of the steady viscosity with the shear rates occurs at a moderate stretching of the network strands. They then concluded that the thickening was due to an anisotropic enhancement of the number of bridges in the shear gradient direction, while the overall density of the network strands remains approximately constant.[140] Afterwards, Brownian dynamics simulations confirmed that a shear flow can induce such spatial heterogeneities in the network connectivity.[141] Nevertheless, Ianniruberto and Marrucci revisited the results of Suzuki *et al.* and concluded that the thickening could also be due to a repulsive interaction between the micelles forced to interpenetrate one another by the shear flow.[142]

However, in a very recent investigation by Zhang *et al.*, shear thickening was notably absent in concentrated non telechelic poly(vinyl alcohol)/borax aque-

ous solution.[143] Instead, they observed a moderate thinning effect and noted the absence of any overshoot peaks in the stress growth data, as shown in Figure 2.2. Additionally, the solutions exhibited an electrical conductivity that remained nearly independent of the applied strain rates. These observations were drawn from experiments conducted at a moderate Wi.

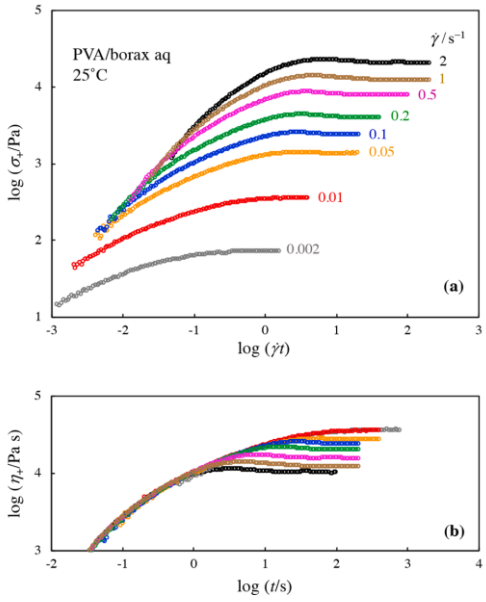

Figure 1.38: Transient stress growth coefficient of PVA/borax solution at different shear rates $\dot{\gamma}$. The longest relaxation of the solution is equal 30 s according to SAOS data. Reproduced from [143].

According to their analysis, the lack of overshoot suggests that polymer chains experienced neither substantial alignment nor stretching. Rather, the shear thinning behavior and the constant conductivity imply that the network is disrupted but rapidly reformed under flow. However, the transient network is not reformed in the original conformation due to the shear-induced separation of the stickers. Building on this molecular picture, the researchers extended the sticky Rouse model to the nonlinear regime by introducing the mechanism of conformational averaging, arising due to the disorientation caused by the continuous disruption and reformation of the network. Although a quantitative

agreement with the data was not achieved, the resulting model was able to qualitatively reproduce the observed time-strain and time-flow rate separability obtained in the relaxation data. One can mention that the study of Zhang *et al.* neglects the formation of elastically inactive loops. This is another mechanism that can contribute to shear thinning without a variation in the fraction of dissociated bonds.[144]

Finally, in extensional flow, the inclusions of associative bonds in polymeric melts is reported to increase very significantly strain hardening.[145,146] However, unentangled associative polymers containing one type of supramolecular junctions are generally very brittle and fracture before reaching the steady state.[147–149] This brittleness can be mitigated by introducing entanglements and/or different supramolecular junctions to form a double-dynamic network structure.[145,148,150]

Chapter 2

Methods

In this chapter, we introduce the experimental techniques used to characterize the polymeric materials investigated in this thesis. First, rotational rheometers were used to evaluate the linear viscoelastic behavior of these materials. Then, nonlinear extensional responses were determined through a filament stretching rheometer (FSR), whereas the nonlinear shear response was obtained using a cone-partitioned plate (CPP) fixture. Lastly, the thermal properties of the polymers were assessed using Differential Scanning Calorimetry (DSC).

2.1 Rotational rheometry

In this work, the linear measurements were performed using two rotational rheometers: the ARES-2000 (TA Instruments, USA) and the MCR 301 (Anton Paar, Austria). These rheometers were combined with an 8 mm plate-plate geometry.

2.1.1 ARES-2000 (TA Instruments, USA)

ARES-2000 is a strain-controlled rheometer designed for high viscous materials. A representation of the device is shown in Figure 2.1. The sample is positioned

between two parallel plates : the bottom plate is connected to a DC motor, while the upper plate is attached to a force transducer. A shear strain is applied by the motor to the sample, and the resulting torque is measured by the transducer. This transducer uses a controlled loop mechanism that applies a force opposing the force exerted by the sample, thereby maintaining the plate in the null position. Additionally, a convection oven can be used to control the temperature and allows to measure under inert atmosphere.[151]

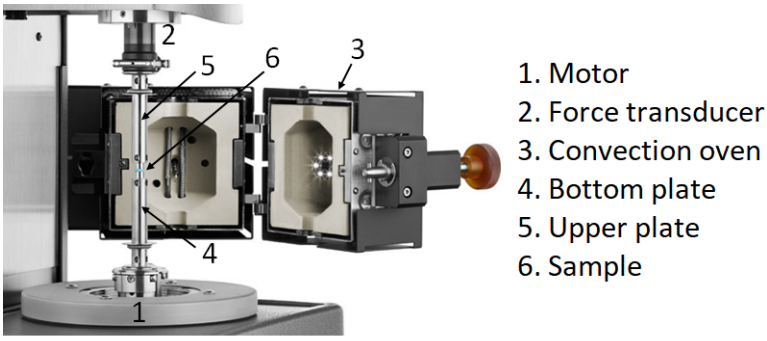

Figure 2.1: Representation of an ARES rheometer with a parallel-plate geometry. Adapted from [151].

2.1.2 MCR 301

The commercialy available stress-controlled MCR 301 rheometer (Anton Paar) has also been used in this work to evaluate the linear reponse of polymeric melts. In this rheometer, a synchronous motor applies a torque to the sample through the upper plate, and the resulting shear strain is measured using an optical encoder located in the top part of the device.[152]

As in the the ARES-200, the MCR 301 is equipped with an air/nitrogen convection oven which allows to precisely control the temperature. A representation of the rheometer with its key components is shown in Figure 2.2.[152]

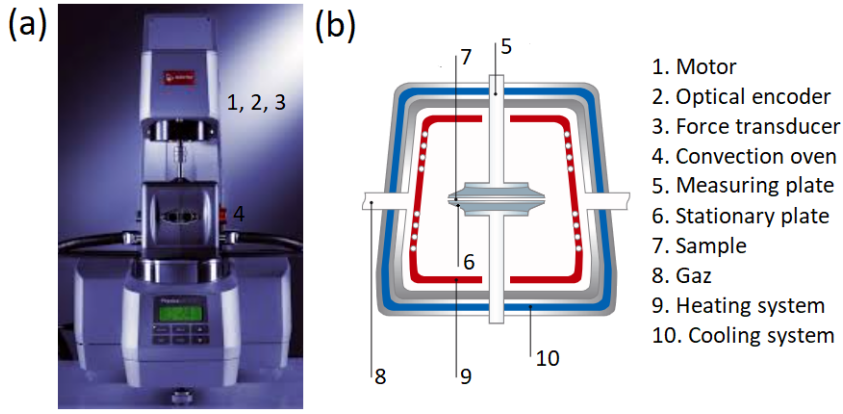

Figure 2.2: (a) Representation of MCR301 rheometer. (b) Schematic representation of the internal structure of the convection oven. Adapted from [152].

2.2 Cone-partioned plate (CPP)

A cone-partioned plate (CPP) fixture is used to perform nonlinear shear measurements of polymeric melts. The CPP was initially developed by Meissner[153] and later extensively studied by Schweizer and coworkers.[154–157] Building upon these studies, Vlassopoulos *et al.*[45,158,159] introduced a design that is compatible with the convection oven of the ARES rheometer (TA Instruments, USA). Figure 2.3 shows a schematic depiction and a photograph of this rheometer tool.

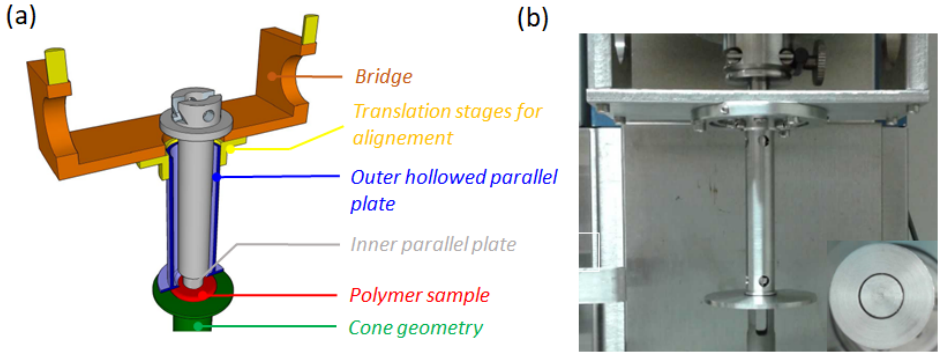

Figure 2.3: (a) Schematic representation of the CPP setup. (b) Photograph of the CPP setup. The inset shows the outer ring and the inner parallel plate. Panel (a) is adapted from [45].

In this tool, the bottom geometry consists of a standard 50mm-cone with an angle of 0.1 rad and a truncation of 51 μm. This cone is directly connected to the motor of the rheometer.

Regarding the top geometry, an inner plate with a diameter of 6 mm is directly attached to the force transducer. This plate is surrounded by a stationary hollowed plate with an inner diameter of 6.2 mm and an outer diameter of 15 mm. Importantly, the outer plate remains unconnected to the transducer. Instead, it is attached to the head of the rheometer via a hollow bridge. The hollow bridge and the outer plate are connected via a translation stage, which enables horizontal and vertical alignment.

The polymeric sample is loaded in the manner depicted in Figure 2.4.

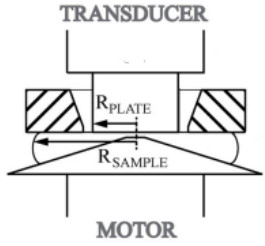

Figure 2.4: Schematic depiction of sample loading. Adapted from [158].

The CPP fixture allows to effectively delay the anomalies in measurements caused by edge fractures, compared to a regular cone and plate geometry. Indeed, when the sample is subjected to sufficiently high shear rate, the edge of the sample undergoes fracture. Initially, this does not influence the measurements because the transducer is solely connected to the inner plate. However, as the shear rate increases, the fracture progressively propagates into the measured sample, consequently affecting the measurements.[155,158]

Furthermore, the use of the CPP also postpones the onset of wall slip due to the substantial normal force applied to the sample.[45]

2.3 Filament stretching rheometer (FSR)

Extensional stress measurements were performed on the commercially available Filament Stretching Rheometer (FSR) VADER 1000 (Rheo Filament, USA). A schematic representation of the rheometer is presented in Figure 2.5.

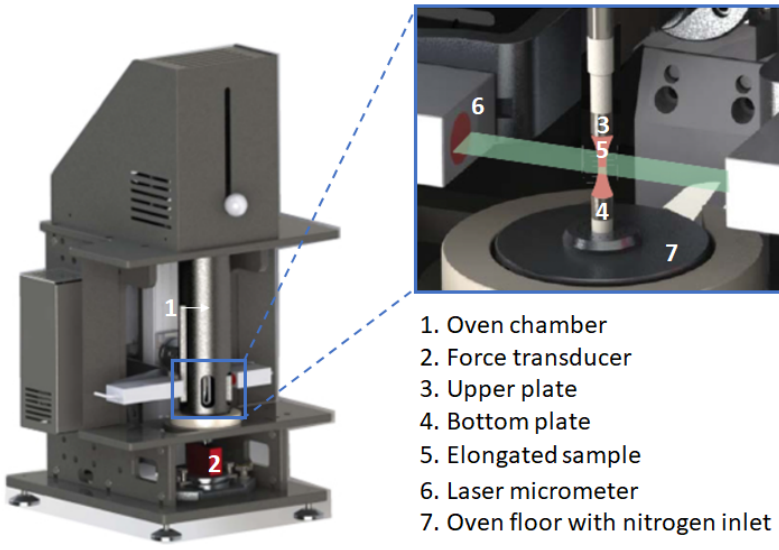

Figure 2.5: Schematic depiction of the filament stretching rheometer VADER 1000. Adapted from [160].

In this rheometer, the sample is placed between two stainless steel parallel plates with diameters of 6 mm. The bottom plate is stationary and directly connected to the force transducer, while the upper plate is attached to a linear motor. The motor allows to apply controlled deformations to the sample. The diameter of the sample is continuously monitored by a mobile laser micrometer. The entire system is contained in a convection oven, which allows measurements across a range spanning from room temperature up to a maximum of 250 ℃. The device has also the capability to maintain a continuous flow of inert gas in the oven chamber, which is regulated using a flowmeter.

The distinctive feature of the VADER 1000 rheometer, in comparison to other filament stretching rheometers, is the active feedback control loop that enables to apply the desired kinematic history to the sample in real-time.[161,162] This approach eliminates the need for the iterative experimental process, which involves performing numerous stretching experiments to determine the appropriate separation rate of the plates required to achieve the targeted kinematic history.[163,164]

The FSR can conduct various types of experiments, such as constant strain rate, constant stress or stress relaxation experiments. However, in this work, only constant strain rate experiments have been performed. In this experiment, the true Hencky strain ϵ is obtained via the following relationship:

$$\epsilon = -2\log\left(\frac{R(t)}{R_0}\right) = \dot{\epsilon}t \tag{2.1}$$

Here, $R(t)$ denotes the radius at the mid-filament plane of the sample, as measured by the laser micrometer, while R_0 represents the initial radius of the sample. The visualization of these radii is provided in Figure 2.6.

The control scheme of the rheometer contantly adjusts the vertical speed of the top plate to maintain a constant strain rate $\dot{\epsilon}$ in the midplane of the sample. Concurrently, the force $F(t)$ exerted by the sample on the load cell is recorded.

During this experiment, part of the force comes from the radial variation due

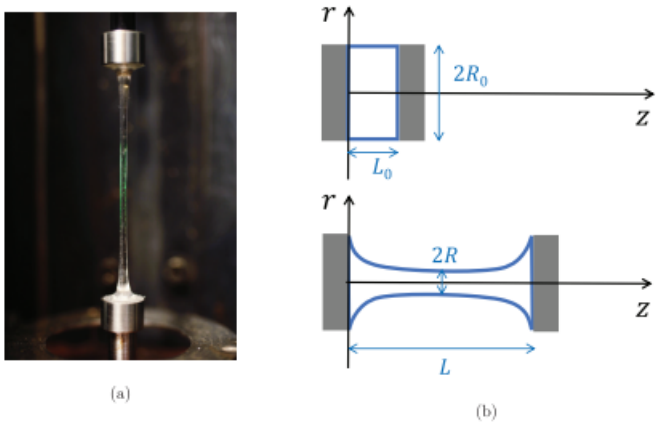

Figure 2.6: (a) Photo of a stretched sample in a VADER1000. (b) Schematic depiction of a filament stretching experiment. Reproduced from [165].

to the shear component of the deformation field, which can be compensated by a correction factor, as mentioned by H. K Rasmussen *et al.* Subsequently, for larger strains, the correction vanishes, and the radial variation of the stress in the symmetry plane becomes negligible. Assuming the mid filament has planar as well as axial symmetry, the extensional stress growth coefficient $\eta_E^+(t)$ can be calculated using the equation:[166]

$$\eta_E^+(t) = \frac{F(t) - mg/2}{\pi R(t)^2 \dot{\epsilon}} \frac{1}{1 + \left(\frac{R(t)}{R_0}\right)^{10/3} \exp\left(-\frac{\Lambda_0^3}{3\Lambda_0^2}\right)} \tag{2.2}$$

Here m is the mass of the sample, g is the gravitational acceleration, and $\Lambda_0 = L_0/2R_0$ is the initial aspect ratio of the sample. The second factor in equation 2.2 correction factor for the shearing contribution. This factor ensures less than 3% deviation from the correct initial stress if $\Lambda_0 > 0.3$.

2.4 Differential scanning calorimetry (DSC)

DSC was used to determine the the glass transition temperature of the samples. The measurements were carried out using a Q2000 instrument (TA instruments, USA) under N_2 atmosphere. The sealed aluminum DSC pans were filled with approximately 5 - 10 mg of sample.

Chapter 3

Investigating the transition between polymer melts and solutions in nonlinear extensional flow

In this chapter, we employed a Filament Stretching Rheometer (FSR) to assess the elongation properties of linear PS melts with varying molar masses, diluted at different concentrations in styrene oligomers. The obtained dataset was complemented with experimental data from Shahid's thesis.[167] This systematic study highlights scaling laws that illustrate how concentration, molar mass, and polydispersity impact the elongational viscosity of polymer melts. The resulting scaling laws are subsequently rationalised based on the molecular theories detailed in the introduction. This investigation highlights the significant role of the molecular environment in influencing the stretching of polymeric chains in extensional flow.

The content of this chapter was published as a part of the following publica-

tion:

A. André, T. Shahid, F. Oosterlinck, C. Clasen, and E. van Ruymbeke. Investigating the Transition between Polymer Melts and Solutions in Nonlinear Elongational Flow. *Macromolecules*, 54(6):2797-2810, 2021.

3.1 Introduction

The Doi-Edwards tube model,[20] coupled with relaxation mechanisms such as reptation, CLF and constraint release allows to quantitatively predict the linear viscoelastic properties of entangled polymeric systems.[21] Specifically, the model allows to express the linear response as an universal function that only depends on the average number of entanglements Z along the chains, the average molar mass between two entanglements M_e and the entanglement time τ_e.

The tube model constitutes the foundation of the so-called "standard molecular theory", which aims to predict the linear and the nonlinear properties of entangled polymers. In this theory, two additional mechanisms, namely, Chain Stretch (CS) and Convective Constraint Release (CCR) are present and can become dominant when entering in nonlinear flow.[9,49] Despite this extension of the tube model in the nonlinear regime, large discrepancies between the theory and experimental results still persist today. In particular, experimental data show that PS melts adopt a monotonous extension thinning behavior with a scaling of $\eta_E \propto \dot{\epsilon}^{-0.5}$,[168] while PS solutions with the same Z initially exhibit extensional thinning and, at elongation rates comparable to the reciprocal Rouse time τ_R^{-1}, switch to an extension-thickening behavior.[169–171] These experimental observations contradict the standard molecular theory, which predicts, for all entangled systems, an upturn of the extensional viscosity above $\dot{\epsilon} \sim \tau_R^{-1}$ due to the rapid stretching of the chains.[49]

Ianniruberto *et al.* and Yaoita *et al.* provided an explanation of this non-universal behavior between melts and solutions based on the concept of flow-induced reduction of monomeric friction.[61,62] According to this idea, the monomeric friction coefficient ζ_0 decreases due to the strong local anisotropy

caused by the coalignment of the Kuhn segments under the influence of fast flows. This reduction in friction coefficient leads to decreased relaxation times and consequently reduces the overall level of stretch experienced by the chains. In polymeric solutions, this ζ-reduction is mitigated by the isotropic nature of the solvent molecules, which explains the difference of qualitative behavior between melts and solutions.

In this study, we investigate the changes in extensional flow behavior going from polymer solutions to the melt state. Our aim is to assess the significance of the concept of friction reduction. To achieve this goal, we conducted elongation experiments to generate a new dataset, which we then compared with data provided by Shahid.[167] The polymeric systems in both dataset are obtained by dissolving moderate and relatively high molecular weight monodisperse PS in an oligomeric solvent, or moderate molecular weight PS at different weight fractions. This approach allows us to discuss the influence of concentration and molar mass on the steady state elongational viscosity to highlight scaling relations.

3.2 Materials and experimental details

3.2.1 Materials and chromatography

Polystyrene of varying molar masses was commercially obtained from Polymer Source, Inc. (Montreal, Canada). The materials were chosen to ensure a polydispersity index (Đ) as low as possible. The molar mass and Đof the ingredients were determined with size-exclusion chromatography (SEC) technique. The T_g of the melts has also been determined by differential scanning calorimetry (DSC). A standard heat-cool-heat procedure was carried out with a heating rate of 10 K/min under an inert atmosphere. The results, which were found to agree with the specifications received from Polymer Source, Inc. are summarized in Table 3.1.

Sample	M_w [kg/mol]	Đ	T_g [°C]
PS820	820	1.02	106.6
PS389	390	1.08	106.6
PS261	260.5	1.05	106.6
PS256	256	1.09	-
OS9	8.8	1.1	94.6

Table 3.1: Specifications of the raw materials.

3.2.2 Preparation of solutions and bidisperse blends

Four polystyrenes solutions and three bidisperse melts were prepared using a precipitation process following a procedure inspired by ref [51].

Once the respective PS and OS have been weighted according to the targeted weight fraction, they are dissolved in Tetrahydrofuran (THF) in a sealed contained under gentle magnetic stirring overnight ($>$ 12h) to yield concentrations from 10 to 15 mg/ml. Subsequently, the THF solution is added drop by drop into 10 times the volume of methanol under continuous stirring. When the whole solution is added into the methanol, the stirring is interrupted and the beaker is covered with an aluminium foil. After 1 to 2 h of rest in a covered container, the PS is precipitated and settled down. The precipitate is filtered off and subsequently dried under vacuum ($\sim$ 0.1 bar) at 70°C for 4 days to remove the residual solvent.

The composition of the prepared systems and their glass transition temperature T_g, determined by DSC (following the same method as for the melts) is summarized in Table 3.2. The table also includes the polymeric systems prepared and measured by Shahid as part of his PhD thesis.[167] The molar mass between two entanglements M_e and the number of entanglement Z were calculated using the equations $M_e = \frac{M_{e,0}}{\phi}$ and $Z = \frac{M}{M_e}$, respectively. The value of $M_{e,0}$ was fixed at 15 kg/mol, as established in the research conducted by Shahid *et al.*[31]

As shown in Figure 3.1, the glass-transition temperatures of the polymeric systems exhibit a linear dependence on the weight fraction of the long chains,

	Weight fraction of the long chains [wt%]	M_e [kg/mol]	Z	T_g [℃]
PS820 - OS9*	50	30	27.3	102.3
	40	37.5	21.9	101.3
	30	50	16.4	100.7
	20	75	10.9	99.8
	10	150	5.5	98.6
	5	300	2.7	98.4
PS389 - OS9	40	37.5	10.4	101.7
	20	75	5.2	101.1
PS261 - OS9	40	37.5	7	101.2
	20	75	3.5	99.8
PS820 - PS256	10	15	-	-
PS820 - PS256	30	15	-	-
PS820 - PS256	10	15	-	-

Table 3.2: Composition and glass transition temperature of the PS solutions. *: Polymers prepared and measured by Shahid.[167]

ϕ. This result is in agreement with the Fox equation, which describes the glass-transition temperature of miscible blends.[172]

$$\frac{1}{T_g} = \frac{\phi}{T_{g,PS}} + \frac{1-\phi}{T_{g,OS}} \tag{3.1}$$

In this equation, $T_{g,PS} = 106.6$ ℃ is the glass-transition temperature of the high molar mass PS, and $T_{g,OS} = 97.8$ ℃ , is that of the OS9. It should be noted that the experimental glass temperature for OS9 shown in Table 3.2 was not used due to its abnormally low value compared with the other data in the set. This discrepancy can be attributed to the presence of residual solvent resulting from an improper drying of the sample. Instead, this value was extrapolated from the linear fitting of all the other experimental results.

3.2.3 Mechanical spectroscopy

The rheological properties of the PS systems were characterized using the MCR 301 rheometer for the LVE properties, and the VADER1000 to obtain the transient elongational responses. Prior to the experiments, all samples were dried

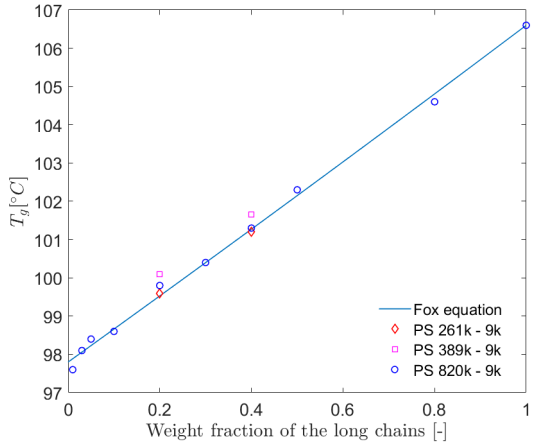

Figure 3.1: Glass-transition temperatures of PS systems as a function of the weight fraction of the long chains. The symbols are the experimental results, and the solid line is the predictions of the Fox equation. Data for PS 820-9k are taken from the thesis of Shahid.[167]

overnight at 70 ℃ and then placed into a disc-shaped and in-house developed mold. In the mold, the samples were molten, pressed and annealed at 160 ℃ under vacuum. For the linear measurements, a mold that yields disks of 8 mm diameter, and a thickness of 0.8 ± 0.2 mm was used. For the extensional measurements, a 6 mm mold was employed, resulting in disks with a final aspect ratio Λ_0 of 0.5 ± 0.15 mm.

3.2.3.1 Linear viscoelastic properties

Small amplitude oscillatory shear flow measurements were conducted using a stainless steel 8 mm parallel plate geometry with a convection oven for temperature control (∼0.1 ℃) under a N_2 atmosphere. For each sample, an amplitude sweep was carried out to determine the LVE region. Subsequently, at each selected experimental temperature, a time sweep was carried out until the dynamic moduli reached a constant value. Afterwards, a frequency sweep was performed at different temperatures ranging from 130 to 170 ℃ to determine the LVE data of each sample. Subsequently, for each polymeric system, the data were shifted onto a single master curve at a reference temperature T_{ref}

of 130 ℃ using the TTS principle. No vertical shift was considered as the density change in the experimental temperature range is negligible. To validate the experimental shift factors of the PS melt, they are compared with those predicted by the Williams-Landel-Ferry (WLF) equation[173]

$$\log(a_T) = \frac{-c_1^0(T - T_{ref})}{c_2^0 + (T - T_{ref})} \tag{3.2}$$

with $c_1^0 = 8.99$ and $c_2^0 = 81.53$ K. Data for c_1^0 and c_2^0 is taken from ref [51].

Due to the different glass-transition temperatures of the PS solutions, their horizontal shift factors are different and have a smaller temperature dependence than those of their parent melts. Indeed, as T_{ref} - T_g increases, the activation energy decreases and so does the dependence of the relaxation times with the temperature. Despite this, as demonstrated by Wagner[174] and Liu *et al.*,[175] it is still possible to draw a master curve for the shift factors of both the melts and the solutions. This can be performed by multiplying the shift factors of the solutions by a correction factor a_{T_g} which takes into account the effect of the different T_g. This shift a_{T_g} can be computed by a WLF-like equation[174]

$$\log\big(a_{T_g}\big) = \frac{-c_1^0(T_{g,ref} - T_g)}{c_2^0 + (T_{g,ref} - T_g)} \tag{3.3}$$

Here, $T_{g,ref}$ corresponds to a reference glass-transition temperature. In this study, $T_{g,ref}$ was set to a value of 106.6 ℃, which corresponds to the T_g of the polymers PS820, PS389 and PS261.

As shown in Figure 3.2, when the corrected shift factors are plotted as a function of $T - T_g$, they exhibit excellent agreement with the WLF equation. This agreement confirms the validity of the experimental shift factor a_T, as well as the values of c_1^0 and c_2^0 at T_{ref}. Based on this validation, one can frequency-shift the LVE responses of the different polymeric systems onto a temperature $T_0 = T_g$ + 23.4 ℃ and $T_0 = T_g$ + 31.4 ℃ to compare them at iso-T_g conditions.

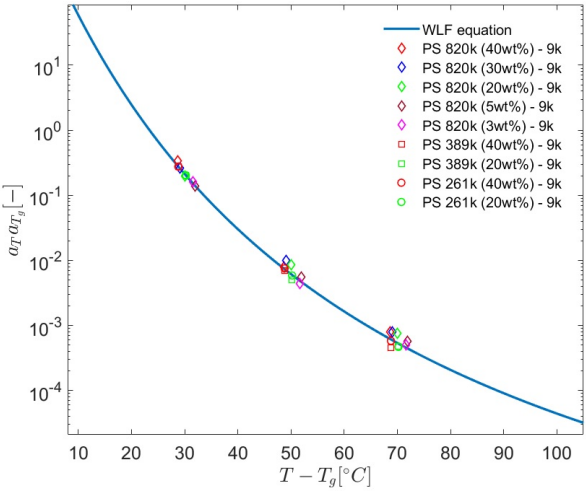

Figure 3.2: Corrected shift factors $a_T a_{T_g}$ of PS systems as a function of $T - T_g$ at the reference temperature $T_{ref} = 130$ °C. The symbols are the experimental results and the solid line is the predictions of the WLF equation. Data for PS 820 - 9k systems is taken from ref [167].

3.2.3.2 Viscoelastic Response under Uniaxial Elongation

Extensional stress measurements were performed on the FSR using stainless steel 6 mm plates. The filament stretching measurements were carried out using the subsequent protocol, inspired by ref [170].

Once the temperature in the oven reaches 165 °C, the sample is placed inside the rheometer on the bottom plate. The polymer is then melted, and the sample is slightly compressed by lowering the top plate to ensure proper adhesion between the sample and the geometries, preventing detachment during stretching. This squeezing was continuously interrupted to allow the sample to relax. Afterwards, the sample is pre-stretched to a smaller radius to reduce the force build-up during the actual stretching and thus to avoid detachment during the main stress measurement. Similar to the compression step, the pre-stretching is temporarily halted multiple times to allow the sample to relax. This pre-stretching process is performed until the desired starting radius R_0 is reached, which ranges from 1.2 to 3.5 mm. The choice of the radius R_0 depends on the

specific characteristics of the sample and the experimental conditions. When high strain rates are applied to highly viscous samples, the force build-up is so high that rupture at both ends of the filament cannot be prevented without reducing the radius R_0. Conversely, when a low-viscous sample is stretched at low strain rates, a sufficiently large R_0 is required to avoid a noisy signal. Finally, the temperature of the oven is lowered to the temperature of the experiment. Once the sample is relaxed, it is stretched at a constant strain rate ranging from 3×10^{-5} to 0.2 s^{-1}.

3.3 Results and Discussion

3.3.1 Linear Rheology

Figures 3.3 and 3.4 display the storage and the loss moduli of the PS systems at iso-Tg conditions. The linear responses of the PS melts and of PS820-OS9 can be found in thesis of Shahid.[167] To model the LVE responses of the long chains diluted in oligomers with well separated relaxation times, the modified TMA tube-based model developed by van Ruymbeke *et al.*[1] is used. A good prediction of the experimental data is achieved at $T = T_g + 23.4$ ℃, by considering M_e to be equal to 15 kg/mol, τ_e to be 0.55 s, and G_N^0 to be 230 kPa, consistent with the work of Shahid *et al.*[31] The molecular weight of a PS Kuhn segment is assumed to be equal to $M_K = 833$ g/mol,[53] and the dynamic dilation exponent α (as defined in section 1.8.2.3) is set at 1.[176] These values allow to determine consistently the different characteristic times of the flow dynamics of the polymer on a physical basis.

Table 3.3 presents the Rouse times $\tau_R = Z^2\tau_e$ of the different chains, which characterizes the stretch relaxation time. These values were computed at two different iso-T_g conditions as in this chapter $\Delta T_g = T_{ref} - T_g$ is set to 31.4 ℃ in Section 3.2 and 23.4 ℃ in the other sections. Additionally, the reciprocal Rouse time τ_R^{-1}, which is approximately the onset of stretching in the standard tube model, is also included in Table 3.3. Nevertheless, it should be considered with care as the criteria for the critical strain rate for chain stretching are still under debate.[177,178]

	$\Delta T_g = 23.4$ ℃		$\Delta T_g = 31.4$ ℃	
	τ_R [s]	τ_R^{-1} [s^{-1}]	τ_R [s]	τ_R^{-1} [s^{-1}]
PS820	1643.6	6×10^{-4}	258.5	0.0039
PS389	369.9	2.7×10^{-3}	58.2	0.017
PS261	166.5	6×10^{-3}	26.2	0.038
OS9	0.2	5	0.03	33.34

Table 3.3: Rouse times and reciprocal Rouse times of the chains.

As shown in Figure 3.3 and 3.4, all PS systems overlap at high frequencies. This overlapping occurs because, in this particular range, polymer chains relax through the Rouse process, which starts locally and is not affected by chain length or dilution.

This regime continues until the entire chain relaxes at a frequency $\omega_R \sim \tau_R^{-1}$ for the OS, or until it is interrupted by the entanglements at a frequency $\omega_e \sim \phi^2/\tau_e$ for the long chains. In the case of the solutions diluted at 20 wt%, the difference in the high frequency response of the OS and the long chain polymer is clearly perceptible. While the high frequency regime is dominated by the OS relaxation, the frequency window between 1 and 20 rad/s corresponds to a transition state between the relaxation of the OS of molar mass 9 kg/mol and the Rouse relaxation of the long chains, up to the relaxation of segments between two entanglements of mass $M_e/\phi = 60$ kg/mol, taking place near $\omega_e \approx 0.73$ rad/s.

At intermediate frequencies, the solutions display a rubbery plateau, which gradually decreases with the level of chain dilution. It should be noted that, for the most diluted solutions, the plateaus are barely noticeable due to the very small number of entanglements.

Finally, the terminal relaxation time decreases with decreasing concentration as predicted by the DTD theory.[30]

These experimental data are then used to create LVE envelopes that reconstruct the stress growth coefficient of elongational measurements in the linear regime. Any upward deviation of the transient extensional data from these envelopes

indicates strain hardening.

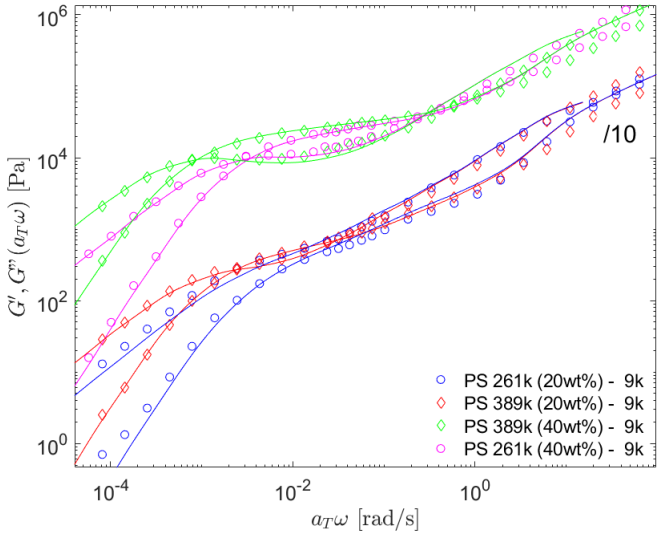

Figure 3.3: Linear viscoelastic response of PS 261k - 9k and PS 389k - 9k at $T = T_g + 23.4$ ℃. For clarity, the data of the PS 261k (20 wt%) - 9k and PS 389k (20 wt%) - 9k systems are downshifted by 1 decade. The symbols are the experimental results and the solid lines are the predictions of the TMA tube-based model.

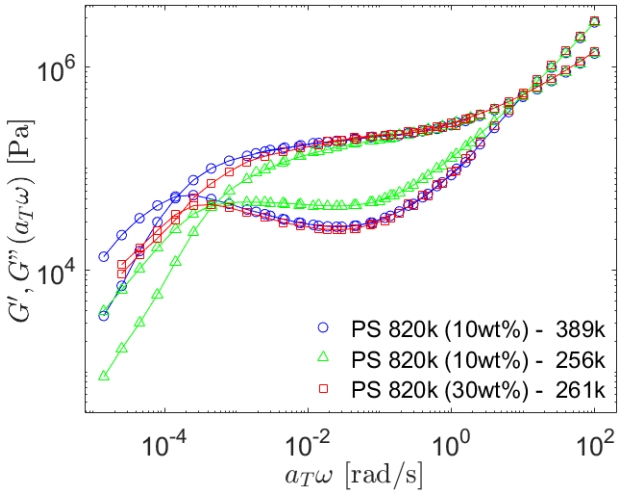

Figure 3.4: Linear viscoelastic response of PS 820k (10 wt%) - 389k, PS 820k (10 wt%) - 256k and PS 820k (30 wt%) - 261k at $T = T_g + 23.4$ ℃.

3.3.2 Elongation viscosity: From the melt state to solution

Figure 3.5 exhibits the elongational results of Shahid[167] conducted on PS solutions with varying concentration, along with the corresponding LVE envelopes. At very low strain rates (typically at $\dot{\epsilon} < \tau_{rep}$), $\eta_E^+(t)$ follows the LVE envelopes. This behavior is exemplified in panel (a), which shows two cases of elongational flow measurements at very low rates.

At high strain rates, an experimental deviation from the LVE responses can be observed at very short times. This deviation, which is also observed in our data as shown in the following section, can be attributed to two main factors. Firstly, when initiating the experiments, there remains a small residual stress due to the pre-stretching of the polymer that cannot relax within reasonable experimental timescales. Additionally, the fluctuations inherent in the control loop implemented in the FSR causes the force to exhibit oscillations at short times. At the start-up of the experiment, these oscillations are significant as the flow is not stabilized due to the limitations in the control of the FSR for

starting the plate displacement from the rest state. However, this deviation only affects the data at short times, the steady states and data at longer times being unaffected as the stress involved is few orders of magnitude higher. Apart

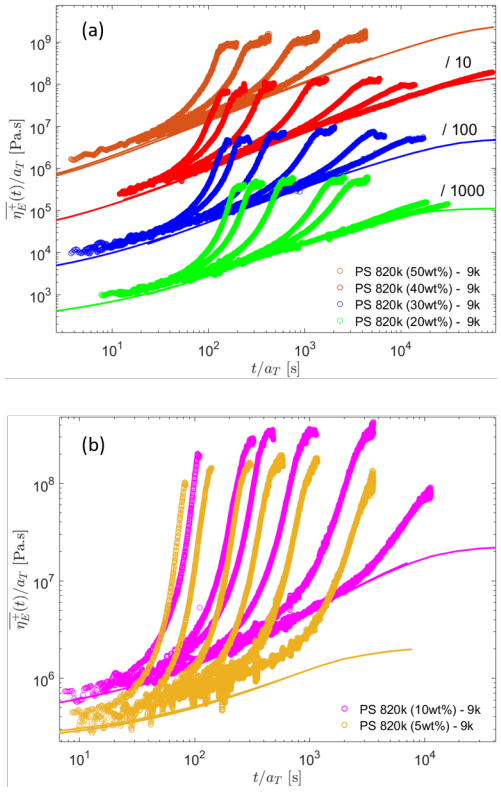

Figure 3.5: Stress growth coefficient of PS solutions taken from the thesis of Shahid. Data were measured for different strain rates at $T = 130$ ℃. In panel (a), the strain rates are from right to left 0.001, 0.003, 0.01, 0.03, 0.06, 0.09 s^{-1}, except for PS 820k (50 wt%) for which the strain rates are from right to left 0.003, 0.01, 0.03, 0.06 s^{-1}. Additionally, for PS 820k (40 wt%) and PS 820k (20 wt%), LVE envelopes were also measured in elongational flow at 0.0001 and 0.00003 s^{-1} respectively. In panel (b), the strain rates are from right to left 0.003, 0.01, 0.03, 0.06, 0.09, 0.2 s^{-1} for PS 820k (10 wt%) and 0.01, 0.03, 0.06, 0.1, 0.2, 0.3 s^{-1} for PS 820k (5 wt%). All the data are shifted to $T = T_g + 23.4$ ℃. For clarity, some of the extensional data are downshifted by 1, 2 or 3 decades as indicated.

from that, the transient viscosity of the solutions first superimposes with the linear responses and then rapidly deviates before reaching a steady state. For all the strain rates presented here, at least the onset of the steady-state value was reached.

The elongational results highlight the influence of the dilution level on strain hardening behavior. As the concentration decreases, the strain hardening becomes more pronounced. The effect is more obvious in Figure 3.6. In this figure, the steady state viscosity is presented as function of the strain rate, alongside the LVE envelopes, adjusted according to the Trouton ratio.

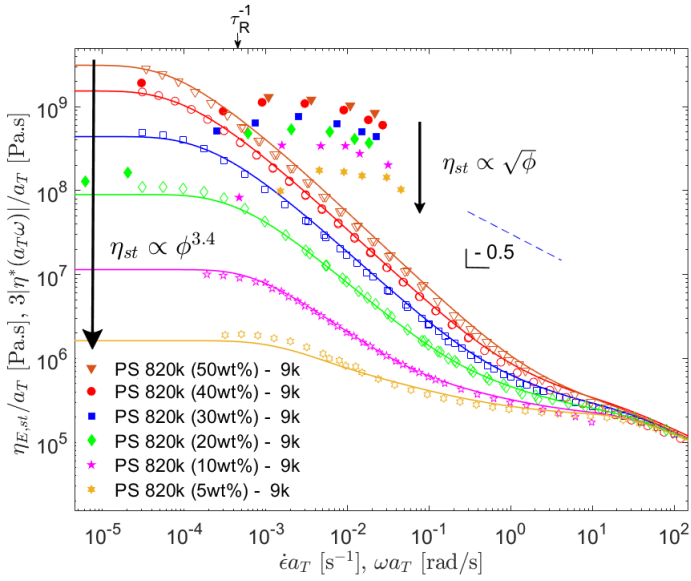

Figure 3.6: Elongational steady-state viscosity data for PS polymers are displayed by closed symbols, while the corresponding LVE data are represented with open symbols. The solid lines indicate the TMA tube-based model's predictions for the LVE data. Data are respectively measured or shifted to $T = T_g + 23.4$ °C.

At high strain rates, all steady state viscosity values exhibit a similar decrease with elongation rate with a scaling of $\eta_{E,st} \propto \dot{\epsilon}^{-0.5}$. In the literature, a similar scaling has already been observed for different chain architectures, including

linear[168] and star PS chains[179] as well as PS rings.[54] It has also been observed in both entangled[168] and diluted polymer systems.[55] However, this scaling law is not expected to be universal across different polymer chemistries, as demonstrated by the recent work of Morelly *et al.* which revealed different power-law exponents for PMMA, PS, and poly(tert-butylstyrene) (PtBS).[53]

As observed, Figure 3.6 unveils three regimes with different dependence of the steady state elongational viscosity on the concentration.

A. Low strain rates

At low strain rates, the LVE envelopes and the steady state viscosity $\eta_{E,st}$ coincide. $\eta_{E,st}$ is therefore well predicted by the Doi-Edwards theory.[20] By neglecting the contribution of the short chains, $\eta_{E,st}$ exhibits the following scaling:

$$\eta_{E,st} = 3\eta_0 \propto \frac{\rho N_A}{M_K} \frac{N^x}{N_e^{x-1}} \zeta_0 \propto M^x \phi^x \qquad \text{with} \quad x \in [3, 3.6] \tag{3.4}$$

where N_A is the Avogadro constant. Thus, in the linear regime, the steady viscosity scales with the number of entanglement segments, Z. The ϕ-dependence of the steady viscosity can be found by considering that η_0 is well approximated by $G_N^0 \tau_d$. Indeed, the plateau modulus G_N^0 scales with ϕ^2 (if we consider that the dilation exponent α is equal to 1), while the terminal relaxation time τ_d scales with $\phi^{1-1.4}$, since the reptation time of the chains scales with ϕ^1 and their fluctuations times scales with ϕ^2. As for polymer melts, different scalings are thus obtained, depending on the importance of the CLF, these last ones depending on the entanglement state of the chains.

B. High strain rates

At high strain rates ($Wi_R \gg 1$), polymer chains experience stretching. In this regime, the influence of concentration on the system is significantly reduced compared to the linear regime. To evaluate the effect of the concentration on the steady state extensional viscosity, linear regressions were performed on

the data using the following expression obtained though dimensional analysis:

$$\frac{\eta_{E,st}}{G_N^0 \tau_R} = \frac{A\phi^x}{\sqrt{\tau_R \dot{\epsilon}}} \tag{3.5}$$

In the equation above, similarly to the work of Bach *et al.*,[168] the Rouse time τ_R is chosen to normalize the elongation rate. Additionally, the viscosity is made dimensionless using the plateau modulus and the Rouse time. Since the Rouse time scales with the square of the molar mass, it is expected that the extensional viscosity scales linearly with the molar mass. This linear dependence is verified in section 3.3.3.

Figure 3.7 demonstrates a good agreement between Equation 3.5 and the data, with an exponent x set to 0.5 and a prefactor A of 13.3. The data set encompasses the highest strain rates for all PS solutions considered in this work. To enhance the accuracy of the regression analysis, the steady state viscosity values of two polymer melts from ref [169] were included into the dataset. Consequently, we conclude that, at high strain rates, the steady state viscosity of polymeric solutions evolves with the square root of the concentration. It is important to note that this 0.5 scaling must be taken as indicative in view of the scatter in the data. Nevertheless, the concentration scaling of the steady viscosity is definitely more in line with a $\sqrt{\phi}$ dependence than a ϕ dependence. The experimentally observed scaling cannot be explained by the classical DEMG theory. In this theory, the steady state viscosity for fully oriented chains is given by the following equation:[9]

$$\eta_{E,st} = 3G_N^0 k(\lambda)\lambda^2 \dot{\epsilon} \tag{3.6}$$

Here, the coefficient $k(\lambda)$, which is given by the inverse Langevin function, describes the deviation of the FENE spring from the pure Hookean spring.

At high strain rates ($Wi_R \gg 1$), the DEMG theory predicts that the steady state viscosity saturates as the chains become nearly fully stretched. The corresponding value of the elongation viscosity in this regime, is given by:[180]

$$\eta_{FENE} = \frac{1}{12}\frac{\rho N_A}{M_K}\zeta_0 N^2 b^2 \tag{3.7}$$

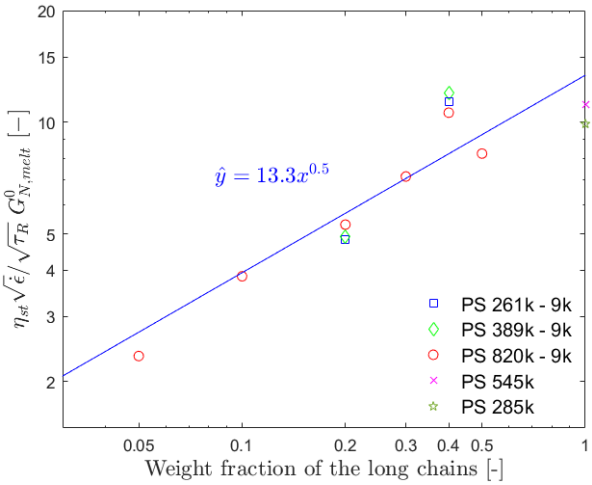

Figure 3.7: Assessment of the influence of the concentration on the steady state elongation viscosity.

As a consequence, η_{FENE} is predicted to evolve linearly with ϕ as it scales with the density of the long chains ρ.

Figure 3.8 shows the ratio of η_{FENE} to the maximum viscosity $\eta_{E,max}$ obtained for the PS solutions after $Wi_R > 1$. While by increasing the dilution, $\eta_{E,st}$ draws nearer to η_{FENE}, it clearly stays below this limit, indicating that, according to equation 3.7, these systems are not fully stretched. However, even if the chain stretching in the steady regime is lower than the finite extensibility, one would have expected a ϕ-dependence of the steady viscosity in this high strain rate regime. Indeed, the chains have the same Rouse time and are therefore expected to stretch in the same way, whatever their concentration. Only the density should be affected by the dilution of the polymer chains (see Equation 3.6). This ϕ - dependence can also be found if we consider that the steady viscosity is well approximated by $\eta_{E,st} = 3G^0_N\lambda^2_{melt}\dot{\epsilon}^{-1}$ in the large elongation rate regime ($Wi_R > 1$), since by diluting the sample, the plateau modulus is rescaled as $G^0_N\phi^2$, while the stretch factor is rescaled as $\lambda = L_{pp}/L_{eq,0} = \lambda_{melt}\phi^{1/2}$.

As discussed in the introduction, this unexpectedly high steady viscosity found

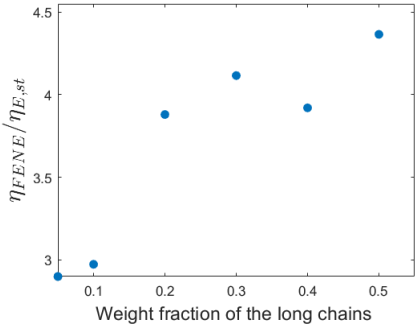

Figure 3.8: Ratio of η_{FENE} to the maximum steady state viscosity $\eta_{E,stmax}$ obtained for PS820k - 9k solutions at $T = T_g + 23.4$ °C and at $Wi_R > 1$ (Wi_R = 7.44, 7.76, 3.34, 4.11, 1.48, 1.77 for 5%, 10%, 20%, 30%, 40% and 50% of PS820k, respectively).

when diluting the sample has already been observed, and has been discussed by Ianniruberto *et al.* based on the concept of monomeric friction reduction:[61] as one increases the concentration, the stretched and long chains have a lower probability to be surrounded by the nearly isotropic short chains and thus have a higher potential for reduction of monomeric friction. As a consequence, the retraction time decreases and the shrinkage of the chain increases. Thus, according to this concept, polymer chains are stretching more when they are diluted in oligomers. This idea is tested in Figure 3.9 for the transient response. Panel (a) shows a comparison of the stress growth coefficient of the samples containing 5 wt%, 10 wt% and 20 wt% of PS820 in OS9, deformed at a similar elongation rate. The data are divided by ϕ, in order to account for the influence of concentration on the chain density. It is observed that the curves superimpose well, before and during a large part of their strain hardening. Only at long times, just before reaching the steady state regime, differences between the transient viscosities of the samples are observed, leading to the $\sqrt{\phi}$ scaling, as illustrated in panel (b). Thus, these results suggest that, at short times, the chains stretch in a similar way in the three samples, with no influence of the concentration and of their molecular environment. According to the friction reduction concept, this means that at these times ($t < 150$ s), despite the fact that the coalignment of the chains is large enough to induce chain stretching, it

stays too low to induce friction reduction. Differences with concentration due to friction reduction only emerges at longer times, when the chain coalignment is more important.

As it has been discussed by Schroeder[181] and Young *et al.*,[182,183] a change of the concentration dependence of the extensional viscosity could also be caused by the emergence of local hydrodynamics when diluting the polymeric chains, with the oligomers acting more and more like a good solvent. However, as it is shown in ref. [69], the same steady viscosity is found if oligomers are replaced by short entangled chains (PS chains of 73 kg/mol). The role of the environment is therefore, not clear and should be further investigated.

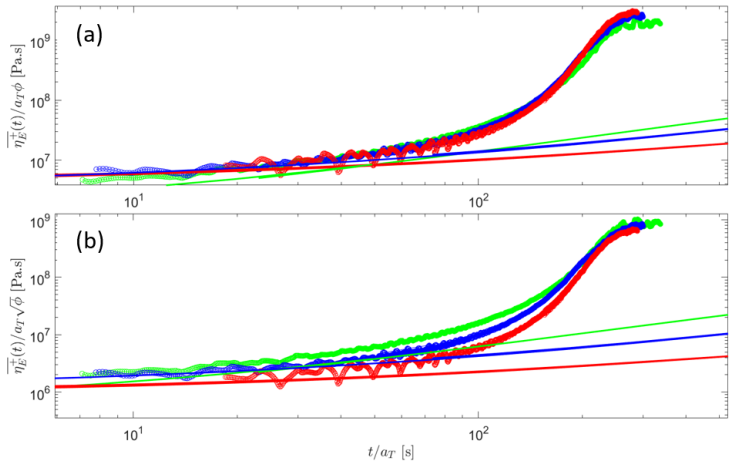

Figure 3.9: Stress growth coefficient for diluted solutions containing 5 wt% (red), 10 wt% (blue) or 20 wt% (green) PS820, divided by ϕ (a) or by $\sqrt{\phi}$ (b). Their corresponding strain rates are 0.0151 s^{-1}, 0.0142 s^{-1} and 0.0122 s^{-1}, respectively. Data are shifted at $T = T_g + 23.4$ °C.

C. Intermediate strain rates

As shown in Figure 3.6, an intermediate regime between the linear and the high stretch regime is obtained at $Wi_R \sim 1$. In low-concentrated solutions, an upturn in the steady-state viscosity is obtained, leading to the formation of a steady-thickening region. Conversely, the more concentrated polymer con-

sistently maintain values of $\eta_{E,st}$ below below $3\eta_0$, indicating a monotonous steady thinning behavior.

These results also suggest that the steady-state viscosity reached in the nonlinear regime should be interpreted independently from the LVE envelope or the transient hardening as viscosity values in the different regimes scales in a fundamentally different way. Similar arguments have also been made by O'Connor *et al.*[184] in the case of polymer melts, to explain the rate dependence of the steady viscosity with varying molar mass and number of Kuhn segments per entanglement segment.

3.3.3 Elongation Viscosity: Influence of the Molar Mass.

The influence of the molar mass of the long PS chains in solution is studied by looking at samples with different molar masses while keeping a constant level of dilution. Much like the results introduced in the preceding section, the onset of the steady-state values was reached for all strain rates presented in Figure 3.10. However, for the blends PS261k (20 wt%) and PS389k (20 wt%), when the steady state was about to be reached, large oscillations were recorded by the FSR. Despite this, we decided to keep the data as they still allow discussions. Figure 3.10 reveals that the smaller the molar mass of the long chains, the smaller the strain hardening and the greater the ratio between the steady-state values and the zero-elongation viscosity $3\eta_0$ becomes. Again, this result seems to be related to the different molecular weight dependence in the linear regime and in the nonlinear regime.

This effect can be seen better in Figure 3.11, which plots the steady-state viscosity of the solutions as a function of the strain rates. Indeed, the linear regime is much more affected by the molar mass of the chains than the nonlinear regime. The curves also show a similar three-regime picture, as described in the previous section. In the linear regime, the steady-state viscosity scales with $\eta_E \propto M^x$, where $x \in [3,3.4]$, while, in the nonlinear regime, as shown in Figure 3.12, it scales linearly with the molecular mass of the chains. At intermediate strain rates, there is an upturn of the steady-state viscosity, which becomes much more prominent for the low molar mass samples.

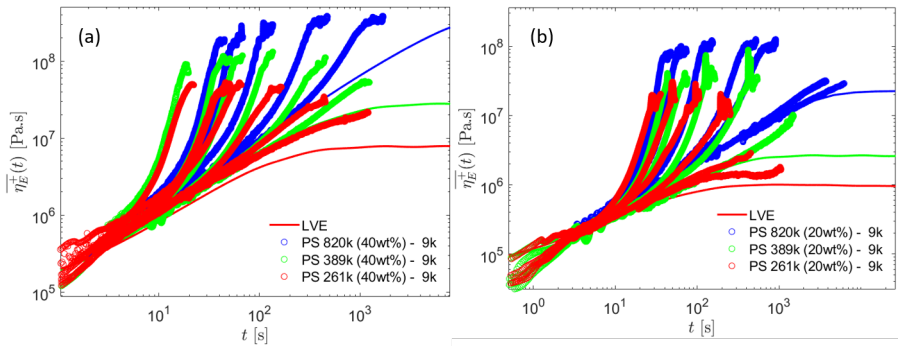

Figure 3.10: Stress growth coefficient of PS solutions for different strain rates at $T = 130$ ℃. Data were measured for different strain rates. In panel (a), the strain rates are from right to left 0.003, 0.01, 0.03, 0.06, 0.09, 0.2 s^{-1} for PS 389k (40 wt%) and PS 261k (40 wt%) and 0.003, 0.01, 0.03, 0.06, 0.09 s^{-1} for PS 820k (40 wt%). In panel (b), the strain rates are from right to left 0.003, 0.01, 0.03, 0.06, 0.09 for PS 389k (20 wt%) and PS 820k (20 wt%) and 0.003, 0.01, 0.03, 0.06, 0.09, 0.2 s^{-1} for PS 261k (20 wt%). Additionally, for PS 820k (20 wt%), LVE envelopes were also measured in elongational flow at 0.0001 and 0.00003 s^{-1} respectively. All the data were subsequently shifted to $T = T_g + 23.4$ ℃.

Note that the linear scaling in the high stretch regime is in discrepancy to the quadratic scaling predicted by equation 3.7 when all chains are oriented and nearly fully extended. A linear dependence with the molar mass was also obtained by Bach *et al.* in the context of nondiluted polymeric melts.[168]

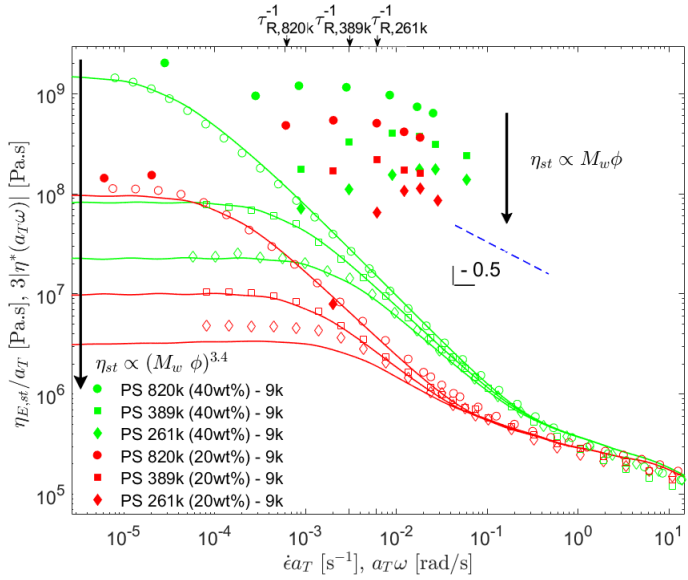

Figure 3.11: Elongational steady-state viscosity data for PS polymers are displayed by closed symbols, while the corresponding LVE data are represented with open symbols. The solid lines indicate the TMA tube-based model's predictions for the LVE data. Data are respectively measured or shifted to $T = T_g + 23.4$ °C.

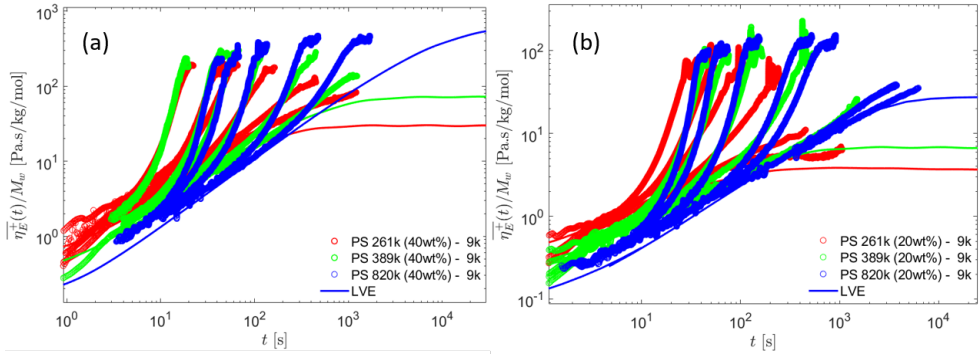

Figure 3.12: Stress growth coefficient $\eta_E^+(t)$ of PS solutions divided by the molar mass.

3.3.4 Elongation Viscosity: Influence of the Polydispersity.

In this section, we study the response of bidisperse systems of long and short chains. The bidisperse blends are used as model systems to investigate the influence of the polydispersity on the extensional viscosity of PS systems.

The short components in the bimodal blends are PS256, PS261, and PS389. These selections are made such that the highest strain rates significantly exceed their reciprocal Rouse time τ_R^{-1}, ensuring that all the chains in the polymer are stretched (see Table 3.3). It should be noticed, however, that this criterion may not be valid if the concept of reduction of the monomeric friction is considered. Indeed, in such a case, the initial stretching of the long chains is expected to make the environment of the short chains more anisotropic and thus to delay the onset of stretching. However, the strain rates used here are significantly higher than τ_R^{-1}, which should be sufficient to compensate any possible decrease in the stretch relaxation time.

In addition, the molar mass of the chains is sufficiently high to prevent the effect of tube dilation. The Graessley number $Gr = \dfrac{M_L M_e^2}{M_S^3}$ of the polymers is much higher than the critical Graessley number Gr_c.[185] Therefore, the entanglements with short chains are long-lasting and the long chains relax in a thin tube formed by entanglements with both long and short chains. This means that all the systems have the same finite extensibility $\lambda_{max} = \sqrt{N_e}$, and each entanglement segment has the same ability to stretch.

According to the concept of friction reduction, viscosity of bidisperse melts is expected to approximately scale with $M_w\phi$. This prediction arises from the notion that changing the concentration in bidisperse blends should not considerably modify the anisotropic character of the environment. This stands in contrast to solutions where changes in the concentration lead to variations in the overall fraction of stretched chains, consequently significantly influencing the anisotropic character of the environment of the chains. In the preceding sections, we have shown that the steady-state extensional viscosity of long chains diluted in unentangled short chains scales with $M_w\sqrt{\phi}$. This scaling is

therefore expected to disappear here for bidisperse polymers, provided that the idea of monomeric friction reduction is valid.

The stress growth coefficient $\eta_E^+(t)$ of the three bidisperse systems is shown in Figure 3.13.

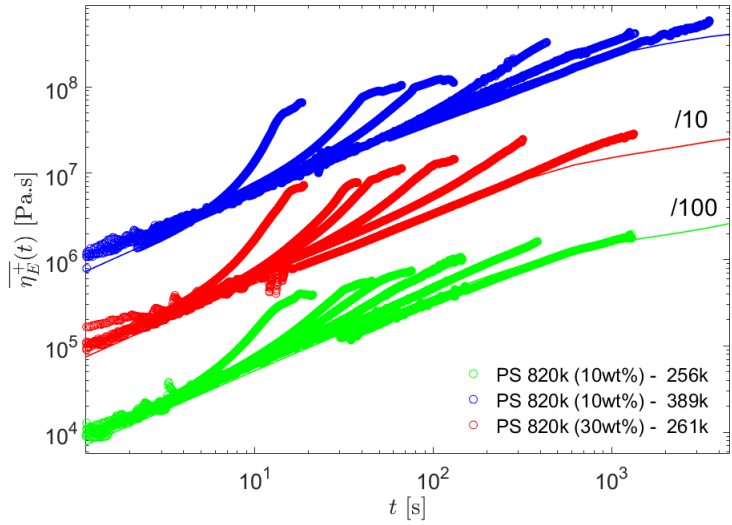

Figure 3.13: Stress growth coefficient $\eta_E^+(t)$ of PS solutions divided by the molar mass.

Here, two mixing laws, which would allow to predict the extensional viscosity of polydisperse polymers, are tested. The first one is based on the scaling observed for polymer solutions, i.e., $\eta_E \propto M_w\sqrt{\phi}$. In this case, an effective Rouse time $\tau_R^\alpha = \left(\sum_i \sqrt{\phi_i \tau_{R,i}}\right)^2$ can be defined for polydisperse systems via

$$\begin{aligned} \eta_{E,st} &= \sum_i \eta_{E,st,i} \\ &= AG_N^0 \dot{\epsilon}^{-0.5} \sum_i \sqrt{\phi_i \tau_{R,i}} \\ &= AG_N^0 \dot{\epsilon}^{-0.5} \sqrt{\tau_R^\alpha} \end{aligned} \tag{3.8}$$

Here, ϕ_i corresponds to the concentration of chains with a mass M_i and a Rouse time $\tau_{R,i}$.

On the other hand, assuming $\eta_E \propto M_w\phi$ leads to the subsequent expression for the effective Rouse time τ_R^β of polydisperse systems:

$$\tau_R^\beta = \left(\sum_i \phi_i \sqrt{\tau_{R,i}}\right)^2 \tag{3.9}$$

These two mixing laws were assessed in Figure 3.14. It is observed that the data superimpose well if a scaling $\eta_E \propto \sum_i \phi_i \tau_{R,i}$ is considered. These results suggest that a blending rule, as the one proposed in equation 3.9, can be determined to predict the steady viscosity of entangled bidisperse polymers.

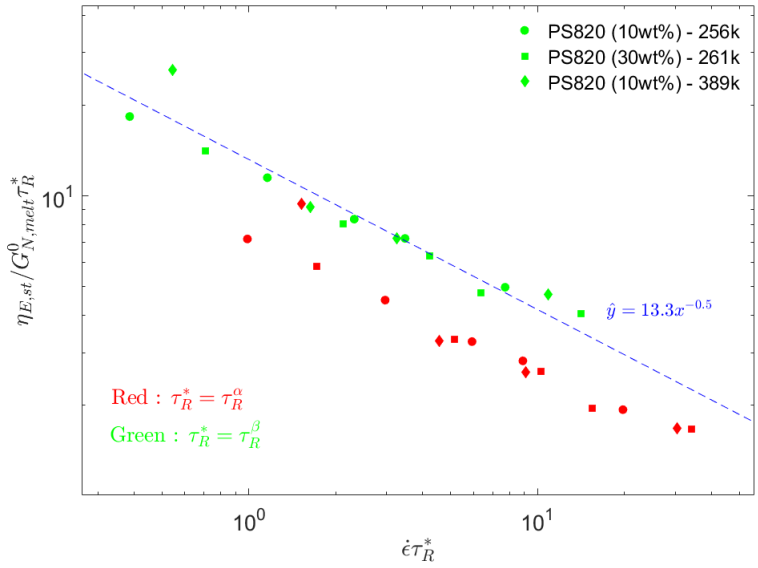

Figure 3.14: Assessment of the empirical laws for bidisperse blends (see text) . The blue line comes from the linear regression shown in Figure 3.7.

To further validate equation 3.9, the stress growth coefficient of two bimodal

systems with similar average molar mass $\overline{M_w} = \sum_i \phi_i M_{w,i}$ and well-entangled short chains was measured. As observed in Figure 3.15, the steady-state viscosities of the samples nearly coincide at high strain rates. This observation thus confirms the proposed scaling law for the steady viscosity of polydisperse polymers.

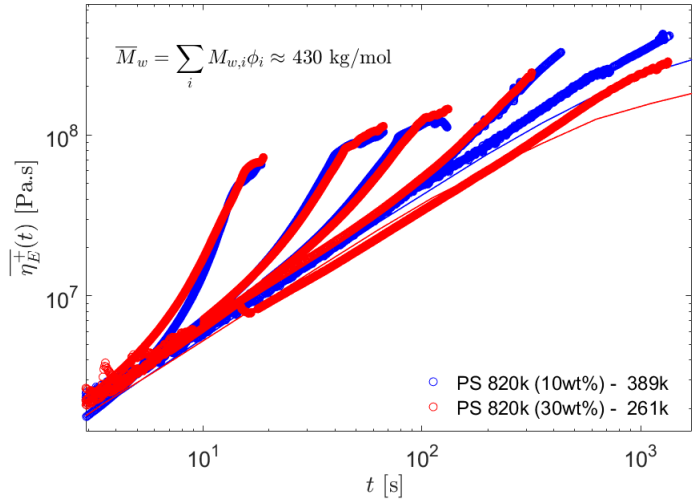

Figure 3.15: Stress growth coefficient of two bimodal systems with a similar average molar mass $\overline{M_w}$ (i.e. 432.1 kg/mol for PS820k (10 wt%) - 389k and 428.7 kg/mol for PS820k (30 wt%) - 261k) at $T = 138$ ℃ (or T- $T_g = 31.4$℃).

3.3.5 Elongation steady state viscosity: Overall scaling for polymer melts and solutions.

Based on our current observations, the scaling laws for polymer solutions and bimodal systems at high strain rates is respectively $\eta_{E,st} \propto M_w\sqrt{\phi}$ and $\eta_{E,st} \propto \sum \phi_i M_{w,i}$. These two scaling laws can be combined, as proposed in Figure 3.16, which shows the normalized steady-state viscosity value of all measured polymer systems as a function of the Rouse Weissenberg number. For the bidisperse polymers, equation 3.14 was used to define the Rouse time τ_R^*. Additionally, steady-state viscosities of two polymer melts coming from the work of Huang *et al.*[170] were incorporated into the data set. As expected, at high Weissenberg numbers, a universal trend emerges from the data, where all PS systems follow a common slope of -1/2.

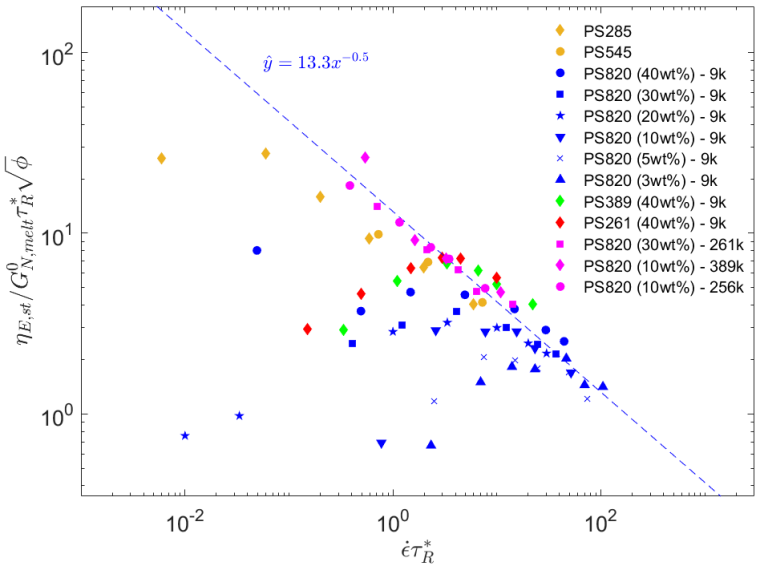

Figure 3.16: Dimensionless elongational steady state viscosities $\eta_{E,st}/G^0_{N,melt}\tau^*_R\sqrt{\phi}$ of PS polymers as a function of the Weissenberg number $Wi_R = \dot{\epsilon}\tau^*_R$. All the data are shifted at $T = T_g + 23.4$ °C.

3.4 Conclusion

In this work, we have measured and discussed the nonlinear extensional responses of moderate and relatively high molecular weight monodisperse PS chains, diluted, or not, with oligomers at various concentrations. The concentrations were chosen so that all the polymeric systems stay entangled. For all measured systems, three distinct regimes of the rate-dependent steady-state elongational viscosity $\eta_{E,st}$, with different dependencies on the concentration and molar mass, were observed. At very low strain rates, the polymeric chains succeed to maintain an equilibrium structure and the steady-state extensional viscosity tends to the Trouton value $3\eta_0$. At high strain rates, polymer chains are predominantly stretched and exhibit monotonous extension thinning. In this high stretch regime, three main results, which are in qualitative agreement with the concept of friction, have been obtained:

1. First, we have proved that it is possible to find a scaling law that describes the influence of the concentration for the steady-state extensional viscosity $\eta_{E,st}$ of entangled polymer solutions. Specifically, in this work, we have demonstrated that the steady viscosity of PS chains dissolved in oligomers of 9k evolves with the square root of the concentration.

2. Second, we have shown that the steady-state of polymeric solutions evolve linearly with the molar mass. It is worth noting that this scaling law was previously observed by Bach *et al.* in the context of non-diluted polymeric melts.[168]

3. Third, the results reveal that the steady-state extensional viscosity $\eta_{E,st}$ of bimodal entangled systems adhere to the simple mixing rule: $\eta_{E,st} \propto \sum_i M_{w,i}\phi_i\eta_{E,st}$, where $M_{w,i}$ and ϕ_i are the molar mass and the weight fraction of the components of the bimodal blends.

We have also observed in the high stretch regime, that the importance of the transient strain hardening strongly depends on the molar mass and the concentration, becoming very large when diluting the polymer chains in oligomers. This observation is due to the different concentration and molar mass depen-

dence of the linear envelope and of the steady-state viscosity under strong extensional flow.

In our investigation, it was found that the amount of strain hardening scales as $\frac{\eta_{E,st}(\dot{\epsilon})}{\eta_{LVE}} \propto \frac{M_w\sqrt{\phi}}{\phi^2 G_N^0} \propto \frac{M_w}{\phi^{3/2}}\sqrt{\dot{\epsilon}}$. Furthermore, the ratio of the extensional viscosity to the zero-elongation viscosity follows a scaling relationship given by $\frac{\eta_{E,st}}{3\eta_0} = \frac{M_w\sqrt{\phi}}{(M_w\phi)^x}\frac{1}{\sqrt{\dot{\epsilon}}} = \phi^{1/2-x}M_w^{1-x}\frac{1}{\sqrt{\dot{\epsilon}}}$, where $x \in [3, 3.4]$. As a consequence, increasing the molar mass and/or the concentration leads to an increase of the amount of steady thinning. These scaling relationships also reveal that a similar nonlinear response cannot be obtained if a larger dilution of the polymer is compensated by a higher molar mass of the chains in such a way that $Z = \frac{M_w}{M_{e,0}}\phi$ remains constant.

Chapter 4

Linear viscoelastic response of physically cross-linked polymers through side-chain incorporation of rreidopyrimidinone

In this chapter, we investigated the linear viscoelastic response of unentangled supramolecular polymers using a bead-spring model developed by Liu *et al.*[186] We introduced a modification to the model, incorporating more realistic assumptions about the distribution of sticker lifetimes. Our modification resulted in a slight decrease in the longest relaxation time. Ultimately, we successfully fitted these data by combining the Liu *et al.*[186] model with a phenomenological model that describes the glassy modes. The data for this study originates from the thesis of Verjans.[187]

Part of the content of this chapter was published as a part of the following publication:

J. Verjans, **A. André**, E. van Ruymbeke, R. Hoogenboom. Physically cross-linked polybutadiene by quadruple hydrogen bonding through side-chain incorporation of ureidopyrimidinone with branched alkyl side chains. *Macromolecules*, 55(3):928-941, 2022.

4.1 Introduction

Hydrogen bonding provides an excellent platform for the development of supramolecular polymers, as it offers an efficient means to build strong, reversible and highly directional interactions.[188] By adjusting the number of hydrogen bonds in the binding moieties, the strength of the supramolecular junctions can be tailored. These junctions exhibit a broad range of strengths, encompassing relatively weak 2-H bound dimers,[189] moderately strong triple[190,191] or quadruple hydrogen bonding arrays,[94,188] as well as highly stable duplexes with six H-bonding sites.[192-194]

The development of the self-complementary quadruple hydrogen-bonding group 2-ureido-4[1H]-pyrimidinone (UPy) by Sijbesma *et al.*[94] constitutes a landmark result as it combines an easiness of synthesis with a strong association constant ($K_{ass} = 6 \times 10^7$ M^{-1} in $CDCl_3$).[195,196] The moderate strength of the H-bonds greatly influences the temperature dependence of the dynamic of the physical bonds, which enables to create highly thermally responsive polymers.[197] Moreover, UPy-based polymers demonstrated self-healing properties,[198,199] enhanced toughness and stiffness[200-202] as well as biocompatibility[203,204] and bioabsorbability.[205,206] These characteristics have led to diverse applications in areas such as reversible adhesives,[207] coatings,[208] heart valves,[209] printing[210] and flexible electronics.[202,211]

To achieve precise control over the material properties of polymers functionalized with UPy units, a deep understanding of their rheological responses is essential. In this chapter, the focus is on the linear responses of unentangled polymers with pendants UPy groups.

The relaxation behavior of such systems is strongly affected by the average number of associating groups per chain N_s.[88,122,212] When N_s exceeds two, all the polymeric chains become interconnected, resulting in the formation of a single, large percolated network. To describe the linear viscoelastic response of such systems, Baxandall introduced the "sticky Rouse" model.[104] In this model, the associative polymeric chains are viewed as massless arcs with reversible cross-link sites characterized by a unique lifetime τ_S. By analyzing the configuration probability distribution function of chains with evenly distributed stickers, Baxandall demonstrated that such chains display a relaxation behavior that closely resembles that of the Rouse model. Building upon the pioneering work of Baxandall, Chen *et al.* expressed the relaxation modulus of unentangled associative polymers as follows:[105]

$$G(t) = \frac{\rho RT}{M}\left[\sum_{p=1}^{N_s}\exp\left(\frac{-tp^2}{\tau_S N_s^2}\right) + \sum_{p=N_s+1}^{N}\exp\left(\frac{-tp^2}{\tau_0 N^2}\right)\right] \tag{4.1}$$

In this equation, the first term on the right-hand side originates from the work of Baxandall and represents the sticky Rouse relaxation resulting from the sticker dynamics. The second term corresponds to the Rouse relaxation of the network strands.

While this equation shows satisfactory agreement with experimental data of unentangled associative polymers, significant discrepancies persist, especially in the rubbery plateau and the terminal regime.[105] Multiple causes for these discrepancies have been proposed and investigated in the literature.

First, equation 4.1 assumes an uniform distribution of the stickers along the chains. This is in contrast with the random placement of the stickers typically obtained with the synthesis of supramolecular polymers. To adress this issue, Cui *et al.* developed a stochastic model in which the sticky are randomly distributed along the chains.[126] This model include finite-sized hops of the sticky groups to simulate the chain motion. As a result, this model yields a slightly improved agreement with experimental data. Another approach proposed by Jiang *et al.* involves utilizing a modified version of the Rouse model,

originally developed to predict the linear rheology of block copolymers without microphase separation.[213] In this model, different friction coefficients are assigned to the different constituents of the block copolymer. Jiang *et al.* extended this concept to associative polymers, where the associative groups act as effective friction centers.[213] However, despite considering the random distribution of stickers along the chains, this model was not able to accurately fit the relaxation behavior of unentangled associative polymers obtained with MD simulations, especially in the rubbery plateau regime.[214]

Liu *et al.* explained the persisting deviations by stating that the bound stickers are able to diffuse over a certain distance, thereby partially relieving the stress.[186] Subsequently, they integrated these non-affine spatial fluctuations into a Rouse model using a phenomenological approach. This integration allowed them to obtain an accurate fit of the linear data of unentangled melt data for two distinct copolymer chemistries at varying concentrations of supramolecular associations. Importantly, their model maintains the crucial assumption that the fluctuations do not affect the level of the rubbery plateau. This important hypothesis is in agreement with the earlier work of Indei and Takimoto who analytically treated the effect of the junction fluctuations on the rubbery plateau in a single-chain model.[215] To investigate these fluctuations, they introduced virtual springs that connect one end to the bound stickers and the other end to the affinely deforming background. Tanaka and Koga obtained a similar result in their single-chain model of telechelic associating polymers.[216] However, these results obtained for single-chain models appear to contradict multichain approaches such as the phantom network model[217,218] or recent Brownian dynamics simulations of associative polymers performed by Schaefer and McLeish,[219] both of which indicate a softening of the plateau modulus.

Part of the divergences could also emanate from the presence of a distribution of sticker lifetimes, as postulated by Cui *et al.*[126] The introduction of such distribution can be justified by adopting arguments similar to the ones used in the bond lifetime renormalization model.[122] According to this model, associative polymers with different densities of stickers are expected to have different

lifetimes. One could therefore expect that the fluctuations in density of stickers along the polymeric chains also lead to a multitude of lifetimes. Moreover, as explained by Cui *et al.*,[126] when the supramolecular junctions are in close proximity, the segments between two associative groups may lack the required flexibility for the associative groups to effectively search for potential partners within their exploration volume. Consequently, in order to exchange partners, it may be necessary for multiple junctions to dissociate simultaneously, leading to a significant increase of the effective lifetime.

Finally, in the sticky Rouse model, only pure pairwise associations are assumed to be present. However, in reality, supramolecular polymers based on UPy groups often exhibit microphase separation with the formation of large aggregates of stickers.[119] The contrast of polarity between the UPy groups and the polymer backbone generally results in phase separation, with the UPy moieties stacking laterally due to π-π interactions.[121] While the presence of urethane and urea linkers close to the UPy groups enhances this trend,[220] the presence of bulky substituents curbs it.[221] Recent work of Ahmadi *et al.* demonstrated the presence of unordered aggregates in entangled PnBA functionalized with UPy pendants units.[222] This was evidenced by the absence of first-order thermal transitions in DSC curves and the emergence of diffraction peaks at nanometer lengths in SAXS profiles. The presence of these aggregates considerably modified the relaxation behavior with the emergence of an additional low-frequency plateau. This type of low-frequency plateau has already been observed in the past, notably by Hawke *et al.* in the case of entangled poly(n-butyl acrylate) PnBA copolymerized with acrylic acid group.[118] They attributed the appearance of this plateau to the delay of the relaxation of the strands trapped between clusters. Nonetheless, it is worth-mentioning that the low-frequency plateau is not always observed for the systems containing aggregates. Indeed, for example, Tang *et al.* have shown by combining Forced Rayleigh Scattering (FRS) with SAOS that the relaxation of model protein hydrogels is solely governed at low frequency by the sticky Rouse motion of associative protein molecules in an aggregated state.[223] Another notable effect arising from the presence of aggregates is that the cluster size influences the lifetime of the stickers. This relationship, which has been demonstrated through hybrid MD/MC

simulations in the case of unentangled telechelic associative polymers, results in a distribution of sticker lifetimes.[224]

In this chapter, the influence of UPy groups on the linear viscoelastic response of unentangled melt is investigated using the molecular model developed by Liu *et al.*[186] The effect of the distributions of lifetimes due to bond renormalization has also been incorporated, although only marginal deviations from the original model of Liu *et al.* were observed.[186] The data used in this chapter were provided by Verjans,[187] who studied systems where linear polymeric chains were functionalized with UPy groups. These data were successfully fitted by combining the model of Liu *et al.*[186] with a phenomenological model which describe the glassy modes.

4.2 Materials

UPy motifs were grafted onto low molecular weight linear Polybutadiene (PB), Poly (methyl acrylate) (PMA) and Poly(butyl acrylate) (PBA) with different functionalization degrees. The different chemical structures of the polymers are depicted in Figure 4.1. As observed, the UPy side chains were adapted to incorporate a branched alkyl group instead of the typical methyl group found in the literature. This modification serves to limit aggregation tendencies by increasing the steric hindrance on the UPy units and reducing the difference of polarity between the supramolecular junctions and the apolar backbones. Details about the synthesis of these supramolecular polymers can be found in elsewhere.[187]

Key characteristics of the samples, as provided by Verjans,[187] are presented in Table 4.1. Additionally, the average molar mass between two UPys groups M_{UPy} was calculated using the following equation:

$$M_{UPy} = \frac{M_n}{n_{UPy} + 1} \tag{4.2}$$

Here n_{UPy} corresponds to the average number of UPy groups per chain.

	Sample Names	M_n [g/mol]	Đ	T_g [°C]	Mol % UPy	UPy/chain	M_{UPy} [g/mol]
PB	PB	3600	1.39	-29	-	-	-
	PB - U4	4470	1.32	-8	4	2.3	1355
	PB - U6	5070	1.44	10	6	4.2	980
	PB - U8	5070	1.44	28	8	5.1	830
	PB - U13	4930	1.4	44	13	6.8	630
PMA	PMA	5085	1.18	10	-	-	-
	PMA - U5	3775	1.59	10	5	2.9	970
	PMA - U10	3820	1.78	27	10	4.5	695
	PMA - U15	4075	1.57	32	15	5.9	590
PBA	PBA	3825	1.15	-53	-	-	-
	PBA - U3	3360	1.31	-41	3	1.3	1675
	PBA - U8	4180	1.34	-30	8	3.5	920
	PBA - U13	3985	1.33	-14	13	4.6	710

Table 4.1: Key characteristics of the samples.

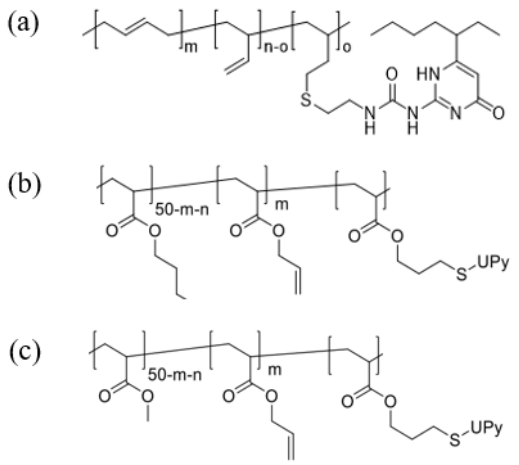

Figure 4.1: Chemical structure of copolymers (a) PB-UPy, (b) PBA-UPy, and (c) PMA-UPy. The structure of the UPy unit is shown only for the PB-UPy system.

4.3 Dynamics of supramolecular chains

Unentangled chains relax through the Rouse process. Similar to the approach of Jiang *et al.*[213] and Liu *et al.*,[186] the Rouse model is extended to unentangled associative polymers through the effective friction concept. This means that the supramolecular junctions are assimilated to beads of high friction, as shown in Figure 4.2.

The position of the n^{th} bead $\mathbf{r}(n,t)$ at time t in the linear regime of deformation is therefore described by the following Langevin equation.[10]

$$\zeta(n)\frac{\partial \mathbf{r}(n,t)}{\partial t} = -\kappa \sum_{m=0}^{N} A_{nm}\mathbf{r}(m,t) + \mathbf{F}_{\mathrm{B}}(n,t) \tag{4.3}$$

Here $\zeta(n)$ corresponds to the friction coefficient of the n^{th} bead and κ to the elastic constant of the springs. Additionally, the zero-mean Brownian force $\mathbf{F}_{\mathrm{B}}(n,t)$ is assumed to follow the fluctuation-dissipation theorem. The Rouse matrix A_{nm} corresponds to the connectivity matrix of a linear polymeric chain

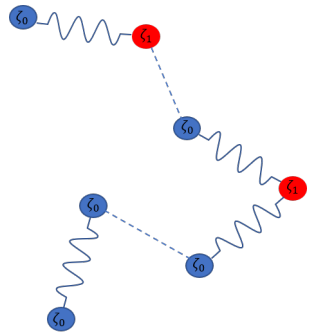

Figure 4.2: Illustration of the Bead-spring model. Blue beads of friction ζ_0 and red beads of friction ζ_1 account for the friction due to the monomers and the associative bonds respectively.

(see section 1.7).

4.3.1 Decoupling of the normal modes

For the modelling of the data, a procedure very similar to the model of Liu *et al.*[186] is employed. In their work, the solution of 4.3 is approximated by decoupling the long time dynamics from the short time dynamics. This hypothesis is valid provided that $N_s^2\tau_S \gg N^2\tau_0$. This inequality means that the friction of the backbone monomers is significantly lower than the friction brought by the stickers.

Fast relaxation modes

At short times, the network strands relax through the non-sticky Rouse process. Following the work of Jiang *et al.*,[213] the Rouse equation, in this regime, can be reformulated as follows:

$$\zeta_0 \Xi \frac{\partial \mathbf{Q}}{\partial t} = -\kappa \mathbf{A}\mathbf{Q} + \mathbf{F}_B \mathbf{I} \tag{4.4}$$

Here the position vectors $\mathbf{r}(n,t)$ are included in the column matrix $\mathbf{Q}$.

$$\mathbf{Q} = \begin{bmatrix} \mathbf{r}(1,t) \\ \mathbf{r}(2,t) \\ \vdots \\ \mathbf{r}(N,t) \end{bmatrix} \tag{4.5}$$

Equation 4.4 also introduces a diagonal matrix $\boldsymbol{\Xi}$ that contains the relative friction coefficients of the beads $\delta_i = \zeta_i/\zeta_0$. This matrix is defined as follows:

$$\boldsymbol{\Xi} = \begin{bmatrix} \delta_1 & & & \\ & \delta_2 & & \\ & & \ddots & \\ & & & \delta_N \end{bmatrix} \tag{4.6}$$

In equation 4.4, the coefficient δ_i associated with the sticky beads are assumed to be infinite. This assumption implies that the supramolecular junctions remain stationary, effectively fixed in space.

Solving this set of Langevin equations yields the following expression for the dynamic moduli.

$$G'(\omega) = \frac{\rho RT}{M} \sum_{p=N_s}^{N-1} \frac{(\omega\tau_{R,p})^2}{1+(\omega\tau_{R,p})^2} \qquad G''(\omega) = \frac{\rho RT}{M} \sum_{p=N_s}^{N-1} \frac{(\omega\tau_{R,p})}{1+(\omega\tau_{R,p})^2} \tag{4.7}$$

Here the relaxation time $\tau_{R,p}$ is given by the ratio $\zeta_0/k_0\lambda_{R,p}$. The symbol $\lambda_{R,p}$ corresponds to the p^{th} nonzero eigenvalues arranged in descending order of the matrix $\boldsymbol{\Xi}^{-1}\mathbf{A}$. Also, it should be noted that only the $N - N_s - 1$ modes associated with the fast relaxation processes were taken into account.

As another option, Liu *et al.*[186] proposed to start the sum over the Rouse modes at $p = 1$ rather than $p = N_s$. According to them, this adjustment enables correction for the spatial fluctuations of the stickers. Consequently, the resulting sum now includes $N - 1$ modes instead of the $N - 1 - N_s$ modes obtained in the classical theory.[105] In order to keep the total number of beads

to N, we multiplied the dynamic moduli by a normalization constant $\xi = (N-1-N_s)/(N-1)$. This constant ensures that the contributions of the fast modes to the dynamic moduli is equal to $(N-1-N_s)\,k_BT$. Therefore, in this case, the moduli G' and G'' can be expressed as

$$G'(\omega) = \xi\frac{\rho RT}{M}\sum_{p=1}^{N-1}\frac{(\omega\tau_{R,p})^2}{1+(\omega\tau_{R,p})^2} \qquad G''(\omega) = \xi\frac{\rho RT}{M}\sum_{p=1}^{N-1}\frac{(\omega\tau_{R,p})}{1+(\omega\tau_{R,p})^2} \tag{4.8}$$

Here the relaxation time $\tau_{R,p}$ is given by:

$$\tau_{R,p} = \frac{1}{4\sin^2(\frac{p\pi}{2N})}\frac{\zeta_0}{k_0} \tag{4.9}$$

Slow relaxation modes

At long times, the flow dynamics is solely governed by the motion of the sticky beads. The bead-spring chain shown in Figure 4.2 can therefore be replaced by a chain containing exclusively sticky beads. The long-time chain dynamics therefore follows this set of equations.

$$\zeta_1\frac{dq_1}{dt} = \kappa_1(q_2-q_1)+f_1 \tag{4.10}$$

$$\zeta_1\frac{dq_i}{dt} = \kappa_i(q_{1+1}-q_i)+\kappa_{i-1}(q_i-q_{i-1})+f_i \tag{4.11}$$

$$\zeta_1\frac{dq_S}{dt} = \kappa_{S-1}(q_{S-1}-q_S)+f_S \tag{4.12}$$

Here q_i denotes the position of the i^{th} sticky beads and κ_i the corresponding elastic constants.

When the stickers are equally spaced along the chains, the elastic constant κ of the strands are given by

$$\kappa = \frac{3k_BT}{Nb^2}(N_s-1) \tag{4.13}$$

In contrast, when the supramolecular junctions are distributed randomly, the elastic constant of the springs connecting the $i-1^{th}$ and i^{th} sticky beads is given $\kappa_i = \alpha_i \kappa$ with α_i equal to

$$\alpha_i = \frac{N}{n_i(N_s - 1)} \tag{4.14}$$

where n_i is the number of Rouse segments on the i^{th} strand of the polymeric chain. The solution to this set of equations produces the following expression for the dynamic moduli.

$$G'(\omega) = \frac{\rho RT}{M} \sum_{p=1}^{N_s-1} \frac{(\omega\tau_{R,p})^2}{1+(\omega\tau_{R,p})^2} \qquad G''(\omega) = \frac{\rho RT}{M} \sum_{p=1}^{N_s-1} \frac{G_i(\omega\tau_i)}{1+(\omega\tau_i)^2} \tag{4.15}$$

Here the relaxation time τ_p is determined by the ratio $\zeta_1/\kappa\lambda_p$ with λ_p being the p^{th} highest nonzero eigenvalues of the matrix $\mathbf{\Lambda}$.

$$\mathbf{\Lambda} = \begin{bmatrix} \alpha_1 & -\alpha_1 & 0 & \cdots & \cdots & 0 \\ -\alpha_1 & \alpha_1+\alpha_2 & -\alpha_2 & 0 & \cdots & 0 \\ \cdots & \cdots & \cdots & \cdots & \cdots & \cdots \\ 0 & \cdots & 0 & -\alpha_{S-2} & \alpha_{S-2}+\alpha_{S-1} & -\alpha_{S-1} \\ 0 & \cdots & \cdots & 0 & -\alpha_{S-1} & \alpha_{S-1} \end{bmatrix} \tag{4.16}$$

4.3.2 Distribution of sticky beads and of molecular weight

To account for the random placement of the stickers, an ensemble of R chains of N beads was generated. Each bead in the chains has a probability p to be associated. The number of Kuhn segments in a strand m is computed based on the following geometric distribution.

$$P(X = m) = p(1-p)^{m-1} \tag{4.17}$$

To obtain the lengths of the network strands in a specific chain, we repeatedly

compute values of length using the probability distribution defined by equation 4.17 until the cumulative sum surpasses the total number of beads N. The resulting series of strand lengths determines the placement of the stickers, starting from one end of the chain.

Figure 4.3 presents the distribution of the number of sticky beads per chain and the distribution of strand length obtained using $R = 30000$ and $N = 100$ for various values of $\lambda = Np$. In panel (a), it can be observed that when N is significantly large, the distribution of the number of sticky beads closely approximates the following Poisson distribution.

$$P(X = m) = \frac{\lambda^m \exp(-\lambda)}{m!} \tag{4.18}$$

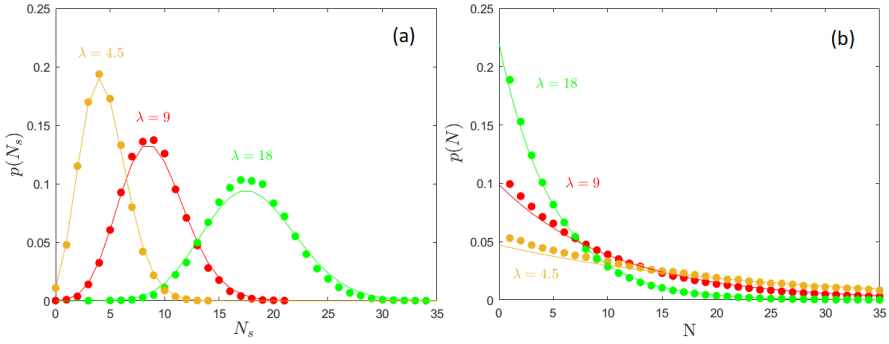

Figure 4.3: Distribution in number of (a) the number of sticky beads per chain and (b) the length of the network strands per chain for three different values of λ. The solid lines show the corresponding (a) Poisson distributions and (b) geometric distributions. The full circle were obtained using $R = 30000$ and $N = 100$.

Finally, a log-normal distribution is used to characterize the distribution of molecular weights of the polymer chains, following a similar approach as described in reference.[225] The probability density function of the log-normal distribution is given by

$$P(M = m) = \frac{1}{m\sigma\sqrt{2\pi}} \exp\left(-\frac{(\ln(m) - \mu)^2}{2\sigma^2}\right) \tag{4.19}$$

The parameters μ and σ^2 can be expressed as a function of the mean $\mathrm{E}[X]$ and the variance $\mathrm{Var}[X]$ of the distribution in the following way.

$$\mu = \ln\left(\frac{(\mathrm{E}[X])^2}{\sqrt{\mathrm{E}[X])^2 + \mathrm{Var}[X])^2}}\right) \tag{4.20}$$

$$\sigma^2 = \ln\left(1 + \frac{\mathrm{Var}[X])^2}{(\mathrm{E}[X])^2}\right) \tag{4.21}$$

The mean $\mathrm{E}[X]$ is by definition equal to M_n and the variance $\mathrm{Var}[X]$ can be computed using the following relation.

$$\mathrm{Var}[X] = \mathrm{E}[X^2] - \mathrm{E}[X]^2 = M_w M_n - M_n^2 = M_n^2(Đ - 1) \tag{4.22}$$

As a consequence, the distribution can be fully characterized by the values of the Đand M_n presented in Table 4.1.

4.3.3 Distribution of sticker lifetimes

The introduction of a distribution of sticker lifetimes can be justified by the bond lifetime renormalization model. As discussed in Chapter 1, in the original theory proposed by Rubinstein and Semenov,[122] the renormalized lifetime τ_s is given by the product $N_{ret}\tau_b$, where N_{ret} is the number of times a sticker returns to its original parter and τ_b the actual bond lifetime. To evaluate N_{ret}, Rubinstein and Semenov used the following expression

$$N_{ret} \approx \frac{\tau_{open}/\tau_0}{V_{strand}/b^3} \tag{4.23}$$

In this equation, τ_{open} represents the duration of the open stage, V_{strand} corresponds to the volume of the network strand, τ_0 the relaxation time of a Kuhn segment.

Consequently, the numerator τ_{open}/τ_0 corresponds to the number of elementary time steps of duration τ_0 taken during the exploration of V_{strand} by the disso-

ciated stickers. Likewise, the denominator V_{strand}/b^3 represents the number of elementary volume b^3 in V_{strand}.

According to Rubinstein and Semenov,[122] τ_{open} depends on the concentration of open stickers ϕ_{open} via $\tau_{open} \sim \tau_0/\phi_{open}$. Therefore, equation 4.23 can be reduced to

$$N_{ret} \approx \frac{b^3}{V_{strand}\phi_{open}} \approx \frac{p_R}{\phi_{open}} \tag{4.24}$$

where p_R is the probability that two initially paired stickers are within a distance b to each other.

In Figure 4.4, two stickers are shown detached after participating in an interchain bond. As the stickers are randomly distributed along the chains, these stickers are trapped in different exploration volumes $V_1 \sim (N_1^{1/2}b)^3$ and $V_2 \sim (N_2^{1/2}b)^3$. Here, N_1 and N_2 represent the number of Kuhn segments in the corresponding strands.

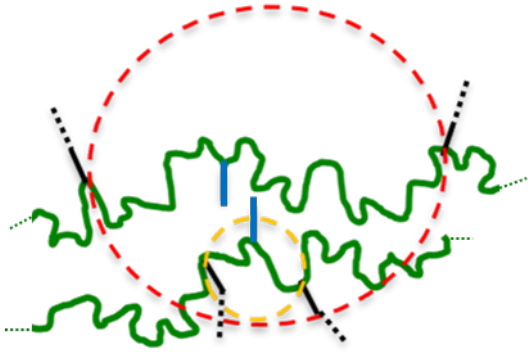

Figure 4.4: Conformation of unentangled chains with stickers. The volume V_1 and V_2 are shown in orange and in red and the open stickers in blue.

As a first approximation, the smaller volume completely overlaps with the larger volume. Consequently, if $V_2 > V_1$, the probability p_R that the two stickers are in the same elementary volume b^3 is given by

$$p_R \approx \frac{V_1/b^3}{V_1/b^3 \times V_2/b^3} = \frac{b^3}{V_2} = \frac{b^3}{V_{max}} \tag{4.25}$$

In the equation above, V_{max} corresponds to the maximum volume between V_1 and V_2.

By substituting equation 4.25 in equation 4.24, the following expression for τ_S can be obtained.

$$\tau_S \propto \frac{\tau_b b^3}{\phi_{open} V_{max}} \approx \frac{A}{V_{max}} \tag{4.26}$$

Here A is an arbitrary constant. It must be noted that the fraction of open stickers is assumed to be constant in time and uniformly distributed in space.

To incorporate this effect in the model proposed by Liu *et al.*,[186] the friction coefficient of the sticky beads can be modified as follows.

$$\zeta_{s,i} = \frac{V_{strand}}{V_{max}} \zeta_1 = \gamma_i \zeta_1 \tag{4.27}$$

Here ζ_1 would correspond to the friction coefficient obtained when both stickers are trapped in $V_{strand} = (N_s^{1/2} b)^3$. By substituting the modified friction coefficient into equations 4.10, 4.11, and 4.12, the matrix $\mathbf{\Lambda}$ takes the following form.

$$\mathbf{\Lambda} = \begin{bmatrix} \alpha_1/\gamma_1 & -\alpha_1/\gamma_1 & 0 & \cdots & \cdots & 0 \\ -\alpha_1/\gamma_2 & (\alpha_1+\alpha_2)/\gamma_2 & -\alpha_2/\gamma_2 & 0 & \cdots & 0 \\ \cdots & \cdots & \cdots & \cdots & \cdots & \cdots \\ 0 & \cdots & 0 & -\alpha_{S-2}/\gamma_{S-2} & (\alpha_{S-2}+\alpha_{S-1})/\gamma_{S-2} & -\alpha_{S-1}/\gamma_{S-2} \\ 0 & \cdots & \cdots & 0 & -\alpha_{S-1}/\gamma_{S-1} & \alpha_{S-1}/\gamma_{S-1} \end{bmatrix} \tag{4.28}$$

To evaluate the dynamic moduli, an ensemble of R chains consisting of N Kuhn segments was generated, following a similar approach as described in section 4.3.2. The exploration volume for each sticker was computed by summing the volumes of the two corresponding adjacent strands. This computation allows to evaluate the distribution $V_{max} = \max(V_{cst}, V_2)$, where V_{cst} represents the exploration volume of a given sticker, and V_2 is a random trapped volume. The

volume V_2 can be determined based on the distribution shown in 4.3 (b). By using the mean of V_{max} to assess the coefficients γ_i, the symmetry matrix $\mathbf{\Lambda}$ as well as G' and G'' were evaluated.

Figure 4.5 illustrates the effect of the distribution. As observed, the introduction of the different lifetimes leads to a slight decrease in the terminal relaxation time. This is because the factors γ are on average smaller than 1. However, beyond this effect, the influence of the distribution is marginal, as the shape of G' and G'' remains unchanged. Consequently, the influence of the lifetime distribution is disregarded in the remaining part of this chapter.

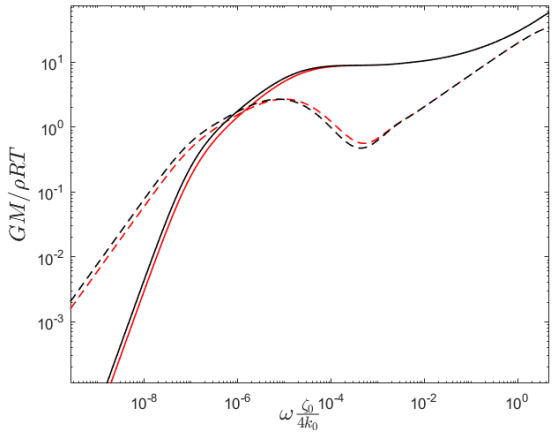

Figure 4.5: Prediction of the dynamic moduli considering the model of Liu *et al.*[186] without (black lines) and with the distribution of lifetimes (red lines). Predictions were obtained using $\zeta_1 k_0/\zeta_0\kappa = 5 \times 10^5$, $N_s = 10$ and $N = 100$.

4.3.4 Comparison with the sticky Rouse model

In this section, we compare the predictions of the dynamic moduli obtained from the model described in the previous section with those from the sticky Rouse model. The equations of the dynamic moduli of the sticky Rouse model are given by the following equations:

$$G'(\omega) = \frac{\rho RT}{M} \sum_{p=N_S}^{N-1} \frac{(\omega\tau_p)^2}{1+(\omega\tau_p)^2} + \frac{\rho RT}{M} \sum_{p=1}^{N_S-1} \frac{(\omega\tau_{R,p})^2}{1+(\omega\tau_{R,p})^2} \tag{4.29}$$

$$G''(\omega) = \frac{\rho RT}{M} \sum_{p=N_s}^{N-1} \frac{\omega\tau_p}{1+(\omega\tau_p)^2} + \frac{\rho RT}{M} \sum_{p=1}^{N_s-1} \frac{\omega\tau_{R,p}}{1+(\omega\tau_{R,p})^2} \tag{4.30}$$

with the time $\tau_{R,p}$ and τ_p defined by

$$\tau_{R,p} = \frac{1}{4\sin^2(\frac{p\pi}{2N})} \frac{\zeta_0}{k} \tag{4.31}$$

$$\tau_p = \frac{1}{4\sin^2(\frac{p\pi}{2N})} \frac{\zeta_1}{\kappa} \tag{4.32}$$

Figure 4.6 displays the predictions of the model from the previous section, both with and without the inclusion of Liu *et al.*'s ansatz.[186] The figure also shows the predictions of the classical sticky Rouse model. The calculations were performed using the following parameters: $\frac{\zeta_1 k_0}{\zeta_0 k_1} = 5 \times 10^5$, $N_s = 10$, and $N = 100$.

First, at high frequencies, it is observed that the inclusion of the ansatz proposed by Liu *et al.*[186] results in a higher modulus compared to the classical sticky Rouse model, both at high and intermediate frequencies. Furthermore, the incorporation of the distribution of strand lengths also widens the spectrum of relaxation at high frequencies. Finally, in the terminal regime, a faster relaxation is achieved due to the non-uniform arrangement of the stickers, which is consistent with the findings of Liu *et al.*[186]

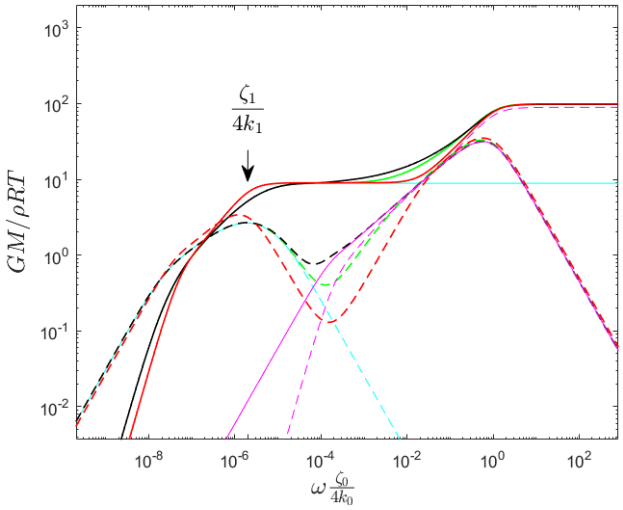

Figure 4.6: Predictions of the dynamic moduli using the model detailed in section 4.3.1, considering either fixed stickers (green lines) or fluctuating junctions (black lines). The predictions of the classical sticky Rouse model (red lines) are also shown. An arrow indicates the location of the first slow mode, $\zeta_1/(4\kappa)$. Additionally, the contributions of the fast modes (magenta lines) and the slow modes (cyan lines) from the model with fluctuating junctions are also displayed.

4.3.5 Glassy relaxation

In order to capture the glassy part, the phenomenological Kohlrausch-Williams-Watts (KWW) model is used. Its expression in the frequency domain is given by[226]

$$G'_{KWW}(\omega) = \omega G_g \int_0^\infty \exp\left(-\left[\frac{-t}{\tau_{KWW}}\right]^\beta\right) \sin(\omega t) dt \tag{4.33}$$

$$G''_{KWW}(\omega) = \omega G_g \int_0^\infty \exp\left(-\left[\frac{-t}{\tau_{KWW}}\right]^\beta\right) \cos(\omega t) dt \tag{4.34}$$

Here the fitting parameters are the glassy modulus G_g, the characteristic time of the glassy relaxation τ_{KWW} and the stretch parameter β. The latter specifies the broadness of the distribution of the glassy modes. A decreasing β leads to

a broader distribution.

4.4 Results and Discussion

For each references, the linear responses were shifted onto a single master curve as shown in Figure 4.7. The relaxation behavior of the PB reference was not measured.

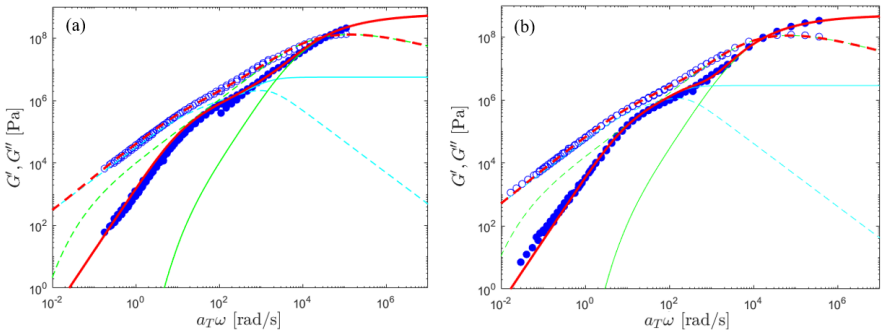

Figure 4.7: Linear viscoelastic mastercurves of (a) PMA at T_{ref}= 30°C and (b) PBA at T_{ref} = -30°C. Red lines correspond to the model predictions obtained with the values shown in Table 4.1 and 4.2. The contributions from the KWW model (in green) and the Rouse model (in cyan) are also presented.

In this Figure, the high frequency parts correspond to the glass-to-rubber transition region, which persists until $\omega_0 \sim 4k_0/\zeta_0$. Subsequently, the chains relax through the Rouse process. The expected slope of 0.5 that G' and G'' should follow in the Rouse regime is barely noticeable due to the low molar mass of the samples. Finally, at frequencies equal to $\omega \sim 1/\tau_R$, the chains relax completely, resulting in G' and G'' following a slope of 2 and 1 respectively.

Good fits of the mastercurves were obtained by combining the Rouse model (equations 1.26 and 1.27) with the KWW equations (equations 4.33 and 4.34). The number of beads N was estimated by dividing the molar mass of the chains by the molar mass of one Kuhn segment M_K. For PBA, similarly to the work of Liu *et al.*,[186] a Kuhn segment molar mass M_K of 700 g/mol was used while, for PMA, a M_K of 450 g/mol was computed using the persistence length $l_p = 0.64$

nm obtained from atomistic MD simulations.[227] Also, a density of $\rho = 1000$ kg/m^3 was assumed for both systems. The values of the fitting parameters are tabulated in Table 4.2.

As explained in the Introduction, the dynamics of unentangled supramolecular polymers are primarily controlled by two different timescales, τ_0 and τ_S. This is shown in Figure 4.8 in which the LVE responses are analyzed using a procedure initially proposed by Zhang *et al.*[125]

In panels (a), the storage and the loss moduli of the PB-U4 and PB-U8 are horizontally shifted by a factor a_T to achieve superposition in the high-frequency region. As expected, these shifts lead to a failure in the superposition in the low-frequency part due to the stronger temperature dependence of the mechanism of the sticker dissociation.

Conversely, in panels (b), the moduli are shifted by a factors a'_T so that the data coincide at low frequencies. As observed, the curves cease to superimpose at high frequencies, when the segmental motions starts to contribute to the stress relaxation. The sticky and the Rouse modes progressively approach each other with increasing temperature, gradually erasing the rubbery plateau, and eventually merge at high temperature. This is because the time-scale separation between τ_0 and τ_s depends on the absolute temperature via[113]

$$\log\left(\frac{\tau_0}{\tau_S}\right) \propto \frac{E_a}{RT} \tag{4.35}$$

Consequently, at sufficiently high temperature, the dependence of the friction of the backbone on the longest relaxation time can no longer be neglected. That is why the responses obtained at $T = 120$°C and $T = 130$°C for PBA-U9, shown in Figure 4.9 do not superimpose with the data collected at lower temperature.

Pseudo-mastercurves were then constructed using the following procedure. First, a temperature T_{ref} is selected among the different experimental temperature. The chosen isothermal curve should cover a wide frequency range, that spans from the end of the relaxation of the Rouse modes to the beginning of the

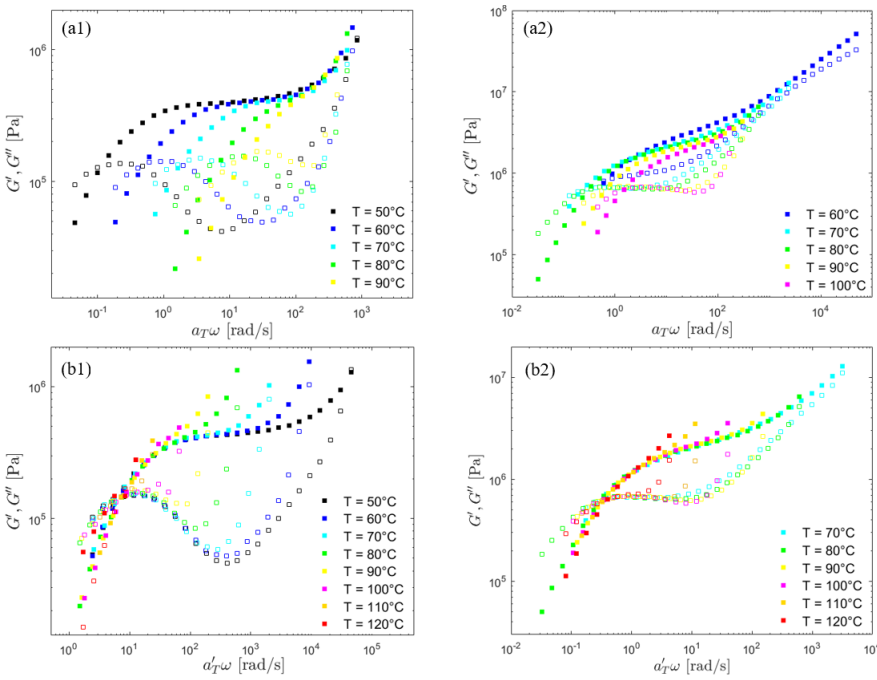

Figure 4.8: Test of TTS principle of the dynamic moduli of PB-U4 (a1) and PB-U8 (a2). In panel (a), the raw data were shifted by a horizontal shift factor a_T until they superimpose at high frequencies. In panel (b), the raw data were shifted by a factor $a_T^{'}$ until they superimpose at low frequencies. The data were shifted using the reference temperature $T_{ref} = 80$℃ (b2) and $T_{ref} = 60$℃ (b1). Due to the limited range of frequencies, part of the data collected at high (a) and low (b) temperature were not included in the panels (a) and (b) respectively.

relaxation of the sticky modes. In this manner, the rubbery plateau is entirely described at $T = T_{ref}$. For the curves measured at $T < T_{ref}$, a shift a_T is applied to extend the frequency range in high frequency portion of the moduli. In similar fashion, the moduli obtained at $T > T_{ref}$ are shifted by $a_T^{'}$ to extend the window of angular frequency in the regime of the sticker dissociations. Finally, for the curves measured at $T < T_{ref}$ and at $T > T_{ref}$, data points associated with the relaxation of the slow modes and fast modes respectively, are excluded. The resulting pseudo-mastercurves are shown in Figure 4.10.

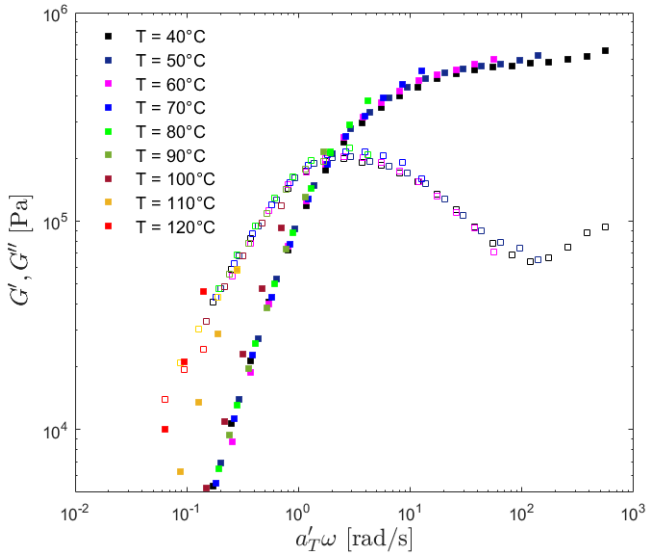

Figure 4.9: Frequency sweep data of PBA-U9 shifted by $a_T^{'}$ at the reference temperature T_{ref} = 40℃.

As observed in Figure 4.10, the associative polymers clearly show the formation of a transient network as indicated by the formation of a plateau in G' despite the unentangled state of the building blocks. For the systems with the fewest supramolecular junctions PB - U4, the plateau modulus is significantly lower than $\frac{\rho RT}{M}$, which suggests that these system is still a mixture of sol and gel. This could explains why the slope obtained at high frequencies is closer to 1 than 0.5.[212]

Regarding the systems containing a well-developed network, the moduli scale with $\omega^{1/2}$ in the high-frequency portion, as the polymer chains relax by the Rouse process. They do not superimpose as the increase in T_g leads to a larger monomeric friction when the flow dynamics is compared at the same temperature. Then, at intermediate frequencies, the systems display a rubbery plateau, which gradually increases in magnitude with the density of stickers. Finally, at low frequency, one can observe that the longest relaxation time τ_{rel} tends to increase with the number of UPy groups in the polymeric chains.

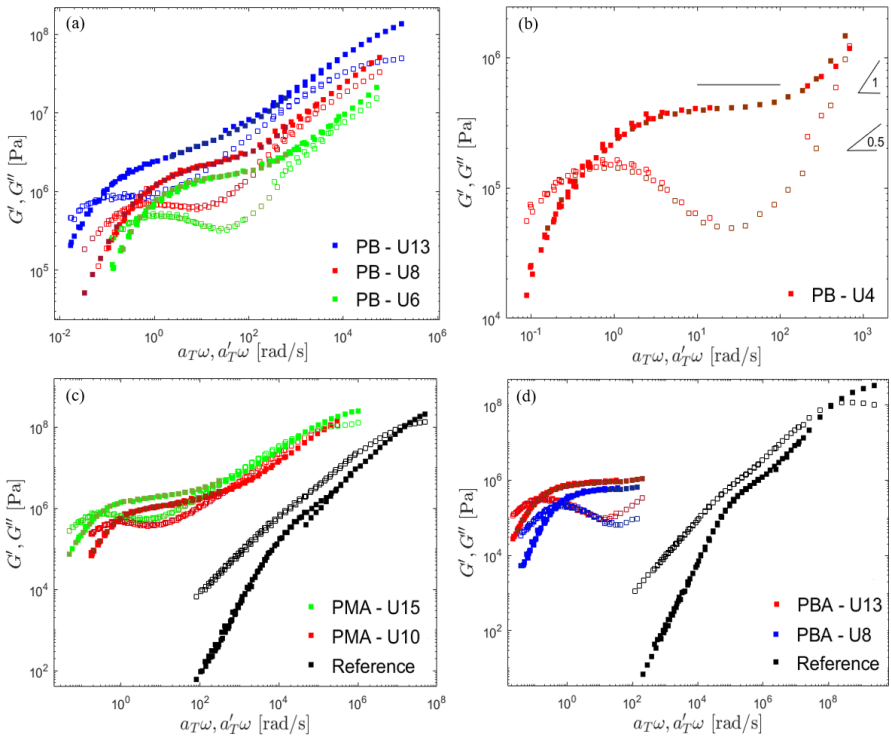

Figure 4.10: Pseudo-mastercurves or curves of PB systems at T_{ref} = 80 ℃ (a) and (b), of PMA systems at T_{ref} = 70 ℃ (c) and of PBA systems at T_{ref} = 40 ℃ (d). The thick solid lines denotes the value of $\rho RT/M$. Data shown in dark colors correspond to the linear response obtained at T_{ref}.

Figure 4.11 compares the shift factors a_T and $a_T^{'}$ used to build the pseudo-mastercurves and the mastercurves shown in Figure 4.10 and 4.7. The shifts shown in panel (a) and (b) are multiplied by a free volume correction factor a_{T_g}, enabling a comparison of the systems under iso-T_g conditions.[174,175] The values of the shifts a_{T_g} can be found in the appendix of this chapter.

As observed, the shifts a_T closely align with the WLF equation.[173] At the reference temperature T_{ref}, which are -30℃ and 30℃ for PBA and PMA respectively, the values of c_1^0 and c_2^0 are 7.22 and 61.5 K for PBA, and 7.65 and 67.77 K for PMA. These constants were calculated based on the linear data of

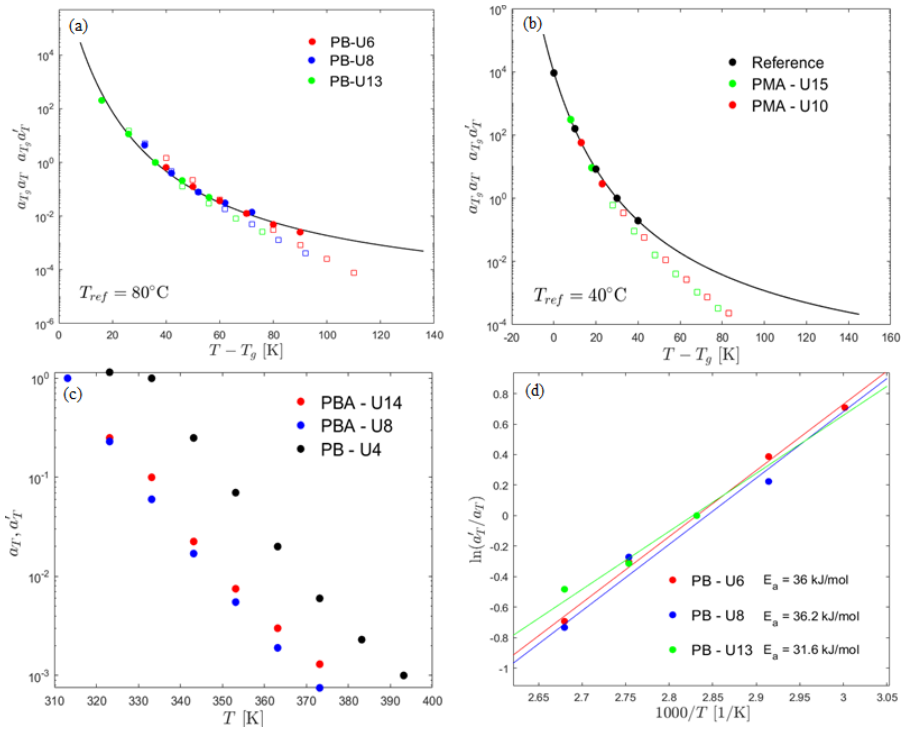

Figure 4.11: Shift factors of associative polymers (a) at $T_{ref} = 80°C$ (b) at $T_{ref} = 40°C$ and (c) at $T_{ref} = 40°C$ for PBA and 60°C for PB. The black line corresponds to the prediction of the WLF equation. In panels (a) and (b), open symbols refer to the shifts a_T', whereas closed symbols denote the shifts a_T. (d) Extraction of the activation energy through linear fitting.

the reference materials shown in Figure 4.7.

On the other hand, the temperature dependence of $a_T^{'}$ can be expressed as follows.[125]

$$a_T^{'} = a_T \exp\left(\frac{E_a}{R}\left(\frac{1}{T} - \frac{1}{T_{ref}}\right)\right) \tag{4.36}$$

The values for E_a can be determined through linear fitting, where $\ln\left(\frac{a_T^{'}}{a_T}\right)$ is

plotted against 1000/T. By applying this approach, values of E_a ranging from 31.6 kJ/mol to 36 kJ/mol were obtained for polymers based on PB, whereas polymers based on PMA exhibited values ranging from 36.5 kJ/mol to 44.5 kJ/mol. In the linear regression, the values of a_T were extrapolated using the WLF equation. For associative polymers based on PBA, the regression was not performed as the WLF equation is not valid when $\frac{T}{T_g} > 1.3$. Nevertheless, Zhang *et al.* found an activation energy of E_a = 33 - 37 kJ/mol for PBA-UPy polymer with a molar mass of 9.8 kg/mol.[125] The small differences in activation energy among the supramolecular polymers based on UPy groups are not sufficient to conclude any significant effect of the backbone on the strength of the physical bonds.

Figure 4.12, 4.13 and 4.14 show the predictions of the molecular model detailed in the preceding section. The fitting parameters are tabulated in Table 2. Following Fetters *et al.*,[228] a value of 120 g/mol for M_k was used to model the responses of the PB polymers. A density of $\rho = 1000$ kg/m^3 was also assumed for the supramolecular polymers.

Overall, the model demonstrates good agreement in capturing the flow behavior of associative polymers. Discrepancies obtained in the high frequencies region of PB - U6 and PB - U8 arise due to the omission of glassy modes in the model. As observed in Figure 4.12, predictions with the ansatz of Liu *et al.*[186] are relatively close to those obtained with the fixed stickers. This similarity is due to the moderate number of stickers present in the systems, as the ansatz only introduces N_s additional relaxation modes.

However, as observed in Figure 4.12, 4.13 and 4.14, the model poorly fits the experimental data in the terminal regime. Indeed, $G'(\omega)$ decreases much faster than what is predicted by the model. This discrepancy means that the spectrum described by the Rouse equation is excessively broad. This discrepancy could be related to the presence of another relaxation mechanism in the terminal regime resulting from the presence of aggregates.

Another discrepancy with the sticky Rouse model can be found by analyzing the ratio τ_S/τ_0 shown in Table 4.12. As observed, the sticker lifetime $\tau_S \sim$

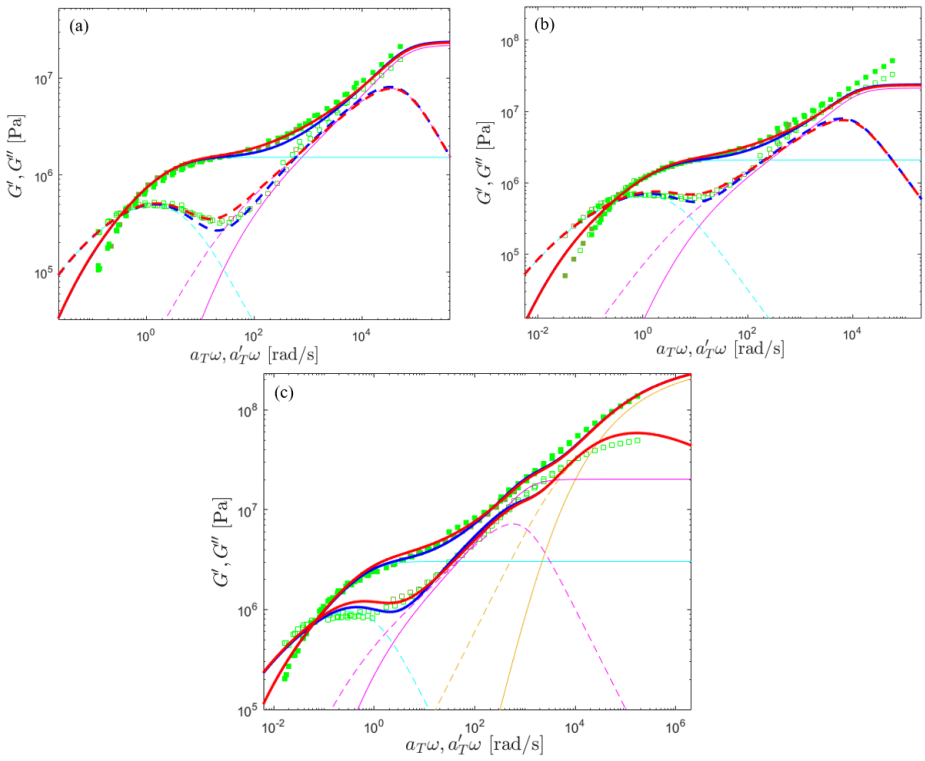

Figure 4.12: Linear viscoelastic mastercurves of (a) PB - U6, (b) PB - U8 and (c) PB - U13. PB at T_{ref} = 80℃. Red and blue lines correspond to the model predictions with and without fluctuations. The contributions from the KWW model (in orange), the Rouse model (in magenta) and the slow modes (in cyan) are also presented for the model with the fluctuations.

ζ_1/κ_1 increases with the incorporation of the UPy groups. This increase is partially caused by the rise in T_g with the incorporation of the UPy groups, which tends to slow down the segmental motion of the chains. Assuming the validity of equation 4.36, the influence of T_g on τ_S can be eliminated by comparing the breadth of the rubbery plateau, or equivalently, by considering the ratio τ_S/τ_0. As observed in Table 4.12, the ratio τ_S/τ_0 decreases with the grafting of the UPy groups. In the literature, a similar result was obtained by Cui *et al.* for UPyPEHA copolymers composed of ethylhexyl acrylate (EHA) and 2-[3-(6-methyl-4-oxo-1,4-dihydropyrimindin-2-yl)ureido]-ethyl

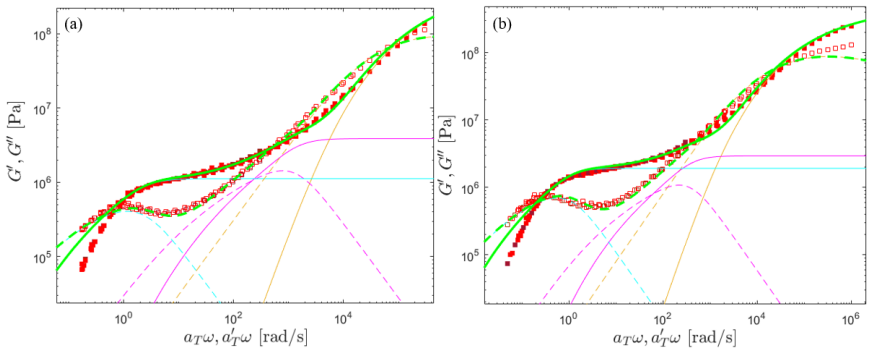

Figure 4.13: Linear viscoelastic mastercurves of (a) PMA - U10, (b) PMA - U15 at T_{ref} = 40℃. Green lines correspond to the model predictions with fluctuations. The contributions from the KWW model (in orange), the Rouse model (in magenta) and the slow modes (in cyan) are also presented for the model with the fluctuations.

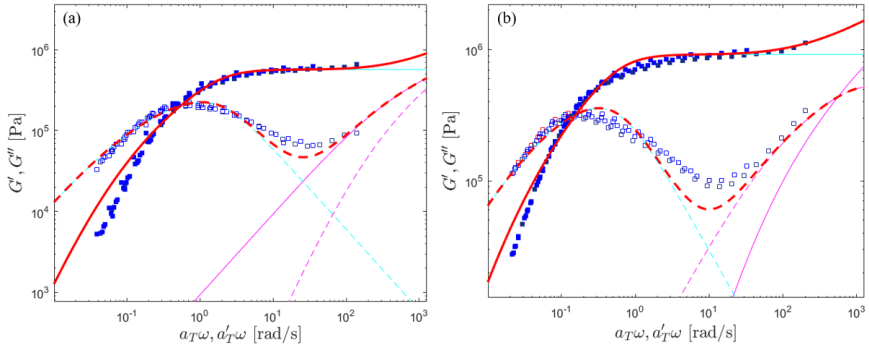

Figure 4.14: Linear viscoelastic mastercurves of (a) PBA - U8 and (b) PBA - U13 at T_{ref} = 40℃. Red lines correspond to the model predictions obtained with the values shown in Table 4.1 and 4.2. The contributions the Rouse model (in magenta) and the slow modes (in cyan) are also presented for the model with the fluctuations.

acrylate (UPyEA).[126] This trend differs from the behavior predicted by the bond lifetime renormalization model according to which an increase of density of stickers should lead to an increase of number of returns (see equation 4.25). This discrepancy could arise from the potential invalidity of equation 4.36, which might overestimate the coupling between the sticker dissociation and the

segmental motion of the chains, as explained by Ghosh and Schweizer.[123]

Finally, a significant divergence between the number of stickers predicted by NMR and the fitting parameters. The predicted plateau modulus is lowered, presumably due to the presence of topological defects, junctions containing multiple stickers or non-affine fluctuations of the bound stickers.

	ζ_0/κ_0 [s]	ζ_1/κ_1 [s]	τ_S/τ_0	p	p_{th}	G_g [GPa]	τ_{KWW} [s]	β [-]
PB - U6	6.5×10^{-5}	3.5	5.4×10^{4}	0.085	0.1	-	-	-
PB - U8	3.5×10^{-4}	4	1.1×10^{4}	0.11	0.12	-	-	-
PB - U13	4×10^{-3}	13	3.2×10^{3}	0.15	0.17	0.3	0.4×10^{-5}	0.35
PMA	2.5×10^{-3}	-	-	-	-	0.6	0.5×10^{-5}	0.39
PMA - U10	2.8×10^{-3}	4	1.4×10^{3}	0.29	0.53	0.5	1×10^{-6}	0.33
PMA - U15	1×10^{-2}	7	7×10^{2}	0.44	0.65	0.5	2×10^{-6}	0.31
PBA	1.65×10^{-2}	-	-	-	-	0.5	1×10^{-5}	0.4
PBA - U8	3×10^{-4}	4.9	1.6×10^{4}	0.33	0.59	-	-	-
PBA - U13	1.5×10^{-3}	14	9.3×10^{3}	0.47	0.81	-	-	-

Table 4.2: Fitting parameters of the curves shown in Figure 4.12, 4.13 and 4.14. The theoretical fraction of sticky beads p_{th} is also shown.

4.5 Conclusion

In this work, we analyzed the linear rheology of unentangled associative chains functionalized with UPy pendants groups. In order to do so, we fitted master-curves using an adaptation of the sticky Rouse model which includes a random placement of the stickers and a phenomenological correction for the spatial fluctuations of the supramolecular junctions in their associated states. The latter comes from an ansatz, meaning that it is likely that an additional refinement is needed to precisely capture the early diffusion of the stickers. The model leads to a very good description of the data. However, it is worth-mentioning that the description in the terminal regime is far from being perfect. In this regime, the storage modulus exhibits a narrower spectrum of relaxation than what is predicted by the sticky Rouse model. This could indicate the presence of another mechanism of relaxation due to the presence of aggregates. In a future work, small-angle X-ray scattering (SAXS) measurements would be needed to confirm the formation of these aggregates. Also, a more rigorous approach such as MD simulations for studying the fluctuations could be employed to validate the ansatz proposed by Liu *et al.*[186] This method may provide further insight into the system's behavior.

Appendix

Evaluation of the shifts a_{T_g}

Due to the different glass transition temperatures of the polymers, the horizontal shift factors a_T are different and have a smaller temperature dependence with decreasing UPy concentration. In order to account for the effects of the different T_g, a shift a_{T_g} has been computed by the following equation:

$$\log\left(a_{T_g}\right) = \frac{-c_1^0(T_{g,ref} - T_g)}{c_2^0 + (T_{g,ref} - T_g)} \tag{4.37}$$

Here $T_{g,ref}$ is the reference glass transition temperature. The computed shift a_{T_g} are presented in Table 4.3. Here, PB - U13 and PMA - U15 are treated as the reference materials.

	PB - U13	PB - U8	PB - U6	PMA - U15	PMA - U10
a_{T_g}	1	0.0791	0.0126	1	0.064

Table 4.3: Correction factor a_{T_g}

Chapter 5

Linear viscoelasticity of entangled metallo-supramolecular polymers with pendant groups

In this chapter, we present measurements of the linear rheology of entangled supramolecular polymers based on metal-ligand coordination bonds. The tailorable properties of these systems were explored by varying the quantity and the nature of the metal ions. The viscoelastic responses were then effectively modeled by adapting the TMA, originally developed by van Ruymbeke *et al.*,[1] to suit these specific supramolecular systems.

5.1 Introduction

Among the wide variety of supramolecular systems, metallo-supramolecular polymers are of particular interest. In these systems, the strength of the bonds can be widely tuned by adjusting the density and the nature of the metal ions,[87,229,230] the counterions[231] and the ligands.[230,232]

Depending on the chosen association, the metallic complexes can confer valuable magnetic, electrochemical, electrochromic, emissive and catalytic properties.[233–237] The multitude of potential combinations makes metal-containing polymers highly versatile, finding applications in various fields such as optoelectronic devices, sensors, adhesives, energy storage devices and anticancer drugs.[233,237]

When metallo-supramolecular are amorphous and flexible with a glass transition temperature below the room temperature, it becomes possible to exploit their properties as a soft material in the bulk state and at ambient conditions.[238] Despite the significant amount of research conducted on such metallo-supramolecular bulk polymers (MSBP), there remains much to uncover regarding the dynamics of the metal-ligand bonds. For instance, limited information is available regarding the stability constants of metal complexes in MSBP.

The combination of rheological experiments and molecular modeling is a valuable approach for characterizing the material properties of associative polymers and relating them to the chain dynamics. In this chapter, we study the rheology of entangled polymers with supramolecular side-groups.

As detailed in the introduction, the sticky reptation model, proposed Leibler *et al.*,[109] was introduced to describe the linear rheology of such systems in the case of pairwise associations. However, this model neglects relaxation mechanisms other than reptation. In reality, quantitative approaches need to include Contour Length Fluctuation (CLF) and Constraint Release (CR) to describe accurately the data of entangled associative systems.

Chen *et al.*[110] considered these secondary relaxation processes by adapting the double reptation model of des Cloizeaux,[28] originally used for entangled

polymeric melts. Their only modification, compared to the initial model, was to use the sticky reptation time τ^*_{rep} instead of the reptation time τ_{rep}. This led to a compact and practical set of equations which allows to obtain a rather good quantitative fit of the data. Nevertheless, in this model, CLF and CR are imprecisely captured and a refinement of these ideas is needed to capture the linear rheology of systems with more complex architectures and polydispersity in molar mass.[21] This could be obtained, for example, by using the tube-based time marching algorithm (TMA) model developed by van Ruymbeke *et al.*[1]

However, the sticky reptation is not valid anymore when the supramolecular junctions strongly associate and form large aggregates. The presence of these aggregates is often encountered in the case of polymeric chains associated through metal-ligand coordination bonds. For example, Jackson *et al.* showed that PnBA linear chains functionalized with 2,6-bis(1'- methylbenzimidazolyl)pyridine (MeBIP) ligands exhibit microphase separation of the complexes when it is crosslinked with transition metal ions. The rubbery plateau of these polymers was observed to be around 10 times higher than what is predicted based on the rubber elasticity theory.[239]

In the present work, we assessed the viscoelastic properties of entangled linear PnBA chains with terpyridine side groups randomly placed along the backbones. Two types of divalent transition metal ions (Zn(II) and Cu(II)) were incorporated in the polymer melt at various densities of terpyridine ligands. This wide range of ion content allows to explore the case of aggregates and that of pairwise associations. In the latter case, the rheological responses were fitted using the TMA extended for the modelling of associative polymers. We obtained a good agreement with the experimental data in the terminal regime and at high frequencies. However, a significant mismatch was obtained in the rubbery plateau.

5.2 Materials and experimental details

5.2.1 Copolymers

The synthesis of a linear PnBA functionalized with terpyridine ligand was achieved by reversible addition-fragmentation chain-transfer (RAFT) polymerization. The synthesis was performed by Zhuge, as part of his PhD project.[240] The molecular structure of the polymer is shown in Figure 5.1.

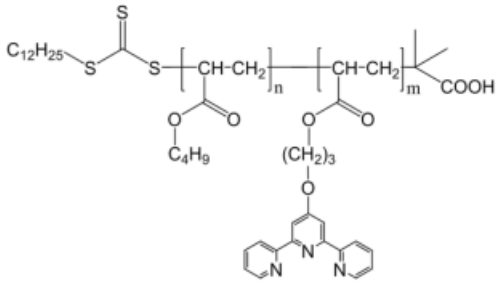

Figure 5.1: Chemical structure of PnBA-tpy.

The molar mass (M_n = 139.3 kg/mol) and the polydispersity index (Đ= 1.3) of the systems were determined with SEC. In addition, the resulting number of junctions along the chains (Z_s = 13) and the glass transition temperature (T_g = -52 °C) were obtained using nuclear magnetic resonance (NMR) and differential scanning calorimetry (DSC) respectively. The complete characterization of the polymer was performed by Zhuge. The system is estimated to contain around 8 entanglements, which was computed based on a value of M_e = 18 kg/mol found in the work of Zhuge *et al.*[241]

5.2.2 Preparation of metallo-supramolecular bulk polymers

The procedure employed to prepare the metallo-supramolecular polymers involves the following steps.

First, the synthesized PnBA-tpy$_{11}$ was dissolved in acetone in a sealed vessel

under gentle shaking. A high polymeric concentration ranging from 400 g/L to 500 g/L was used to promote the formation of interchain associations. Subsequently, a specific amount of either zinc(II) or copper(II) chloride was dissolved in methanol at a concentration of approximately 10-15 mg/mL and then added to the polymeric solution. The sealed container was sonicated again to ensure complete complexation of the metal ions. Afterwards, the solvent was evaporated under vacuum using a rotovap. Lastly, the resulting MSBP was put under vacuum ($\sim$ 0.1 bar) for 2 days to remove the residual solvent.

The composition of the prepared MSBP is summarized in Table 6.2. The term "equivalents" (eq.) indicates the ratio of the number of metal ions to the number of ligands in the polymer. Hence, the stoichiometric amount corresponds to 0.5 eq. Here, the range of ion content allows to cover the case where the value of M_s is greater than M_e, as well as the scenario where M_s is slightly lower than M_e.

	Metal ion content
PnBA-tpy + $ZnCl_2$	0.25 eq. 0.5 eq. 0.75 eq. 1.5 eq.
PnBA-tpy + $CuCl_2$	0.5 eq. 0.75 eq. 1.5 eq. 2.5 eq.

Table 5.1: Composition of PnBA polymers functionalized with tpy ligand

5.2.3 Literature data

To explore the case $M_e \gg M_s$, we also analyzed the linear response of entangled supramolecular polymer melts reported by Gold *et al.*[127] and Kim *et al.*[242]

The polymers of Gold *et al.*[127] are PI melts functionalized with different amounts of hydrogen-bonding urazole groups. On a different note, Kim *et al.*[242] focused on poly(styrene-co-sodium methacrylate) (PSMA-Na) ionomers,

where the molar mass between associative groups M_s remains fixed but the overall molar mass M_w varies. The main characteristics of these associative polymers, as provided by Gold *et al.*[127] and Kim *et al.*,[242] are shown in Table 5.2. The parameter n corresponds to the number of stickers along the chains, as computed by equation 4.2.

Sample names	M_w [kg/mol]	Đ	n	References
PI - 84k	84	1.02	-	[127]
PI - 84k - U1	84	1.02	12.9	[127]
PI - 84k - U2	84	1.02	25.7	[127]
PI - 84k - U3	84	1.02	51.5	[242]
PSMA-108k-3.7%Na	108	2.04	38.5	[242]
PSMA-445 K-3.8%Na	445	2.02	165.2	[242]

Table 5.2: Main characteristics of the associative polymers of Gold *et al.*[127] and Kim *et al.*[242] used in this work.

5.2.4 Rheological characterization

5.2.4.1 Linear response

The linear viscoelastic (LVE) properties of the different systems were assessed using the rheometer ARES 2000 (TA Instrument, USA). Small amplitude oscillatory shear was performed using a 8 mm parallel plate geometry with a convection oven under a N_2 atmosphere. For each system, an amplitude sweep was performed at 10 rad/s to determine the linear viscoelastic region. Once the sample was well equilibrated, a frequency sweep was carried out at frequencies ranging from 100 to 0.01 rad/s and at temperatures spreading from 100 to -20 °C.

5.3 Modelling the linear response of entangled sticky chains

The relaxation modulus $G(t)$ of entangled supramolecular systems can be expressed as the sum of three distinct contributions.[110]

$$G(t) = G_{Rouse}(t) + G_{SR}(t) + G_d(t) \tag{5.1}$$

The first contribution $G_R(t)$ accounts for the high-frequency Rouse relaxation, which occurs at length scales smaller than the mesh size of the polymeric network defined by both the entanglements and the stickers. Then, the second contribution $G_{SR}(t)$ reflects the sticky Rouse relaxation of the entanglement strands. Lastly, the third contribution $G_d(t)$ captures the disengagement of the chains from their tubes.

5.3.1 The Rouse relaxation

Based on the work of Chen *et al.*,[110] the non-sticky Rouse modes can be expressed as:

$$G_{Rouse}(t) = \kappa \frac{G_e}{Z_e} \sum_{p=N_s+1}^{N} \exp\left(-\frac{\beta p^2 t}{N^2 \tau_0}\right) \tag{5.2}$$

Here κ and β are factors equal to 1 and 2 if $p \geq Z_e$ and equal to $1/5$ and 1 if $p < Z_e$ respectively.

In equation 5.2, the modes obtained when $p \geq Z_e$ correspond to the 3D Rouse relaxation. This relaxation starts locally at the Kuhn segment scale and continues until it is interrupted either by the entanglements or the stickers.

On the other hand, the modes obtained when $p < Z_e$ correspond to the persisting longitudinal modes that equilibrate the chain density along the axis of the tube. As soon as the molecular segments of mass M_s are relaxed, the longitudinal Rouse process stops, as the stickers prevent the transportation of the monomers between the tube segments.[21]

It should be noted that the equation originally presented by Chen *et al.*[110]

has been adjusted to include the factor β, which is determined from the Rouse expression of an entangled melt[21] (as detailed in section 1.8.1).

5.3.2 The sticky Rouse relaxation

Analogous to the Rouse relaxation, the sticky Rouse contribution can be described in the following manner:

$$G_{SR}(t) = \kappa \frac{G_e}{Z_e} \sum_{p=1}^{N_s} \exp\left(-\frac{\beta p^2 t}{N_S^2 \tau_S}\right) \tag{5.3}$$

Here, it is assumed that the friction of the backbone is negligible compared to the one due to the associations, and that most of the stickers are bound, leading to a sticky Rouse time equal to $\tau_s N_s^2$.

The sticky Rouse modes starts at the dissociations of the stickers. As soon as the chains start to feel the entanglements (i.e., $p < Z_e$), only the longitudinal modes can relax, at the rhythm of the formation and the breakage of the reversible crosslinks.

5.3.3 The disentanglement modulus

The disentanglement modulus $G_d(t)$ is modeled using the TMA developed by van Ruymbeke et al.[1] In this model, $G_d(t)$ is expressed as

$$G_d(t) = G_N^0 \Phi(t) \phi(t) \qquad \text{with} \qquad G_N^0 = \frac{4}{5} \frac{\rho RT}{M_e} \tag{5.4}$$

Here $\phi(t)$ is the survival fraction of the initial thin tube while $\phi_{CR}(t)$ is the constraint-release function or dilation factor that determines the diameter of the dilated tube. As discussed in Chapter 5, the function $\phi_{CR}(t)$ is generally equal to $\phi(t)$ when the constraint release process is slow. Indeed, $\phi_{CR}(t)$ cannot decrease faster than a Constraint Release Rouse process.

$$\Phi(t) = \max\left(\phi(t_{k+1}), \phi(t_k)\sqrt{\frac{t_k}{t_{k+1}}}\right) \tag{5.5}$$

In equation 5.5, t_{k+1} corresponds to the time obtained just after t_k, i.e. $t_{k+1} = t_k + \delta t$. Also, an initial condition $\phi(\tau_e) = 1$ is imposed.

The survival probability of the initial tube $\phi(t)$ can be obtained by summing all the contributions due to the molecular segments x which are still moving in the initial tube.

$$\phi(t) = \int_0^1 p_{rep}(t_k) p_{fluc}(x, t_k) dx \tag{5.6}$$

Here the coordinate x corresponds to the fractional distance from the free ends ($x = 0$) to the middle of the chains ($x = 1$).

In equation 5.6, $p_{rep}(t_k)$ and $p_{fluc}(x, t_k)$ represent the survival probabilities related to the reptation and the fluctuation processes respectively. They can be evaluated by the following expressions.

$$p_{rep}(t_k) = \exp\left(\frac{-t_k}{\tau^*_{rep}(t)}\right) \tag{5.7}$$

$$p_{fluc}(x, t_k) = \exp\left(\frac{-t_k}{\tau^*_{fluc}(x, t)}\right) \tag{5.8}$$

Similarly to the case of entangled polymeric melt, the outer segments relaxed by the fluctuations do no play a role in the reptation. Hence, the sticky reptation time, $\tau^*_{rep,0} = \tau_S N_s^2 Z_e$, can be rescaled as follows: $\tau^*_{rep}(t) = \tau^*_{rep,0}\phi(t)$.

While the sticky reptation time, τ^*_{rep}, is known, the value of $\tau^*_{fluc}(x)$, the sticky fluctuation times, still remains to be modeled. Similarly to reptation, CLF is widely affected by the presence of the junctions. In order to illustrate this influence, the different generations of segments trapped by stickers are depicted in Figure 5.2. At the extremities of the chains, the dangling ends, represented by the segment α, can relax through the classical CLF. Then, in order to relax the molecular segment β, one needs to wait that the first sticker dissociates, which should happen in a timescale comparable to τ_S. For the relaxation of the third generation, it is required that the first two stickers dissociate simultaneously, which is an unlikely process. As a result, for the relaxation of deep segments, CLF is considerably slowed down and progresses at the rhythm of the

successive associations and disassociations of the reversible crosslinks.

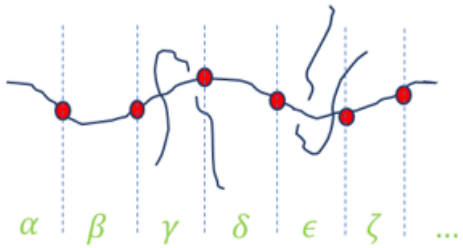

Figure 5.2: Representation of different generations of trapped segments. Adapted from [240]

Here, two distinct approaches for modeling $\tau^*_{fluc}(x)$ are introduced. The first approach is approximate and straightforward, while the second approach is considerably more sophisticated.

1. Sticky CLF

The fluctuations times $\tau_{fluc}(x)$ of a neutral polymer melt can by determined by taking into account early fluctuations and activated retraction of the chain ends. Based on the work of van Ruymbeke *et al.*,[1] $\tau_{fluc}(x)$ is given by:

$$\tau_{fluc}(x) = \begin{cases} \tau_{early}(x), & \text{if } x < x_{trans}. \\ \tau_{early}(x) \exp\left(\dfrac{\Delta U(x_{trans} \rightarrow x)}{k_B T}\right), & \text{if } x \geq x_{trans}. \end{cases} \tag{5.9}$$

In the equation above, $\tau_{early}(x)$ can be determined using the following equation.

$$\tau_{early}(x) = \frac{9\pi^3}{16} \tau_R x^4 Z_e^2 \tag{5.10}$$

Additionally, the difference of potential energy $\Delta U(x_{trans} \rightarrow x)$ can be obtained through the following equation:

$$\Delta U(x_{trans} \rightarrow x) = \frac{3 k_B T}{2} Z_e (x^2 - x_{trans}^2) \tag{5.11}$$

Here, the coordinate x_{trans} is equal to $\sqrt{\frac{2}{3Z_e\phi}}$.

Replacing τ_R by τ_{SR} in equation 5.9 provides a rapid and straightforward method for modeling $\tau^*_{fluc}(x)$. In this case, the relaxation by CLF is completely analogous to that of an ordinary polymeric melt. This approach is expected to be imprecise for deep segment as it fails to consider that the simultaneous opening of n consecutive stickers is a rare event, whose probability decreases exponentially with n. Furthermore, as it averages the influence of the stickers, it is expected to be more suitable for associative chains with many short lifetime stickers.

2. Stepwise fluctuations

An alternative strategy to address the fluctuations involves employing stepwise fluctuations. This approach uses comparable concepts to those used by Leibler *et al.*[109] to evaluate the scaling laws of the sticky reptation model.

In order to relax the k^{th} generation of trapped segments, it is necessary to have a minimum of k open consecutive stickers. A succession of k open stickers followed by a closed sticker is referred to as a "k-strand" using the terminology introduced by Leibler *et al.*[109]

The probability P_k of obtaining a k-strand can be computed as follows:

$$P_k = p_{free}^k \times (1 - p_{free}) \tag{5.12}$$

Here, p_{free} represents the average fraction of open stickers.

The probability that an open sticker reassociates after a time t is given by the following exponential distribution.

$$P(t, \tau_{open}) = \exp\left(-\frac{t}{\tau_{open}}\right) \tag{5.13}$$

In the equation above, τ_{open} corresponds to the average lifetime of an open sticker.

Hence, the characteristic timescale associated with the lifetime of a k-strand is $\tau_k = \dfrac{\tau_{open}}{k}$ as the probability that none of the stickers of the k-strand have reassociated is $P^k(t, \tau_{open})$.

As a result, for a time period Δt, the total time during which a k-strand is existing is equal to $p_k\ \Delta t$, and since each k-strand has a lifetime of τ_k, the number of k-strand observed during this period is equal to $\dfrac{p_k \Delta t}{\tau_k}$. Therefore, the frequency of occurrence of a k-strand can estimated by the following ratio.

$$\nu_k = \frac{p_k}{\tau_k} = \frac{k p_{free}^k (1 - p_{free})}{\tau_{open}} \tag{5.14}$$

In the specific scenario where only two associating units need to meet to form a supramolecular junction, there exists a relationship between τ_{open}, p_{free}, and τ_s, which can be expressed by the following equation:

$$\frac{\tau_{open}}{\tau_S} = \frac{p_{free}}{1 - p_{free}} \tag{5.15}$$

By substituting equation 5.15 in 5.14, the frequency ν_k can be expressed as:

$$\nu_k = \frac{k p_{free}^{k-1} (1 - p_{free})^2}{\tau_s} \tag{5.16}$$

Consequently, the time delay $\tau_{f,k}$ required to relax the k^{th} generation of trapped segments can be estimated by summing the frequencies of occurrence of all the k-strand in which the k^{th} sticker along the chain is open.

$$\tau_{f,k} \approx \left(\sum_{q=k}^{k_m} \nu_q \right)^{-1} \tag{5.17}$$

Here k_m denotes the maximum number of k-strands in the chains. Equation 5.17 can be simplified if we assume that $k_m \to \infty$. In this case, $\tau_{f,k}$ reduces to

$$\tau_{f,k} \approx \left(\frac{(1-p)^2}{\tau_S} \sum_{q=k}^{\infty} q p_{free}^{q-1} \right)^{-1} = \frac{\tau_S}{p_{free}^k + (1-p_{free}) k p_{free}^{k-1}} \tag{5.18}$$

To derive the last equality, the following formulas were used:

$$\sum_{k=1}^{n} k r^{k-1} = \frac{1-r^{n+1}}{(1-r)^2} - \frac{(n+1)r^n}{1-r} \tag{5.19}$$

$$\sum_{k=1}^{\infty} k r^{k-1} = \frac{1}{1-r^2} \tag{5.20}$$

This approach results in stepwise fluctuations. Specifically, the sticky fluctuation time $\tau^*_{fluc}(x)$ of the dangling ends is the same as the fluctuation time of its neutral polymer counterpart. Subsequently, for deeper segments, $\tau^*_{fluc}(x)$ is delayed by a timescale equal to $\tau_{f,k}$ compared to $\tau_{fluc}(x)$. Since $\tau_{f,k}$ is typically much longer than $\tau_{fluc}(x)$, the trapped segments rapidly equilibrate shortly after the opening of the k consecutive stickers.

Based on this, the survival probability p_{fluc} can be expressed as follows:

$$p_{fluc}(x, t_k) = \exp\left(-\frac{p(x) t_k}{\tau_{fluc}(x)} \right) \tag{5.21}$$

Here the function $p(x)$ serves as a penalty function, capturing the delaying effect caused by the stickers. It takes a value of 1 when $x < x_1$, where x_1 is the position of the first sticker along the chain. When $x > x_1$, $p(x)$ can be evaluated using equation 5.18 in the following manner:

$$p(x) = \frac{\tau_{fluc(x)}}{\tau_S} \left(p_{free}^{k(x)} + (1-p_{free}) k(x) p_{free}^{k(x)-1} \right) \tag{5.22}$$

In the equation above, the number of sticker $k(x)$ is treated as a continuous variable and is equal to $\frac{Z_s}{2} x$.

This fluctuation process ends when the lifetime of a k-strand becomes smaller than the diffusion time needed to relax such k-strand.

$$\frac{\tau_{open}}{k_{max}} = \tau_{fluc}(x = x_{k_{max}}) \tag{5.23}$$

This condition defines the coordinate $x_{k_{max}}$ above which $\tau^*_{fluc}(x)$ tends to infinity.

Verification of the stepwise approach

To verify the validity of equation 5.18, a procedure similar to Ahmadi *et al.*[243] is performed. An ensemble of C stickers is generated, where an initial fraction p_{free} of these stickers is assumed to be in the open state, while the remaining fraction is in the associated state.

At each time step δ, the open stickers have a probability $\exp\left(-\frac{\delta}{\tau_{open}}\right)$ to associate, whereas the closed stickers have a probability $\exp\left(-\frac{\delta}{\tau_{closed}}\right)$ to dissociate. The time step δ is chosen to be sufficiently small to maintain a constant p_{free} over time.

By simulating the dynamics of the stickers, the equations incorporating the stepwise fluctuations can be effectively validated. Figure 5.3 exhibits the average waiting time $\tau_{f,k}$ for observing a k-strand. These values of $\tau_{f,k}$ are compared with the analytical predictions obtained with equation 5.18.

As observed, the analytical predictions closely match the numerical results, exhibiting only a minor discrepancy. This deviation can be attributed to the approximation made in equation 5.18, which assumes that p_{free} tends towards zero and thus neglects the initial concentration of open stickers. This assumption is well illustrated by the fact that the equation predicts a waiting time $\tau_{f,1}$ equal to τ_S while, in the simulations, $\tau_{f,1}$ is given by the product $(1-p_{free})\tau_S$, accounting for the initial presence of open stickers.

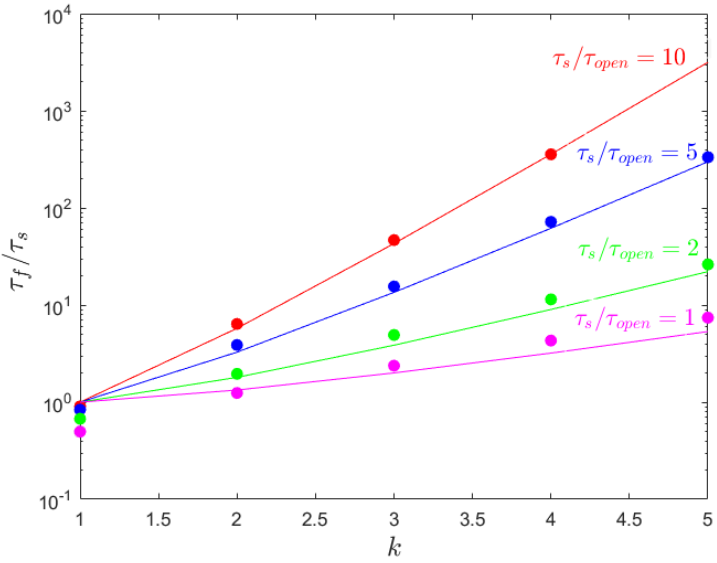

Figure 5.3: Normalized average waiting time $\tau_{f,k}$ for observing a k-strand at different ratio τ_S/τ_{open}. The solid lines correspond to the analytical predictions of equation (20) whereas the symbols are the numerical predictions obtained with $C = 6000$.

5.3.4 Comparison between the different approaches

Figure 5.4 compares the predictions of the dynamic moduli, surviving fraction of the tube $\phi(t)$ and the fluctuations times $\tau^*_{fluc}(x)$ using the different approaches for hindered fluctuations in the TMA.

As expected, the predictions give significant different results. First, the stepwise fluctuations predict a relaxation in the first plateau, accounting for the relaxation of the dangling ends. The magnitude of this relaxation is damped due to the high level of the plateau.

Then, at frequencies comparable to $\omega \approx 1/\tau_S$, the dissociation of the stickers start to influence the CLF. In this region, the stepwise CLF leads to a much stronger relaxation than the sticky CLF. This relatively important relaxation is caused by the relaxation of the first trapped segments in the tube.

Finally, at longer times, the sticky CLF persist whereas the stepwise CLF is interrupted due to equation 5.23, according to which this process stops at $x = x_{k_{max}}$.

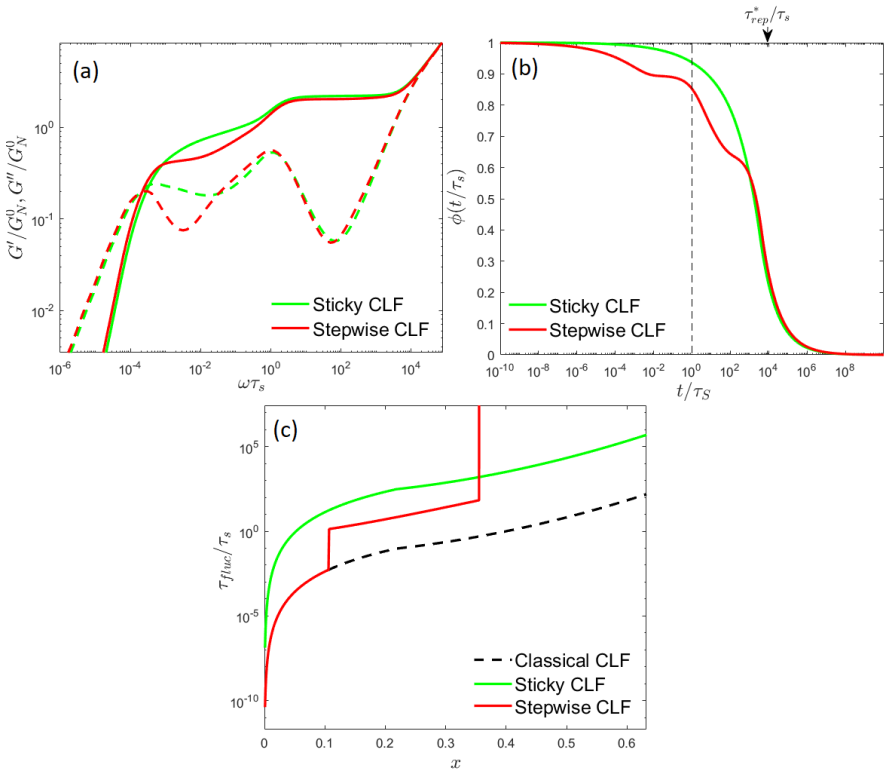

Figure 5.4: Prediction of (a) the relaxation modulus (b) the surviving fraction of the tube and (c) the fluctuation times τ_{fluc} considering the different approaches for hindered fluctuations (see text) incorporated into the Time Marching Algorithm (TMA). The predictions are obtained with $p_{free} = 0.2$, $Z_s = 25$, $Z_e = 14$ and $\tau_S/\tau_e = 1000$.

5.4 Results and Discussion

In this section, the linear responses of the supramolecular PnBA polymers and their neutral counterparts are presented and discussed.

5.4.1 Linear rheology

5.4.1.1 Effect of the density of ions

The panels in Figure 5.5 illustrate the effects of ion density on Zn(II)-containing samples. By analyzing these graphs, various observations and conclusions can be drawn.

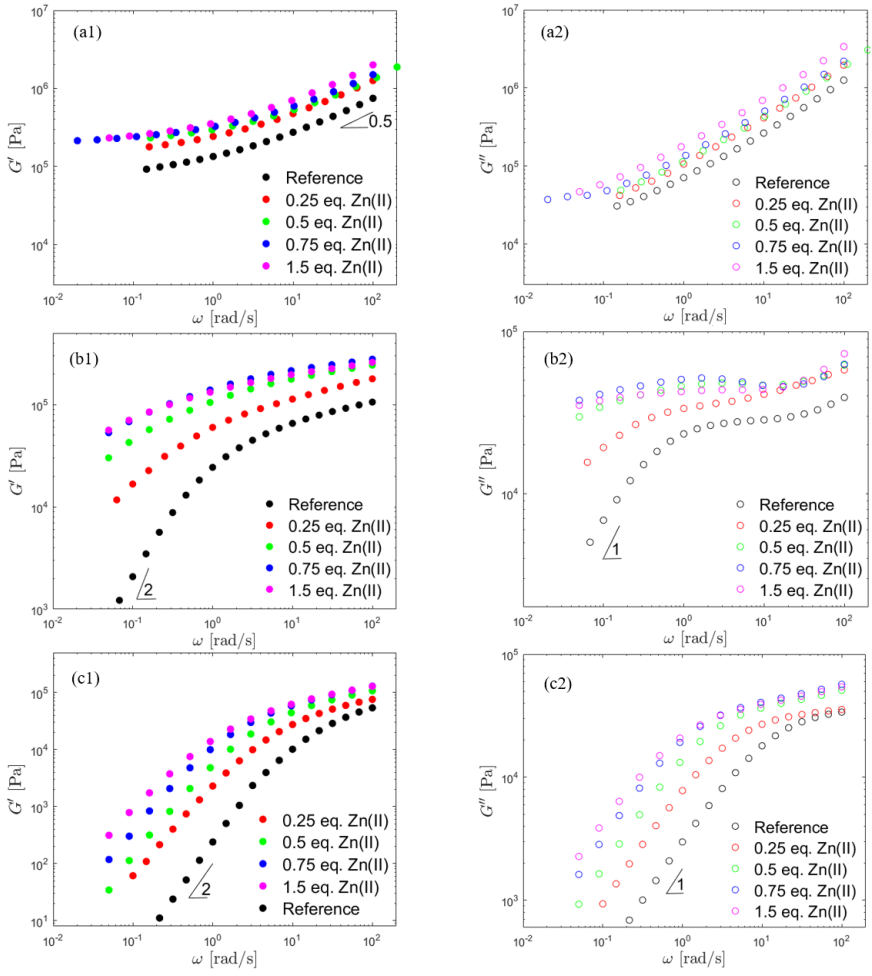

Figure 5.5: Storage (x1) and Loss modulus (x2) of PnBA-tpy$_{11}$ with different amounts of Zn(II) ions at (a) T = -20 °C, (b) T = 20 °C and (c) T = 60 °C.

First, in panel (a), it can be observed that the supramolecular polymers and the reference material display comparable relaxation behavior at high frequency. This similarity arises because, in this regime, the polymeric systems primarily relax through the Rouse motion of the chains. The Rouse process is a local relaxation mechanism that takes place at length scales smaller than the mesh size of the network, and as such, is expected to not be influenced by the connectivity of the polymeric chains. However, a slight delay in the relaxation caused by the presence of the supramolecular associations can still be noticed. This coupling between the motion of the backbone and the supramolecur junctions has previously been observed by Jiang *et al.*,[244] also in the context of Zn-based metallo-supramolecular networks. Notably, this coupling was observed despite the absence of a significant change in T_g when metal-ions were introduced, as indicated by DSC results.

Then, in panel (b) and (c), it is apparent that the longest relaxation time and the magnitude of the rubbery plateau increase with the amount of ions in samples containing less than 0.75 eq. Zn(II). Surprisingly, above 0.75 eq. Zn(II), both the relaxation time and the rubbery plateau remain constant. This saturation behavior was not expected as adding ions above the stoichiometric ratio generally influences the complex formation.

If only mono and bis-complex (metal ions bound to one and two ligands respectively) can be formed, the following reaction scheme is often assumed.[245,246]

$$\mathrm{X}^{2+} + \mathrm{L} \rightleftharpoons \mathrm{XL}^{2+} \quad \text{with} \quad \mathrm{K}_1 = \frac{[\mathrm{XL}^{2+}]}{[\mathrm{X}^{2+}][\mathrm{L}]} \tag{5.24}$$

$$\mathrm{XL}^{2+} + \mathrm{L} \rightleftharpoons \mathrm{XL_2}^{2+} \quad \text{with} \quad \mathrm{K}_2 = \frac{[\mathrm{XL}_2^{2+}]}{[\mathrm{XL}^{2+}][\mathrm{L}]} \tag{5.25}$$

Here $\left[\mathrm{X}^{2+}\right]$, [L], $\left[\mathrm{XL}^{2+}\right]$ and $\left[\mathrm{XL}_2^{2+}\right]$ correspond to the equilibrium concentration of free metal ions, free ligands, mono-complexes and bis-complexes respectively. Additionally, K_1 and K_2 are the equilibrium constant for mono- and bis-complexes.

The mass balance for [L] and $\left[\mathrm{X}^{2+}\right]$ is therefore governed by the following

equations.

$$\left[X^{2+}\right]_0 = \left[X^{2+}\right] + \left[XL^{2+}\right] + \left[XL_2^{2+}\right] \tag{5.26}$$

$$[L]_0 = [L] + \left[XL^{2+}\right] + 2\left[XL_2^{2+}\right] \tag{5.27}$$

In the equation above, $[L]_0$ and $\left[X^{2+}\right]_0$ are the initial concentration of free ligands and free metal ions.

By combining equations 5.24, 5.25, 5.26 and 5.27, the equilibrium activity of each species can be obtained. In the literature, equilibrium constants K_1 and K_2 were determined to have values of $10^{6.7}$ M^{-1} and $10^{5.2}$ M^{-1} at 25°C in aqueous solution.[246] As shown in panel (a) of Figure 5.6, these values of K_1 and K_2 result in a concentration maximum of bis-complexes at the stoichiometric amount. The presence of this concentration maximum has been well-demonstrated in the viscoelastic responses of telechelic metallo-supramolecular polymers in solutions, as reported by Schmatloch *et al.*[247] Specifically, in these systems, the relaxation time reaches a maximum at the stoichiometric ratio, followed by a decrease due to the increasing concentration of mono-complex which acts as chain stoppers.

However, this observed behavior does not correspond to what is observed in Figure 5.5, as the longest relaxation time is unchanged with the addition of ions. This discrepancy could mean that higher effective values for the ratio K_2/K_1 and the equilibrium constants K_1 and K_2 are obtained at the bulk state, which helps to stabilize the reversible network against a metal cation excess. In this scenario, as shown in panel (b) of Figure 5.6, the formation of bis-complexes is favored while the density of mono-complexes stays minimal above the stoichiometric ratio. This implies an almost linear increase of the concentration of free ions with the overall ion content. A similar result has been obtained in a very recent study of Li, where a saturation of the rubbery plateau was observed at 1 eq. Zn(II) in entangled terpyridine end-capped PnBA star. It is noteworthy that phase separation of the complexes was not observed in these systems, based on SAXS measurements.[248]

The observed behavior in Figure 5.5 illustrates well that it is not straightfor-

ward to relate the equilibrium constants estimated in solution with the rheology of the MSBP. Ligand protonation, solvent coordination and the effect of the ionic strength can all potentially affect the effective values of both equilibrium constants and therefore contribute to the difference of qualitative behaviour between polymeric melts and solutions.[87,249]

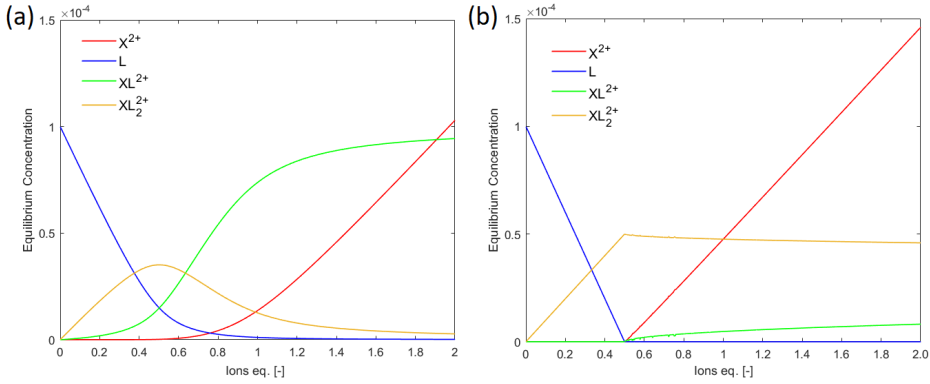

Figure 5.6: Equilibrium concentration of $[X^{2+}]$,$[L]$,$[XL^{2+}]$ and $[XL_2^{2+}]$ against the quantity of ions in the system. The equilibrium constants are set as $K_1 = 10^{6.7}$ M^{-1} and $K_2 = 10^{5.2}$ M^{-1} in panel (a) and as $K_1 = 10^{8}$ M^{-1} and $K_2 = 10^{10}$ M^{-1} in panel (b). The initial concentration $[L]_0$ is assumed to be equal to 10^{-4} M^{-1}.

Figure 5.7 presents the influence of the addition of Cu(II) ions, from stoichiometric to large excess of ions. Similar to the behavior observed for Zn(II)-based networks, samples with quantities of ions equal or slightly higher than the stoichiometric ratio (i.e. 0.5 eq. Cu(II) and 0.75 eq. Cu(II)) exhibit similar linear responses. Nonetheless, for quantities well above the stoichiometric ratio, the rubbery plateau starts to increase significantly. The samples containing 1.5 and 2.5 eq. Cu(II) display a much slower flow dynamics as well as a broader spectrum of relaxation times. In addition, the samples do not fully relax in the experimental temperature range. This behavior could suggest the formation of microphase-separated domain with long lifetime. This clustering effect is promoted due to the difference in polarity between the charged terpyridine metal ion complexes and the apolar PnBA polymer matrix. The faster relax-

ation obtained for the MSBP with 1.5 eq with respect to that of 2.5 eq. Cu(II) is attributed to an increase of the aggregation number which slows down the relaxation of the clusters.

However, it is to interesting to notice, as indicated in Table 5.3, that the values of the plateau modulus stay below the theoretical plateau modulus $G \approx 320$ kPa $= G_{melt} + \dfrac{\rho RT}{M_s}$ which considers that the sample elasticity is only due to the presence of entanglements and sticky associations.

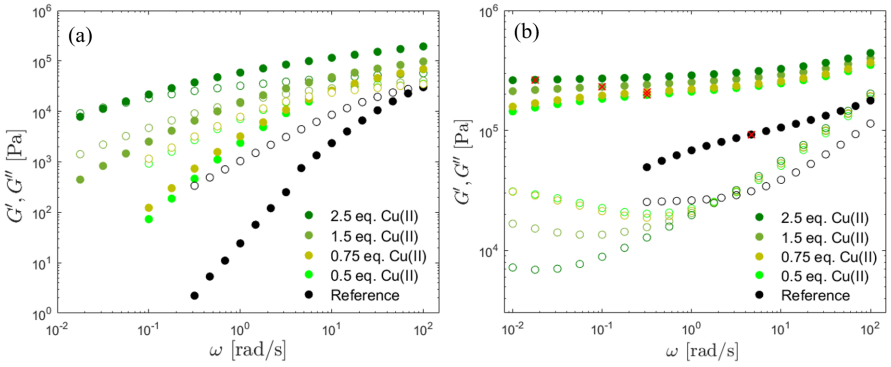

Figure 5.7: Linear viscoelastic response of PnBA-tpy$_{11}$ with Cu(II) ions and without ions at a) T = 0 ℃ and b) T = 80℃. The star symbols indicate the plateau modulus G.

Ion content	Plateau modulus [Pa]
Reference	1×10^5
0.5 eq.	1.9×10^5
0.75 eq.	1.9×10^5
1.5 eq.	2.3×10^5
2.5 eq.	2.6×10^5

Table 5.3: Value of the plateau modulus G_N^0 for the of PnBA-tpy11 complexed with Cu(II). G_N^0 has been evaluated by taking the value of G' at the local minimum of G' at $T = 0$℃. For the reference, the theoretical value has been used.

5.4.1.2 Effect of the nature of ions

Figure 5.8 shows the effects of the nature of ions, revealing that the relaxation time increases upon replacing Zn(II) by Cu(II) ions. This result is in agreement with the Irving-Williams series, which predicts a higher stability for Cu(II) complexes.[250] Furthermore, the magnitude of the rubbery plateau is identical in both associative polymers as the number of obstacles (pairwise junctions and entanglements) is similar in both systems.

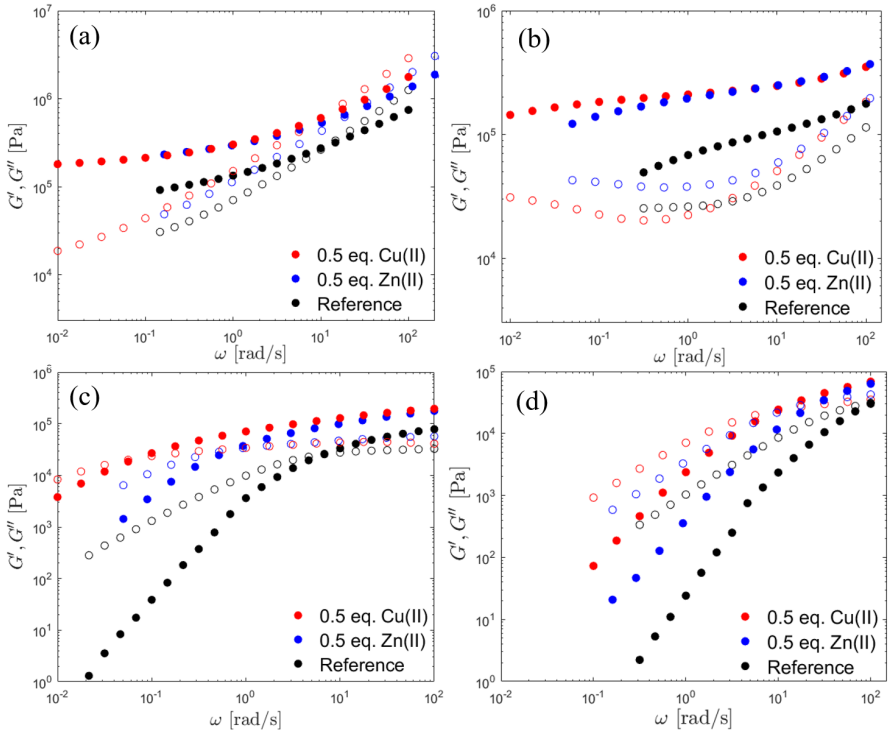

Figure 5.8: Linear viscoelastic response of PnBA-tpy11 with 0.5 eq. Cu(II), 0.5 eq. Zn(II) and no ions at (a) T = -20 ℃, (b) T = 0 ℃, (c) T = 40 ℃ and (d) T = 80 ℃.

By analyzing the frequency at which the linear viscoelastic responses of the associative polymers diverge, it is possible to determine the sticker lifetime of the Zn(II)-based network.[248] This procedure provides a lifetime value $\tau_{S,Zn(II)}$

of 0.32 s at T = 0℃.

As observed in Table 5.4, almost 2 orders of magnitudes separate the crossover frequency ω_c of the reference from that of the MSBP crosslinked with 0.5 eq. Cu(II). This illustrates the high tunability of the metal ligand interactions.

	Reference	0.5 eq. Zn(II)	0.5 eq. Cu(II)
$1/\omega_c$	0.146	1.07	17.8

Table 5.4: Inverse of the crossover frequencies of PnBA polymers functionalized with tpy ligand at T = 80 ℃.

5.4.1.3 Time-Temperature Superposition (TTS)

To evaluate the temperature dependence of the spectrum of relaxation times of the polymeric systems, pseudo-mastercurves and mastercurves have been built using the procedure outlined in Chapter 4.

Pseudo-mastercurves for Zn(II) and Cu(II)-based networks are presented in Figure 5.9 and 5.10, respectively, alongside the mastercurve of the reference material at T_{ref} = 20 ℃. The physically-crosslinked networks which contain the same ions were subjected to identical shift factors a_T and a'_T. Since the density remains relatively constant across the experimental temperature range, the vertical shift b_T has been neglected.[241,251] As expected, a noticeable discrepancy is observed in the rubbery plateau region due to the distinct temperature dependencies between the Rouse and sticky modes.

As observed in Figure 5.11, the shift factors found for the reference sample follow the WLF equation with the corresponding parameters c_1^0 = 6.35 and c_2^0 = 141.52 K.

Furthermore, the activation energy E_a of the assocaitive bonds can be evaluated by assuming that the shift factors a'_T follow the equation:

$$a'_T = a_T \exp\left(\frac{E_a}{R}\left(\frac{1}{T_{ref}} - \frac{1}{T}\right)\right) \tag{5.28}$$

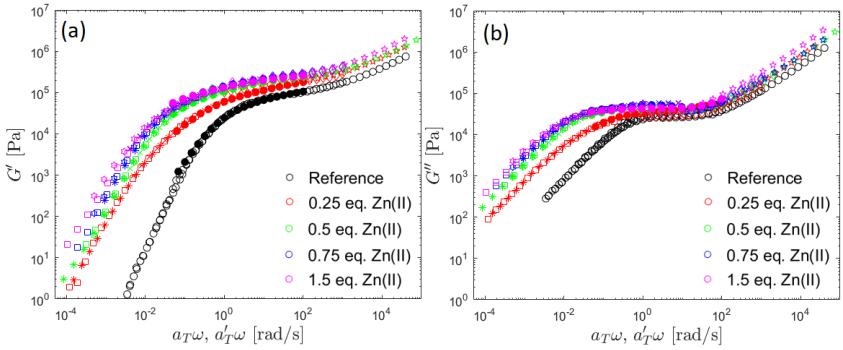

Figure 5.9: Storage (a) and Loss modulus (b) of PnBA-tpy$_{11}$ with different amounts of Zn(II) ions at T_{ref} = 20 °C.

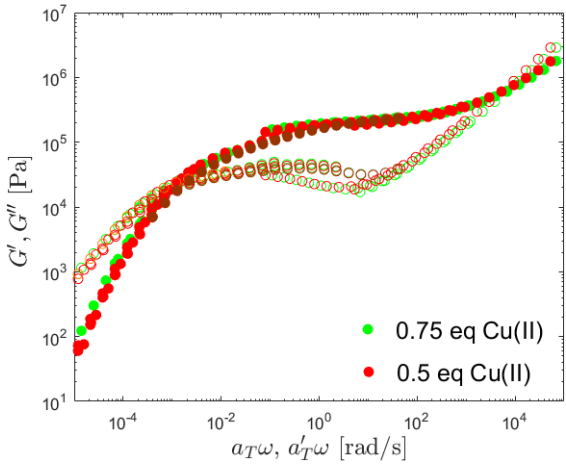

Figure 5.10: Linear viscoelastic response of PnBA-tpy$_{11}$ with different amounts of Cu(II) ions at T_{ref} = 20 °C.

By applying this equation, an E_a of 27.2 kJ/mol was obtained for all the samples containing Zinc ions, from 0.25 to 1.5 eq. Zn(II). Additionally, an E_a of 52.1 kJ/mol for polymers containing 0.5 and 0.75 eq. Cu(II) ions was determined. These values indicate that Zn(II) complexes are much more labile than the Cu(II) complexes and thus exchange much more rapidly.

Activation energies of similar systems have already been measured in the lit-

erature. For instance, a linear and unentangled PnBA melt with sticky-side groups based on metal-ligand bonds using Zn(II) ions exhibited an activation energy of 40 kJ/mol.[252] Li *et al.* also reports activation energy values going from 18 to 30 kJ/mol for a 4-armed telechelic star PnBA melt crosslinked with Zn(II) ions and from 50 to 60 kJ/mol for the same system with Cu(II) ions.[253] It can also be interesting to compare these values with the activation energy range of 33 to 37 kJ/mol found for PnBA-based copolymers containing quadruple hydrogen-bonding UPy units, as discussed in Chapter 4.

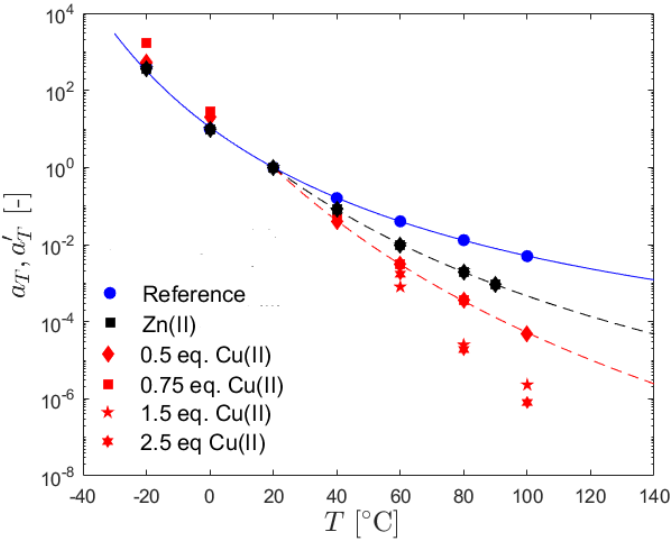

Figure 5.11: Shift factors a_T (continuous curve) and $a_T^{'}$ (dashed curves) of the references and the MSBP at T_{ref} = 20°C. The shifts obtained at high temperature for 1.5 eq. Cu(II) and 2.5 eq. Cu(II) are also shown. Inset: Temperature dependence of $a_T^{'}/a_T$ of 0.5 eq. Zn(II) and 0.5 eq. Cu(II).

When the quantity of Cu(II) ions exceed 0.75 eq., E_a dramatically increases. This growth is illustrated in Figure 5.12 which displays the linear responses of the polymers with 1.5 and 2.5 eq. Cu(II) after being shifted using the same set of shift factors as the MSBP containing 0.5 eq. Cu(II). As observed, a failure of TTS is obtained at low frequencies due to the existence of a relaxation mechanism with much stronger temperature dependence. This behavior is most

probably due to the formation of aggregates, as discussed earlier.

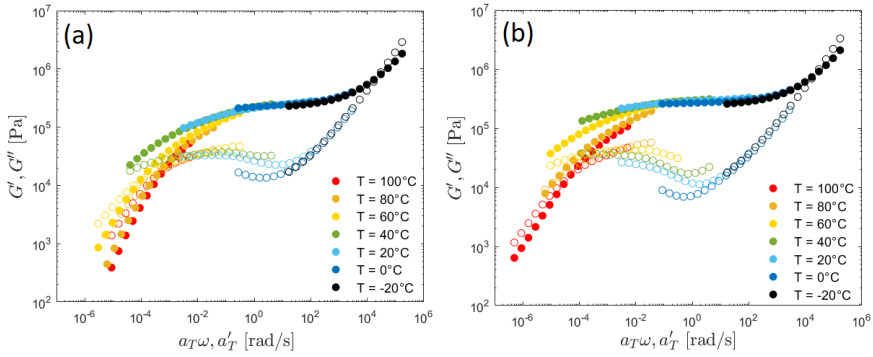

Figure 5.12: Linear viscoelastic responses of PnBA-tpy11 with (a) 1.5 eq. Cu(II) and (b) 2.5 eq. Cu(II), shifted using identical shift factors as the PnBA-tpy11 system with 0.5 eq. Cu(II) at T_{ref} = 20 °C.

Figure 5.13 depicts an attempt to construct pseudo-mastercurves for these systems. Building a pseudo-mastercurve of associative systems in presence of microphase-separated domain has already been done in the literature, notably by Ahmadi *et al.* for entangled chains functionalized with UPy units[222] or by Stadler *et al.* in the case of ionomers.[128]

For $T < 20$°C, the same shift as the PnBA-tpy$_{11}$ with 0.5 eq. Cu(II) were applied. Similarly to the sample containing 0.5 eq. Cu(II), a significant mismatch is obtained for the lowest frequencies at T = 0°C. This discrepancy is attributed to the difference of temperature dependence between the Rouse and the sticky regime.

Then, for $T > 20$°C, the dynamic moduli were shifted with special emphasis on superposition in the low-frequency region. This procedure results in losing a part of the superposition in the window of frequency spreading from around 10^{-3} to 10^{-5} rad/s. These failures could be caused by the difference of activation energies between the reptation motion of the chains and the relaxation of the clusters. The presence of three regimes with different temperature dependences makes difficult to build reliable mastercurves across a broad frequency range. As explained by Cui *et al.*,[126] errors of the shifting obtained at each

temperature accumulates, which can result in a widely inaccurate positioning of the data. Consequently, the mastercurves shown in Figure 8 should only be used as a guide to differentiate the different regimes of relaxation.

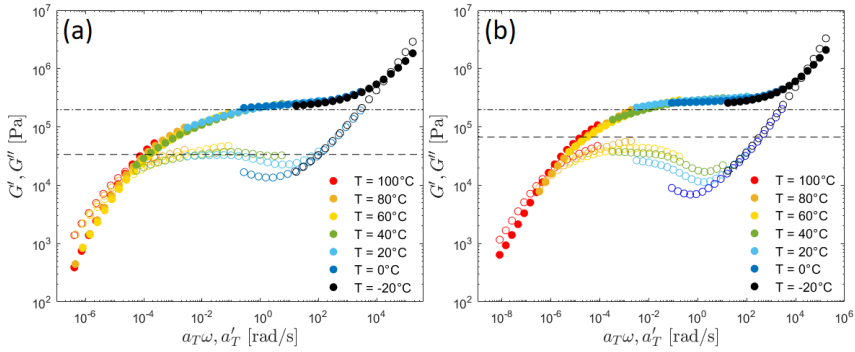

Figure 5.13: Pseudo-mastercurve of PnBA-tpy$_1$1 with (a) 1.5 eq. Cu(II) and b) 2.5 eq. Cu(II) at T_{ref} = 20°C. The dashed-dotted line corresponds to the value of the plateau modulus obtained for the sample 0.5 eq. Cu(II). The dashed line corresponds to the difference between the value of the plateau modulus of the sample with 0.5 eq. Cu(II) and the value of the plateau modulus of the sample (a) 1.5 eq. Cu(II) and (b) 2.5 eq. Cu(II).

Nonetheless, it is possible to evaluate the onset of the relaxation of the aggregates. The system containing 0.5 eq. Cu(II) ideally corresponds to the case where all ligands are involved in bis-complexes, without the presence of aggregates. Therefore, by subtracting the value of the plateau modulus of this systems from that of the systems containing 1.5 and 2.5 eq Cu(II), we can obtain a rough estimate of the extra-stress resulting from the presence of the aggregates. The dashed lines depicted in Figure 5.13 represents this stress contribution. According to the hierarchical sequence of relaxation mechanisms proposed by Semenov and Rubinstein,[111] above the dashed lines and below the rubbery plateau, the relaxation is caused by the reptative motion of the chains.

Using Equation 5.28 and considering the shifts obtained at temperatures T $\geq$ 60 °C, which should roughly correspond to the regime of relaxation of the aggregates, an activation energy of 99 kJ/mol or 146 kJ/mol was evaluated for

the samples containing 1.5 eq. Cu(II) or 2.5 eq. Cu(II), respectively.

5.4.1.4 Modeling the linear viscoelastic responses

To fit the data of the reference material and the supramolecular polymers, the classical TMA developed by van Ruymbeke *et al.*[1] and the sticky TMA detailed in section 5.3 were employed, respectively. In both cases, polydispersity in molecular weight was incorporated using a log-normal distribution, following a similar approach as described in Chapter 4. The resulting relaxation modulus was converted to the frequency domain using the Schwarzl approximation.[254]

As shown in Figure 5.14, a good agreement is found between the prediction of the TMA and the linear response of the reference sample. To achieve the fit, the values of the parameters of the tube model were set as follows: M_e = 18 kg/moland, G_N^0 = 160 kPa and τ_e = 0.025 s. The values of M_e and G_N^0 are consistent with the values used in the work of Zhuge *et al.* [241].

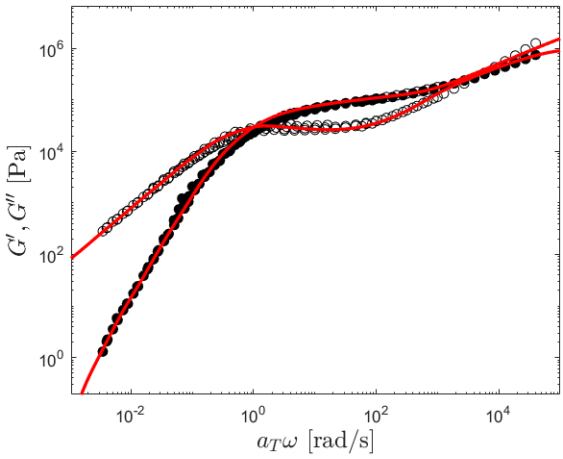

Figure 5.14: Linear viscoelastic response of PnBA-tpy11 at T_{ref} = 20 °C. The solid line corresponds to the prediction of the extended TMA.

Figure 5.15 displays the fits of the pseudo-mastercurves for the metallo-supramolecular polymers. The two approaches for hindered CLF presented in section 5.3.3 were employed, and these fits were obtained using the same values of M_e, G_N^0, and

τ_e as the reference sample. The remaining fitting parameters can be found in Table 5.15.

As observed, the TMA incorporating the sticky CLF provides a decent fit of the data. In contrast, the TMA which includes stepwise fluctuations tends to overestimate the relaxation in the plateau modulus region, particularly for the sample containing 0.25 eq. Zn(II). It is also worth noting that the data obtained from the samples containing 0.25 eq. Zn(II) and 0.5 eq. Zn(II) do not exhibit the small shoulder as predicted by the stepwise CLF. This shoulder originates from the stop condition mentioned in equation 5.23). This mismatch between the data and the model likely arises from the excessively abrupt nature of the stop condition.

As observed in Table 5.15, the resulting values of M_s for the samples containing a density of ions equal to and above the stoichiometric ratio are slightly higher than the value of $M_s = 10.7$ kg/mol obtained by NMR. The difference may be attributed to the presence of topological defects in the supramolecular networks. In addition, as explained in Chapter 4, overlooked contributions of the stress relaxation in the model could be associated to the diffusion of the closed stickers in the compliant network. Introducing such mechanisms would certainly improve the fitting but it would also increase the complexity of the model.

Moreover, it is observed that significant discrepancies persist in the plateau modulus region especially for the sample with 0.5 eq. Cu(II). While according to the model, no relaxation of molecular segments larger than M_S occurs before τ_S, it seems, from the experimental results, that this is not corresponding to the real case. This discrepancy could be due to the presence of a spectrum of τ_S. This hypothesis is reinforced by the fact that the terminal regimes of the experimental LVE are broader than the predictions (except for the 0.25 eq. Zn(II)). The presence of a distribution can be justified following the ideas developed by Rubinstein and Semenov.

This method yields the best fits with values of p_{free}, ranging from 0.05 to 0.01.

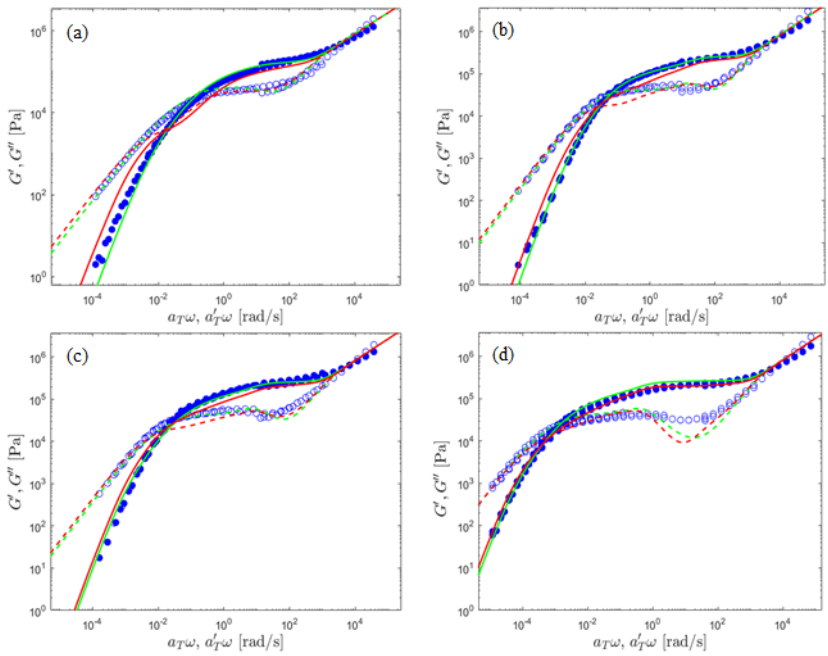

Figure 5.15: Linear viscoelastic response of PnBA-tpy11 at $T_{ref} = 20\,°C$ with (a) 0.25 eq. Zn(II) b) 0.5 eq. Zn(II) c) 0.75 eq. Zn(II) and d) 0.5 eq. Cu(II). The solid lines correspond to the prediction of the extended TMA with stepwise fluctuations (red) and sticky CLF (green).

	M_s [kg/mol]	τ_S^{stic}	p	τ_S^{step}
0.25 eq. Zn(II)	28	0.18	0.05	0.7
0.5 eq. Zn(II)	15	0.09	0.02	0.09
0.75 eq. Zn(II)	13	0.19	0.01	0.17
0.5 eq. Cu(II)	15	3.6	0.02	4

Table 5.5: Fitting parameters used in Figure 5.15. τ_S^{stic} and τ_S^{step} correspond to the sticker lifetime using the sticky CLF and stepwise fluctuations, respectively.

Figure 5.16 compares the model predictions with the data of Gold *et al.*[127] Based on the linear response of the reference sample shown in panel (a), a value of 4.5 kg/mol for M_e and of 300 kPa for G_N^0 were determined using the classical TMA. These values were then utilized in the modeling of the associative PI.

As observed, the sticky reptation model captures accurately the double plateau observed in the experiments. However, a significant mismatch is obtained in the high frequency plateau, where the model predicts insufficient relaxation. This discrepancy can be attributed to the limitations of equation 5.3, which assumes an uniform distribution of the stickers along the chains and neglect the spatial fluctuations of the bounded stickers. Additionally, in the second plateau region, the model incorporating stepwise fluctuations also fails to predict sufficient relaxation. This limitation arises because the relaxation process is effectively frozen by the stop condition defined in equation 5.23.

As shown in Figure 5.17, when the stop condition is removed, the fitting for the PI - 84k - U1 sample significantly improves. This suggests that the discrepancy may arise from the excessively abrupt nature of the stop condition. Finally, the model fails at describing experimental data at low frequencies as, in this region, the experimental G' and G'' deviate from the expected power law dependence of two and one, respectively. This deviation suggests the presence of long lifetime aggregates in the polymers of Gold *et al.*[127]

Figure 5.18 presents the fitting of the ionomers of Kim *et al.*[242] The parameters M_e and G_N^0 of these ionomers are set to the same values as those of a PS melt, which are $M_e = 15$ kg/mol and $G_N^0 = 160$ kPa. In panel (a), the supramolecular polymer exhibits a viscoelastic response similar to that of an unentangled associative polymer with a wide sticky Rouse ramp. This behavior arises because the polymer has a small number of entanglements ($Z_e \approx 5$) and a large number of stickers ($Z_S \approx 38$). The sticky reptation model moderately captures this trend, providing a reasonable description of the data.

Moving on to panel (b), the system possesses a much higher number of entanglements, resulting in a more pronounced second plateau. Here, the TMA model does not capture accurately the transition between the two plateaus. As observed, the slope in this range is slighly lower than the expected slope of 0.5 as predicted by the sticky Rouse theory.

The fitting parameters used to fit the responses of the polymers of Kim *et al.*[242] and Gold *et al.*[127] are presented in Table 5.15.

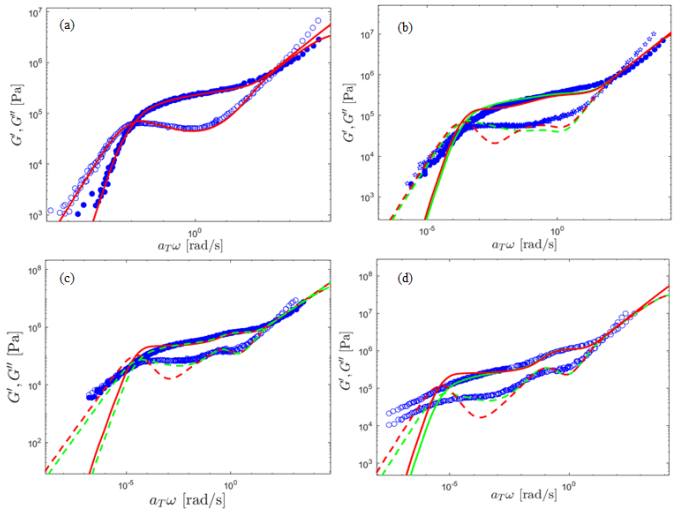

Figure 5.16: Linear viscoelastic response of (a) PI - 84k, (b) PI - 84k - U1, (c) PI - 84k - U2 and (d) PI - 84k - U3 at T_{ref} = -30 ℃. The solid lines correspond to the predictions of the extended TMA with stepwise fluctuations (red) and sticky CLF (green).

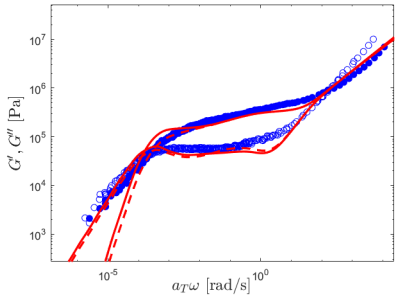

Figure 5.17: Linear viscoelastic response (blue symbols) of PI - 84k - U1 at T_{ref} = -30 ℃. The predictions of the extended TMA with stepwise fluctuation with the stop condition (red solid lines) and without the stop condition (red dashed lines) are also shown.

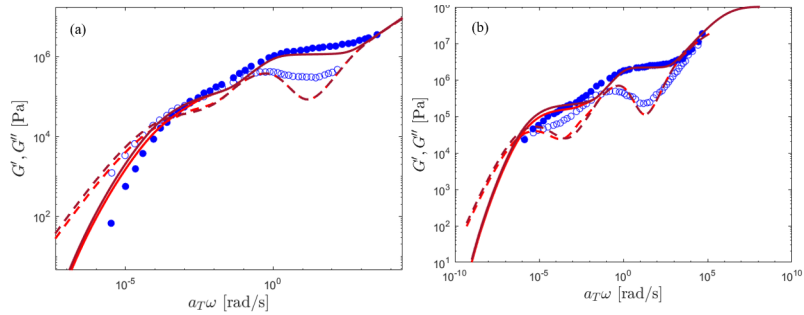

Figure 5.18: Linear viscoelastic response (a) PSMA-108k-3.7%Na and (b) PSMA-445 K-3.8%Na at T_{ref} = 160 ℃. The predictions of the extended TMA with stepwise fluctuations with the stop condition (dark red) and without the stop condition (red) are also shown.

	M_s^{th} [kg/mol]	M_s [kg/mol] -	τ_e	τ_S^{stic}	p	τ_s^{step}
PI - 84k	-	-	0.02	-	-	-
PI - 84k - U1	5.9	6	0.06	2.4	0.02	2.4
PI - 84k - U2	3.1	2.5	0.25	3	0.05	3
PI - 84k - U3	1.6	1.5	2.3	8	0.1	8
PSMA-108k-3.7% Na	1.34	3	0.15	1.4	0.1	1.4
PSMA-445 K-3.8 %Na	1.32	2	0.15	1.4	0.1	1.4

Table 5.6: Fitting parameters used in Figure 5.18 and 5.16. τ_S^{stic} and τ_S^{step} correspond to the sticker lifetime using the sticky CLF and stepwise fluctuations, respectively. Additionally, M_s^{th} refers to the M_s computed based on NMR results.

5.4.2 Conclusion

In this work, we conducted rheological measurements on entangled linear poly(n-butyl acrylate) (PnBA) chains functionalized with terpyridine side groups. By introducing divalent ions (Zn(II) and Cu(II)), we were able to create metallo-supramolecular networks. The magnitude of the rubbery plateau and the longest relaxation time were modulated by varying the ion concentration in the polymeric systems. We observed that both properties increase with the amount of ions until reaching a constant and stable value when the stoichiometric amount was exceeded. However, at very high concentrations (above 1.5

eq. for Cu(II)), the relaxation time and the rubbery plateau experienced a significant increase once again. We explained the existence of last regime by the formation of large aggregates of stickers in the samples.

Then, we extended the TMA initially developed to predict the linear viscoelasticity of polymer melts to entangled associative polymers with sticky-side group and binary associations. The modifications were based mainly on the sticky reptation model developed by Leibler *et al.*[109] Two distinct approaches to model the CLF hindered by the dynamics of the stickers were proposed. The resulting sticky TMA model were used to fit the linear response of the PnBA polymers and literature data. While the model provides a good description of the data, a significant mismatch still persists in the rubbery plateau. Accountinf for a distribution of lifetimes and allowing the pairs of closed stickers to diffuse over a certain length would allow to refine the theoretical curves. This sticky TMA could form a basis for predicting the linear rheology of polymers of different architectures and with more complex distribution of molar masses.

Chapter 6

Linear and nonlinear viscoelasticity of unentangled metallo-supramolecular polymers with pendant groups

In this chapter, we conducted linear and nonlinear shear measurements on unentangled metallo-supramolecular polymers. The viscoelastic responses observed in these systems display intriguing characteristics, including an unusually high rubbery plateau, transient strain hardening behavior, and a yield strain that remains independent of the applied strain rate. These features are discussed in relation to the molecular theories outlined in the introduction of this manuscript.

6.1 Introduction

In this chapter, we examine the linear and nonlinear rheological responses of unentangled metallo-supramolecular polymers. Concentrating the investigations on unentangled systems allows to eliminate the complex dynamics resulting from the entanglements.

Extensive research has already been dedicated to understand the linear dynamics of such polymers. An illustrative instance is the formulation of the sticky Rouse model, which captures accurately experimental data of polymers featuring pairwise associations or small clusters of stickers, as demonstrated in Chapter 4. Nonetheless, there remains fundamental questions about the rheological properties of the systems containing large aggregates of stickers. Notably, a comprehensive understanding of the mechanical reinforcement generated by sticker aggregation remains incomplete.[116,255] Moreover, despite the proposal of multiple pathways for the relaxation of such systems, a definitive sequence for the relaxation has not yet been firmly established.[112]

In comparison to the linear regime of associative polymers, the nonlinear regime in shear flow has received much less attention. Nevertheless, various studies conducted in this regime have unveiled intriguing features.

First, a steady shear thickening region has been observed at moderate strain rates in telechelic and nontelechelic associative systems.[132–135,139] In the literature, this shear thickening behavior has been attributed to several factors, including non-Gaussian stretching of the network strands,[136] increase of interchain associations at the expense of intrachain associations,[139] emergence of spatial heterogenities in the connectivity network,[140] and repulsive interaction between micelles.[142] However, it is important to note that the shear thickening is not universally present in nontelechelic polymers. For exemple, studies conducted by Zhang *et al.* in the molten state,[143] or by Tirtaatmadja *et al.*[256] and Pellens *et al.*[257] in solutions only revealed shear thinning.

Moreover, associative polymers nearly always display deviations from the Cox-Merz rule, even in absence of shear thickening.[257] In most cases, the steady

shear data are found to surpass the corresponding dynamic data.[134,257,258] According to Pellens *et al.*, this discrepancy originates from the fact that shear flow affects the structure of associative polymers in a different manner than in conventional polymeric fluids.[257]

Finally, transient thickening has been observed in startup shear measurements of telechelic and dendronized polymers in the molten state.[258–260] This thickening is followed by an overshoot peak and subsequently an asymptotic decreases towards a steady state. In both instances, the strains at the stress peaks, often referred to as yield strains, are almost insensitive of the applied shear rates. This observation suggests that this strain corresponds to a critical strain for the initiation of force-induced dissociation.

In this chapter, we present a systematic study of the linear and nonlinear shear properties of unentangled metallosupramolecular PnBA. Similar to Chapter 5, the networks are crosslinked using various densities of Zn(II) and Cu(II) ions. These polymeric materials are employed to critically examine the aforementioned features observed in the rheological responses of associative polymers and to investigate their temperature dependences.

6.2 Materials and experimental details

6.2.1 Linear sticky PnBA-co-PTPA random copolymer

In this study, short linear poly(n-butyl acrylate) (PnBA) chains functionalized with terpyridine (tpy) functionalized are investigated. They were synthetized with low polydispersity using RAFT polymerization in a previous work of Lyons.[261] The intended molar mass of the chains was designated to remain less than twice the average molar mass between two entanglements of pure PnBA, a value established as 18 kg/mol in the study of Zhuge *et al.*[241] This approach ensures that the chains remain in an unentangled state

The structural parameters of the copolymers are summarized in Table 6.1. The molar mass, the polydispersity index (Đ), the number of functional groups per chains were determined by size-exclusion chromatography (SEC) and Nuclear

Magnetic Resonance (NMR).[261]

Name of of the sample	M_n [kg/mol]	Đ	Functional groups/chain	T_g [℃]
PnBA25k-7Tpy	27.5	1.18	7	-48
PnBA25k-11Tpy	24.5	1.18	11	-40

Table 6.1: Structural parameters of unentangled PnBA functionalized with tpy groups

6.3 Sample preparation

The supramolecular gels were prepared using a procedure similar to the one detailed in Chapter 5.

The composition of the resulting MSBP is summarized in Table 6.2.

	Metal ion content
PnBA25k-7Tpy + $ZnCl_2$	0.75 eq. 1 eq.
PnBA25k-11Tpy + $ZnCl_2$	0.25 eq. 0.5 eq. 0.75 eq. 1 eq.
PnBA25k-11Tpy+ $CuCl_2$	0.5 eq.

Table 6.2: Composition of PnBA polymers functionalized with tpy ligand

6.4 Rheometry

Rheological experiments were conducted using the ARES-2000 (TA Instruments, DE) rheometer. Both linear and nonlinear shear measurements were carried out utilizing a cone-partitioned plate (CPP) geometry.

The experimental procedure involved several steps. Once the sample was loaded, it was equilibrated for 20 minutes at 130 ℃. Then, the linear viscoelastic responses were assessed at temperature ranging from 130 to -10 ℃. To achieve this, the classical approach was followed: after thermal equilibration, a strain

sweep was achieved to determine the linear viscoelastic region. This was followed by a frequency sweep spanning a frequency range of 0.1 - 100 rad/s. For temperatures below 25 ℃, the cooling was performed under N_2 atmosphere. Finally, step-rate experiments were conducted at shear rates spreading from 0.1 to 100 s^{-1} and at temperature ranging from 60 to 25 ℃.

6.5 Results and discussion

6.5.1 Linear rheology

Figure 6.1 presents the LVE response of the precursors PnBA25k-11Tpy in presence or not of Zn(II) metal ions at temperatures ranging from 0 to 80 ℃. As expected, the physically crosslinked networks exhibit a rubbery plateau, which is absent in the unentangled reference sample. Furthermore, both the longest relaxation time and the magnitude of the rubbery plateau increase monotonically with the addition of Zn(II) ions, even beyond the stoichiometric amount. Lastly, similar to the findings in Chapter 5, the segmental relaxation is delayed as the density of Zn(II) ions increases. This effect is evident in the LVE plots of the samples at T = 0 ℃.

Much like the associative polymers presented in Chapter 4 and 5, the polymers studied in this chapter demonstrate two distinct temperature dependencies in their linear rheological responses. The high frequency region of the dynamic moduli is governed by the segmental motion of the chains, whereas the low frequency region is dominated by the association dynamics. These two distinct temperature dependencies are well illustrated in Figure 6.2, which displays the linear responses of the PnBA27k-7Tpy containing 1 eq. Zn(II). These responses have been frequency-shifted to achieve superposition at high frequencies (panel (a)) and at low frequencies (panel (b)).

By following the procedure outlined in Chapter 4, the mastercurves and pseudo-mastercurves of the unentangled polymers containing Zn(II) ions have been constructed. These curves are presented in Figure 6.3 and 6.4.

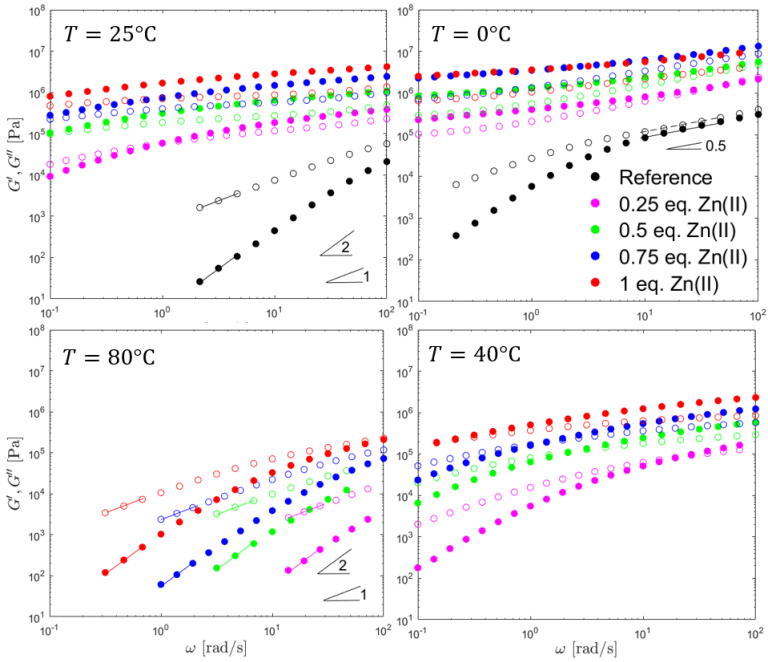

Figure 6.1: Linear viscoelastic response of PnBA25k-11Tpy at different temperatures

As indicated by the solid black lines in Figure 6.3, the plateau observed for PnBA25k-11Tpy with 0.75 eq. and 1 eq. of Zn(II) ions significantly exceeds the value $G^0_{N,el} = \frac{\rho RT}{M_s}$. This value corresponds to the maximum contribution of the elastically active chains to the rubbery plateau. Consequently, the magnitude of the plateau suggests the presence of another mechanism contributing to the elasticity. Potential causes of this reinforcement might be related to the stretching of the network strands and/or the presence of large aggregates of stickers.[111]

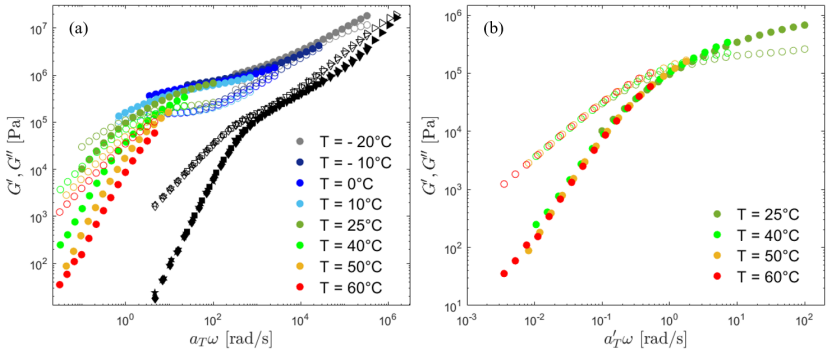

Figure 6.2: Linear viscoelastic responses of PnBA25k-7Tpy, crosslinked with 1 eq. Zn(II) and non-crosslinked at T_{ref} = 25 °C. In panel (a), the linear responses of the associative polymer have been shifted using the same shift as that of the reference material indicated by the black symbols. In panel (b), the responses have been shifted to achieve overlapping at high temperature.

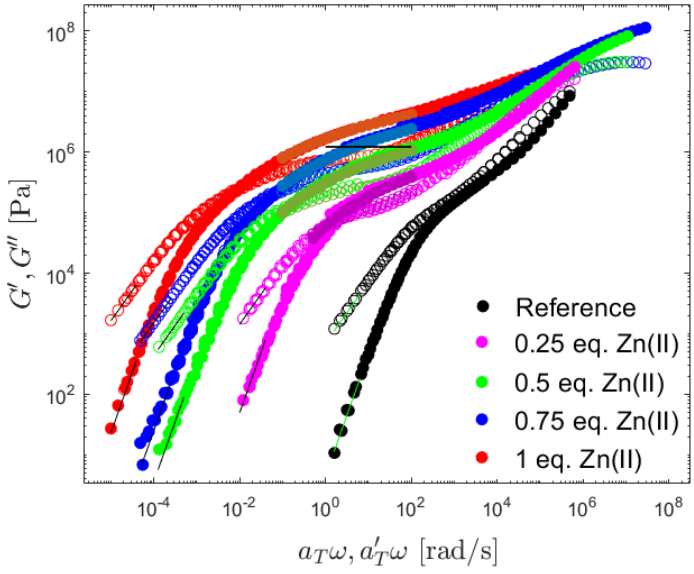

Figure 6.3: Pseudo-mastercurves of PnBA25k-11Tpy crosslinked or not with Zn(II) ions at T_{ref} = 25 °C. Data of the associative polymers measured at T_{ref} are represented in dark colors.

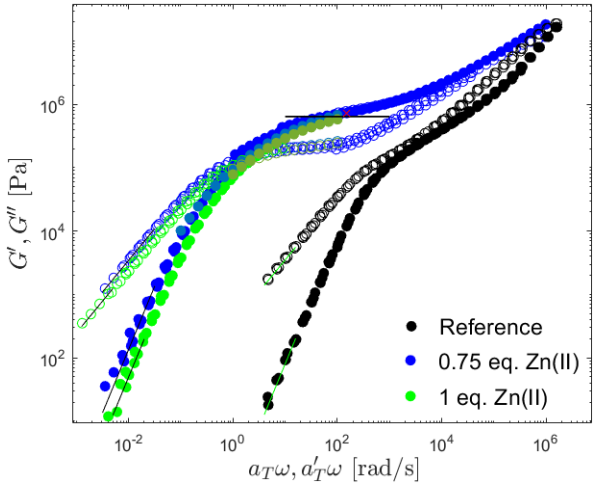

Figure 6.4: Pseudo-mastercurves of PnBA25k-7Tpy crosslinked or not with Zn(II) ions at $T_{ref} = 25$ °C. Data of the associative polymers measured at T_{ref} are represented in dark colors.

In contrast, as shown in Figure 6.4, the plateau obtained for PnBA27k-7Tpy at similar densities of Zn(II) ions is much closer to $G^0_{N,el}$. This distinction is even more apparent in Figure 6.5. As observed, although the linear viscoelastic responses of the precursor chains are similar, substantial differences in viscoelasticity arise upon the introduction of Zn(II) ions.

The thin solid lines which fit the terminal regime of the mastercurves and pseudo mastercurves represent the asymptotic behavior of $G' \propto \omega^2$ and $G'' \propto \omega$. From these lines, the weight average relaxation time τ_w can be estimated using the following equation.

$$\tau_w = \lim_{\omega \to 0} \left[\frac{G''}{\omega G''} \right] \tag{6.1}$$

The resulting values of τ_w can be found in Table 6.4 presented in Appendix. Figure 6.6 illustrates the variation of τ_w with the ion content, revealing that an exponential law describes rather well this evolution. This result would support the notion that the terminal flow behavior of these polymeric systems is

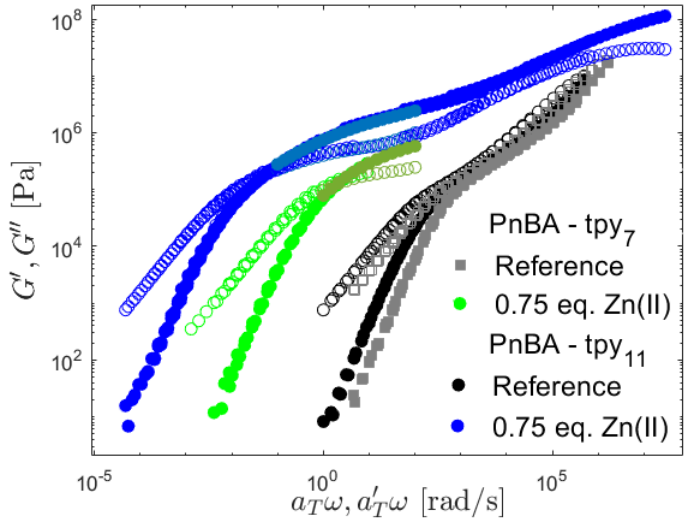

Figure 6.5: Comparison of the pseudo-mastercurves and the mastercurves of PnBA27k-7Tpy and PnBA25k-11Tpy polymers at T_{ref} = 25 °C.

predominantly governed by the dynamics of aggregates. However, the quadratic scaling predicted by the sticky Rouse theory also exhibits a satisfactory fit. At present, there is not enough data to definitively favor one option over the other.

Figure 6.7 presents the shift factors a_T and a'_T used for constructing the pseudo-mastercurves of the Zn(II)-based networks. As shown in panel (a), the predictions of the WLF equation closely align with the shift factors of the reference material, as well as with those obtained at low temperature with the associative polymers. Additionally, panel (b) demonstrates that the activation energy E_a associated with the terminal regime increases with the amount of Zn(II) ions. The computed values of E_a are provided in Table 6.3.

In addition to the presence of aggregates, the increase in E_a can be attributed to the limited number of potential partners N_{part} available for detached stickers. In a study by Cui *et al.*,[126] it was demonstrated that N_{part} scales with the square root of the number of Kuhn segments between two associative groups. In our specific case, the average number of Kuhn segments between two ter-

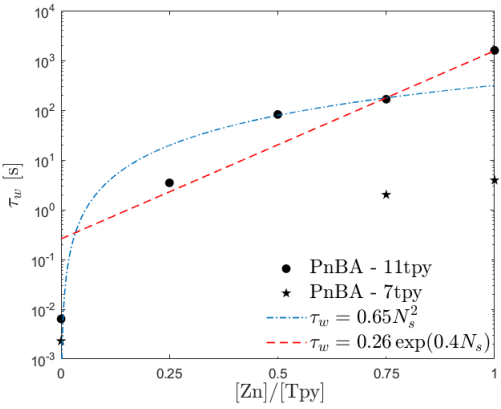

Figure 6.6: Evolution of the longest relaxation times of the polymeric systems with the ion content. The red and blue curves were obtained using a best fitting procedure.

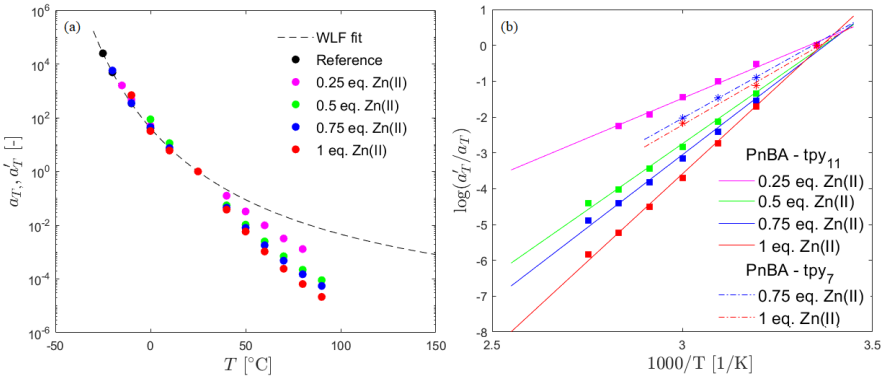

Figure 6.7: (a) Shift factors a_T and a'_T used to build (pseudo)-mastercurves shown in Figure 6.3. The black solid line shows the prediction of the WLF equation with c_1 and c_2 (b) Shift factors a'_T expressed a function of temperature

	1 eq.	0.75 eq.	0.5 eq.	0.25 eq.
PnBA25k-11Tpy	81.4	67.6	61.5	36.9
PnBA25k-7Tpy	51.2	49.4	-	-

Table 6.3: Activation energies of Zn(II)-containing associative unentangled PnBA-co-PTPA copolymer

pyridine groups is approximately $\frac{M_s}{M_K} \approx 2.8$ and 5.6 in PnBA - 11tpy and PnBA - 7tpy, respectively, considering that M_K is approximately equal to 700 g/mol.[55]

The scarcity of potential partners may imply that the simultaneous dissociation of multiple neighboring junctions is necessary to change partners. In the scenario of a fully cooperative disassociation of n stickers, it can be expected that $E_a \approx nE_a^*$ where E_a^* is the activation energy corresponding to the dissociation of one single bond.[262] In Chapter 5, it was demonstrated that the activation energy of entangled PnBA-tpy crosslinked with Zn(II) ions, and with a large spacing between the stickers, is around 27 kJ/mol. Assuming that E_a^* takes this value, n ranges from 1.4 to 3. However, it is important to note that these values of n serve as an upper bound, as the formation of aggregates can also contribute to the increase in the activation energy.

On a different note, the slowdown of the segmental relaxation due to the presence of the stickers can also be caused by the rigidity of the stickers. As the stiffness of the network strand increases, its size gets larger and the corresponding longest relaxation time rises.

Panel (a) of Figure 6.8 exhibits the linear response of PnBA-11tpy with a stoichiometric amount of Cu(II) ions, shifted using the WLF equation. Over the temperature range of $T = -10$ to 40 °C, the behavior of the sample is similar to that of the Zn(II)-based networks. In this range, the Cu(II)-based network exhibits a Rouse ramp, followed by a long rubbery plateau spanning several frequency decades. Then, as the temperature increases, the storage modulus starts to decrease again. This decrease remains moderate and is mitigated at low frequencies. Finally, at $T = 130$°C, the sample transitions into a liquid-like state, with the loss modulus surpassing the storage modulus. It is important to note that the sample is not fully relaxed within the experimental temperature range, as both G' and G'' do not exhibit a slope of 2 and 1, respectively.

Clearly, it is evident that constructing a pseudo-mastercurve is not possible. Ghiassinejad *et al.* also observed a similar behavior in a study involving short hydrogenated polybutadiene chains capped with terpyridine ligands

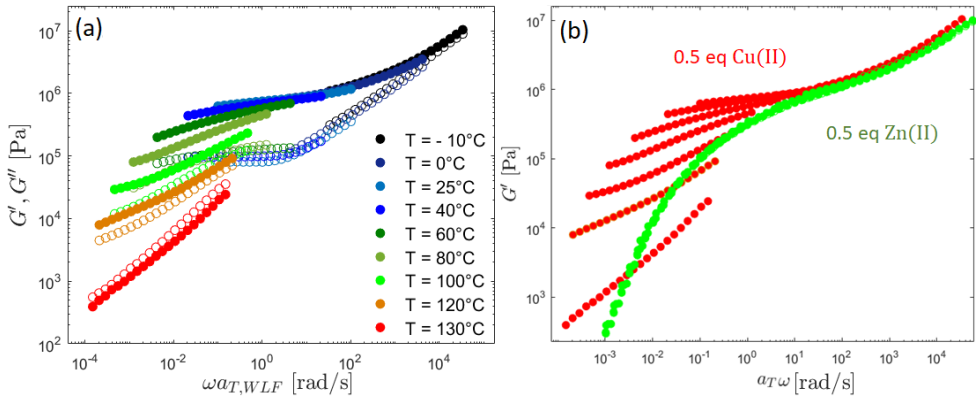

Figure 6.8: (a) Linear response of PnBA25k-11Tpy crosslinked with 0.5 eq. Cu(II) and frequency-shifted using the prediction of the WLF equation. (b) Comparison of the storage moduli of PnBA25k-11Tpy crosslinked with 0.5 eq. Cu(II) (red) and 0.5 eq. Zn(II) (green). For the system containing 0.5 eq. Zn(II), the pseudo-mastercurve is shown.

and crosslinked with Zn(II) (see Figure 1.34).[120] Through SAXS analysis, they observed that the metal complexes phase-separated in a highly organized lamellar structure. This crystalline structure acts as permanent crosslinks and thus prevents the polymer from fully relaxing. While less important, a similar phenomenon is believed to occur in our sample. The thermorheological complexity observed at low frequencies would therefore be due to the combined effects of the structural evolution of the aggregates and the dissociation dynamics.

In panel (b) of of Figure 6.8, it is shown that the introduction of Cu(II) ions does not result in any significant reinforcement when compared to polymers that contain Zn(II) ions. This absence of reinforcement could be caused by an insufficient proportion of micro-phased domains in the polymeric material and probably, the absence of well-ordered structure.

6.5.2 Nonlinear rheology

In this section, the results of the step-rate experiments are presented and analyzed.

Figure 6.9 displays the stress growth coefficient $\eta^+(t)$ of the reference materials PnBA25k-7Tpy and PnBA25k-12Tpy at different shear rates, juxtaposed with the corresponding linear responses. The strain rates are given in terms of Rouse Weissenberg numbers $Wi_R = \dot{\gamma}\tau_w$.

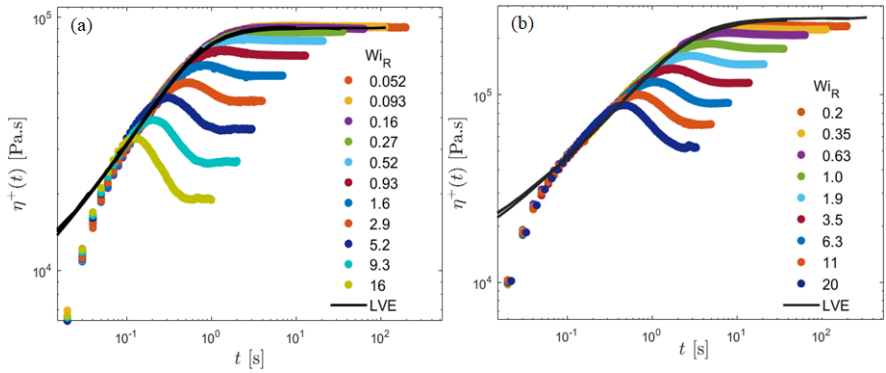

Figure 6.9: Transient shear viscosity at T = -10 °C of (a) PnBA25k-7Tpy, (b) PnBA25k-11Tpy at various nondimensional shear rates (Wi_R).

As expected, when Wi_R is significantly less than 1, $\eta^+(t)$ closely aligns with the linear viscoelastic response. Nonetheless, substantial deviations from the linear viscoelastic envelope can still be observed at short times due to the limitations in the time resolution of the rheometer. When subjected to higher shear rates, both unentangled melts demonstrate a transient and steady shear-thinning behavior. This behavior is consistent with previous studies where nonlinear shear measurements were performed on unentangled PS melts.[263,264]

As shown in Figure 6.10, the introduction of transient crosslinking units in an unentangled melt leads to significant modifications of its nonlinear shear response. The sticky polymers exhibit transient shear thickening. This finding stands in stark contrast to recent nonlinear shear data reported by Zhang *et al.*,[143] who investigated unentangled poly(vinyl alcohol) (PVA) crosslinked by borax in aqueous solutions. In their study, the sticky polymers demonstrate moderate thinning behavior without exhibiting any overshoot peaks. In contrast, transient shear hardening has been observed in studies involving telechelic associative polymers both in solutions[132,133] and in the molten state[260] as well

as dendronized polymers with UPy moieties in the molten state.[259]

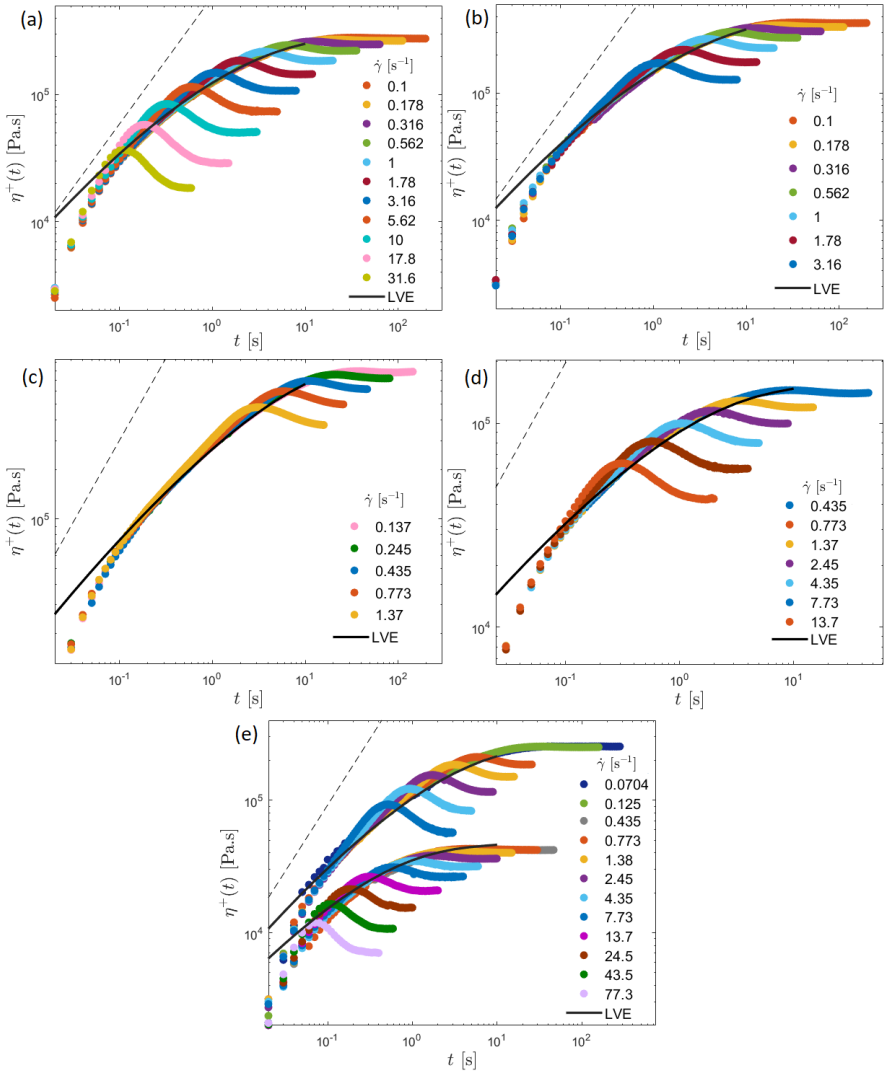

Figure 6.10: Stress growth coefficient of (a) PnBA25k-7Tpy (a) with 0.75 eq. Zn(II) and (b) with 1 eq. Zn(II) at T = 25 °C as well as of PnBA25k-12Tpy with (c) 1 eq. Zn(II) (d) 0.75 eq. Zn(II) and (e) 0.5 eq. Zn(II) at T = 50 °C at various shear rates (Wi_R). In panel (e), the response at T = 40 °C is also shown. The dashed represents the baseline $\eta^+(t) = G_N^0 t$.

The dashed lines in Figure 6.10, represent the baseline behavior $\eta^+(t) = G_N^0 t$, and thus depict the response of an ideal linear elastic solid. As the shear rates increase, the stress growth function approaches this baseline. Nevertheless, it consistently remains below it due to the relatively slow imposed shear rates $\dot{\gamma}$ compared to the rate of dissociation of the stickers τ_s^{-1}. This indicates that the supramolecular networks experience significant relaxation at these shear rates.

In Figure 6.11, the shear stress is expressed as a function of the shear strain. In panel (a), it can be observed that for the reference samples, the strain γ_{max} at the stress peak, often called the yield strain, increases with the strain rates. This behavior stands in contrast to the behavior for transient networks shown in panel (b), where γ_{max} remains relatively unaffected by the shear rates. This finding is consistent with previous studies on telechelic associative polymers, which have shown a similar trend.[132,258] The difference in behavior reflects the presence of distinct physical mechanisms governing the flow of the samples.

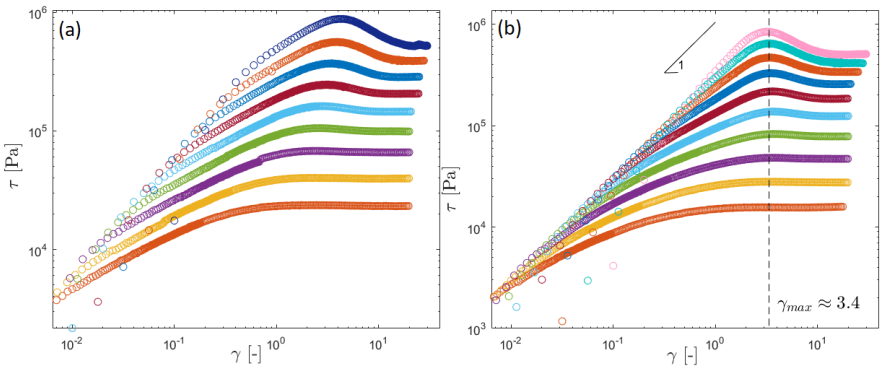

Figure 6.11: Transient shear stress as a function of strain for (a) PnBA25k-12Tpy at T = -10 °C and (b) PnBA25k-7Tpy with 0.75 eq. Zn(II) at T = 25 °C.

Concerning the reference samples, the stress peak is closely associated with the finite extensibility of the chains, the flow-induced reduction of the monomeric friction ζ and possibly the breakdown of the fluctuation-dissipation theorem

under flow.[78] Figure 6.12 shows the evolution of γ_{max} with the shear rates, revealing a power-law behavior with exponents of 0.14 and 0.17 for PnBA27k-7Tpy and PnBA25k-11Tpy, respectively. These values can be compared to the exponent value of 0.33 reported by Costanzo *et al.* obtained for PS unentangled and entangled melts.[45,264] The observed non-universal scaling may be attributed to differences in the potential for reduction of friction among the chemically distinct melts. Indeed, Masubuchi *et al.* demonstrated that PnBA melts were less prone to ζ-reduction compared to PS melts. This difference was attributed to the presence of flexible side chains in the PnBA backbone, which screen the interactions between the backbone segments.[67]

In telechelic polymers, γ_{max} is commonly regarded as the critical strain at which the network undergoes significant alteration due to force-induced bond dissociation.[258,259] However, in our specific case, as depicted in Figure 6.10, the stress overshoots are obtained at strain rates slower than the dissociation rate, suggesting that the stickers can already detach by thermal disassociation. Therefore, the underlying cause of the overshoot is likely to be more complex.

In the panel (b) of Figure 6.12, it can be observed that γ_{max} ranges from 3 to 5. Surprisingly, it is observed that γ_{max} does not vary significantly with changes in ion density. Furthermore, despite having a smaller mesh size, the network based on PnBA chains that contain 11 pendant terpyridine groups exhibit greater resistance to deformation compared to those with 7 terpyridine units. This enhanced resistance in the PnBA25k-11Tpy systems might be due to the development of microphases which contribute to the formation of stronger supramolecular bonds.

Further insights into the overshoot can be gained by examining the ratio of the peak viscosity η_{max} to the steady-state viscosity η_{st}, commonly referred to as the fractional overshoot. In the literature, this ratio is regarded as a measure of the mechanical coherence of the networks and thus provides valuable information about the ability of the network to accomodate large deformation.[258,265] As observed in Figure 6.13, the fractional overshoot increases with the introduction of ions. This increase can be attributed to the formation of stickers

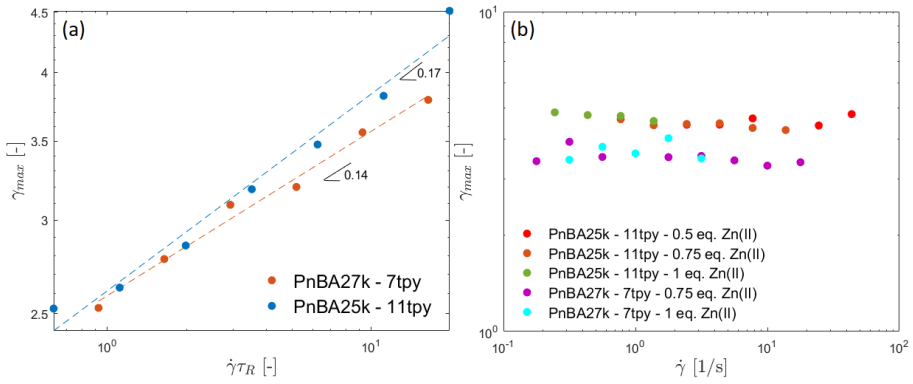

Figure 6.12: Comparison of γ_{max} for (a) the precursors and (b) the associative polymers. Panel (a) presents data collected at T = -10 ℃, while in panel (b), γ_{max} values for PnBA27k-7Tpy and PnBA25k-11Tpy were obtained at T = 50℃ and T = 25℃, respectively.

with longer lifetime. As observed in panel (b) of Figure 6.13, all the data exhibit an increasing trend, following a power law with an exponent of 0.16. A similar exponent was obtained in metallosupramolecular assemblies based on entangled telechelic star polymers and crosslinked with Zn(II), Cu(II) or Co(II) ions.[258] Furthermore, entangled PS melts exhibit a slightly higher power law exponent (0.2),[45] while PI entangled star polymers demonstrate a much lower exponent of 0.05.[266]

While the references appear to obey the Cox-Merz rule within experimental error, this empirical rule is not valid anymore for the transient networks as shown in Figure 6.14. The steady shear data are systematically larger than the dynamic data within the experimentally accessible shear rates window. In the literature, the failure of this rule is almost systematic in associative polymers.[257]

Interestingly, the steady-state viscosities of the different samples demonstrate a universal dependence as shown in Figure 6.15. Notably, all these viscosities follow a power law with an exponent close to -0.5. This value is similar to the slope found in unentangled PS melt.[267]

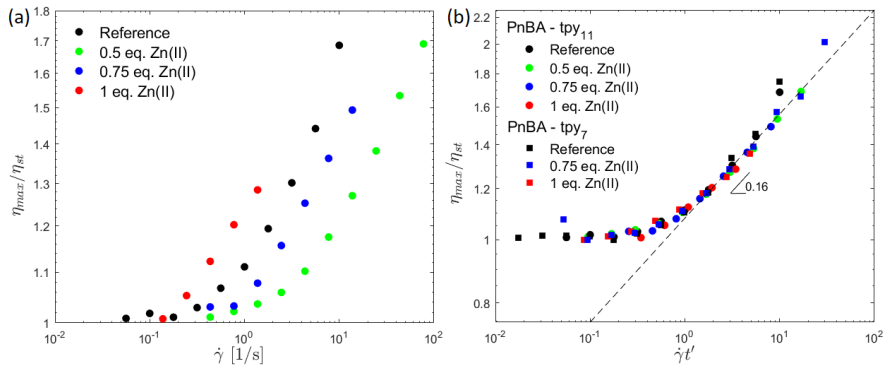

Figure 6.13: (a) Fractional viscosity overshoot of PnBA25k-11Tpy as a function of the strain rate. (b) Master curve of the fractional overshoots. Data of the references are shown at T = -10 ℃, of associative PnBA25k-7Tpy at 25 ℃ and associative PnBA25k-11Tpy at 50 ℃. The time t' is an empirical shift factor.

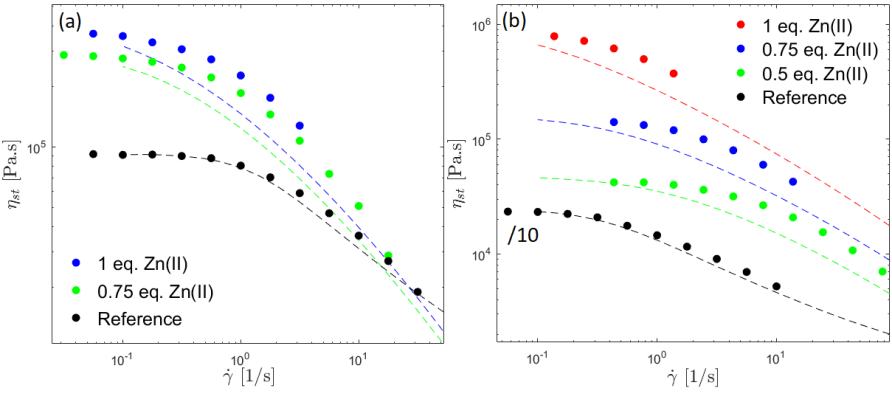

Figure 6.14: Assessment of the Cox-Merz rule for (a) PnBA27k-7Tpy and (b) PnBA25k-11Tpy both with and without Zn(II) ions. Data for the associative systems are presented at (a) T = 25 ℃and (b) at T = 50 ℃, while the data for reference materials are displayed at T = -10 ℃. Additionally, data for the reference material shown in panel (b) has been downshifted by one decade for improved clarity.

Finally, TTS principle has been evaluated for PnBA25k-11Tpy using 0.5 and 0.75 eq. Zn(II) ions. The nonlinear responses of these samples were mea-

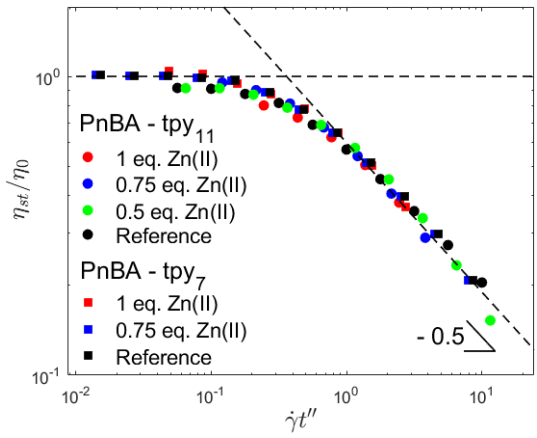

Figure 6.15: Normalized steady state viscosity η_{st}/η_0 as a function of the normalized shear rates $\dot{\gamma}t'$. The time t'' is an empirical shift factor.

sured at 40 and 50 °C, and subsequently shifted using the shift factors $a_T = \frac{\eta_0(T = 40°C)}{\eta_0(T = 50°C)}$. Surprisingly, as shown in Figure 6.16, the shifted data coincide, indicating that the temperature dependence of $\eta^+(t)$ within this restricted temperature window is the same as that of thermal dissociation. Note that the part governed by the segmental motion of the chains cannot be probed experimentally as it involves very short timescales.

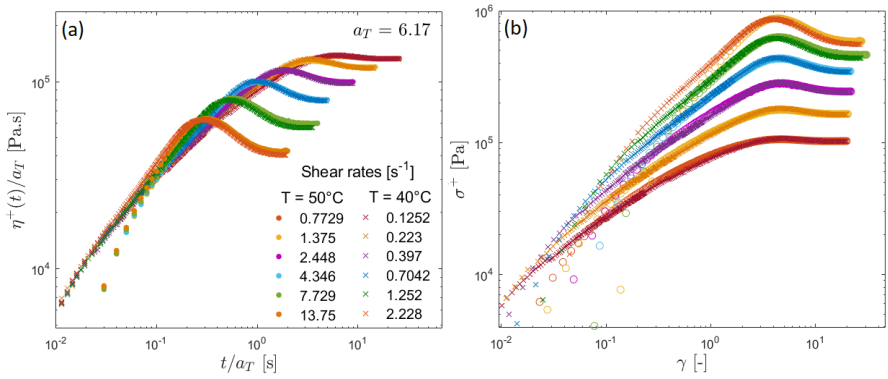

Figure 6.16: Evaluation of TTS principle in nonlinear shear flow for PnBA25k-11Tpy with 0.75 eq. Zn(II). Both plots share a common legend.

6.6 Conclusion

In summary, we investigated the viscoelastic properties of unentangled PnBA chains with terpyridine side groups positioned along the backbone and crosslinked using Zn(II) or Cu(II) ions.

The linear viscoelastic responses of the supramolecular networks displayed the anticipated behavior of transient networks, featuring a rubbery plateau whose magnitude increased with ion concentration, followed by terminal relaxation. Surprisingly, at high ion concentrations, the magnitude of the rubbery plateau exceeded predictions from the rubber elasticity theory. This lead us to conclude that the polymeric system underwent microphase separation.

Moving into the nonlinear regime of deformation, the presence of supramolecular bonds caused transient shear hardening behaviour. Interestingly, the yield strain γ_{max} was noted to remain nearly unaffected by changes in strain rates, a behavior previously observed in telechelic associative polymers. Moreover, the associative polymers displayed comparable shear thinning compared to their neutral precursors. Finally, TTS principle was surprisingly found to hold true in a moderate temperature window.

Overall, this study contribute to the limited pool of nonlinear data available for sticky polymers in the molten state. Further investigations are necessary to explore the impact of key parameters such as the morphology, the association strength and the temperature on nonlinear rheology.

Appendix

Relaxation times

The values of the relaxation times τ_w are shown in Table 6.4.

Sample	PnBA25k-11Tpy	PnBA25k-7Tpy
Reference	6.4×10^{-3}	2.3×10^{-3}
0.25 eq. Zn(II)	3.47×10^{0}	-
0.5 eq. Zn(II)	8.22×10^{1}	-
0.75 eq. Zn(II)	1.66×10^{2}	2×10^{0}
1 eq. Zn(II)	1.59×10^{3}	3.91×10^{0}

Table 6.4: Relaxation times of the associative polymers studied in this chapter.

Values of the empirical factors

The values of the empirical shift factors t' and t'' are shown in Table 6.5.

Sample	t'	t''
PnBA25k-11Tpy	1	1
PnBA25k-11Tpy - 0.5 eq. Zn(II)	4.6	6.7
PnBA25k-11Tpy - 0.75 eq. Zn(II)	1.7	3.6
PnBA25k-11Tpy - 1 eq. Zn(II)	0.4	0.55
PnBA25k-7Tpy	3.2	3.7
PnBA25k-7Tpy - 0.75 eq. Zn(II)	0.6	2.25
PnBA25k-7Tpy - 1 eq. Zn(II)	0.65	1.14

Table 6.5: Values of the empirical shift factors t' and t''.

Chapter 7

Orthogonal superposition rheology of polymeric melts

In this chapter, we present and validate the design of a novel rheometer tool tailored for conducting orthogonal superposition measurements on polymer melts. The design is derived from a prototype developed by Thomas Schweizer at ETH Zurich.

7.1 Introduction

While the linear viscoelastic behavior of polymer melts has been deeply studied and is rather well understood, the nonlinear regime is still a matter of discussion and many questions remain unanswered. For example, the origin of shear thinning in unentangled polymer melts has not been fully elucidated. In the current picture, the decrease of the steady-state shear viscosity of such systems is explained using a bead-spring model with a spring constant κ, a friction coefficient ζ of the monomeric units and a Brownian force intensity B, that

deviate from their equilibrium values. However, the precise way these parameters evolve is still not well understood, primarily due to a lack of experimental data.[74–77,267]

In order to investigate the nonlinear shear responses of polymeric melts, various experimental approaches can be employed. These approaches encompass techniques measuring time-domain functions such as stress relaxation, start-up shear flow experiments or creep experiments. Additionally, there are methods that enable frequency-dependent measurements such as large amplitude oscillatory shear (LAOS) or superposition rheology techniques.[9]

LAOS involves applying a nonlinear sinusoidal deformation to a material and observing its resulting stress response over time. In contrast to SAOS where the stress response remains sinusoidal, LAOS induces higher harmonics in the stress output due to nonlinearities. Consequently, LAOS results cannot be analyzed in terms of storage and loss moduli. Instead, numerous approaches have been developed in the literature to understand LAOS. These approaches include studying the amplitude of the odd harmonics present in the output signals or examining the Lissajous curves of the measured stress versus strain. However, the complex kinematic history associated with LAOS makes it highly challenging to interpret the stress response in molecular terms.[268]

On the other hand, the superposition rheology technique uses much simpler kinematics, allowing to bring a better understanding of the stress output based on the molecular mechanisms. The principle of this technique is to superimpose a small oscillatory perturbation to a system already subjected to nonlinear steady shear flow. The perturbation can be applied either parallel or perpendicular to the main flow direction (see Figure 7.1).[269]

In the case of parallel superposition (PSR), the main and superimposed flows are strongly coupled, posing challenges in evaluating a linear perturbation spectrum. Consequently, the observed parallel moduli $G'_{\parallel}$ and $G''_{\parallel}$ not only depend on the relaxation spectrum but also on how it evolves with the shear rates. In some cases, this coupling effect can even result in negative values for $G'_{\parallel}$ and $G''_{\parallel}$. However, at high frequencies, the moduli are less affected by the main

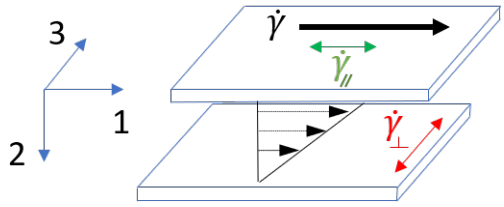

Figure 7.1: Illustration of the principle of superposition rheology.

flow, enabling some degree of interpretation.[269–271]

On the other hand, in orthogonal superposition (OSR), both flows are effectively decoupled, making it easier to correlate the observed relaxation spectrum with the molecular relaxation behavior.[269,271]

In the past, OSR instruments developed by Simmons,[272] Mewis and Schoukens,[273] and Zeegers *et al.*[274] required complex mechanical construction and were limited in their applicability to low viscous fluids and a relatively narrow viscosity range. In 1997, Vermant *et al.* made a significant advancement by modifying the closed loop system of a force-rebalanced transducer in a commercial rheometer, allowing the generation of an axial oscillatory motion. Additionally, they developed a novel flow cell design which consists of a double-walled Couette cell which is open at the bottom to prevent pumping flow. These developments allowed to successfully perform OSR measurements on polymeric solutions.[275] Subsequently, the OSR technique was integrated into commercial rheometers such as the strain-controlled ARES-G2.[276]

OSR measurements performed on solutions of melts revealed a decrease in the longest relaxation times, along with a monotonic drop in the OSR moduli. These findings were initially discussed in the context of phenomenological models such as the Wagner I model[269] or the Leonov model.[277,278]

However, subsequent investigations shifted their focus towards the application of tube-based models. First, Mead computed analytical solutions for the OSR moduli using the MLD model. Nevertheless, a notable limitation in his derivation is the assumption of negligible chain stretching.[279] Recently, Zhang *et*

al. evaluated the OSR moduli using the Rolie-Poly and the Rolie-Double-Poly models, this time incorporating chain stretching. In their analysis, they demonstrated that the perturbation spectra obtained at different shear rates can be shifted onto a single master curve. The horizontal and vertical shift factors employed to build these master curves were found to be dependent on the level of chain stretching and on a parameter governing the effectiveness of CCR. Furthermore, they also established that such master curves could be generated for a broader class of constitutive models, which include the DCR-CS (double-convection-reptation model with chain stretch) model of Marrucci and Ianniruberto.[280,281]

Finally, it is worth noting that, while the time-shear rate superposition (TSRS) principle has not yet been experimentally validated in the context of polymeric systems, it has been effectively observed in colloidal systems.[282–284]

In this chapter, the design of a novel rheometer tool which aims to perform OSR measurements on polymer melts is presented. The tool is intended to be used with an ARES-G2 rheometer. The principle is based on a prototype developed and built by Dr. T. Schweizer at ETH Zurich. The design is subsequently validated using computational fluid dynamics (CFD) simulations in COMSOL multiphysics. Finally, in the last part of this chapter, the molecular model developed by Sato *et al.*[75] for unentangled melts is analyzed. Our analysis reveals that this model predicts the validity of the TSRS principle. Moreover, we have demonstrated that the rate-dependent shift factors employed in constructing the master curves allow to quantify the evolution of the spectrum of relaxation times as well as the breakdown of the fluctuation-dissipation theorem with Wi_R.

7.2 Design of the rheometer tool

An annular Couette-type geometry is used to superimpose the oscillatory flow with the steady-state shear flow. The flow cell, as depicted in Figure 7.2, comprises two coaxial cylinders, with the polymeric fluid flowing in the gap between them. The inner cylinder rotates to generate the steady shear flow, while the

outer cylinder oscillates in the axial direction to produce the perturbation flow. This configuration ensures that both flow components are applied orthogonally, and results in a well-controlled and consistent flow pattern. Additionally, the design incorporates reservoirs at both ends of the annular gap to delay the onset of edge fracture of the polymeric fluid in the actual flow cell.

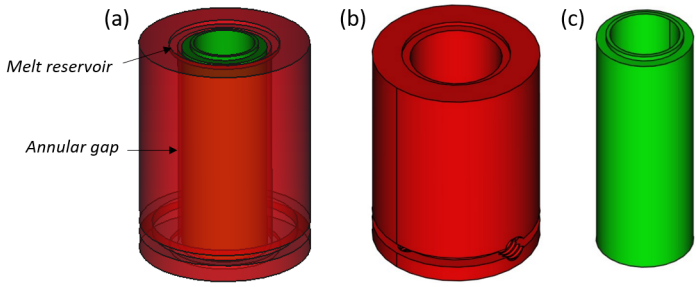

Figure 7.2: Annular Couette cell geometry for orthogonal superposition rheometry. The assembled cell (a), the inner cylinder (b) as well as the outer cylinder (c) are represented. For the sake of clarity, the holes have been omitted in (a).

Both cylinders are connected to the drive units of an ARES-G2 rheometer through two shafts, as illustrated in Figure 7.3. The inner cylinder is directly screwed to the lower shaft, while the outer cylinder is secured to the upper shaft using two small screws.

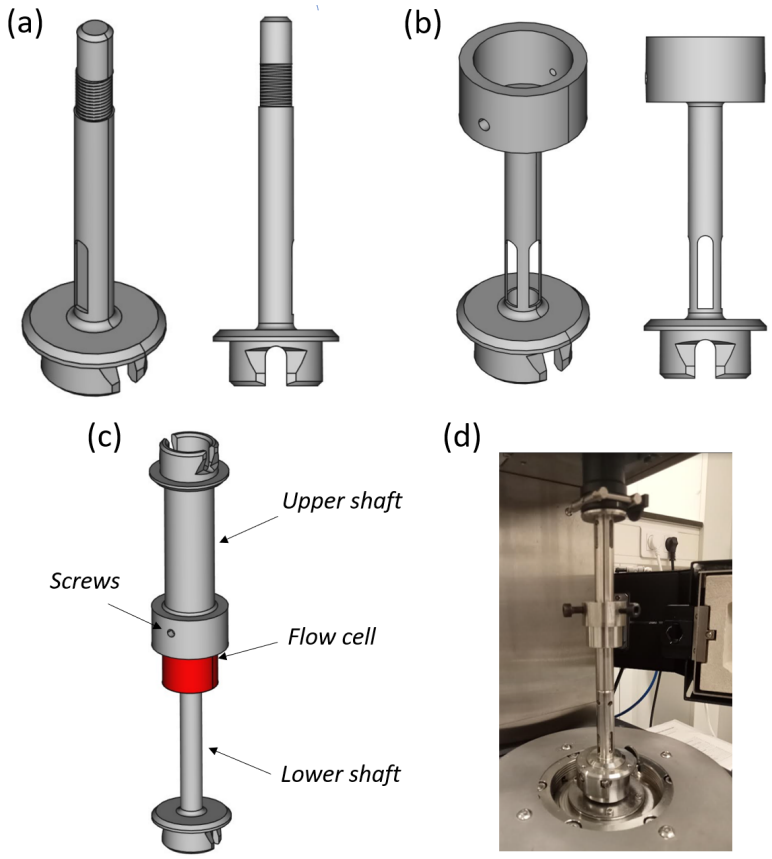

Figure 7.3: The lower shaft (a), the upper shaft (b), as well as the assembly (c) of the orthogonal rheometer tool are shown. Additionally, a photo of the assembly is presented (d).

Before conducting the measurement, it is necessary to fill the gap between the coaxial cylinders with the polymeric material. To achieve this, the loading setup shown in Figure 7.4 is used. In addition to the inner and outer cylinders shown in Figure 7.2, this setup includes six additional pieces which are depicted in Figure 7.5.

Figure 7.4 illustrates the step-by-step procedure for loading the sample:

1. In the first step, the cavity in the bottom of the outer cylinder is filled

with 0.5 g of polymeric powder. A metallic plate (in bronze) that is screwed to the bottom of the outer cylinder prevents the polymer material from escaping. Afterwards, a vacuum pump is connected to the setup via the vacuum inlet of the vacuum chamber. The assembly is then placed in a hot press, where the temperature is set above the T_g of the polymer. Waiting for approximately 15 minutes is crucial at this stage to ensure that the temperature throughout the setup becomes uniform and to effectively remove any bubbles that may be present in the polymeric fluid.

2. Subsequently, the spacer (in blue) is pressed down with the help of the hollowed bar (in orange). The spacer obstructs the vacuum inlet and ensures that the inner and outer cylinders remain concentric.

3. After removing the hollowed bar, pressure is applied to the auxiliary insert (in red). This insert, which is screwed to the inner cylinder, is a tool that replaces the upper shaft during the loading process. It is also worth-mentioning that the cylinders are positioned on a support, which guarantees that the setup remains in the accurate position while undergoing pressing.

4. Finally, the polymer enters the annular gap and expels the spacer. When the inner cylinder makes contact with the metallic plate, no further force is applied. At this point, the cooling is switched on, and the vacuum pump is switched off. Subsequently, the auxiliary insert, metallic plate, and vacuum chamber are unscrewed from the cylinders, while the spacer and support are manually taken out.

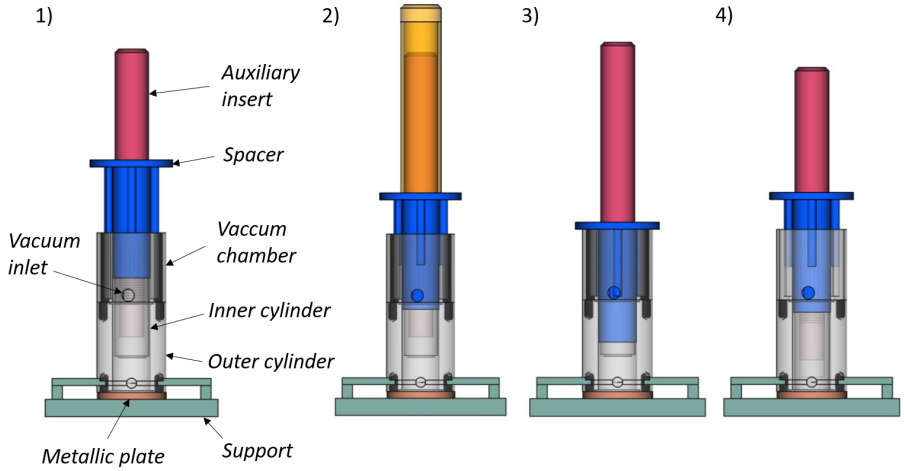

Figure 7.4: Step-by-step procedure for filling the flow cell with polymeric melt.

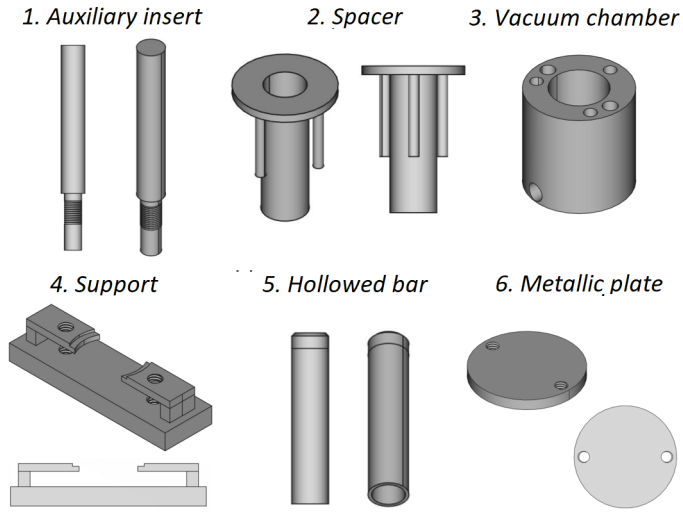

Figure 7.5: Components employed during the loading process.

7.3 Equations of the flow

7.3.1 Main flow

In the case of a narrow gap size, the curvature becomes negligible, making it possible to treat the geometry as that of parallel plates. This assumption remains valid when the ratio $\delta = R_0/R_i$ is close to 1. Here, R_0 and R_i represent the radii of the outer and inner cylinders, respectively.

Under these conditions, both the shear stress and the shear rate can be regarded as uniform throughout the gap. This simplification greatly facilitates the determination of the true viscosity versus shear rate curve. To evaluate this flow curve, the equations of the Narrow Gap Couette (NGC) geometry are applied, which are internationally standard for measuring the non-Newtonian viscosity of polymers.[285] These equations are summarized in Table 7.1. Here, M_i and N_{rev} indicate the measured torque and rotation speed expressed in rev/s and in [N · m], respectively. The values of the geometric factors of our flow cell are also shown.

Shear parameters	Geometric factors	Conversion equations
$\dot{\gamma}$ [1/s]	$K_{\dot{\gamma}} = 2\pi \frac{\delta^2+1}{\delta^2-1} = 66.123$	$\dot{\gamma} = K_{\dot{\gamma}} \times N_{rev}$
$\tau_{r\theta}$ [Pa]	$K_\tau = \frac{1}{2\pi R_i^2 L_{cyl}} \frac{1+\delta^2}{2\delta^2} = 232550$	$\tau_{r\theta} = K_\tau \times M_i$
η_{st} [Pa · s]	$K_\eta = \frac{K_\tau}{K_{\dot{\gamma}}} = 3516.9$	$\eta_{st} = K_\eta \times \frac{M_i}{N_{rev}}$

Table 7.1: Equations of the main flow. ($R_i = 5$ mm, $\delta = 1.1$, $L_{cyl} = 25$ mm)

7.3.2 Perturbation flow

Regarding the perturbation, a pure laminar annular Couette flow is assumed. The corresponding equations are presented in Table 7.2.

Shear parameters	Geometric factors	Conversion equations
$\gamma_{\perp}$ [-]	$K_{\gamma}^{\perp} = \dfrac{1}{R_0 \ln\left(\frac{R_0}{R_i}\right)} = 1907.6$	$\gamma = K_{\gamma}^{\perp} \times z_0$
$\tau_{\perp}$ [Pa]	$K_{\tau}^{\perp} = \dfrac{1}{2\pi R_0 L_{cyl}} = 1157.5$	$\tau_{\perp} = K_{\tau}^{\perp} \times F_0$
$G'_{\perp}$ [Pa · s]	$K_{G'}^{\perp} = \dfrac{K_{\tau}^{\perp}}{K_{\gamma}^{\perp}} = 0.6068$	$G'_{\perp} = K_{G'}^{\perp} \times \dfrac{F_o}{z_0}\cos(\phi)$
$G''_{\perp}$ [Pa · s]	$K_{G''}^{\perp} = \dfrac{K_{\tau}^{\perp}}{K_{\gamma}^{\perp}} = 0.6068$	$G''_{\perp} = K_{G''}^{\perp} \times \dfrac{F_o}{z_0}\sin(\phi)$

Table 7.2: Equations of the perturbation flow. (R_i = 5 mm, δ = 1.1, L_{cyl} = 25 mm)

7.4 COMSOL Simulations

Experimental errors arise due to the presence of melt reservoirs at both ends of the annular gap. To account for this effect in the equations of the flow, end-effect factors can be introduced as corrections.[286] To determine the appropriate values for these correction factors, flow profiles of different incompressible fluids were simulated using the Computational Fluid Dynamics (CFD) module in COMSOL Multiphysics. The laminar flow interface was selected to perform time-dependent analyses. This interface effectively solves the Navier-Stokes equations as well as the continuity equation for conservation of mass. Additionally, the air-liquid interface was treated as a stress-free boundary, whereas a no-slip condition was assumed at the walls of the flow cell. A representation of the 3D model used for the simulation is shown in Figure 7.6. HereA Newtonian fluid with a viscosity of 10^5 Pa.s is subjected to shear by moving the outer walls at a velocity of 30×10^{-3} mm/s. The color legend represents the shear rates.

First, a Carreau fluid was sheared by rotating the outer walls at different speeds.

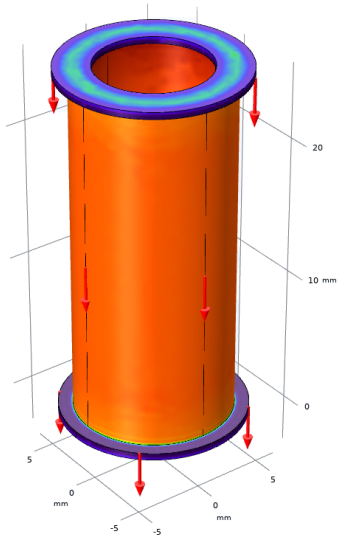

Figure 7.6: Illustration of the 3D model used for the CFD simulations. Here a fluid is subjected to shear by moving downwards the outer walls.

The resulting force was determined by integrating the stress in the corresponding direction over the outer walls. By applying the conversion equations presented in Table 7.1, an estimation of the viscosity of the fluid was obtained. As shown in panel (a) of Figure 7.7, this prediction yielded a relative error of 16.25% in the Newtonian plateau compared to the actual value of the viscosity. However, the relative error was found to decrease in the shear thinning region. As it is seen in panel (b), the error is primarily caused by the shear flow generated by the motion of the horizontal (horiz) and vertical (edges) walls of the reservoirs. By removing the reservoirs, a much more accurate prediction of the viscosity is achieved, resulting in a relative error of approximately 2%.

To account for the end-effects, K_τ can be adjusted using a correction factor c_L. The resulting corrected geometric factor K_τ^{corr} can be expressed as follows:

$$K_\tau^{corr} = \frac{K_\tau}{c_L(n)} \tag{7.1}$$

Here, c_L is assumed to depend on the power law index n which can be evaluated

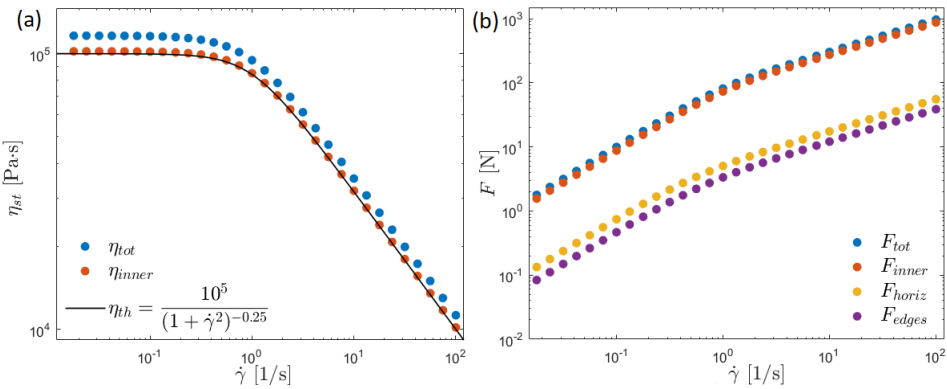

Figure 7.7: (a) Steady-state viscosity predictions for a Carreau fluid. (b) Contributions of the different surfaces to the total force.

through the derivative of the torque with respect to the rotation speed of the outer cylinder.

$$n = \frac{d\ln(M_i)}{d\ln(2\pi N_{rev})} \tag{7.2}$$

The values of c_L, which are shown in Figure 7.8, have been determined by examining the velocity profile of power-law fluids with different n. For reference, PS melts were reported to exhibit shear-thinning properties with n ranging from around 0.2 to 0.5.[45,263,264] This range corresponds to c_L values of approximately 1.09 and 1.12, respectively. These values are to be compared with the values of 1.16 obtained in the Newtonian plateau.

Subsequently, the inner walls were oscillated at a frequency of 1 rad/s at various strain amplitudes z_0. As shown in Figure 7.9, using the equation presented in Table 7.2 results in a negligible error of less than than 2%. Consequently, there is no requirement for introducing an orthogonal end-effect factor.

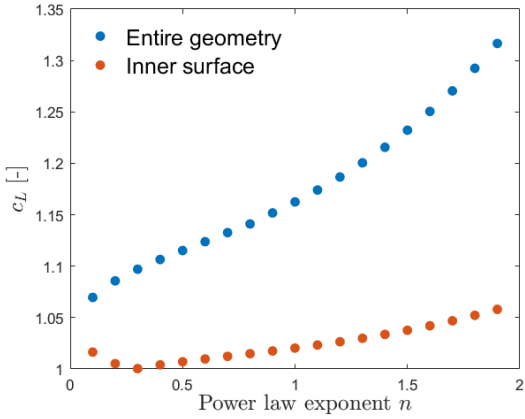

Figure 7.8: Values of c_L computed from simulations using a power-law fluids with a vicosity equal to $\eta = 10^5 \times \dot{\gamma}^{n-1}$ Pa $\cdot$ s.

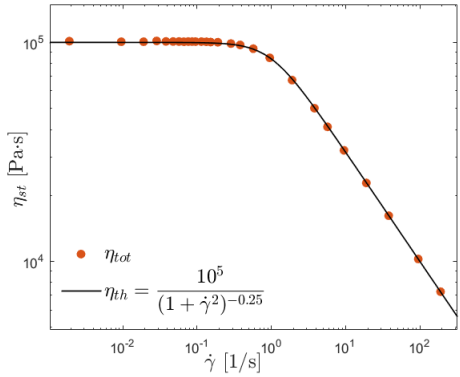

Figure 7.9: Steady-state viscosity predictions for a Carreau fluid. The inner walls are oscillating at a frequency of 1 rad/s and at different strain amplitudes z_0.

7.5 Analysis of the OSR moduli of unentangled polymeric melts

In this section, the model proposed by Sato *et al.*[75] for unentangled melts is used to predict the OSR moduli. To achieve this, the same procedure as that of Zhang *et al.* is followed.[280] The first part involves the computation of an

analytical solution through a linear perturbation analysis. In the second part, the results are validated by numerically solving the constitutive equation of Sato *et al.*

7.5.1 Linear perturbation analysis

According to the bead-spring model of Sato *et al.*, the stress response of an unentangled melt is governed by the following equations:[75]

$$\tilde{\boldsymbol{\sigma}} = \sum_{p=1}^{N} \tilde{\boldsymbol{\sigma}}_p(t)\theta_p \tag{7.3}$$

$$\tilde{\boldsymbol{\sigma}}_p(t) = \frac{3(N+1)}{2g} r_\kappa(t) \tilde{\boldsymbol{A}}_p(t) \tag{7.4}$$

$$\tilde{\boldsymbol{A}}_{p(1)}(t) = -\frac{1}{\tilde{\tau}_p(t)} \tilde{\boldsymbol{A}}_p(t) + \frac{g}{3\theta_1} \left(\frac{2}{N+1} \right) \frac{r_B}{r_\zeta^2} \boldsymbol{I} \tag{7.5}$$

In the above equations, $\tilde{\boldsymbol{\sigma}} = \dfrac{\boldsymbol{\sigma}}{\nu k_B T}$, $\tilde{\tau}_p(t) = \dfrac{r_\zeta}{2\theta_p r_\kappa}$ and $\theta = 4\sin^2\left(\dfrac{p\pi}{2(N+1)}\right)$ are the dimensionless stress tensor, dimensionless relaxation time for the p^{th} mode, and the p^{th} eigenvalue of the Rouse matrix A_{nm} (see section 1.7), respectively. Additionally, r_B, r_ζ and r_κ denote the ratio of the values of B, ζ and κ at time t to their respective equilibrium values. Finally, $\tilde{\boldsymbol{A}}_{p(1)}$ designates the upper-convected derivative of the tensor $\tilde{\boldsymbol{A}}_p$.

In OSR rheometry, the fluid is subjected to an axial steady shear flow as well as an orthogonal perturbation flow. The velocity gradient tensor is therefore given by:

$$K_{ij} = \begin{pmatrix} 0 & \dot{\gamma}_0 & 0 \\ 0 & 0 & 0 \\ 0 & \dot{\gamma}_\perp & 0 \end{pmatrix} \tag{7.6}$$

Here, $\dot{\gamma}_0$ represents the shear rate of the steady-state flow, while $\dot{\gamma}_\perp = \dot{\gamma}_{\perp,0}\omega\cos(\omega t)$ indicates the shear rate of the perturbation flow. The amplitude $\dot{\gamma}_{\perp,0}$ flow should be kept minimal to stay in the linear perturbation regime.

The mathematical procedure for deriving the expression of the OSR moduli is explained by Zhang *et al.*[280] It consists of applying a linear perturbation to the constitutive equation with a parameter $\epsilon = \frac{\dot{\gamma}_\perp}{\dot{\gamma}_0}$. Given that the intermediate tensor $\tilde{\mathbf{A}}_p$ is linearly proportional to $\tilde{\boldsymbol{\sigma}}$, the following expressions can be written:

$$A_{ij}(t,\epsilon) = A_{ij}(t,0) + \epsilon \frac{\partial A_{ij}}{\partial \epsilon}\Big|_{\epsilon=0} + O(\epsilon^2) \tag{7.7}$$

$$\approx A_{ij}^{(0)}(t) + \epsilon A_{ij}^{(1)}(t) \tag{7.8}$$

Here the superscript "(0)" indicates the steady state solution, while the superscript "(1)" represents the first-order perturbation correction.

To evaluate the OSR moduli, the computation of the term σ_{yz} is necessary. This process begins by substituting equation 7.8 into equation 7.5. Then, by differentiating the resulting equation with respect to the perturbation parameter ϵ, the following equation for $A_{yz,p}^{(1)}$ can be obtained.

$$\frac{dA_{yz,p}^{(1)}}{dt} + \frac{A_{yz,p}^{(1)}}{\tau_p} = \dot{\gamma}_{\perp,0}\omega\cos(\omega t)A_{yy,p}^{(0)} \tag{7.9}$$

Solving this differential equation yields the following expression for $A_{yz,p}^{(1)}$

$$A_{yz,p}^{(1)} = \frac{\gamma_e A_{yy,p}^{(0)}\omega^2\tau_p^2}{1+\omega^2\tau_p^2}\cos(\omega t) + \frac{\gamma_e A_{yy,p}^{(0)}\omega\tau_p}{1+\omega^2\tau_p^2}\sin(\omega t) \tag{7.10}$$

Here, the value of $A_{yy,p}^{(0)}$ can be determined by solving the steady-state solution of equation 7.5. Its expression is given by:

$$A_{22,p}^{(0)} = \frac{2g}{3(N+1)}\frac{\tau_p}{\theta_1}\frac{r_B}{r_\zeta^2} \tag{7.11}$$

Injecting equations 7.10 and 7.11 into equation 7.3 results in the following expression for the component $\tilde{\sigma}_{23}(t)$ of the stress tensor:

$$\frac{\tilde{\sigma}_{23}}{\gamma_0} = \frac{r_B}{r_\zeta}\left(\cos(\omega t)\sum_{p=1}^{N}\frac{\omega\tau_{p,eq}}{\left(\frac{r_\kappa}{r_\zeta}\right)+\omega^2\tau_{p,eq}^2} + \sin(\omega t)\sum_{p=1}^{N}\frac{\omega^2\tau_{p,eq}^2}{\left(\frac{r_\kappa}{r_\zeta}\right)^2+\omega^2\tau_{p,eq}^2}\right) \tag{7.12}$$

In the above equation, $\tau_{p,eq}$ refers to the relaxation times obtained at equilibrium.

The OSR storage and loss moduli can thus be expressed as follows:

$$G_\perp^{'} = \nu k_B T\frac{r_B}{r_\zeta}\sum_{p=1}^{N}\frac{\omega^2\tau_{p,eq}^2}{\left(\frac{r_\kappa}{r_\zeta}\right)^2+\omega^2\tau_{p,eq}^2} \qquad G_\perp^{''} = \nu k_B T\frac{r_B}{r_\zeta}\sum_{p=1}^{N}\frac{\left(\frac{r_\kappa}{r_\zeta}\right)\omega^2\tau_{p,eq}^2}{\left(\frac{r_\kappa}{r_\zeta}\right)^2+\omega^2\tau_{p,eq}^2} \tag{7.13}$$

Interestingly, a close inspection of equation 7.14 reveals that the only effect of the flow is to induce horizontal and vertical shifts in the moduli, quantitified by the values $a^* = \frac{r_\kappa}{r_\zeta}$ and $b^* = \frac{r_B}{r_\zeta}$, respectively. The horizontal shift factor a^* describes the evolution of the spectrum of relaxation time with the flow, caused by the finite extensibility of the chains and the reduction of monomeric friction. On the other hand, the vertical shift factor b^* arises due to the deviation from the fluctuation-dissipation theorem.

7.5.2 Numerical validation

To validate the perturbation analysis, the constitutive equation was solved numerically. For the computation, the following forms for r_κ, r_ζ and r_B, as suggested by Sato *et al.*, were employed.[75]

$$r_\kappa(t) = \frac{1-1/g^2}{1-\langle\tilde{u^2}\rangle/g^2} \qquad r_\zeta(t) = \frac{1}{\left(1+\left(\frac{F^{so}}{F_c^{so}}\right)^\alpha\right)^{n/\alpha}} \qquad r_B(t) = 1 \tag{7.14}$$

The function used for r_κ accounts for the non-linearity of the spring and serves as a rough approximation of the inverse Langevin function. Here $\langle\tilde{u^2}\rangle$ represents

the mean square length of the spring, and g corresponds to the number of Kuhn segments in a spring.

Regarding r_ζ, F^{so} stands for the order parameter of the polymeric chains, whereas F_c^{so} corresponds to a critical order parameter. The parameters α and n are additional fitting parameters. When F^{so} falls below F_c^{so}, $\zeta(t)$ reaches its equilibrium value ζ_{eq}. Conversely, when F^{so} exceeds F_c^{so}, $\zeta(t)$ decreases following a power-law behavior. The order parameter F^{so} can be evaluated through

$$F^{so} = \frac{\lambda^2}{\lambda_{max}^2}\sqrt{(S_{xx} - S_{yy})^2 + 4S_{xy}^2} \tag{7.15}$$

In this equation, $\lambda^2 = \langle\tilde{u^2}\rangle/g^2$ represents the stretch ratio of the chain, while S_{ij} denotes the orientation tensor. Both S_{ij} and $\langle\tilde{u^2}\rangle$ are computed based on the conformation tensor $\mathbf{W}$ and its trace. $\mathbf{W}$ given by:

$$\mathbf{W}(t) = \frac{N+1}{2N}\sum_{p=1}^{N}\mathbf{A}_p(t)\theta_p \tag{7.16}$$

From this tensor, S_{ij} and $\langle\tilde{u^2}\rangle$ using the following equations:

$$\mathbf{S} = \frac{\mathbf{W}}{\mathrm{Tr}(\mathbf{W})} \tag{7.17}$$

$$\langle\tilde{u^2}\rangle = \mathrm{Tr}(\mathbf{W}) \tag{7.18}$$

By numerically solving the constitutive equation proposed by Sato *et al.*, the computation of the OSR moduli can be performed using the following equations:

$$G_\perp^{'} = \frac{\sigma_{23,0}^{st}}{\gamma_\perp}\cos\left(\delta^{st}\right) \tag{7.19}$$

$$G_\perp^{''} = \frac{\sigma_{23,0}^{st}}{\gamma_{0,\perp}}\sin\left(\delta^{st}\right) \tag{7.20}$$

Here $\sigma_{23,0}^{st}$ and δ^{st} respectively represent the amplitude of the shear stress and the phase shift between the shear stress and the applied strain. Both quantities are determined when the stress tensor reaches its steady-state.

Figure 7.10 exhibits the predicted OSR moduli at different $Wi_R = \dot{\gamma}\tau_{R,eq}$. As observed, when appropriately shifted, the curves superimpose and form a master curve. This observation further validates the results obtained through the perturbation analysis.

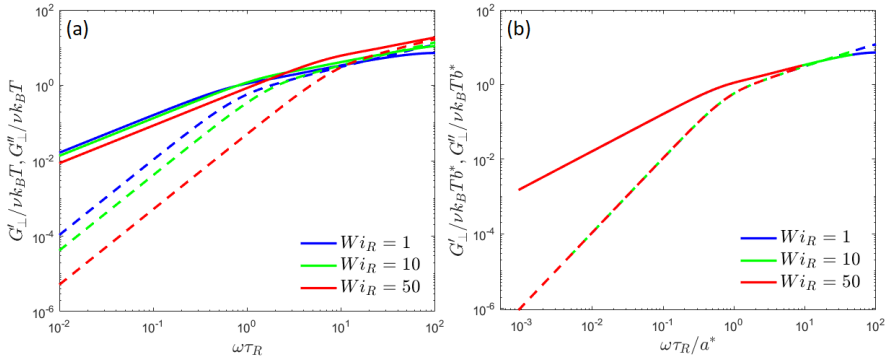

Figure 7.10: (a) Orthogonal superposition moduli at different Wi_R. (b) Application of the TSRS principle. The simulations were performed for $N = 200$, $g = 10$, $\alpha = 4$, $n = 2$ and $F^{so} = 0.1$.

As observed in Figure 7.11, the shifts a^* and b^* monotonously increase with Wi_R.

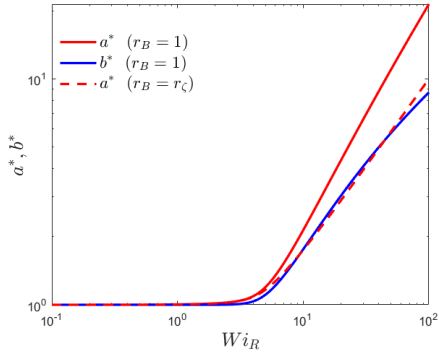

Figure 7.11: Shift factors a^* and b^* as a function of Wi_R. The simulations were performed for $N = 200$, $g = 10$, $\alpha = 4$, $n = 2$ and $F^{so} = 0.1$.

7.6 Conclusion

In this chapter, we have presented the design of a rheometer tool that aims to perform orthogonal superposition measurements on polymeric melts. However, the flow field generated by the flow cell is not perfectly homogeneous, primarily due to the inclusion of reservoirs at the edges of the tool. To address this geometric effect, we determined the values of end-effect factors using CFD in COMSOL Multiphysics. Subsequently, we have used the constitutive equation of Sato *et al.* for unentangled melts[75] to derive analytical expressions of the orthogonal moduli. The resulting expressions reveals the possibility of shifting the viscoelastic spectra obtained at different Wi_R to produce of a master curve. The set of shift factors used to build the master curve allow to quantify the evolution of the spectrum of relaxation times as well as the deviation from the fluctuation-dissipation theorem.

It is worth mentioning that the fabrication of the rheometer tool have recently been completed. In the future, our plan is to conduct measurements on polymeric samples using this newly developed tool to validate its functionality. The successful completion of this validation could contribute to a better understanding of the nonlinear shear rheology of polymer melts.

Chapter 8

Conclusion and perspectives

In this PhD dissertation, we investigated the rheological behavior of linear polymeric melts with well-defined molar mass distribution in simple shear and uniaxial extensional flow. The primary objective of this research was to contribute to the development of more accurate and predictive molecular constitutive equations, which in turn can guide the optimization of processing conditions and the design of polymeric materials. The thesis was organized into three distinct parts: 1) Extensional rheology of polymeric melts, 2) Linear and nonlinear rheology of associative polymers, and 3) Development of a rheometer tool for orthogonal superposition measurements. These parts can be summarized as follows:

Extensional rheology of polymer melts (Chapter 3)

In this part, we explored the extensional responses of PS melts. Specifically, we have shown that the extensional viscosity of bidisperse PS, comprising well-entangled linear chains, scales linearly with the concentration of the chains. However, when the shortest component of the bidisperse melts is substituted

with oligomeric chains, the extensional viscosity exhibits a different scaling law, being proportional to the square root of the concentration of the long chains in the polymeric material. This result was rationalized with the concept of reduction of monomeric friction. By diluting polymeric chains with oligomers, the environment becomes less anisotropic, thus hampering the ζ-reduction mechanism. As a consequence, the flow gains a greater grip on the polymer molecules, leading to increased stretching of the long chains. This result holds significant importance for industrial applications, considering that most industrial processes involve polydisperse polymers.

Linear and nonlinear rheology of associative polymers (Chapter 4, 5 and 6)

Afterwards, we explored the rheological behavior of associative polymers, where the stickers are located as side groups along the chains. This part comprises 3 different chapters.

In Chapter 4, the focus is on the modeling of the linear rheology of unentangled UPy-based supramolecular networks. To capture the response of these polymers, the study employs a "sticky Rouse" model that accounts for a random placement of the stickers as well as a distribution in molar mass. Additionally, the model allows paired junctions to move in space without dissociating, with their displacements described by an ansatz.[186] The model provides a reasonable description of the data. However, further research is needed to validate the ansatz and explore these non-affine spatial fluctuations.

Chapter 5 explores the relaxation dynamics of entangled metallo-supramolecular PnBA functionalized with terpyridine ligand and crosslinked with Zn(II) and Cu(II) ions. Interestingly, these polymers demonstrate a surprising mechanical stability. Specifically, when a moderate excess of Zn(II) ions is introduced, minimal changes occur in the plateau modulus and in the longest relaxation time. This behavior contrasts with that of metallo-supramolecular polymers in solutions, where the addition ions above the stoichiometric amount results in a monotonic decrease in viscosity due to the formation of mono-complexes.[247] Consequently, this result suggests that the stability constants of the mono and

bis-complexes are significantly modified when transitioning from the solution state to the melt state.

In this same chapter, the linear rheological response of the PnBA polymers is also modeled using a TMA that has been specially adapted for entangled polymers with sticky groups. This model introduces a novel approach to describe the CLF of associative polymers. Interestingly, the model successfully fits the data of the PnBA polymer, as well as literature data from other entangled associative linear polymers.

Lastly, the section on associative polymers was concluded by examining the linear and nonlinear shear rheology of unentangled metallo-supramolecular PnBA. In the linear regime, the rheological characterization strongly indicates the aggregation of stickers, as evidenced by the pronounced mechanical reinforcement. Specifically, the rubbery plateau is significantly higher than the level predicted by the rubber elasticity theory. In the nonlinear regime of deformation, various intriguing features became apparent. Firstly, the associative systems display transient shear hardening behaviour. Additionally, the strain obtained at the peak stress, identified as a yield strain, remains unaffected by the shear rates. Finally, the TTS principle holds true in a moderate temperature window. These pecular behaviors arise due to phenomenon of force-induced and thermal bond dissociation. Further investigations are necessary to assess the role of morphology in the nonlinear regime and to understand precisely the details of the molecular conformations adopted by the chains in nonlinear shear flow.

Development of a rheometer tool for orthogonal superposition measurements (Chapter 7)

In the final chapter of this work, a design for a rheometer tool which aims to perform orthogonal superposition measurements is presented. The design draws inspiration from a prototype shared by T. Schweizer (ETH, Switzerland), and has been validated through CFD simulations. In the last part of this chapter, analytical predictions of the orthogonal dynamic moduli for unentangled melts are also presented, utilizing a molecular model proposed by Sato et al.[75] The results demonstrate the validity of the time-shear rate superposi-

tion principle. Additionally, the shift factors necessary to construct the master curves are found to be dependent solely on the changes in monomeric friction, finite extensibility, and the Brownian force intensity. The quantification of these shift factors could provide valuable information about the behavior of polymeric systems under fast flow and constitute an important test of a constitutive model.

Perspectives

Finally, potential future research are outlined for the different parts:

Extensional rheology of polymer melts

An important topic in the study of nonlinear rheology of entangled polymer melts that needs to be elucidated is the role played by the entanglements. While several molecular models assume a constant tube diameter in extensional flow, MD simulations performed by O'Connor *et al.* indicate a reduction in the tube diameter as Wi_R increases, a phenomenon which can be attributed to an increasing number of entanglements.[184] As explained in the recent review of Ianniruberto *et al.*, this potential mechanism could be crucial as it could significantly amplify the degree of orientation of the chains, and possibly lead to a more pronounced decrease in monomeric friction reduction.[63] Conducting additional MD simulations could therefore be an interesting approach to explore the changes in entanglement density and its impact on the rheological response of polymeric melts.

Linear and nonlinear rheology of associative polymers

In Chapter 5, a new expression modeling the CLF of associative polymers is formulated. To validate this expression, a possible approach involves performing linear rheology measurements on star-shaped sticky polymers (represented in Figure 8.1). In such polymers, reptation is inherently suppressed due to the presence of a central core. Consequently, CLF becomes the predominant relaxation mechanism in these polymers.

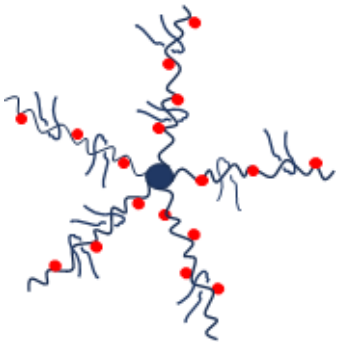

Figure 8.1: Schematic depiction of an entangled sticky star-shaped polymer. The red dots represent the stickers.

In this context, the introduction of a characteristic depth for the star's arms becomes pertinent. This characteristic depth would correspond to the location where the relaxation time of the outer segments of the star's arms is equal to the average duration during which all supramolecular junctions along this segment remain open. It could be anticipated that, for segments involving higher depth, the CLF process would experience significant deceleration, as the presence of closed stickers would regularly interrupt the free diffusion of the chain ends. Investigating stars with long arms could therefore shed light on how segments in proximity to the polymer core undergo relaxation.

To gain a deeper understanding of the nonlinear rheological response of associative polymer melts, combining rheological characterization with additional experimental techniques is essential. For instance, methods like Small-angle X-ray scattering (SAXS) and Wide-angle X-ray scattering (WAXS) are crucial for characterizing the morphology of phase-separated domains. Another valuable technique is the recently developed rheo-fluorescence technique of Rasid *et al.*, which quantifies the fraction of dissociated bonds in associative polymers subjected to nonlinear shear flow based upon a change in fluorescence. Rasid *et al.* applied this technique to metal-coordinate gel crosslinked via nickel-terpyridine complexation. The bis-complexes do not display any fluorescence, while, upon bond dissociation, terpyridine groups fluoresces.[287] This method could therefore be used to analyze the systems presented in Chapter 6 and 5.

Additionally, performing Small-angle neutron scattering (SANS) on partially deuterated samples quenched from nonlinear steady flow can provide a valuable information about the nonlinear responses of polymer samples. Particularly, SANS can offer insights into chain stretching, as demonstrated by Hassager *et al.* in the case of PS melts.[288]

Development of a rheometer tool for orthogonal superposition measurements

Validating the rheometer tool presented in Chapter 7 aimed to perform orthogonal superposition measurements could contribute to the limited pool of characterization methods of polymeric melts in the nonlinear regime. As explained by various authors, superposition experiments serve as a robust assessment for constitutive equations.

Additionally, instead of using sine waves as perturbation signals, exploring alternative signal types is valuable. For instance, Geri *et al.* introduced an optimally windowed chirp signal which allows for a rapid determination of the frequency response of viscoelastic materials, making it particularly suitable for studying time-evolving materials.[289–291]

Bibliography

[1] E. van Ruymbeke, C. Bailly, R. Keunings, and D. Vlassopoulos. A general methodology to predict the linear rheology of branched polymers. *Macromolecules*, 39(18):6248–6259, 2006.

[2] R. G. Larson. Instabilities in viscoelastic flows. *Rheol. Acta*, 31(3):213–263, 1992.

[3] C. J. S. Petrie and M. M. Denn. Instabilities in polymer processing. *AlChe J.*, 22(2):209–236, 1976.

[4] M. M. Denn. Issues in Viscoelastic Fluid Mechanics. *Annu. Rev. Fluid Mech.*, 22(1):13–32, 1990.

[5] H. Münstedt. Extensional Rheology and Processing of Polymeric Materials. *Int. Polym. Process.*, 33(5):594–618, 2018.

[6] J.-F. Agassant, D. R. Arda, C. Combeaud, A. Merten, H. Münstedt, M. R. Mackley, L. Robert, and B. Vergnes. Polymer processing extrusion instabilities and methods for their elimination or minimisation. *Int. Polym. Process.*, 21(3):239–255, 2006.

[7] H. S. Ji, G. Park, and H. W. Jung. Rheological Properties and Melt Spinning Application of Controlled-Rheology Polypropylenes via Pilot-Scale Reactive Extrusion. *Polymers*, 14(15):3226, 2022.

[8] P. C. Hiemenz and T. P. Lodge. *Polymer Chemistry*. CRC Press, 2007.

[9] J. M. Dealy and R. G. Larson. *Structure and Rheology of Molten Polymers.* Carl Hanser Verlag, Munich, Germany, 2006.

[10] R. G. Larson. *Constitutive Equations for Polymer Melts and Solutions.* Butterworths, London, 1988.

[11] E. van Ruymbeke and D. Vlassopoulos. *Macromolecular Rheology.* in Macromolecular Engineering, pages 1-56. Wiley, 2022.

[12] A. C. Pipkin. *Lectures on Viscoelasticity Theory.* Springer, New York, 1986.

[13] Q. Huang. *Molecular rheology of complex fluids.* PhD thesis, Technical University of Denmark, 2013.

[14] H. K. Rasmussen and T. Eriksson. Gas displacement of polymer melts in a cylinder: Experiments and viscoelastic simulations. *J. Non-Newtonian Fluid Mech*, 143(1):1–9, 2007.

[15] A. S. Lodge and Y. Wu. Constitutive equations for polymer solutions derived from the bead/spring model of rouse and zimm. *Rheol. Acta*, 10(4):539–553, 1971.

[16] A. S. Lodge. A network theory of flow birefringence and stress in concentrated polymer solutions. *Trans. Faraday Soc.*, 52:120–130, 1956.

[17] W. W. Graessley. Entangled linear, branched and network polymer systems - Molecular theories. *Adv. Polym. Sci.*, 47(4):67–117, 1982.

[18] Rouse P. E. A theory of the linear viscoelastic properties of dilute solutions of coiling polymers. *J. Chem. Phys.*, 21(7):1272–1280, 1953.

[19] P. G. de Gennes. Reptation of a Polymer Chain in the Presence of Fixed Obstacles. *J. Chem. Phys.*, 55(2):572–579, 1971.

[20] M. Doi and S. F. Edwards. *The Theory of Polymer Dynamics.* Oxford University Press, New York, 1986.

[21] A. E. Likhtman and T. C. B. McLeish. Quantitative theory for linear dynamics of linear entangled polymers. *Macromolecules*, 35(16):6332–6343, 2002.

[22] S. T. Milner and T. C. B. McLeish. Parameter-Free Theory for Stress Relaxation in Star Polymer Melts. *Macromolecules*, 30(7):2159–2166, 1997.

[23] D. S. Pearson and E. Helfand. Viscoelastic properties of star-shaped polymers. *Macromolecules*, 17(4):888–895, 1984.

[24] S. T. Milner and T. C. B. McLeish. Reptation and contour-length fluctuations in melts of linear polymers. *Phys. Rev. Lett.*, 81(3):725–728, 1998.

[25] Watanabe H. Rheology of Entangled Polymeric Liquids: Current Molecular Pictures and Problems. *J. Soc. Rheol. Japan*, 31(1):3–14, 2003.

[26] W. H. Tuminello. Molecular Weight and Molecular Weight Distribution From Dynamic Measurements of Polymer Melts. *Polym. Eng. Sci.*, 26(19):1339–1347, 1986.

[27] C. Tsenoglou. Viscoelasticity of Binary Polymer Blends. *ACS Polym. Prepr*, 28(2):185–186, 1987.

[28] J. Des Cloizeaux. Relaxation and viscosity anomaly of melts made of long entangled polymers time-dependent reptation. *Macromolecules*, 23(21):4678–4687, 1990.

[29] E. van Ruymbeke, C.-Y. Liu, and C. Bailly. Quantitative tube model predictions for the linear viscoelasticity of linear polymers. *Rheology Reviews*, pages 53–134, 2007.

[30] G. Marrucci. Relaxation by Reptation and Tube Enlargement: A Model for Polydisperse Polymers. *J. Polym. Sci. Polym. Phys. Ed.*, 23(1):159–177, 1985.

[31] T. Shahid, Q. Huang, F. Oosterlinck, F. Clasen, and E. van Ruymbeke. Dynamic Dilution Exponent in Monodisperse Entangled Polymer Solutions. *Soft Matter*, 13(1):269–282, 2017.

[32] S. S. Park and R. G. Larson. Dilution exponent in the dynamic dilution theory for polymer melts. *J. Rheol.*, 47(1):199–211, 2003.

[33] J.-L. Viovy, M. Rubinstein, and R. H. Colby. Constraint release in polymer melts: Tube reorganization versus tube dilation. *Macromolecules*, 24(12):3587–3596, 1991.

[34] S. T Milner. Relating the shear-thinning curve to the molecular weight distribution in linear polymer melts. *J. Rheol.*, 40(2):303–315, 1996.

[35] S. T. Milner, T. C. B. McLeish, R. N. Young, A. Hakiki, and J. M. Johnson. Dynamic dilution, constraint release, and starâlinear blends. *Macromolecules*, 31(26):9345–9353, 1998.

[36] E. van Ruymbeke, R. Keunings, V. Stéphenne, A. Hagenaars, and C. Bailly. Evaluation of Reptation Models for Predicting the Linear Viscoelastic Properties of Entangled Linear Polymers. *Macromolecules*, 35(7):2689–2699, 2002.

[37] S. L. Wingstrand, N. J. Alvarez, Q. Huang, and O. Hassager. Linear and nonlinear universality in the rheology of polymer melts and solutions. *Phys. Rev. Lett.*, 115(7):078302, 2015.

[38] G. Marrucci and N. Grizzuti. Fast flow of concentrated polymers: Predictions of the tube model on chain stretching. *Gazz. Chim. Ital.*, 118(7):179–185, 1988.

[39] G. Marrucci and N. Grizzuti. Dynamics of entanglements: A nonlinear model consistent with the coxâmerz rule. *J. Non Newtonian Fluid Mech.*, 62(2-3):279–289, 1996.

[40] J. L. White. Dynamics of viscoelastic fluids, melt fracture, and the rheology of fiber spinning. *J. Appl. Poly. Sci.*, 8(5):2339–2357, 1964.

[41] J. M. Dealy. Weissenberg and Deborah Numbers - Their Definition and Use. *Rheology Bulletin*, 79(2), 2010.

[42] R. S. Graham, A. E. Likhtman, T. C. B. McLeish, and S. T. Milner. Microscopic theory of linear, entangled polymer chains under rapid deformation including chain stretch and convective constraint release. *J. Rheol.*, 47(5):1171–1200, 2003.

[43] D. W. Mead, R. G. Larson, and M. Doi. A molecular theory for fast flows of entangled polymers. *Macromolecules*, 31(22):7895–7914, 1998.

[44] H. Taghipour, S. Costanzo, D. Vlassopoulos, E. van Ruymbeke, and L. G. Hawke. Entangled linear polymers in fast shear flows: Comparison of tube-model predictions and experimental data. *J. Rheol.*, 65(6):1111–1137, 2021.

[45] S. Costanzo, Q. Huang, G. Ianniruberto, G. Marrucci, and D. Hassager, O. Vlassopoulos. Shear and Extensional Rheology of Polystyrene Melts and Solutions with the Same Number of Entanglements. *Macromolecules*, 49(10):3925–3935, 2016.

[46] J. M. Kim, B. J. Edwards, D. J. Keffer, and B. Khomami. Single-chain dynamics of linear polyethylene liquids under shear flow. *Phys. Lett. A*, 373(7):769–772, 2009.

[47] Y. Masubuchi, G. Ianniruberto, and G. Marrucci. Stress undershoot of entangled polymers under fast startup shear flows in primitive chain network simulations. *Nihon Reoroji Gakkaishi*, 46(1):23–28, 2018.

[48] M. H. N. Sefiddashti, B. J. Edwards, and B. Khomami. Individual chain dynamics of a polyethylene melt undergoing steady shear flow. *J. Rheol.*, 59(1):119–153, 2018.

[49] G. Marrucci and G. Ianniruberto. Interchain pressure effect in extensional flows of entangled polymer melts. *Macromolecules*, 37(10):3934–3942, 2004.

[50] Q. Huang. When polymer chains are highly aligned: A perspective on extensional rheology. *Macromolecules*, 55(3):715–727, 2022.

[51] Q. Huang, L. Hengeller, N. J. Alvarez, and O. Hassager. Bridging the Gap between Polymer Melts and Solutions in Extensional Rheology. *Macromolecules*, 48(12):4158–4163, 2015.

[52] G. Ianniruberto. Extensional flows of solutions of entangled polymers confirm reduction of friction coefficient. *Macromolecules*, 48(17):6306–6312, 2015.

[53] S. L. Morelly, L. Palmese, H. Watanabe, and N. J. Alvarez. Effect of Finite Extensibility on Nonlinear Extensional Rheology of Polymer Melts. *Macromolecules*, 52(3):915–922, 2019.

[54] Q. Huang, J. Ahn, D. Parisi, T. Chang, O. Hassager, S. Panyukov, M. Rubinstein, and D. Vlassopoulos. Unexpected Stretching of Entangled Ring Macromolecules. *Phys. Rev. Lett.*, 122(20):208001, 2019.

[55] T. Sridhar, M. Acharya, D. A. Nguyen, and P. K. Bhattacharjee. On the extensional rheology of polymer melts and concentrated solutions. *Macromolecules*, 47(1):379–386, 2014.

[56] Q. Huang, N. J. Alvarez, Y. Matsumiya, H. K. Rasmussen, H. Watanabe, and O. Hassager. Extensional Rheology of Entangled Polystyrene Solutions Suggests Importance of Nematic Interactions. *ACS Macro Lett.*, 2(8):741–744, 2013.

[57] M. H. Wagner and V. H. Rolón-Garrido. Nonlinear rheology of linear polymer melts: modeling chains stratch by interchain tube pressure and rouse time. *Korea Aust. Rheol. J.*, 21(4):203–211, 2009.

[58] M. H. Wagner. An extended interchain tube pressure model for elongational flow of polystyrene melts and concentrated solutions. *J. Non-Newtonian Fluid Mech*, 222:121–131, 2015.

[59] M. H. Wagner, E. Narimissa, and V. H. Rolón-Garrido. From melt to solution: Scaling relations for concentrated polystyrene solutions. *J. Rheol.*, 59(4):1113–1113, 2015.

[60] E. Narimissa, Q. Huang, and M. H. Wagner. Elongational rheology of polystyrene melts and solutions: Concentration dependence of the interchain tube pressure effect. *J. Rheol.*, 64(1):95–110, 2020.

[61] G. Ianniruberto, A. Brasiello, and G. Marrucci. Friction coefficient does not stay constant in non linear viscoelasticity. *Proceedings of the 7th Annual European Rheology Conference*, 1:p. 61, 2011.

[62] T. Yaoita, T. Isaki, Y. Masubuchi, H. Watanabe, G. Ianniruberto, and G. Marrucci. Primitive chain network simulation of elongational flows of entangled linear chains: stretch/orientation-induced reduction of monomeric friction. *Macromolecules*, 45(6):2773–2782, 2012.

[63] G. Ianniruberto, G. Marrucci, and Y. Masubuchi. Melts of Linear Polymers in Fast Flows. *Macromolecules*, 53(13):5023–5033, 2020.

[64] G. Ianniruberto, A. Brasiello, and G. Marrucci. Simulations of fast shear flows of ps oligomers confirm monomeric friction reduction in fast elongational flows of monodisperse ps melts as indicated byheooptical data. *Macromolecules*, 45(19):8058–8066, 2012.

[65] Y. Masubuchi, T. Yaoita, Y. Matsumiya, H. Watanabe, G. Ianniruberto, and G. Marrucci. Stretch/orientation induced acceleration in stress relaxation in coarse-grained molecular dynamics simulations. *Nihon Reoroji Gakkaishi*, 41(1):35–37, 2013.

[66] P. S. Desai and R. G. Larson. Constitutive model that shows extension thickening for entangled solutions and extension thinning. *J. Rheol.*, 58(1):255–279, 2014.

[67] Y. Masubuchi, Y. Matsumiya, and H. Watanabe. Test of Orientation/Stretch-Induced Reduction of Friction via Primitive Chain Network Simulations for Polystyrene, Polyisoprene, and Poly(n-butyl acrylate). *Macromolecules*, 47(19):6768–6775, 2014.

[68] G. W. Park and G. Ianniruberto. Flow-induced Nematic Interaction and Friction Reduction Successfully Describe PS melt and Solution Data in Extension Startup and Relaxation. *Macromolecules*, 50(12):4787–4796, 2017.

[69] T. Shahid, C. Clasen, F. Oosterlinck, and E. van Ruymbeke. Diluting Entangled Polymers Affects Transient Hardening but Not Their Steady Elon-

gational Viscosity. *Macromolecules*, 52(6):2521–2530, 2019.

[70] Y. Matsumiya, H. Watanabe, Y. Masubuchi, Q. Huang, and O. Hassager. Nonlinear Elongational Rheology of Unentangled Polystyrene and Poly (p-tert-butylstyrene) Melts. *Macromolecules*, 51(23):9710–9729, 2018.

[71] G. Ianniruberto, A. Brasiello, and G. Marrucci. Modeling Unentangled Polystyrene Melts in Fast Elongational Flows. *Macromolecules*, 52(12):4610–4616, 2019.

[72] H. Watanabe, Y. Matsumiya, and T. Sato. Nonlinear Rheology of FENE Dumbbell with Friction-Reduction: Analysis of Brownian Force Intensity through Comparison of Extensional and Shear Viscosities. *J. Soc. Rheol. Japan*, 48(5):259–269, 2020.

[73] Y. Matsumiya and H. Watanabe. Non-universal Feature in Uniaxially Extensional Rheology of Linear Polymer Melts and Concentrated Solutions: A Review. *Prog. Polym. Sci.*, 112:101325, 2021.

[74] H. Watanabe, Y. Matsumiya, and T. Sato. Revisiting Nonlinear Flow Behavior of Rouse Chain: Roles of FENE, Friction-Reduction, and Brownian Force Intensity Variation. *Macromolecules*, 54(8):3700–3715, 2021.

[75] T. Sato, Y. Kwon, Y. Matsumiya, and H. Watanabe. A Constitutive Equation for Rouse Model Modified for Variations of Spring Stiffness, Bead Friction, and Brownian Force Intensity Under Flow. *Phys. Fluids*, 33(6):063106, 2021.

[76] T. Sato, Y. Matsumiya, and H. Watanabe. Rheo-Dielectrics and Diffusion of Type-A Rouse Chain under Fast Shear Flow: Method of Evaluation of Non-equilibrium Parameters for FENE, Friction-Reduction, and Brownian Force Intensity Variation. *J. Soc. Rheol. Japan*, 50(2):253–268, 2022.

[77] Y. Matsumiya, T. Sato, Q. Chen, and H. Watanabe. Rheo-dielectric Behavior of Unentangled Poly(butylene oxide) under Steady Shear: Preliminary Evaluation of Non-equilibrium Parameters at the Onset of Nonlinearity. *J. Soc. Rheol. Japan*, 50(5):371–385, 2022.

[78] N. Jiang and E. van Ruymbeke. Variation of Spring Stiffness, Monomeric Friction, and Brownian Intensity in the Simulation System of Unentangled Melt under Steady Flow. *Macromolecules*, 56(8):2911–2929, 2023.

[79] Y. Masubuchi, G. Ianniruberto, M. Wagner, and G. Marrucci. Primitive chain network simulations of the nonlinear rheology of polystyrene melts: Friction reduction and fluctuation-dissipation theorem. *J. Non-Newton. Fluid Mech.*, 315:105019, 2023.

[80] R. F. M. Lange, M. Van Gurp, and E. W. Meijer. Hydrogen-bonded supramolecular polymer networks. *J. Polym. Sci. Part A Polym. Chem.*, 37(19):3657–3670, 1999.

[81] T. Nakano. *π-Stacked Polymers and Molecules: Theory, Synthesis, and Properties*. Springer, Tokyo, 2013.

[82] S. Burattini, B. W. Greenland, D. H. Merino, W. Weng, J. Seppala, H. M. Colquhoun, W. Hayes, M. E. Mackay, I. W. Hamley, and S. J. Rowan. A healable supramolecular polymer blend based on aromatic pi-pi stacking and hydrogen-bonding interactions. *J. Am. Chem. Soc.*, 132(34):12051–12058, 2010.

[83] A. Eisenberg and J.-S. Kim. *Introduction to Ionomers*. Wiley, New York, 1998.

[84] T. Annable, R. Buscall, R. Ettelaie, and D. Whittlestone. The rheology of solutions of associating polymers: Comparison of experimental behavior with transient network theory. *J. Rheol.*, 37(4):695–726, 1993.

[85] R. J. English, J. H. Laurer, R. J. Spontak, and S. A. Khan. Hydrophobically Modified Associative Polymer Solutions: Rheology and Microstructure in the Presence of Nonionic Surfactants. *Ind. Eng. Chem. Res*, 41(25):6425–6435, 2002.

[86] U. S. Schubert and c. Eschbaumer. Macromolecules containing bipyridine and terpyridine metal complexes: Towards metallosupramolecular polymers. *Angew. Chem.-Int. Edit.*, 41(16):2893–2926, 2002.

[87] J. Brassinne, C.-A. Fustin, and J.-F. Gohy. Polymer gels constructed through metal-ligand coordination. *J. Inorg. Organomet. Polym.*, 23(1):24–40, 2013.

[88] Z. Zhang, Q. Chen, and R. H. Colby. Dynamics of associative polymers. *Soft Matter*, 14(16):2961–2977, 2018.

[89] E. van Ruymbeke. Preface: Special Issue on Associating Polymers. *J. Rheol.*, 61(6):1099–1102, 2017.

[90] M. Lemmers, M. Sprakel, I. K. Voets, J. van der Gucht, and M. A. C. Stuart. Multiresponsive reversible gels based on charge-driven assembly. *Angew. Chem. Int. Ed.*, 49(4):708–711, 2010.

[91] S. Dai, P. Ravi, and K. C. Tam. pH-Responsive polymers: synthesis, properties and applications. *Soft Matter*, 4(3):435–449, 2008.

[92] R. Hoogenboom. *Temperature-Responsive Polymers: Properties, Synthesis and Applications. Smart Polymers and their Applications.* Woodhead Publishing Limited, 2014.

[93] A. O. Razgoniaev, E. V. Butaeva, A. V. Iretskii, and A. D. Ostrowski. Changing Mechanical Strength in Cr(III)- Metallosupramolecular Polymers with Ligand Groups and Light Irradiation. *Inorg. Chem.*, 55(11):5430–5437, 2016.

[94] R. P. Sijbesma, F. H. Beijer, B. J. B. Folmer, J. H. K. K. Hirschberg, R. F. M. Lange, and E. W. Meijer. Reversible Polymers Formed from Self-Complementary Monomers Using Quadruple Hydrogen Bonding. *Science*, 278(5343):1601–1604, 1997.

[95] J. R. Kumpfer and S. J. Rowan. Thermo-, Photo-, and Chemo-Responsive Shape-Memory Properties from Photo-Cross-Linked Metallo-Supramolecular Polymers. *J. Am. Chem. Soc.*, 133(32):12866–12874, 2011.

[96] Z. Wang, W. Fan, R. Tong, X. Lu, and H. Xia. Thermal-healable and shape memory metallosupramolecular poly(n-butyl acrylate-co-methyl methacrylate) materials. *RSC Adv.*, 4(49):25486–25493, 2014.

[97] I. Jeon, J. Cui, W. R. K. Illeperuma, J. Aizenberg, and J. J. Vlassak. Extremely stretchable and fast self-healing hydrogels. *Adv. Mater.*, 28(23):4678–4683, 2016.

[98] S. van der Zwaag, A. J. M. Schmets, and G. van der Zaken. *Self healing materials: an alternative approach to 20 centuries of materials science*. Springer: Dordrecht, The Netherlands, 2007.

[99] P. Cordier, F. Tournilhac, C. Soulié-Ziakovic, and L. Leibler. Self-healing and thermoreversible rubber from supramolecular assembly. *Nature*, 451(7181):977–980, 2008.

[100] J. Y. Sun, X. Zhao, W. R. K. Illeperuma, O. Chaudhuri, K. H. Oh, D. J. Mooney, J. J. Vlassak, and Z. Suo. Highly stretchable and tough hydrogels. *Nature*, 489(7414):133–136, 2012.

[101] F. Tournilhac, P. Cordier, D. Montarnal, C. Soulié-Ziakovic, and L. Leibler. Self-Healing Supramolecular Networks. *Macromol. Symp.*, 291-292(1):84–88, 2010.

[102] M. B. Jackson. *Molecular and cellular biophysics*. Cambridge University Press, New York, 2006.

[103] M. Golkaram and K. Loos. A Critical Approach to Polymer Dynamics in Supramolecular Polymers. *Macromolecules*, 52(24):9427–9444, 2019.

[104] L. G. Baxandall. Dynamics of reversibly cross-linked chains. *Macromolecules*, 22(4):1982–1988, 1989.

[105] Q. Chen, G. J. Tudryn, and R. H. Colby. Ionomer dynamics and the sticky rouse model. *J. Rheol.*, 57(5):1441–1462, 2013.

[106] K. E. Feldman, M. J. Kade, E. W. Meijer, C. J. Hawker, and E. J. Kramer. Model Transient Networks from Strongly Hydrogen-Bonded Polymers. *Macromolecules*, 43(7):3576–3576, 2010.

[107] Q. Chen, S. Liang, H.-S. Shiau, and R. H. Colby. Linear Viscoelastic and Dielectric Properties of Phosphonium Siloxane Ionomers. *ACS Macro Lett.*, 2(11):970–974, 2013.

[108] V. M. S. Syed and S. Srivastava. Time-Ionic Strength Superposition: A Unified Description of Chain Relaxation Dynamics in Polyelectrolyte Complexes. *ACS Macro Lett.*, 9(7):1067–1073, 2020.

[109] L. Leibler, M. Rubinstein, and R. H. Colby. Dynamics of reversible networks. *Macromolecules*, 24(16):4701–4707, 1991.

[110] Q. Chen, Z. Zhang, and R.H. Colby. Viscoelasticity of entangled random polystyrene ionomers. *J. Rheol.*, 60(6):1031–1040, 2016.

[111] A. N. Semenov and M. Rubinstein. Dynamics of Entangled Associating Polymers with Large Aggregates. *Macromolecules*, 35(12):4821–4837, 2002.

[112] M. Ahmadi, A. Jangizehi, K. Saalwächter, and S. Seiffert. Effect of Junction Aggregation on the Dynamics of Supramolecular Polymers and Networks. *Macromol. Chem. Phys.*, 224(3):2200389, 2022.

[113] A. Mordvinkin, M. Suckow, F. Böhme, R.H. Colby, C. Creton, and K. Saalwächter. Hierarchical sticker and sticky chain dynamics in self-healing butyl rubber ionomers. *Macromolecules*, 52(11):4169–4184, 2019.

[114] A. Mordvinkin, D. Döhler, W. H. Binder, R. H. Colby, and K. Saalwächter. Rheology, Sticky Chain, and Sticker Dynamics of supramolecular Elastomers Based on Cluster-Forming Telechelic Linear and Star Polymers. *Macromolecules*, 54(11):5065–5076, 2021.

[115] A. Mordvinkin, D. Döhler, W. H. Binder, R. H. Colby, and K. Saalwächter. Terminal Flow of Cluster-Forming Supramolecular Polymer Networks: Single-Chain Relaxation or Micelle Reorganization? *Phys. Rev. Lett.*, 125(12):127801, 2020.

[116] S. Ge, S. Samanta, B. Li, P. Carden, P.-F. Cao, and A. P. Sokolov. Unravelling the Mechanism of Viscoelasticity in Polymers with Phase-Separated Dynamic Bonds. *ACS Nano*, 16(3):4746–4755, 2022.

[117] D. Amin, A. E. Likhtman, and Z. Wang. Dynamics in supramolecular polymer Networks Formed by Associating Telechelic Chains. *Macromolecules*, 49(19):7510–7524, 2016.

[118] L. G. D. Hawke, M. Ahmadi, H. Goldansaz, and E. van Ruymbeke. Viscoelastic properties of linear associating poly(n-butyl acrylate) chains. *J. Rheol.*, 60(2):297–310, 2016.

[119] A. Jangizehi, M. Ahmadi, and S. Seiffert. Emergence, evidence, and effect of junction clustering in supramolecular polymer materials. *Mater. Adv.*, 2(5):1425–1453, 2021.

[120] S. Ghiassinejad, K. Mortensen, M. Rostamitabar, J. Malineni, C.-A. Fustin, and E. van Ruymbeke. Dynamics and Structure of Metallo-supramolecular Polymers Based on Short Telechelic Precursors. *Macromolecules*, 54(13):6400–6416, 2021.

[121] N. E. Botterhuis, D. J. M. van Beek, G. M. L. van Gemert, A. W. Bosman, and R. P. Sijbesma. Self-assembly and morphology of polydimethylsiloxane supramolecular thermoplastic elastomers. *J. Polym. Sci., Part A-1: Polym. Chem.*, 46(12):3877–3885, 2008.

[122] M. Rubinstein and A. N. Semenov. Thermoreversible Gelation in Solutions of Associating Polymers. 2. Linear Dynamics. *Macromolecules*, 31(4):1386–1397, 1998.

[123] A. Ghosh and K. S. Schweizer. Physical Bond Breaking in Associating Copolymer Liquids. *ACS Macro Lett.*, 10(1):122–128, 2021.

[124] B. J. Gold, C. H. Hövelmann, N. Lühmann, N. K. Székely, W. Pyckhout-Hintzen, A. Wischnewski, and D. Richter. Importance of Compact Random Walks for the Rheology of Transient Networks. *ACS Macro Lett.*, 6(2):73–77, 2017.

[125] Z. Zhang, C. Liu, X. Cao, L. Gao, and Q. Chen. Linear Viscoelastic and Dielectric Properties of Strongly Hydrogen-Bonded Polymers near the Sol-Gel Transition. *Macromolecules*, 49(23):9192–9202, 2016.

[126] G. Cui, V. A. H. Boudara, Q. Huang, G.P. Baeza, A.J. Wilson, O. Hassager, D. J. Read, and J. Mattsson. Linear shear and nonlinear extensional rheology of unentangled supramolecular side-chain polymers. *J. Rheol.*, 62(5):1155–1174, 2018.

[127] B. J. Gold, C. H. Hövelmann, N. Lühmann, W. Pyckhout-Hintzen, A. Wischnewski, and D. Richter. The microscopic origin of the rheology in supramolecular entangled polymer networks. *J. Rheol.*, 61(6):1211–1226, 2017.

[128] F. J. Stadler, W. Pyckhout-Hintzen, J.-M. Schumers, C.-A. Fustin, J.-F. Gohy, and C. Bailly. Linear Viscoelastic Rheology of Moderately Entangled Telechelic Polybutadiene Temporary Networks. *Macromolecules*, 42(16):6181–6192, 2009.

[129] M. S.. Green and A. V. Tobolsky. A new approach to the theory of relaxing polymeric media. *J. Chem. Phys.*, 14(2):80–92, 1946.

[130] M. Yamamoto. The visco-elastic properties of network structure i. general formalism. *J. Phys. Soc. Jpn.*, 11:413–421, 1956.

[131] F. Tanaka and S. F. Edwards. Viscoelastic properties of physically crosslinked networks. 1. Transient network theory. *Macromolecules*, 25(5):1516–1523, 1992.

[132] T. Koga, F. Tanaka, T. Kaneda, and F. M. Winnik. Stress Buildup under Start-Up Shear Flows in Self-Assembled Transient networks of telechelic associating polymers. *Langmuir*, 25(15):8626–8638, 2009.

[133] J.-F. Berret, Y. Séréro, B. Winkelman, D. Calvet, A. Collet, and M. Viguier. Nonlinear rheology of telechelic polymer networks. *J. Rheol.*, 45(2):477–492, 2001.

[134] R. A. Weiss and H. Zhao. Rheological behavior of oligomeric ionomers. *J. Rheol.*, 53(1):191–213, 2009.

[135] R. J. English. Solution rheology of a hydrophobically modified alkali-soluble associative polymer. *J. Rheol.*, 41(2):427–444, 1997.

[136] T. Indei, T. Koga, and F. Tanaka. Theory of Shear-Thickening in Transient Networks of Associating Polymers. *Rapid Commun.*, 25(9):701–706, 2005.

[137] F. Tanaka, T. Koga, I. Kaneda, and F. M. Winnik. Hydration, phase separation and nonlinear rheology of temperature-sensitive water-soluble polymers. *J. Phys. Condens. Matter*, 23(28):284105, 2011.

[138] G. Marrucci, S. Bhargava, and S. L. Cooper. Models of shear-thickening behavior in physically crosslinked networks. *Macromolecules*, 26(24):6483–6488, 1993.

[139] T. A. Witten and M. H. Cohen. Crosslinking in shear-thickening ionomers. *Macromolecules*, 18(10):1915–1918, 1985.

[140] S. Suzuki, T. Uneyama, T. Inoue, and H. Watanabe. Nonlinear Rheology of Telechelic Associative Polymer Networks: Shear Thickening and Thinning Behavior of Hydrophobically Modified ethoxylated Urethane (HEUR) in Aqueous Solution. *Macromolecules*, 45(2):888–898, 2012.

[141] A. K. Omar and Z.-G. Wang. Shear-Induced Heterogeneity in Associating Polymer Gels: Role of Network Structure and Dilatancy. *Phys. Rev. Lett.*, 119(11):117801, 2017.

[142] G. Ianniruberto and G. Marrucci. New Interpretation of Shear Thickening in Telechelic Associating Polymers. *Macromolecules*, 48(15):5439–5449, 2015.

[143] Y. Zhang, Q. Chen, and H. Watanabe. Nonlinear shear rheology of concentrated poly(vinyl alcohol)/borax aqueous solution: Nonlinearity of sticky Rouse relaxation. *J. Non-Newton. Fluid Mech.*, 316:105012, 2023.

[144] M. K. Sing, Z.-G. Wang, G. H. McKinley, and B. D. Olsen. Celebrating Soft matter's 10th Anniversary: Chain configuration and rate-dependent mechanical properties in transient networks. *Soft Matter*, 11(11):2085–2096, 2015.

[145] A. Shabbir, H. Goldansaz, O. Hassager, E. van Ruymbeke, and N. J. Alvarez. Effect of Hydrogen Bonding on Linear and Nonlinear Rheology of Entangled Polymer Melts. *Macromolecules*, 48(16):5988–5996, 2015.

[146] G. Liu, R. G. Larson, L. Li, H. Luo, X. He, Y. Niu, and G. Li. Influence of Chain Entanglement on Rheological and Mechanical Behaviors of Polymerized Ionic Liquids. *Macromolecules*, 56(7):2719–2728, 2023.

[147] S. Wu, X. Cao, Z. Zhang, Q. Chen, Y. Matsumiya, and H. Watanabe. Molecular Design of Highly Stretchable Ionomers. *Macromolecules*, 51(12):4735–4746, 2018.

[148] A. Shabbir, Q. Huang, G. P. Baeza, D. Vlassopoulos, Q. Chen, R. H. Colby, N. J. Alvarez, and O. Hassager. Non-linear Shear and Uniaxial Extensional Rheology of Polyether-Ester-Sulfonate Copolymer Ionomer Melts. *J. Rheol.*, 61(6):1279–1289, 2017.

[149] G. H. Ling, Y. Wang, and R. A. Weiss. Linear Viscoelastic and Uniaxial Extensional Rheology of Alkali Metal Neutralized Sulfonated Oligostyrene Ionomer Melts. *Macromolecules*, 45(1):481–490, 2012.

[150] K. Cui and J. P. Gong. How double dynamics affects the large deformation and fracture behaviors of soft materials. *J. Rheol.*, 66(6):1093–1111, 2022.

[151] ARES. `https://www.tainstruments.com/`. Accessed: 2023-08-23.

[152] Anton Paar. `https://www.anton-paar.com/`. Accessed: 2023-08-23.

[153] J. Meissner, R. W. Garbella, and J. Hostettler. Measuring normal stress differences in polymer melt shear-flow. *J. Rheol.*, 33(6):843–864, 1989.

[154] T. Schweizer. Measurement of the first and second normal stress differences in a polystyrene melt with a cone and partitioned plate tool. *Rheol. Acta*, 41(4):337–344, 2002.

[155] T. Schweizer. Comparing cone-partitioned plate and cone-standard plate shear rheometry of a polystyrene melt. *J. Rheol.*, 47(4):1071–1085, 2003.

[156] T. Schweizer and A. Bardow. The role of instrument compliance in normal force measurements of polymer melts. *Rheol. Acta*, 45(4):393–402, 2006.

[157] T. Schweizer, J. van Meerveld, and C. O. Öttinger. Nonlinear shear rheology of polystyrene melt with narrow molecular weight distributionâexperiment and theory. *J. Rheol.*, 48(6):1345–1363, 2004.

[158] F. Snijkers and D. Vlassopoulos. Cone-partitioned-plate geometry for the ARES rheometer with temperature control. *J. Rheol.*, 55(6):1167–1186, 2011.

[159] Z.-C. Yan, S. Costanzo, Y. Jeong, T. Chang, and D. Vlassopoulos. Linear and Nonlinear Shear Rheology of a Marginally Entangled Ring Polymer. *Macromolecules*, 49(4):1444–1453, 2016.

[160] Rheo filament. `http://rheofilament.com/`. Accessed: 2023-08-23.

[161] J. M. R. Marín, J. K. Huusom, N. J. Alvarez, Q. Huang, A. Rasmussen, H. K. ans Bach, A. L. Skov, and O. Hassager. A control scheme for filament stretching rheometers with application to polymer melts. *J. Non-Newton. Fluid Mech.*, 194:14–22, 2013.

[162] S. L. Anna, C. Rogers, and G. H. McKinley. On controlling the kinematics of a filament stretching rheometer using a real-time active control mechanism. *J. Non-Newton. Fluid Mech.*, 87:307–335, 1999.

[163] N. V. Orr and T. Sridhar. Probing the dynamics of polymer solutions in extensional flow using step strain rate experiments. *J. Non-Newton. Fluid Mech.*, 82:203–232, 1999.

[164] A. Bach, H. K. Rasmussen, and O. Hassager. Extensional viscosity for polymer melts measured in the filament stretching rheometer. *J. Rheol.*, 47(2):429–441, 2003.

[165] O. Hassager, Y. Wang, and Q. Huang. Extensional rheometry of model liquids: Simulations of filament stretching. *Phys. Fluids*, 33(12):123108, 2021.

[166] H. K. Rasmussen, A. G. Bejenariu, O. Hassager, and D. Auhl. Experimental evaluation of the pure configurational stress assumption in the flow dynamics of entangled polymer melts. *J. Rheol.*, 54(6):1325–1336, 2010.

[167] T. Shahid. *Understanding and modelling the extensional rheology of nearly monodisperse linear polymers*. PhD thesis, Université catholique de Louvain, 2018.

[168] A. Bach, K. Almdal, H. K. Rasmussen, and O. Hassager. Elongational viscosity of narrow molar mass distribution polystyrene. *Macromolecules*, 36(14):5174–5179, 2003.

[169] P. K. Bhattacharjee, J. P. Oberhauser, G. H. McKinley, L. G. Leal, and T. Sridhar. Extensional rheometry of entangled solutions. *Macromolecules*, 35(27):10131–10148, 2002.

[170] Q. Huang, O. Mednova, H. K. Rasmussen, N. J. Alvarez, A. L. Skov, K. Almdal, and O. Hassager. Concentrated polymer solutions are different from melts: Role of entanglement molecular weight. *Macromolecules*, 46(12):5026–5035, 2013.

[171] S. Q. Wang. *Nonlinear Polymer Rheology: Macroscopic Phenomenology and Molecular Foundation*. Wiley, Hoboken, N.J., 2017.

[172] T. G. Fox. Influence of Diluent and of Copolymer Composition on the Glass Temperature of a Polymer System. *Bull. Am. Phys. Soc.*, 1:123, 1956.

[173] M. L. Williams, R. F. Landel, and J. D. Ferry. The Temperature Dependence of Relaxation Mechanisms in Amorphous Polymers and Other Glass-forming Liquids. *J. Am. Chem. Soc.*, 77(14):3701–3707, 1955.

[174] M. H. Wagner. Scaling relations for elongational flow of polystyrene melts and concentrated solutions of polystyrene in oligomeric styrene. *Rheol. Acta*, 53(10):765–777, 2014.

[175] C.-Y. Liu, J. He, R. Keunings, and C. Bailly. New Linearized Relation for the Universal Viscosity-Temperature Behavior of Polymer Melts. *Macromolecules*, 39(25):8867–8869, 2006.

[176] E. van Ruymbeke, Y. Masubuchi, and H. Watanabe. Effective Value of the Dynamic Dilution Exponent in Bidisperse Linear Polymers: From 1 to 4/3. *Macromolecules*, 45(4):2085–2098, 2012.

[177] C. R. López-Barrón, Y. Zeng, and J. J. Richards. Chain Stretching and recoiling during startup and cessation of extensional flow of bidisperse polystyrene blends. *J. Rheol.*, 61(4):697–710, 2017.

[178] D. Auhl, P. Chambon, T. McLeish, and D. Read. Elongational Flow of Blends of Long and Short Polymers, Effective Stretch Relaxation Time. *Phys. Rev. Lett.*, 103:136001, 2009.

[179] Q. Huang, S. Agostini, L. Hengeller, M. Shivokhin, N. J. Alvarez, L. R. Hutchings, and O. Hassager. Dynamics of star polymers in fast extensional flow and stress relaxation. *Macromolecules*, 49(17):6694–6699, 2016.

[180] O. Hassager. Kinetic Theory and Rheology of Bead-rod Models for Macromolecular Solutions. I. Equilibrium and Steady Flow Properties. *J. Chem. Phys.*, 60(5):2111–2124, 1974.

[181] C. M. Schroeder. Single polymer dynamics for molecular rheology. *J. Rheol.*, 62(1):371–403, 2018.

[182] C. D. Young and C. E. Sing. Simulation of semidilute polymer solutions in planar extensional via conformationally averaged brownian noise. *J. Chem. Phys.*, 151:124907, 2019.

[183] C. D. Young, Y. Zhou, C. M. Schroeder, and C. E. Sing. Dynamics and rheology of ring-linear blend semidilute solutions in extensional flow. part i: Modeling and molecular simulations. *J. Rheol.*, 65(4):757–777, 2021.

[184] T. C. O'Connor, N. J. Alvarez, and M. O. Robbins. Relating Chain Conformations to Extensional Stress in Entangled Polymer Melts. *Phys. Rev. Lett.*, 121(4):047801, 2018.

[185] S. J. Park and R. G. Larson. Tube dilation and reptation in binary blends of monodisperse linear polymers. *Macromolecules*, 37(2):597–604, 2004.

[186] H. Liu, G. Ianniruberto, and G. Marrucci. A single-chain model for the linear viscoelasticity of unentangled melts of associating polymers. *J. Rheol.*, 66(6):1183–1190, 2022.

[187] J. Verjans. *Post-polymerization modification towards supramolecular polymer materials and functional hydrogels*. PhD thesis, Ghent University, 2022.

[188] J. Verjans and R. Hoogenboom. Supramolecular polymer materials based on ureidopyrimidinone quadruple hydrogen bonding units. *Prog. Polym. Sci.*, 142:101689–101705, 2023.

[189] Y. Ducharme and J. D. Wuest. Use of hydrogen bonds to control molecular aggregation. Extensive, self-complementary arrays of donors and acceptors. *J. Org. Chem. Res.*, 53(24):5787–5789, 1988.

[190] F. Herbst, S. Schröter, I. Gunkel, S. Gröger, T. Thurn-Albrecht, J. Balbach, and W. H. Binder. Aggregation and Chain Dynamics in Supramolecular Polymers by Dynamic Rheology: Cluster Formation and Self-Aggregation. *Macromolecules*, 43(23):10006–10016, 2010.

[191] X. Fu, Q. Zhang, G. Wu, W. Zhou, Q.-.C. Wang, and D-H. Qu. A fluorescent hyperbranched supramolecular polymer based on triple hydrogen bonding interactions. *Polym. Chem.*, 5(23):6662–6666, 2014.

[192] H. Zeng, X. Yang, A. Brown, S. Martinovic, R. Smith, and B. Gong. An extremely stable, self-complementary hydrogen-bonded duplex. *Chem. Commun.*, 13:1556–1557, 2003.

[193] J. Tellers, S. Canossa, R. Pinalli, M. Soliman, J. Vachon, and E. Dalcanale. Dynamic cross-linking of polyethylene via sextuple hydrogen bonding array. *Macromolecules*, 51(19):7680–7691, 2018.

[194] K.P. Nair, M. Breedveld, and M. Weck. Complementary hydrogen-bonded thermoreversible polymer networks with tunable properties. *Macromolecules*, 41(10):3429–3438, 2008.

[195] F. H. Beijer, R. P. Sijbesma, H. Kooijman, A. L. Spek, and E. W. Meijer. Strong Dimerization of Ureidopyrimidones via Quadruple Hydrogen bonding. *J. Am. Chem. Soc.*, 120(27):6761–6769, 1998.

[196] S. H. M. Söntjens, R. P. Sijbesma, M. H. P. van Genderen, and E. W. Meijer. Stability and Lifetime of Quadruply Hydrogen Bonded 2-Ureido-4[1H]-pyrimidinone Dimers. *J. Am. Chem. Soc.*, 122(31):7487–7493, 2000.

[197] J. H. K. K. Hirschberg, F. H. Beijer, H. A. van Aert, P. C. M. M. Magusin, R. P. Sijbesma, and E. W. Meijer. Supramolecular Polymers from Linear Telechelic Siloxanes with Quadruple-Hydrogen-Bonded Units. *Macromolecules*, 32(8):2696–2705, 1999.

[198] J. Cui and A. del Campo. Multivalent H-bonds for self-healing hydrogels. *Chem. Commun.*, 48(74):9302–9304, 2012.

[199] M. Wei, M. Zhan, D. Yu, H. Xie, M. He, K. Yang, and Y. Wang. Novel poly(tetramethylene ether)glycol and poly(ε-caprolactone) based dynamic network via quadruple hydrogen bonding with triple-shape effect and self-healing capacity. *ACS. Appl. Mater. Interfaces*, 7(4):2585–2596, 2015.

[200] H. Xie, D. Sheng, Y. Zhou, S. Xu, H. Wu, Y. Tian, X. Sun, X. Liu, and Y. Yang. Thermally Healable Polyurethane with Tailored Mechanical Performance Using Dynamic Crosslinking Motifs. *New J. Chem.*, 44(32):13584–13590, 2020.

[201] M.-C. Luo, J. Zeng, X. Fu, G. Huang, and J. Wu. Toughening diene elastomers by strong hydrogen bond interactions. *Polymer*, 106:21–28, 2020.

[202] X. Yan, Z. Liu, Q. Zhang, J. Lopez, H. Wang, H.-C. Wu, S. Niu, H. Yan, S. Wang, T. Lei, J. Li, D. Qi, P. Huang, J. Huang, Y. Zhang, Y. Wang, G. Li, J. B. H. Tok, X. Chen, and Z. Bao. Quadruple H-bonding Crosslinked Supramolecular Polymeric Materials as Substrates for Stretchable, Anti-Tearing, and Self-Healable Thin Film Electrodes. *J. Am. Chem. Soc.*, 140(15):5280–5289, 2018.

[203] P. J. Besseling, T. Mes, A. W. Bosman, J. W. Peeters, H. M. Janssen, M. H. Bakker, J. O. Fledderus, M. Teraa, M. C. Verhaar, H. Gremmels, and P. Y. W. Dankers. The in-vitro biocompatibility of ureidoâpyrimidinone compounds and polymer degradation products. *J. Polym. Sci.*, 59(12):1267–1277, 2021.

[204] O. J. G. M. Goor, S. I. S. Hendrikse, P. Y. W. Dankers, and E. W. Meijer. From supramolecular polymers to multi-component biomaterials. *Chem. Soc. Rev.*, 46(21):6621–6637, 2017.

[205] P. Y. W. Dankers, M. C. Harmsen, L. A. Brouwer, M. J. A. Van Luyn, and E. W. Meijer. A modular and supramolecular approach to bioactive scaffolds for tissue engineering. *Nat. Mater*, 4(7):568–574, 2005.

[206] P. Y. W. Dankers, G. Maria, L. H.-V. Gemert, H. M. Janssen, E. W. Meijer, and A. W. Bosman. Modular bioresorbable or biomedical, biologically active supramolecular materials, U.S. Patent No. 8883188 2006.

[207] C. Heinzmann, U. Salz, N. Moszner, G. L. Fiore, and C. Weder. Supramolecular Cross-links in Poly(alkyl methacrylate) Copolymers and Their Impact on the Mechanical and Reversible Adhesive Properties. *ACS Appl. Mater. Interfaces*, 7(24):13395–13404, 2015.

[208] M. Liu, Z. Wang, P. Liu, Z. Wang, H. Yao, and X. Yao. Supramolecular silicone coating capable of strong substrate bonding, readily damage healing, and easy oil sliding. *Sci. Adv.*, 5(11):eaaw5643, 2015.

[209] T. Mes, A. Serrero, H. S. Bauer, M. A. J. Cox, A. W. Bosman, P. Y. W. Dankers, and Meijer E. W. Supramolecular polymer materials bring restorative heart valve therapy to patients. *Mater. Today*, 52:175–187, 2022.

[210] A. M. Pekkanen, R. J. Mondschein, C. B. Williams, and T. E. Long. 3d Printing Polymers with Supramolecular Functionality for Biological Applications. *Biomacromolecules*, 18(9):2669–2687, 2017.

[211] S. Chen, L. Sun, X. Zhou, Y. Guo, J. Song, S. Qian, Z. Liu, Q. Guan, E. M. Jeffries, W. Liu, Y. Wang, C. He, and Z. You. Mechanically and biologically skin-like elastomers for bio-integrated electronics. *Nat. Commun.*, 11:1107–1119, 2020.

[212] Q. Chen, C. Huang, R. A. Weiss, and R. H. Colby. Viscoelasticity of Reversible Gelation for Ionomers. *Macromolecules*, 48(4):1221–1230, 2015.

[213] N. Jiang, H. Zhang, P. Tang, and Y. Yang. Linear Viscoelasticity of Associative Polymers: Sticky Rouse Model and the Role of Bridges. *Macromolecules*, 53(9):3438–3451, 2020.

[214] N. Jiang, H. Zhang, Y. Yang, and P. Tang. Molecular dynamics simulation of associative polymers: Understanding linear viscoelasticity from the sticky Rouse model. *J. Rheol.*, 65(4):3438–3451, 2021.

[215] T. Indei and J. Takimoto. Linear viscoelastic properties of transient networks formed by associating polymers with multiple stickers. *J. Chem. Phys.*, 133(19):194902, 2010.

[216] T. Koga and F. Tanaka. Theoretical Predictions on Normal Stresses under Shear Flow in Transient Networks of Telechelic Associating Polymers. *Macromolecules*, 43(6):3052–3060, 2010.

[217] H. M. James and E. Guth. Theory of the elastic properties of rubber. *J. Chem. Phys.*, 11(10):455–481, 1943.

[218] T. Indei, J. D. Schieber, and J. Takimoto. Effects of fluctuations of cross-linking points on viscoelastic properties of associating polymer networks. *Rheol. Acta*, 51(11):1021–1039, 2012.

[219] C. Schaefer and T. C. B. McLeish. Theoretical rheo-physics of silk: Intermolecular associations reduce the critical specific work for flow-induced crystallization. *J. Rheol.*, 66(3):515–534, 2022.

[220] D. J. M. Van Beek, A. J. H. Spiering, G. W. M. Peters, K. Te Nijenhuis, and R. P. Sijbesma. Unidirectional Dimerization and Stacking of Ureidopyrimidinone End Groups in Polycaprolactone Supramolecular Polymers. *Macromolecules*, 40(23):8464–8475, 2007.

[221] L. Kan, P. Zhang, H. Jiang, S. Zhang, Z. Liu, X. Zhang, N. Ma, D. Qiu, and H. Wei. Microphase separation of a quadruple hydrogen bonding supramolecular polymer: effect of the steric hindrance of the ureidopyrimidone on their viscoelasticity. *RSC Adv.*, 9(16):8905–8911, 2019.

[222] M. Ahmadi, A. Jangizehi, and S. Seiffert. Backbone Polarity Tunes Sticker Clustering in Hydrogen-Bonded Supramolecular Polymer Networks. *Macromolecules*, 55(13):5514–5526, 2022.

[223] S. Tang, M. Wang, and B. D. Olsen. Anomalous Self-Diffusion and Sticky Rouse Dynamics in Associative Protein Hydrogels. *J. Am. Chem. Soc.*, 137(11):3946–3957, 2015.

[224] D. Amin, A. E. Likhtman, and Z. Wang. Dynamics in Supramolecular Polymer Networks Formed by Associating Telechelic Chains. *Macromolecules*, 49(19):7510–7524, 2016.

[225] M. R. Nobile and F. Cocchini. A generalized relation between mwd and relaxation time spectrum. *Rheol. Acta*, 47(5-6):509–519, 2008.

[226] G. Williams and D. C. Watts. Non-symmetrical dielectric relaxation behavior arising from a simple empirical decay function. *Trans. Faraday Soc.*, 66:80–85, 1970.

[227] M. S. Sulatha and U. Natarajan. Molecular dynamics simulations of PAA-PMA polyelectrolyte copolymers in dilute aqueous solution: Chain conformations and hydration properties. *Ind. Eng. Chem. Res.*, 51(33):10833–10839, 2012.

[228] L. Fetters, D. Lohse, and R. Colby. *Physical Properties of Polymers Handbook*. Springer, pp 447-454, 2007.

[229] F. Zhuge, J. Brassinne, C.-A. Fustin, E. van Ruymbeke, and J.-F. Gohy. Synthesis and rheology of bulk metallo-supramolecular polymers from telechelic entangled precursors. *Macromolecules*, 50(13):5165–5175, 2017.

[230] A. Winter and U. S. Schubert. Synthesis and Characterization of Metallo-Supramolecular Polymers. *Chem. Soc. Rev.*, 45(19):5311–5357, 2016.

[231] Y.-L. Rao, V. Feig, X. Gu, G.-J. N. Wang, and Z. Bao. The effects of counter anions on the dynamic mechanical response in polymer networks crosslinked by metal-ligand coordination. *J. Polym. Sci., Part A: Polym. Chem.*, 55(18):3110–3116, 2017.

[232] R. Dobrawa and F. Würthner. Metallosupramolecular Approach toward Functional Coordination Polymers. *J. Polym. Sci., Part A: Polym. Chem.*, 43(21):4981–4995, 2005.

[233] Y. Wang, D. Astruc, and A. S. Abd-El-Aziz. Metallopolymers for advanced sustainable applications. *Chem. Soc. Rev.*, 48(2):558–636, 2019.

[234] S. Bernhard, J. I. Goldsmith, K. Takada, and H. D. Abrunña. Iron(II) and Copper(I) Coordination Polymers: Electrochromic Materials with and without Chiroptical Properties. *Inorg. Chem.*, 42(14):4389–4393, 2003.

[235] O. S. Wenger. Vapochromism in Organometallic and Coordination Complexes: Chemical Sensors for Volatile Organic Compounds. *Chem. Rev.*, 113(5):3686–3733, 2013.

[236] X. Zhang, B. Li, Z.-H. Chen, and Z.-N. Chen. Luminescence vapochromism in solid materials based on metal complexes for detection of volatile organic compounds (VOCs). *J. Mater. Chem.*, 22(23):11427–11441, 2012.

[237] M. Higuchi. *Metallo-Supramolecular Polymers: Design, Function, and Device Application.* Springer, pp 217-248, 2016.

[238] L. Voorhaar and R. Hogenboom. Supramolecular polymer networks: hydrogels and bulk materials. *Chem. Soc. Rev.*, 45(14):4013–4031, 2016.

[239] A. C. Jackson, F. L. Beyer, S. C. Price, B. C. Rinderspacher, and R. H. Lambeth. Role of Metal-Ligand Bond Strength and Phase Separation on the Mechanical Properties of Metallopolymer Films. *Macromolecules*, 46(14):5416–5422, 2013.

[240] F. Zhuge. *Synthesis and dynamics of metallo-supramolecular polymeric assemblies.* PhD thesis, Université catholique de Louvain, 2018.

[241] F. Zhuge, L. G. D. Hawke, C-A. Fustin, J.-F. Gohy, and E. van Ruymbeke. Decoding the linear viscoelastic properties of model telechelic metallosupramolecular polymers. *J. Rheol.*, 61(6):1245–1262, 2017.

[242] J. S. Kim, K. Yoshikawa, and A. Eisenberg. Molecular-weight dependence of the viscoelastic properties of polystyrene-based ionomers. *Macromolecules*, 27(22):6347–6357, 1994.

[243] M. Ahmadi, L. G. D. Hawke, H. Goldansaz, and E. van Ruymbeke. Dynamics of Entangled Linear Supramolecular Chains with Sticky Side Groups: Influence of Hindered Fluctuations. *Macromolecules*, 48(19):7300–7310, 2015.

[244] L. Jiang, P. Griffiths, J. Balouet, T. Faure, R. Lyons, C.-A. Fustin, and G. P. Baeza. Magneto-Responsive Nanocomposites with a Metal-Ligand Supramolecular Matrix. *Macromolecules*, 48(19):7300–7310, 2015.

[245] D. G. Kurth and Higuchi M. Transition metal ions: weak links for strong polymers. *Soft Matter*, 2(11):915–927, 2006.

[246] B. G. G. Lohmeijer. *Playing LEGO with macromolecules: connecting polymer chains using terpyridine metal complexes.* PhD thesis, Eindhoven University of Technology, 2004.

[247] S. Schmatloch, A. M. J. van den Berg, A. S. Alexeev, H. Hofmeier, and U. S Schubert. Soluble High-Molecular-Mass Poly(ethylene oxide)s via Self-Organization. *Macromolecules*, 36(26):9943–9949, 2003.

[248] Y. Li. *Dynamics of metallosupramolecular polymers and networks.* PhD thesis, Université catholique de Louvain, 2023.

[249] A. E. Martell and R. D. Hancock. *Metal complexes in aqueous solutions.* Plenum Press, New York, 1996.

[250] H. Irving and R. J. P. Williams. The stability of transition-metal complexes. *J. Am. Chem. Soc.*, pages 3192–3210, 1953.

[251] D. Walsh and P. Zoller. *Standard Pressure-Volume-Temperature Data for Polymers.* CRC, Lancaster, 1995.

[252] R. Lyons, L. Hammer, A. André, C.-A. Fustin, R. Nicolaÿ, and E. van Ruymbeke. Equilibration dynamics of a dynamic covalent network diluted

in a metallo-supramolecular polymer matrix. *J. Rheol.*, 66(6):1349–1364, 2022.

[253] Y. Li, C. Pyromali, F. Zhuge, C.-A. Fustin, J.-F. Gohy, and E. van Ruymbeke. Dynamics of entangled metallo-supramolecular polymer networks combining stickers with different lifetimes. *J. Rheol.*, 66(6):1203–1220, 2022.

[254] F. R. Schwarzl. Numerical calculation of storage and loss modulus from stress relaxation data for linear viscoelastic materials. *Rheol. Acta*, 10(2):165–173, 1971.

[255] M. Nébouy, J. Morthomas, C. Fusco, L. Chazeau, S. Jabbari-Farouji, and G. P. Baeza. Mechanistic Understanding of Sticker Aggregation in Supramolecular Polymers: Quantitative Insights from the Plateau Modulus of Triblock Copolymers. *Macromolecules*, 55(21):9558–9570, 2022.

[256] V. Tirtaatmadja, K. C. Tam, and R. D. Jenkins. Superposition of oscillations on steady shear flow as a technique for investigating the structure of associative polymers. *Macromolecules*, 30(5):1426–1433, 1997.

[257] L. Pellens, R. G. Corrales, and J. Mewis. General nonlinear rheological behavior of associative polymers. *J. Rheol.*, 48(2):379–393, 2004.

[258] C. Pyromali, Y. Li, F. Zhuge, C.-A. Fustin, E. van Ruymbeke, and D. Vlassopoulos. Nonlinear shear rheology of single and double dynamics metal-ligand networks. *J. Rheol.*, 66(6):1223–1235, 2022.

[259] L. F. Scherz, S. Costanzo, Q. Huang, D. A. Schlüter, and D. Vlassopoulos. Dendronized Polymers with Ureidopyrimidinone Groups: An Efficient Strategy To Tailor Intermolecular Interactions, Rheology, and Fracture. *Macromolecules*, 50(13):5176–5187, 2017.

[260] S. Liu, Y. Zhang, Z. Zhang, and Q. Chen. Nonlinear rheological behavior of telechelic ionomers with the distribution of ionic stickers at the ends. *J. Rheol.*, 66(1):1–16, 2022.

[261] R. Lyons. *Synthesis and rheology of double dynamic polymer networks based on metal-ligand interactions*. PhD thesis, Université catholique de Louvain, 2022.

[262] S. Wu, S. Liu, Z. Zhang, and Q. Chen. Dynamics of Telechelic Ionomers with Distribution of Number of Ionic Stickers at Chain Ends. *Macromolecules*, 52(6):2265–2276, 2019.

[263] P. G. Santangelo and C. M. Roland. Interrupted shear flow of unentangled polystyrene melts. *J. Rheol.*, 45(2):583–594, 2001.

[264] S. Costanzo, V. Ianniello, R. Pasquino, N. Grizzuti, G. Ianniruberto, and G. Marrucci. Strain Hardening of Unentangled Polystyrene Solutions in Fast Shear Flows. *Macromolecules*, 55(20):9206–9219, 2022.

[265] E. Vereroudakis, N. Van Zee, E. W. Meijer, and D. Vlassopoulos. Repeated shear startup response of a supramolecular polymer. *J. Non-Newton. Fluid Mech.*, 315:105021, 2023.

[266] F. Snijkers, K. Ratkanthwar, D. Vlassopoulos, and N. Hadjichristidis. Viscoelasticity, Nonlinear Shear Start-up, and Relaxation of Entangled Star Polymers. *Macromolecules*, 46(14):5702–5713, 2013.

[267] G. Ianniruberto and G. Marrucci. Origin of Shear Thinning in Unentangled Polystyrene Melts. *Macromolecules*, 53(4):1338–1345, 2020.

[268] K. Hyun, M. Wilhelm, C. O. Klein, K. S. Cho, J. G. Nam, K. H. Ahn, S. J. Lee, R. H. Ewoldt, and G. H. McKinley. A review of nonlinear oscillatory shear tests: Analysis and application of large amplitude oscillatory shear (LAOS). *Prog. Polym. Sci.*, 36(12):1697–1753, 2011.

[269] J. Vermant, L. Walker, P. Moldenaers, and J. Mewis. Orthogonal versus parallel superposition measurements. *J. Non-Newton. Fluid Mech.*, 79(2-3):173–189, 1998.

[270] H. C. Booij. Influence of superimposed steady shear flow on the dynamic properties of non-Newtonian fluids. *Rheol. Acta*, 5(3):215–221, 1966.

[271] R. I. Tanner. Comparative studies of some simple viscoelastic theories. *Trans. Soc. Rheol.*, 12(12):155–182, 1968.

[272] J. M. Simmons. A servo-controlled rheometer for measurement of the dynamic modulus of viscoelastic liquids. *J. Sci. Instrum.*, 43(12):887–892, 1966.

[273] J. Mewis and G. Schoukens. Mechanical spectroscopy of colloidal dispersions. *Faraday Discuss. Chem. Soc.*, 65:58–64, 1978.

[274] J. Zeegers, D. van den Ende, C. Blom, E. G. Altena, G. J. Beukema, and J. Mellema. A sensitive dynamic viscometer for measuring the complex shear modulus in a steady shear flow using the method of orthogonal superposition. *Rheol. Acta*, 34(6):606–621, 1995.

[275] J. Vermant, P. Moldenaers, J. Mewis, M. Ellis, R. J. Garritano, and J. Mellema. Orthogonal superposition measurements using a rheometer equipped with a force rebalanced transducer. *Rev. Sci. Instrum.*, 68(11):4090–4096, 1997.

[276] A. Franck. *Orthogonal superposition on the ARES-G2.* Application note, APN035, 2013.

[277] C. M. Wong and A. I. Isayev. Orthogonal superposition of small and large amplitude oscillations upon steady shear flow of polymer fluids. *Rheol. Acta*, 28(2):176–189, 1989.

[278] Y. Kwon and A. I. Leonov. Remarks on orthogonal superposition of small amplitude oscillations on steady shear flow. *Rheol. Acta*, 32(1):108–112, 1993.

[279] D. W. Mead. Small amplitude oscillatory shear flow superposed on parallel or perpendicular (orthogonal) steady shear of polydisperse linear polymers: The MLD model. *J. Non-Newton. Fluid Mech.*, 195(2):99–113, 2013.

[280] J. Zhang, A. Jurzyk, M. E. Helgeson, and L. G. Leal. Modeling orthogonal superposition rheometry to probe nonequilibrium dynamics of entangled polymers. *J. Rheol.*, 65(5):983–998, 2021.

[281] G. Marrucci and G. Ianniruberto. Flow-induced orientation and stretching of entangled polymers. *Philos. Trans. R. Soc. London, Ser. A*, 361(1805):677–688, 2003.

[282] A. R. Jacob, A. S. Poulos, S. Kim, J. Vermant, and G. Petekidis. Convective cage release in model colloidal glasses. *Phys. Rev. Lett.*, 115(21):218301, 2015.

[283] S. S. Sung, S. Kim, J. Hendricks, C. Clasen, and K. H. Ahn. Orthogonal superposition rheometry of colloidal gels: time- shear rate superposition. *Soft Matter*, 14(42):8651–8659, 2018.

[284] Y. J. L. Lee, H. Jin, S. Kim, J. S. Myung, and K. H. Ahn. Brownian dynamics simulation on orthogonal superposition rheology: Time-shear rate superposition of colloidal gel. *J. Rheol.*, 65(3):337–354, 2021.

[285] International Organization for Standardization. *Plastics-Polymers/Resins in the Liquid State or as Emulsions or Dispersions-Determination of Viscosity Using a Rotational Viscometer with Defined Shear State*. ISO 3219:1995, Geneva, Switzerland, 1995.

[286] R. Tao and A. M. Forster. End effect correction for orthogonal small strain oscillatory shear in a rotational shear rheometer. *Rheol. Acta*, 59(2):95–108, 2020.

[287] I. M. Rasid, J. Ramirez, B. D. Olsen, and N. Holten-Andersen. Understanding the molecular origin of shear thinning in associative polymers through quantification of bond dissociation under shear. *Phys. Rev. Materials*, 4(5):055602, 2020.

[288] O. Hassager, K. Mortensen, A. Bach, K. Almdal, H. K. Rasmussen, and W. Pyckhout-Hintzen. Stress and neutron scattering measurements on linear polymer melts undergoing steady elongational flow. *Rheol. Acta*, 51(5):385–394, 2012.

[289] M. Geri, B. Keshavarz, T. Divoux, C. Clasen, C. J. Curtis, and G. H. McKinley. Time-resolved mechanical spectroscopy of soft materials via optimally

windowed chirps. *Phys. Rev. X*, 8(6):041042, 2018.

[290] J. D. J. Rathinaraj, J. Hendricks, G. H. McKinley, and C. Clasen. Orthochirp: A fast spectro-mechanical probe for monitoring transient microstructural evolution of complex fluids during shear. *J. Non-Newtonian Fluid Mech.*, 301:104744, 2022.

[291] M. Bouzid, B. Keshavarz, M. Geri, T. Divoux, E. Del Gado, and G. H. McKinley. Computing the linear viscoelastic properties of soft gels using an optimally windowed chirp protocol. *J. Rheol.*, 62(6):1037–1050, 2018.

Curriculum vitae

Alexis André earned a Master's degree in Chemical and Materials Science from Université catholique de Louvain (UCLouvain, Belgium) in June 2019. He conducted his Master's thesis in the research group of Pr. Evelyne van Ruymbeke (UCLouvain, Belgium), where he studied the extensional rheology of polymer melts. In September of the same year, he enrolled in a dual PhD program under the joint supervision of Prof. Evelyne van Ruymbeke and Prof. Christian Clasen (KULeuven, Belgium). His research, funded by DSM (Heerlen, The Netherlands), focuses on the linear and nonlinear rheology of model polymer melts.